IMPROVING THE INTEGRATION OF PHOTOVOLTAIC GENERATION ON DISTRIBUTION NETWORKS VIA ADVANCED CONTROL OF INVERTERS

A Dissertation
Presented to
The Academic Faculty

by

John Seuss

In Partial Fulfillment
of the Requirements for the Degree
Doctor of Philosophy in Electrical Engineering in the
School of Electrical and Computer Engineering

Georgia Institute of Technology
August, 2016

IMPROVING THE INTEGRATION OF PHOTOVOLTAIC GENERATION ON DISTRIBUTION NETWORKS VIA ADVANCED CONTROL OF INVERTERS

Approved by:

Dr. Ronald Harley, Advisor
School of Electrical and Computer Engineering
Georgia Institute of Technology

Dr. Deepakraj Divan
School of Electrical and Computer Engineering
Georgia Institute of Technology

Dr. Santiago Grijalva, Co-Advisor
School of Electrical and Computer Engineering
Georgia Institute of Technology

Dr. J. Rhett Mayor
School of Engineering
Georgia Institute of Technology

Dr. Magnus Egerstedt
School of Electrical and Computer Engineering
Georgia Institute of Technology

Dr. Lukas Graber
School of Engineering
Georgia Institute of Technology

Date Approved: July 27, 2016

TABLE OF CONTENTS

LIST OF TABLES

LIST OF FIGURES

LIST OF SYMBOLS AND ABBREVIATIONS

PV	Photovoltaic
QSTS	Quasi-Static Time-Series
CAISO	California Independent System Operator
ANSI	American National Standards Institute
MW	Megawatt
ANSI	American National Standards Institute
IGBT	Insulated-Gate Bipolar Transistor
pu	Per-Unit
PCC	Point of Common Coupling
OPF	Optimal Power Flow
EPRI	Electric Power Research Institute
PD	Protection Device
HC	Hosting Capacity
LHC	Locational Hosting Capacity
EOL	End of Line
CPUC	California Public Utilities Commission
LDC	Load Duration Curve
MPPT	Maximum Power Point Tracking

SUMMARY

The number of new rooftop photovoltaic (PV) installations has been unprecedented in recent years and utility distribution networks are beginning to experience negative impacts caused by large amounts of distributed PV generation. In particular, distribution lines experience voltage fluctuations caused by reverse power flows and poor coordination between PV systems and existing voltage regulation. These violations limit the amount of PV that can be installed on a network since utilities must approve each new PV interconnection under the presumption that it will not adversely impact the distribution network.

The first goal of the research presented in this dissertation is to investigate whether a PV installation size may be limited by any adverse effect it may have on distribution network protection. The research concludes that protection issues caused by PV can be readily detected or prevented in most cases.

The focus of the research is then shifted to the study of advanced inverter functions that will aid in mitigating the impact of more common network problems caused by PV generation. Several local inverter control strategies are simulated in the quasi-static time-series (QSTS) domain on real-world distribution networks. A parametric study is performed on each inverter control strategy's settings to determine the range of effectiveness of these advanced control functions.

Lastly, several control strategies are selected to study the simultaneous control of many PV distributed throughout a distribution network to mitigate network over-voltages. Trade-offs are explored between the effectiveness, cost, and fairness of the local inverter controls and centralized control strategies that necessitate a communication infrastructure.

1. INTRODUCTION AND SCOPE

1.1 Motivation

The generation of electricity by distributed, customer-owned photovoltaic (PV) panels has increased dramatically in recent years and is projected to continue to increase in years to come. In August, 2015, the California Independent System Operator (CAISO) reported a utility-scale solar generation peak of 6.39GW, which rivals the output of several large traditional generation plants. However, this is just the PV generation comes from large solar arrays installed far from load centers that are deemed "centralized" plants rather than the small "distributed" PV generation that is commonly found at residential and commercial loads. In fact, the majority of PV systems are distributed and the number of distributed PV installations is projected to rise in the near future [1]. One can even find residential feeders in Hawaii that consistently reverse the flow of electricity from the distribution network to the transmission network at times of peak PV generation. The drivers for this rise in distributed PV are a combination of sustainability, social, economic, and political trends. Early adopting consumers have largely been driven by government subsidies and a desire to help reduce greenhouse gas emissions rather than any cost savings PV can provide [2]. However, falling prices (from roughly $4/W in 2006 to $1/W in 2012) and increasingly efficient and reliable systems has made PV systems reach grid parity in several states and within a decade it will reach parity in most regions, which will further broaden their appeal.

With this increased adoption of distributed PV generation come challenges for the electric utility industry. Distribution utilities refer to the amount of PV on their networks as a *penetration level*, defined as the ratio of installed PV capacity to peak network load as a percentage. When the penetration of PV systems on a distribution network reaches around 25%, many utilities will hesitate to allow future installations without first studying any potential negative impacts more PV may have on the network. The negative impacts on the distribution grid due to large penetration levels of distributed PV that have been the focus of recent research are as follows [3-8]:

- Voltage rise – the capability of distributed PV to produce reverse currents in during certain times of the day means that line voltages will be higher in the downstream network. Most distribution networks lack the sensing and control to handle voltage rise caused by PV.
- Transient voltage variations – short-term voltage fluctuations may also occur with large PV power output transients due to passing clouds or clearing fog, which may occur faster than existing voltage regulating devices can react.
- Reduced effectiveness of protection devices – traditional overcurrent protection in radial distribution networks are not designed to account for distributed generation and there exist various circumstances whereby distribution breakers, reclosers, and fuses may not operate as expected under high PV output.
- Islanding issues – during outages, unintentional islands may be created by PV systems continuing to feed small sections of network and pose a danger to utility workers attempting to restore the grid connection.

Although the above list does not reflect every concern of the utility industry with regard to distributed PV, these issues are prevalent in much of the recent literature and appear to be the most crucial roadblocks to mass adoption of distributed PV. The impact PV has on distribution network voltage magnitudes are of particular concern as these issues are already being observed by utilities. However, it is unknown to what extent the protection and islanding issues may arise with greater PV penetration. Recent regulatory trends to require PV systems to remain connected and outputting during faults further increase their likelihood to impact network protection [9, 10]. Fortunately, regulatory changes are also being put in place that will allow the PV systems to mitigate many of the issues they cause. New PV interconnection standards are being written in California that will allow PV systems to actively regulate network voltage. These standards will utilize so-called “smart” or “advanced” inverter controls that most PV inverter manufacturers are already implementing in anticipation of the new interconnection requirements. Although many of the issues caused by PV can be easily mitigated through network upgrades [11], energy storage

systems [12], or additional volt-var devices [13], leveraging the PV inverters that already exist on the network minimizes the cost to the utility. The application of these advanced inverter controls strategies to mitigate issues caused by interconnecting distributed PV systems is the focus of this research.

1.2 Scope of the Research

The research presented in this dissertation is implemented on mathematical models of real-world distribution networks provided by utilities. In the research that studies how PV systems may interact with distribution protection schemes, fault studies are performed on each possible PV interconnection location to determine how large of a PV system must exist before problems arise. In total, millions of studies are conducted for all possible fault and PV locations, making dynamic simulations impractical. As such, the studies are performed assuming a steady-state model of a PV system under fault conditions.

In the research on advanced inverter control strategies, time-series load and irradiance data is used on time periods up to an entire year at one-second intervals. Performing dynamic simulation with millisecond time steps over these long time periods would be impractical. Therefore, the studies are performed in quasi-static time-series (QSTS) simulations, which produce a time-domain series of steady-state solutions based on previous solutions. The time series is called "quasi-static" because no differential equations or dynamic states are used. However, each solution is not independent of time since the state of network devices, such as voltage regulators and switches, can only be known be simulating all previous time steps.

1.3 Summary of Original and Novel Contributions

The work in this dissertation covers three research thrusts on the topic of integrating PV systems to the distribution network. Chapter 2 investigates the extent of risk posed by new PV installations to interfere with distribution network protection schemes. Chapter 3 studies how proposed advanced PV inverter functions can be implemented to mitigate negative impacts caused

by PV generation on distribution networks. In Chapter 4, the research is focused on mitigating only over-voltage violations caused by a large number of distributed PV systems.

The research on how PV systems may interfere with traditional distribution protection is original in the scale and complexity of networks studied. Real distribution feeder models are used and exhaustive fault studies are performed for each possible PV interconnection. Four different protection violation types are identified simultaneously. A simplified model is developed to approximate the steady-state fault current injection from PV systems to avoid dynamic simulation. Also, to limit the dimensionality of the problem, the change in fault current magnitude due to PV size as measured by protection devices is interpolated with least-squares regression. Without this approximation, the scale of the study is computationally impractical.

The research thrust that studies the impact of advanced inverter control parameters on measurable network impacts is again unique in the scale of the work that is simultaneously compared. This research investigates and compares five different PV inverter control strategies at several interconnection locations on multiple real-world distribution feeder models. This research studies the steady-state impact of the inverter controllers and thus employs a QSTS analysis on each unique parameter setting and interconnection location. In analyzing the results of the parametric study, a novel method is employed to maximize the range of parameters for each control that achieves an objective function threshold.

The last research area presented in this dissertation investigates the level of PV generation curtailment necessary to mitigate voltage rise due to PV generation using real-world feeder models and real-world QSTS data. This research investigates the effectiveness of PV inverter real power curtailment controls applied simultaneously to thousands of PV systems interconnected at every load in a distribution network. This approach makes the research unique in that it directly compares the measureable cost of the control (curtailment of PV generation) to its effectiveness (number of over-voltage violations over a time period) as well as to the fairness of how the control strategies

affect different customers. Two novel centralized control strategies that assume the existence of a robust communication network are compared in addition to three local well-established control strategies. This research concludes that real power curtailing controls are effective at preventing network over-voltages and actually allow more PV generation to be installed across the distribution network.

1.4 Research Goals

The work presented in this dissertation is split between three distinct research thrusts. The specific goal, or research question to be answered, of each thrust is described here for clarity.

- The goal of the research in Chapter 3, on the impact of PV systems on distribution protection, is to find the specific size of a single new PV system that will interfere with the existing distribution network protection scheme.
- The goal of the research in Chapter 4, on tuning advanced PV inverter controls, is to determine whether there exist general control parameter settings that may be applied to recently-proposed advanced inverter controls. Such general parameters should allow the control strategies to improve distribution network operations for a large PV system placed anywhere in the network.
- The goal of the research in Chapter 5, on the interactions of distributed advanced inverter controls, is to compare the effectiveness of local advanced inverter control strategies to centralized, communication-based control strategies. Real power control strategies are the primary focus of this chapter, but a reactive power control is also tested and compared.

2. LITERATURE REVIEW

2.1 Assessing Distribution Network PV Hosting Capacity

The overarching goal of this research is to increase the amount of PV that can be installed on a network without causing an operational violation from the network owner's perspective. This PV installation limit, or hosting capacity, depends on many different factors in the construction and control of a distribution network and the PV on it. The determination of how close a network is to this limit has become important as the number of PV installation permit requests increase and utilities become bogged down in interconnection studies [14]. Utilities are therefore interested in knowing which factors limit PV hosting the most [15]. However, this is no trivial task due to the high variability in PV system sizes, inverter behavior, and forecasted irradiance [16].

In [17], the hosting capacity of a distribution network is defined as the amount of PV that can be placed on it before violating one the utility's reliability standards. In the United States, the American National Standards Institute (ANSI) and IEEE standards are commonly used as safe operating guidelines by utilities and are what will determine the hosting capacity of a distribution feeder. Similarly, in [18] and [19], the hosting capacity of a network is defined by the point at which the UK grid codes are violated by PV systems operating on it. The research presented in [20] indicates that the total harmonic distortion injected by inverters is the limiting factor in network hosting capacity. However, due to the variable nature of inverter manufacturing practices [21] and improvements in inverter harmonics [3], inverter harmonics seem to be preventable in practice. One problem with some research on determining hosting capacity is the assumption of a three-phase balanced system. Due to the highly unbalanced and unpredictable nature of some distribution network loads, only detailed three-phase models should be studied [22]. In fact, some extreme PV placement arrangements may even lead to network balancing issues [5]. The latter issue would be an example of a degradation in network protection, as it could result in a trip of a power circuit breaker [4]. However, it is more likely for PVs to impact the overcurrent protection on a network as they can have undesirable fault current contributions [21, 23]. In particular,

protection devices can be “desensitized” and not trip for a fault that should be within their protection zone [8, 24] or even break down the coordination of which protection device should trip first [25].

Ultimately, the distribution line current rating will prevent the placement of large PV at many locations in a network. However, it is likely that PV systems will cause temporary voltage violations at PV ratings well below the rating of the distribution line. But, using the strict definition of *any* violation in standards does not take into consideration the severity of the violation. In fact the most frequent violations are short excursions in voltage that might be easily rectified by adjusting a voltage regulator setting or the PV inverters themselves [3]. In the interest of this research, the PV hosting capacity of a distribution network is defined as the maximum amount of PV that can be interconnected without causing steady-state violations of ANSI standards.

2.2 Improving Hosting Capacity via Distribution Network Voltage Control

A distribution utility must maintain a certain range of acceptable voltage magnitude supplied to its customers in order to protect customer property. In the United States, these ranges are outlined by the standard ANSI C84.1 [26], which maintains that the voltage supplied by the utility in steady-state must be within 5% of the nominal, or on a per-unit basis $0.95 \leq V \leq 1.05$. This is the so-called Range-A voltage standard. The voltage may deviate from this range temporarily, but it must be actively controlled back within the range. The traditional devices for performing this control on distribution networks are step-voltage regulators and switched capacitor banks [27, 28].

The placement and control of capacitors and voltage regulators is a classic optimization problem in power systems and has been solved many ways. In [29] the problem is decoupled such that capacitors provide optimal reactive power compensation and regulators provide optimal voltage regulation. In [30], new power flow equations are developed for radial distribution networks so that it may be solved as a mixed-integer programming problem. The voltage control problem has also been revisited with more modern techniques, such as the computation intelligence methods of discrete particle swarm optimization and genetic algorithms presented in

[31]. The methods developed in these classic voltage regulation problems lend insight on how best to utilize the reactive power capabilities of the PV inverters to the same end.

2.3 Reactive Power Capabilities of PV Grid-Tie Inverters

The inverters that connect PV systems to the distribution network are power electronic devices that use high power switching transistors, such as IGBTs, to convert the DC power produced by the PV panels to AC for use in the power system. Inverters come in two general types: current-source and voltage-source. These designations indicate how the inverter behaves from the system perspective. Most PV inverters connected to the utility grid are current-source inverters since they assume the existence of a strong grid. These inverters are capable of producing reactive power by shifting the phase angle of the current they produce relative to the voltage at their point of common coupling (PCC) to the grid. The amount of reactive power a PV inverter is capable of producing is limited by the thermal rating of the inverter and its real power output. The PV panels send real power to the inverter based on the variable solar irradiance, $I(t)$, and the maximum power point of the panels, P_{MPP}. These relationships are described in (2.1)-(2.2) and Figure 2.1.

$$p_i^g(t) = P_{MPP} I(t) \tag{2.1}$$

$$q_i^{g,max}(t) = \sqrt{\left(S_i^{rated}\right)^2 - \left(p_i^g(t)\right)^2} \tag{2.2}$$

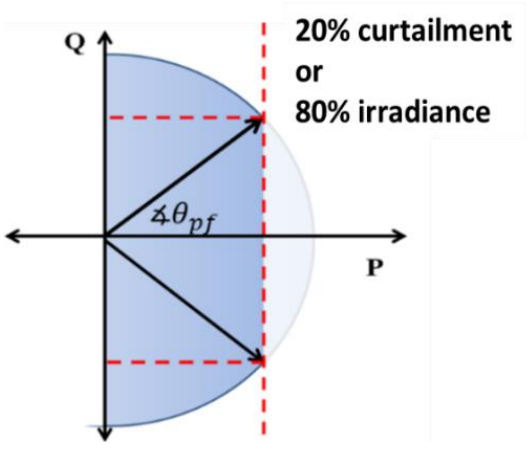

Figure 2.1 Theoretically feasible region of power output for a PV inverter under 90% rated insolation.

Assuming real power through the inverter is prioritized (i.e. "watt-priority control"), then the reactive power capability is time-dependent as in (2.2). Prioritizing real power (2.1) creates the vertical constraint in Figure 2.1 and additional power factor constraints may apply based on the particular inverter. If the inverter is sized larger than the P_{MPP} of the PV panels, then there will always be some reactive power available. Studies have shown this is not only beneficial for voltage control [32], but also may be economically advantageous [33].

2.4 Options for Control of PV Grid-Tie Inverters

There are many different strategies for how to control PV inverters, but at a high level they can be broken down into three general categories based on the amount real-time information about the network that is available [34]: local control, centralized control, and distributed control. Figure 2.2 demonstrates the differences in these control types [35]:

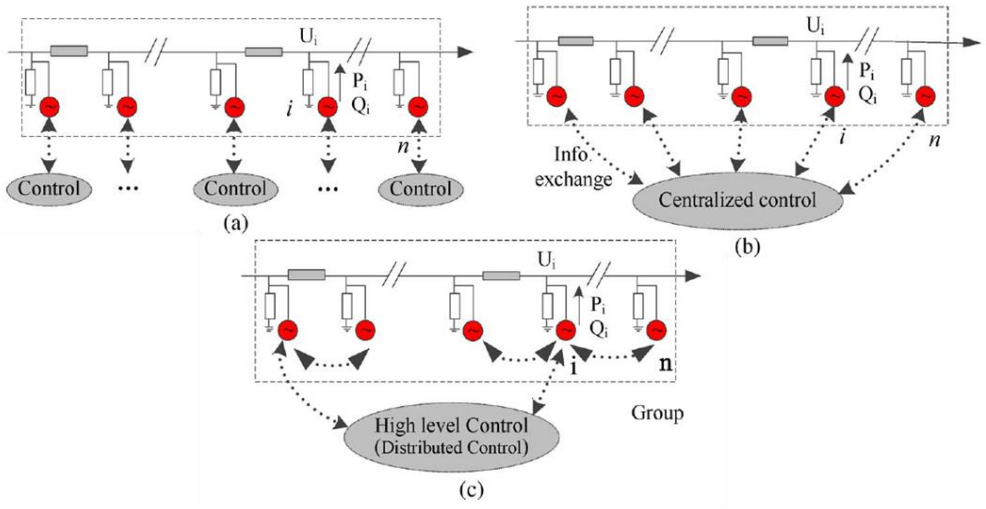

Figure 2.2. (a) Local control, (b) centralized control, and (c) distributed control.

Local control is unilateral, as shown in Figure 2.2(a), depends solely on measurements taken locally at the site of the inverter and therefore there is no coordination between inverters in the network. Figure 2.2(b) shows the configuration of a centralized control architecture where each PV system is assumed to communicate with a controller that then determines the optimal output of each. In fact, with such a communication infrastructure, one can even assume timely knowledge

of any network element in order to achieve a truly optimal control [36]. Lastly, Figure 2.2(c) demonstrates a distributed control, which assumes *some* communication exists between the distributed PV systems and possibly a higher-level controller. A review of recent research utilizing each of these control strategies is presented in the following sections.

2.5 Optimal Dispatch of PV Inverter Reactive Power

The best case scenario for controlling PV inverters is when full communication with each inverter can be assumed. The optimal control of the inverter reactive power output is similar to that of the optimal dispatch of large generator power, or optimal power flow (OPF), only subject to the PV system constraints. Due to the relatively fast dynamics of PV inverters in comparison to the rest of the power system, the optimal dispatch solution can be used as reference signal for PV controllers to follow throughout the day [37].

In general, the OPF problem is non-convex and is therefore very difficult to solve. In [38] the optimization is solved using a linearized system of equations, making it an approximation at best. In [39-42] the problem is relaxed into a convex optimization problem by assuming a balanced network and solved with mixed-integer linear programming techniques. However, the balanced assumption is not well suited for distribution networks and the relaxation of the problem introduces approximations. In contrast, sequential quadratic programming is used in [43] to solve the optimal real and reactive power dispatch in an unbalanced distribution system, however the system equations and objective functions must be modified to fit the solution method. There are other options for optimization objectives as well as solution methods. In [44, 45], heuristic search approaches are used to control PV inverter outputs in order to minimize the number of voltage regulator and capacitor operations in addition to line losses. In all of these studies, however, there is an assumption that a sophisticated communication and sensor network exists on the distribution network, when in practice this is very unlikely.

2.6 Local Control of PV Inverters

Voltage regulation can still be achieved with no communication between PV systems. There are already standard reactive power control modes being made available on modern PV inverters that utilize local measurements. The most common local control modes are constant power factor, Volt-Watt, and Volt-Var controls [16, 46]. Local Volt-Var controls apply a "droop" curve, such as the one in Figure 2.3, to adjust the PV inverter's reactive power output based on the measured voltage at the PCC [47]. Positive vars are capacitive and will boost the voltage at the PCC Negative vars are inductive and lower the voltage. There is an optional deadband shown in Figure 2.3 where there inverter will remain at unity power factor for voltages near nominal at the PCC. The droop curve slope and deadband width alter the effectiveness of the voltage regulation [48].

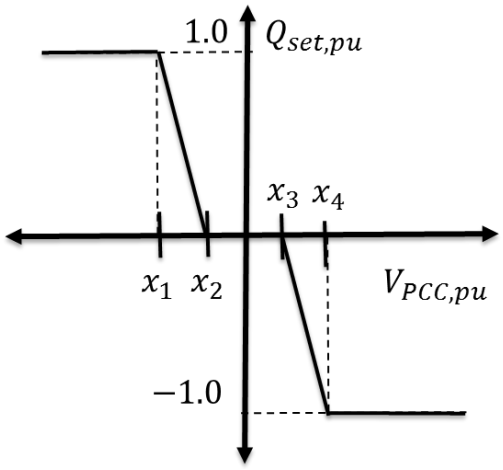

Figure 2.3. Example of a Volt-Var droop curve used to locally control a PV inverter.

The research in [47] and [49, 50] indicates that a Volt-Var droop control is capable of minimizing the voltage variation of the PCC due to the real power output of the PV system. This is also shown in [51], yet so far these works only focus on controlling a single PV system on a distribution network. More sophisticated local controls include fuzzy controllers that update the amount of reactive power to output based on historical success [52] and local controllers that leverage some static knowledge of the network [53]. However, it is yet to be fully understood how many PV inverters on a network may negatively interact while using these various local control strategies. The research in [54] suggests there is indeed a stability limit between two locally

controlled inverters whereupon they begin to oscillate. This is also found to be the case in [55], which finds that local voltage mitigation alone may result in undesirable reactive power levels in the distribution feeder as a whole.

2.7 Distributed Control of PV Inverter Reactive Power

If some limited communication is available then negative issues among many PV may be averted. The idea of using local area communications to coordinate the control of a group of geographically dispersed systems is derived from networked control theory [56] and has the benefit of being scalable and computationally efficient even for large numbers of systems [57]. The work in [58] shows this theory can be applied to PV systems in a distribution network and that their inverters will converge to a shared operating point under well-defined communication requirements. Furthermore, the work in [59] relaxes the communication requirements into geographically hierarchical subsystems so that the control can be applied at different scales, such as within a neighborhood or across a town. The work in [60] demonstrates a similar control strategy and tests the factors limiting the speed of convergence among PV systems outputs. However, none the controls shown in these works consider how this method of control might be used to regulate network voltage.

2.8 Averaged and Steady-State Approximations of Dynamic Inverter Models

Due to the nature of the research performed in this dissertation, it is impractical to perform dynamic analyses of the PV system. This research investigates the connection of PV generators and inverters at many locations in large distribution networks under many different operating conditions. Furthermore, the metrics that determine a PV system's impact on a distribution network can be considered to be steady-state values at the time scale of the PV system's dynamics. Therefore, a steady-state PV model is used, which is derived from the averaged dynamics of the PV inverter's controllers. A review of steady-state PV system models used in recent literature is summarized next and then the model used in this research is presented.

In its most detailed form, a PV system may be modeled at the "switching-level" as shown in Figure 2.4 [61]. At this level, the inverter IGBTs are driven by several kilohertz switching signals which interact with the electromagnetic dynamics of the other inverter elements. These simulations must use very small time steps and are very time consuming. For this reason, these models are not practical to be used in large distribution network models since each time step also requires a power flow solution. Alternatively, a so-called "averaged" dynamic model can be used, as shown in Figure 2.5. This model assumes the inverter controls work as intended and only considers the slower control-loop dynamics and how they interact with network conditions.

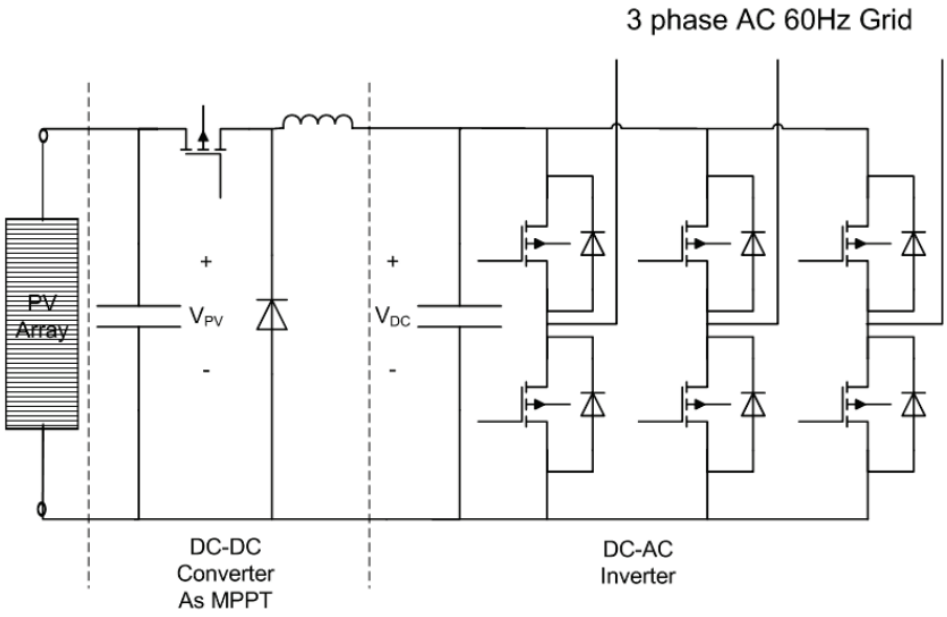

Figure 2.4. Switching-level model of PV system [57].

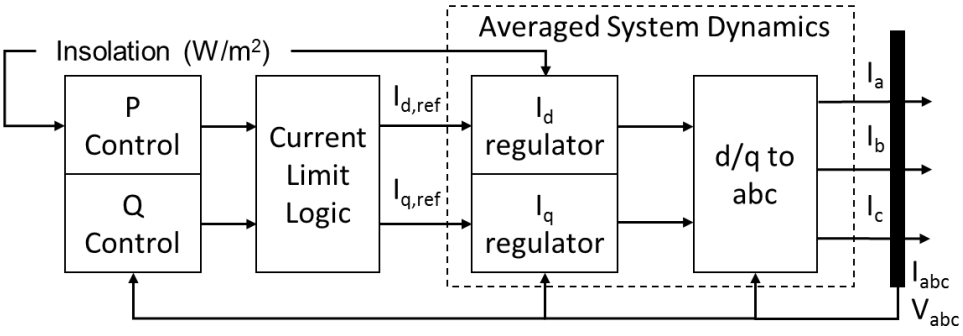

Figure 2.5. Averaged dynamic model of PV System.

The “P Control” and “Q Control” boxes in Figure 2.5 are designed in this research. The “averaged system dynamics” in steady-state are simply a variable current-source that achieves (2.1) in normal operation. However, it is of interest to model the PV system in emergency, or faulted, operation as well. The output of a PV inverter into a network fault is not yet well established in the literature.

The research in [62] implements a full switching-level dynamic model of a PV inverter. The control of the inverter is such that it behaves as a current source, which is typical for utility connected inverters. Under a short-circuit fault, the current-source inverter injects roughly 1.3 pu steady-state current due to the controller’s response to low voltage. This research [60] also shows, however, that an inverter controlled as a voltage source can produce roughly 2.0 pu rated current in steady-state while under a short-circuit fault.

In [20], the PV system is modeled as an ideal voltage source behind a reactance such that 2.05 pu rated current is provided under a short-circuit. This is the short-circuit value provided by the inverter manufacturer. However, using this approach it is not clear that the PV model will even output rated current for any given fault condition in the network without some additional logic to control the voltage source impedance.

In [23], an average dynamic model is used that simulates the time-domain currents under faulted conditions. For a short-circuit fault at the terminals of the inverter, the inverter immediately increases its output to over 3.0 pu rated current before settling down to around 2.0 pu rated current in five cycles. In work by the same authors [25], a current source is used to assess protection coordination issues at 2.0 pu rated current. This value is obtained from the IEEE Guide for Conducting Distribution Impact Studies for Distributed Resource Integration (IEEE-1547.7 [63]), however, the example data provided only lists PV inverter fault contributions at 1.07 pu rated current. Only the *energy storage* inverter data is listed as providing fault contributions at 2.0 pu rated current.

In [64] several actual inverters are experimentally tested under fault conditions. The report concludes that although current magnitudes between two and four times rated current are seen, they are very short-term and may be ignored from a protection standpoint. Testing for steady-state current contribution while the inverter is required to stay online during a fault resulted in the inverter producing 1.2 pu rated current.

Finally, in [24], the authors present the PV system as a current-limited constant power source operating at unity power factor. The authors claim this approximation has been verified with the simulation of a detailed model in PSCAD. Under this assumption, the PV system behaves as a current-limited generator of constant power. However, the authors use a current source that iteratively converges to a steady-state output based on how V_{PCC} changes. With either approach, this assumption makes sense considering the inverter has a maximum power point tracking (MPPT) control that is always adjusting the inverter's current reference to output all power available to the PV panels. This behavior is indicated in Figure 2.5 by the "P control" and "I_d regulator" blocks. A generator model with its current-limited at 2.0 pu rated current is also used to study protection issues in [65].

From this literature review, a conservative conclusion is made that the PV system may be modeled as a current-limited, constant-power current source. Thus, the PV output current I_{PV} is dependent on the size of the PV panels, P_{PV} and the voltage at the point of common connection (PCC), V_{PCC}:

$$|I_{PV}| = |I_{PV}| = \begin{cases} \dfrac{P_{PV}}{|V_{PCC}|}, & |V_{PCC}| \geq 0.5pu \\ \dfrac{2P_{PV}}{|V_{nom}|}, & |V_{PCC}| < 0.5pu \end{cases} \tag{2.3}$$

$$\angle I_{PV} = \angle V_{PCC}$$

Thus, the steady-state current-source model of a PV system used in this research is defined by equations (2.1)-(2.3). Further details of the implementation are provided along with the research.

2.9 Summary

This chapter has presented a literature review of potential negative impacts that large amounts of PV generation may have on distribution networks and how the PV inverters may be used to mitigate these effects. The next step in the research on how to best control PV inverters to mitigate their known effects, such as causing over-voltages, is to first investigate if there are other negative impacts caused by PV systems that are not well understood, such as how they affect overcurrent protection. The next chapter investigates the potential negative impacts that a large PV system (without advanced inverter controls) may have on existing overcurrent protection in a distribution network. As a result of the research in the next chapter, a reasonable upper limit may be set on the size of the PV system used in subsequent chapters studying PV generation's impact on distribution network voltage and how to mitigate its impact with advanced inverter controls.

3. LIMITATIONS TO PV SYSTEM HOSTING CAPACITY DUE TO DISTRIBUTION PROTECTION

3.1 Background and Introduction

The previous chapter presented a literature review of the potential negative impacts that a large amount of PV generation may have on a distribution network. Most research has focused on well-known effects such as voltage fluctuations, but there are several other concerns about large-scale PV integration that are not widely studied. In particular, this chapter investigates whether there is an upper limit to the size a PV system may be before it interferes with a distribution network's overcurrent protection. A PV system of this size would not be allowed to interconnect, but there is not much research on what this size limit should be and how it changes depending on feeder topology and interconnection location.

With the rising penetration of photovoltaic generation in distribution networks, utilities have become concerned about a range of potential negative impacts PV panels and the inverters used to interface them with the grid may have on system security and power quality. In 2007, the IEEE working group on distributed generation integration compiled a list of concerns that utilities voiced about customers connecting generation on traditionally radial distribution networks [66]. Most of the concerns raised apply to PV systems, which have become the preeminent source of generation on distribution networks in recent years. In 2008, Sandia National Labs independently tested and confirmed some potential issues, that distribution networks with increasingly high levels of PV penetration are facing [3]. A primary concern presented is the ability of PV systems to fluctuate the network voltage profile through real power generation throughout the day. Other issues investigated were how PV systems behaved during outages and how they could impact the system frequency. Further studies have been made on how high penetration PV affects the system voltage profile [7] and continue to investigate voltage imbalances [5] and harmonic distortions [20] that may arise. Another major area of concern is how PV will impact the effectiveness of utility protection equipment. It has been shown that PV generation can impact the fault current seen by

protection devices (PDs) [23]. This can adversely affect the protection zone of a PD as well as the time-dependent coordination between PDs [25]. Further studies have looked at the potential disruption caused by fault currents contributed by PV systems [8, 21, 24]. The following subsections narrow the scope of this chapter to research only how PV fault current injection may be an issue to the distribution network and specifically define issues to investigate.

3.1.1 Protection Issues within the Research Scope

The scope of this research thrust is on the impact of PV current injection on network PDs. However, power quality issues that may violate a standard, such as voltage deviations or harmonic distortions, are not considered. Also not considered are islanding issues since these focus on the PV devices. Lastly, the scope of this work is limited to steady-state network analysis, so any issues that require the dynamic or time-domain simulation of the PV system in the distribution network are also not considered. Therefore, of the issues found in a review of recent literature, the issues that fit within the scope of the research presented in this chapter are summarized below:

- Protection under-reach: The protection zone of a PD is the distance into the feeder that it can "see" a fault and it is carefully planned by a distribution network engineer. Certain placements of PV systems can diminish this zone by partially supplying the fault current rather than the transmission network. If this occurs, an investment is required to re-engineer the protection zone or place more PDs, else risk damaging utility and customer equipment [23].
- Loss of coordination: Similarly, a PV system placed upstream of a PD can increase the fault current seen by the PD. Therefore if a PV system is placed between two PDs, it may cause the downstream PD to trip before the upstream PD [25]. In the case of reclosers with "fuse-saving" fast trip settings, tripping the downstream fuse will result in a longer outage than necessary [67]. The converse may also be possible with an upstream PD tripping before a downstream PD, resulting in a greater number of customers losing power unnecessarily.

- Nuisance tripping: There is a concern that many distribution PDs do not have directional sensing and reverse current from PV systems during a fault may be large enough to trip a PD's minimum pick-up.
- Sympathetic tripping: A similar cause of nuisance tripping is due to a fault on a neighboring circuit. Reverse fault current supplied by PV systems may cause issues due to the differences in protection between the two feeders.

3.1.2 Distribution Overcurrent Protection

The focus of this research is the impact of PV generation on existing overcurrent protection devices in medium-voltage distribution networks. Real-world distribution feeder models from several utilities are used in this study. These feeders are modeled in the CYME distribution analysis software and then converted to OpenDSS by parsing through the CYME XML files and recreating feeder objects and connections in OpenDSS. The feeder overcurrent protection device types and settings are also included in the CYME models, but are not explicitly modeled in OpenDSS. Instead, the minimum pick-up time of each protection device (PD) is calculated as a function of current in Matlab by approximating time-current curves (TCC) responses based on the given settings. Only the minimum pick-up time of each PD, not its maximum clearing time, is considered in this research. Breaker, recloser, and fuse time-current curves (TCCs) are identified by the device settings and compared to the PD manufacturer data. Manufacturer manuals provide graphs of TCCs which are converted to a series of time-current points using image-processing software. Figure 3.1 shows the TCCs of the breakers and reclosers in one of the feeders studied. It should be noted that this research only considers the substation breaker and network reclosers as PDs. This feeder has one feeder breaker and seven reclosers. The solid lines represent the phase relay minimum pick-up curves and the dashed lines are the ground relay minimum pick-up curves. The

color grouping indicates devices that are parallel within the feeder and thus do not need to be coordinated. Ground TCCs do not need to coordinate with phase TCCs. The flat parts of the breaker curves are due to the manufacturer TCCs being ill-defined in the 1.0-2.0 pu minimum pick-up current region. From these lines, the minimum pick-up time of the relays is found by linearly interpolating between the digitized time-current points for the simulated measured fault current.

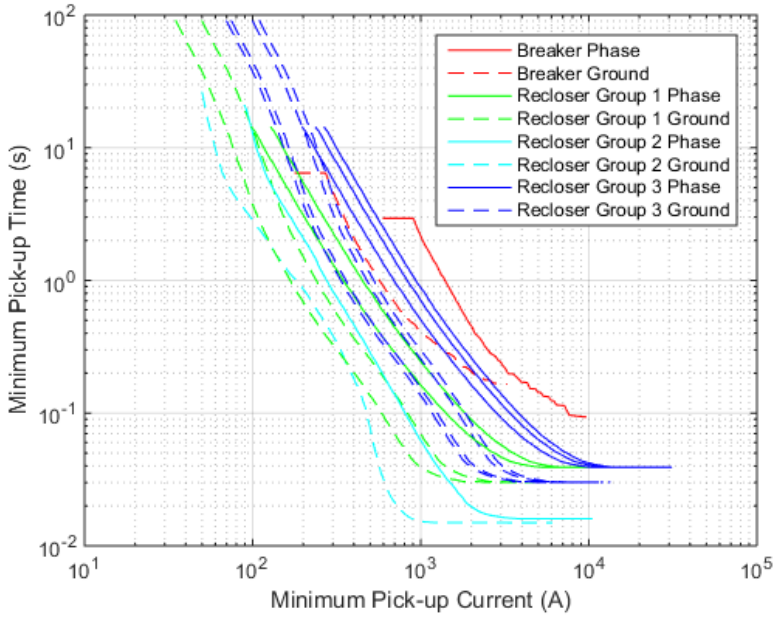

Figure 3.1. Example TCCs recreated from utility-provided protection information.

From the curves in Figure 3.1, depending on the magnitude of the fault current, the PDs may begin their tripping procedure in anywhere from tens of milliseconds to tens of seconds. PV inverters typically have controllers that operate at several kilohertz, meaning they should be capable of disconnecting before the fastest relays pick up. However, the inverter can only detect a fault due to abnormal voltage and frequency measurements. Based on the most recent IEEE PV interconnection standards [68], a PV system is only required to disconnect by 160ms for a severe fault that lowers its minimum measured terminal voltage below 0.45pu. A large PV disconnecting

at this time could certainly impact the timing of the curves in Figure 3.1. However, in considering the worst-case scenarios for how PV systems may impact network protection, one should consider the possibility that the PV protection may fail. Additionally, new PV interconnection standard proposals may require the PV systems to support the faulted network even beyond the slowest time of the TCCs, as can be seen in Figure 3.2. For these reasons, the PV systems are assumed to remain connected and continue to inject current into the grid during the duration of the fault.

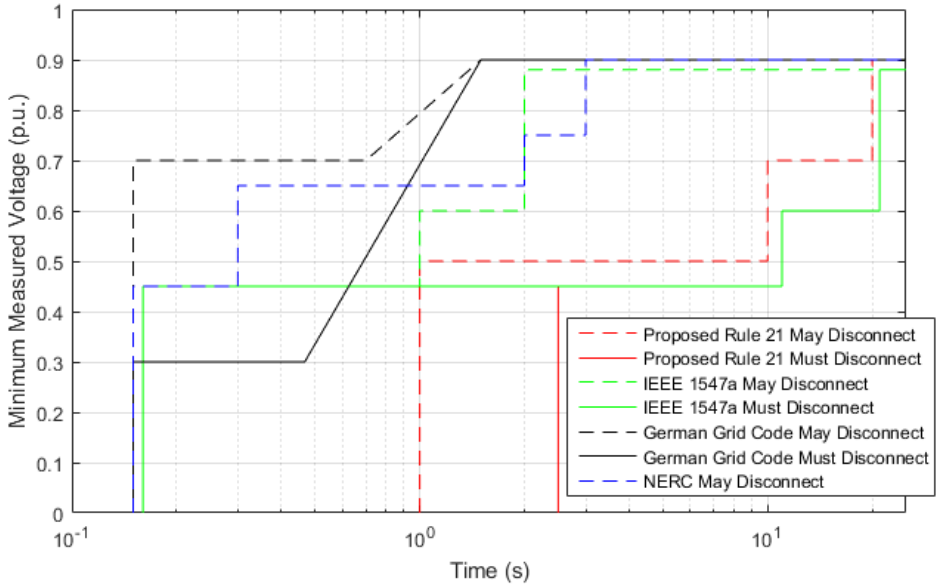

Figure 3.2. Most recent low-voltage ride-through recommendations for PV interconnections.

3.2 Identifying PV-Induced Protection Failures

The literature review in the previous section identified a number of concerns raised by electric utility companies and researchers about how PV systems may interfere with distribution protection. This section focuses the scope of the new research by clearly defining what is considered a protection violation within the context of this research. This section also presents the steady-state PV system model developed to work in the steady-state fault studies performed in this research.

3.2.1 Definition of Protection Violations Considered

As stated in the introduction, the scope of this research is limited to the steady-state analysis of distribution networks under fault conditions. This constrains the research to the study of how fault current injected by a PV system may alter base-case (no PV) fault current seen by network PDs and lead to a violation. Based on a review of literature, the specific definitions of the four possible protection violations used in this research are as follows:

1. Protection Under-Reach

   Each PD has a protection zone defined by the set of buses that when faulted produce a current greater than the minimum pick-up current of that PD. Both phase and ground currents are considered. An under-reach violation occurs when a fault that caused a PD to trip in the base case is no longer picked up by *any* PD. A graphical example of a PD failing experiencing decreased fault current due to a PV on the network is shown in Figure 3.3(a).

2. Coordination Loss

   It is assumed that the PV system fault current remains constant for the duration of the fault cleared by a PD. This is not an unreasonable assumption since the fast transient of the PV system only lasts a few cycles [23] while the fastest a time-characteristic curve (TCC) of a substation breaker will operate is several times slower than this transient. Using this assumption, the trip time of each PD is calculated using each PD's unique phase and ground TCCs. A "coordination violation" is declared if an upstream PD trips for a fault downstream of a PD downstream of it. Under this scenario more customers will be without power than in the base case with no PV. Fuse-saving failures are not considered in this research. A hypothetical example of an upstream PD picking up before a downstream PD due to their respective TCCs is depicted in Figure 3.3(b).

3. Sympathetic Tripping

   To simulate a close fault on a nearby feeder resulting in reverse current from the PV, a short line is added at the substation and faulted. A violation occurs when any PD in the

network picks up on its minimum trip setting for a particular PV size. A graphical depiction of sympathetic tripping is shown in Figure 3.4(a).

4. Nuisance Tripping

This issue occurs when the fault current of a PV causes a PD to trip in error due to reverse current flow. This can happen in two ways. Under normal operation, a PV can simply be so large that its rated current can pick up the PD under light loading conditions. Under a fault, a nuisance tripping violation occurs only when the PD tripping on reverse current trips faster than the PD designed to clear the fault and the fault must not be located downstream of the PD tripping in error. A graphical depiction of nuisance tripping is shown in Figure 3.4(b).

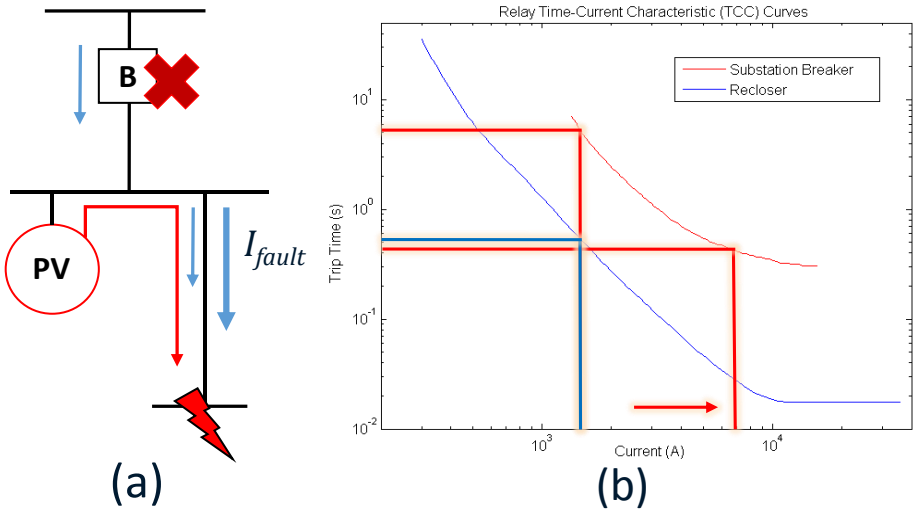

Figure 3.3. (a) Example of PV causing under-reach in breaker (b) Example of increased current seen by breaker causing coordination loss.

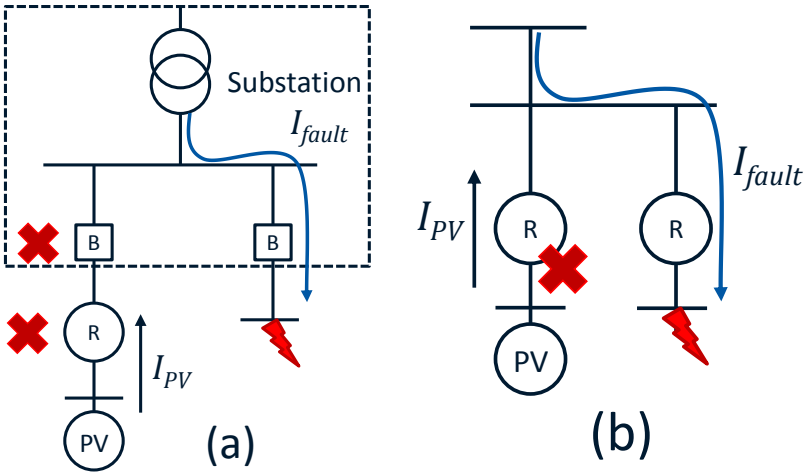

Figure 3.4. (a) Example of PV causing sympathetic tripping by back-feeding PDs to supply a nearby fault (b) Example of PV causing nuisance tripping by feeding a fault within its own network.

3.2.2 Feeder Protection-Limited Hosting Capacity Analysis Procedure

Each of the violations described in Section 3.2.1 are checked under the four fault types shown in Figure 3.5. The network phases are depicted as bold black lines, ground as a dashed line, and the faulted connections in red.

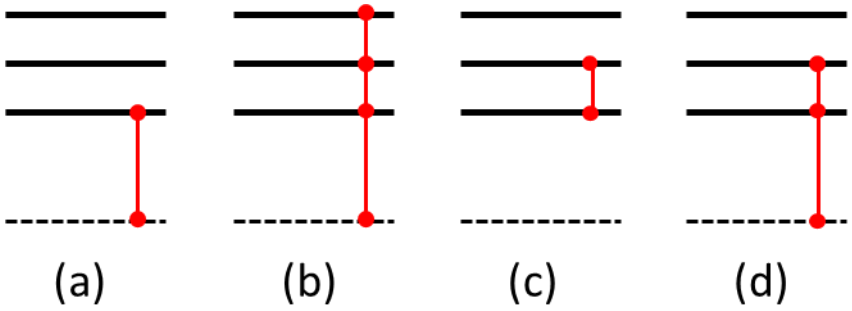

Figure 3.5. Fault types considered for analysis (a) Single-line-to-ground (1LG) (b) Three-line-to-ground (3LG) (c) Line-to-Line (LL) (d) Two-line-to-ground (2LG)

For each fault type, f, a 0.0001Ω resistance is placed between the appropriate phases and ground as depicted in Figure 3.5. For the 1LG fault type, faults are placed at the set of MV buses, B_1, which contain at least one phase. There are at most N_1 buses with at least one phase considered for fault placement in a given feeder. Only MV buses are considered since the fuses at the secondary transformer are not modeled and are presumed to trip for any fault on the secondary

network. Similarly, the 2LG and LL fault types are placed at the N_2 buses with at least two-phases, B_2, and 3LG faults are placed at the set of N_3 three-phase buses, B_3. Each PV interconnection, p, is tested at all MV three-phase buses, so there are N_3 total possible PV interconnection locations. The PV model is described in Appendixes A and B. Each PD phase, m, can measure the absolute value of current flowing through it and there are a total of M measured PD phases in the feeder.

The network variables of interest then are the change in fault current through each PD phase due to each PV for all fault placements and is a function of PV size, $\boldsymbol{I}_{p,f}(P_{PV}) \in \mathbb{R}^M$. Due to the high dimensionality of the problem, rather than quantifying $\boldsymbol{I}_{p,f}(P_{PV})$ through simulation, it is approximated as a set of polynomials, as described in (3.1). Section 4.2 details the procedure by which the coefficients $\boldsymbol{c}_{p,f,i}$ are determined. The current measurement $\boldsymbol{I}_{p,f}(P_{PV})$ is a vector of length M, as indicated by the bold font. Subsequently, the coefficients $\boldsymbol{c}_{p,f,i}$ are also vectors of length M for each PV and fault location.

$$\boldsymbol{I}_{p,f}(P_{PV}) \approx \hat{\boldsymbol{I}}_{p,f}(P_{PV}) = \boldsymbol{c}_{p,f,1}P_{PV}^3 + \boldsymbol{c}_{p,f,2}P_{PV}^2 + \boldsymbol{c}_{p,f,3}P_{PV} + \boldsymbol{c}_{p,f,4} \tag{3.1}$$

When a particular PV size is back-substituted in (3.1), the result is a 3-dimensional matrix, $\hat{\boldsymbol{I}}_f \in \mathbb{R}^{(PxN_FxM)}$, that approximates the fault current seen by each PD for each PV and fault placement at that particular PV size. This matrix is determined for each fault type in Figure 3.5. Once the fault current changes are known for all PV locations, faults, and PD phases, the impact the PV has on the operation of the PDs can be determined and protection violations identified. A series of logic tests are carried out at increments of PV size, ΔP, up to a maximum value, P_{max}, based on the voltage class of the feeder as shown in Table 3.1.

Table 3.1 PV system size ranges tested per feeder voltage class.

Feeder Voltage Class	$\Delta \boldsymbol{P}$ $(\boldsymbol{kW})$	$\boldsymbol{P_{max}}(\boldsymbol{MW})$
$< \boldsymbol{5kV}$	50	5
$\boldsymbol{5kV - 15kV}$	100	10
$> \boldsymbol{15kV}$	150	15

There are four logic tests corresponding to the four violation types described in Section 3.2.2. Each test identifies the set of PV interconnection locations that result in protection under-reach, V_{UR}, sympathetic tripping, V_{ST}, nuisance tripping, V_{NT}, and coordination loss, V_{CL}. Each of these sets of buses can be broken down further into subsets unique to each PD and/or fault type. The union of all test sets identifies the set of all PV interconnection locations that result in any protection violation as a function of PV size:

$$V(P_{PV}) = V_{UR}(P_{PV}) \cup V_{ST}(P_{PV}) \cup V_{NT}(P_{PV}) \cup V_{CL}(P_{PV}) \tag{3.2}$$

The percent of all PV locations that cause a violation can then be expressed as the cardinality (size) of the set of problematic interconnection locations over the total number of viable interconnection locations:

$$V_p(P_{PV}) = |V(P_{PV})|/N_3 \tag{3.3}$$

Since $V(P_{PV})$ in (3.3) is a set, the "absolute value" bars in this case indicate the cardinality, or number of elements, of the set. When (3.3) is plotted, the characteristic of the feeder's hosting capacity (HC) as limited by the PV's impact on protection can be seen. The magnitude of $V_p(P_{PV})$ must be monotonically increasing as it does not make sense to have a PV size that "fixes" a violation caused by a smaller PV size. An example plot of this value is shown in Figure 3.6. From this plot the overall feeder (HC) can be determined. This is the size of PV that can be placed anywhere in the feeder. The PV sizes and locations below the feeder HC are shaded in blue. The yellow region then shows the percent of the network that is still viable for PV placements even after violations have begun to appear. This is a general representation of how the locational hosting capacity (LHC) of individual buses differs from the feeder HC.

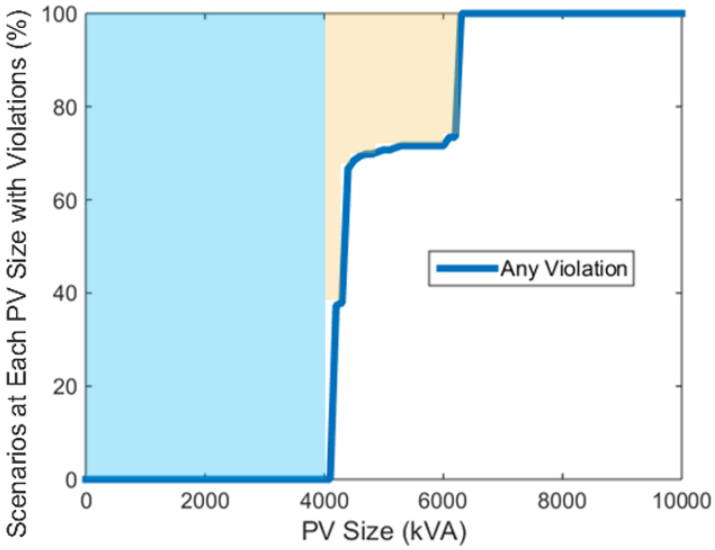

Figure 3.6. Example plot of $V_p(P_{PV})$ PV interconnection violations as a function of PV size with overall feeder hosting capacity (light blue area) and locational hosting capacity (light yellow area) identified.

Logic tests are performed on each $\hat{\boldsymbol{I}}_{\boldsymbol{pf}}$ to identify if any of the four violations described in Section 3.2.2 exist at a particular PV size. The logic tests for each violation are:

1. Under-Reach: The array of M minimum pick-up currents for each measured PD phase is $\boldsymbol{I}_{\boldsymbol{min}}$. Therefore, the logical summation along the dimension of PD phases gives an array that indicates how many PD measurements see each fault at the specific PV placement p and size P_{PV}, which is mathematically described as:

$$U_p(P_{PV}) = \sum_m (\hat{I}_{p,f,m} \leq I_{min,m}) \tag{3.4}$$

If any element of $U_p \in \mathbb{Z}^{N_f}$ equals zero, then it means that fault cannot be seen by any PD and it is an unprotected bus. Mathematically, the set of PV interconnections that cause under-reach is:

$$V_{UR}(P_{PV}) = \{U_p \not> 0\} \tag{3.5}$$

2. Sympathetic Tripping: Since only one fault location needs to be tested for sympathetic tripping (electrically close and upstream of the feeder breaker), the resulting change in measured PD fault current does not need to be approximated. Thus, let $\boldsymbol{I}_{\boldsymbol{pf}}^{\boldsymbol{ST}}(P_{PV}) \in \mathbb{R}^M$ represent the reverse current measured by the PDs due to PV placement p feeding a fault

of type *f* upstream of the feeder breaker. In this case, a violation occurs if this current trips is above a PD's minimum pick-up current, or

$$V_{ST}(P_{PV}) = \{\boldsymbol{I}_{\boldsymbol{pf}}^{\boldsymbol{ST}}(P_{PV}) > \boldsymbol{I}_{\boldsymbol{min,f}}\} \tag{3.6}$$

3. Nuisance Tripping: A PD trip is considered a nuisance if the PD does not pick up in the base case but with PV it will trip *first* for a fault not in its protection zone. To determine the PD that trips first, the tripping time of each PD, or $\boldsymbol{T}(\hat{\boldsymbol{I}}_{pf})$, is calculated by their individual TCCs. If the base case measured fault currents are denoted $\boldsymbol{I}_{0f}$, then the set of PDs that pick-up each fault first in the base case correspond to the minimum pick-up time, or $\boldsymbol{m}_{0f} = \min_{m} \boldsymbol{T}(\boldsymbol{I}_{0f})$. If the set of buses that are downstream of PD *m* is denoted $\boldsymbol{B}_m$, and *n* is the index corresponding to fault location, then the set of nuisance trip violations at each PV size is

$$V_{NT}(P_{PV}) = \{(\boldsymbol{m}_{0f} \neq \boldsymbol{m}_{pf}) \cap (n \notin \boldsymbol{B}_m)\}, \forall m \tag{3.7}$$

4. Coordination Loss: Lastly, a coordination loss violation occurs if a PD trips first for a fault that should have been cleared by a downstream PD. This is similar to the nuisance tripping case in that the sequence of tripping PDs has changed, but the fault for which a PD becomes the first to trip must also be downstream of the PD. This means more customers are without power than the base case PD clearing the fault.

$$V_{CL}(P_{PV}) = \{(m_{0fn} \neq m_{pfn}) \cap (n \in \boldsymbol{B}_m)\}, \forall n, m \tag{3.8}$$

In the above list of tests, determining the sets of buses that correspond to a PD's protection zone or relative location within the network can be complicated. These sets are further complicated when considering directional protection schemes with multiple sources. Appendix E presents some organizational tools based on set theory that help to quickly identify sets of buses.

3.2.3 Steady-State Model of a PV System in a Faulted Network

The details of the development of the steady-state model of the PV system and its interconnection transformer are presented in Appendixes A and B. The model developed for this

research is a three-phase, balanced voltage-dependent current source. This model is developed specifically to converge in OpenDSS fault studies. The equations governing the output of the model are given in (2.3). The current magnitude of all three phases are adjusted equally based on the average magnitude of the PCC voltages, $|V_{PCC}|$. Since changing the output of the PV system will change $|V_{PCC}|$, the following algorithm is employed to ensure the model converges to a current output, similar to the technique used in [23]:

1. Solve direct power flow and measure $V_{PCC,0}$ with $|I_{PV}| = 0$
2. Set I_{PV} magnitudes and angles according to (2.3) to be balanced and unity power factor. If PCC voltage is below 0.5pu, current magnitude is saturated to 2.0 pu rated current.
3. Solve direct power flow and measure $V_{PCC,k}$
4. Stop if $\left|\left|V_{PCC,k}\right| - \left|V_{PCC,k-1}\right|\right| \leq \varepsilon$
5. Else, return to Step 2 using $\left|V_{PCC,k}\right| = \left|V_{PCC,k}\right| + \frac{|V_{PCC,k}|-|V_{PCC,k-1}|}{2}$

Step 5 in the algorithm above adjusts the current magnitude of the PV system model to what it would have been had the measured voltage changed half as much as it did from the previous adjustment. This forces the model to converge to a current output after several iterations. This approach is taken over setting the current magnitude and angle of a single phase to be equal to a voltage phase for the following reasons:

- It is unknown which phase will be faulted and represent a poor voltage measurement.
- Strictly adjusting angle of the current phasor to be equal to the measured voltage angle can lead to the current "chasing" the voltage and never converging.
- Some faults will require the inverter to supply reactive power, which is not possible if unity power factor is strictly modeled.

3.3 Protection Based PV Hosting Capacity Limitations on Test Feeders

Performing the analysis on six test feeder models demonstrates that PV system size is primarily limited by reverse current flows potentially triggering non-directional overcurrent relays. This section presents the detailed results of three test feeders that each demonstrate violations from the list given in Section 3.2. A summary of all six feeders tested is follows. The details of the remaining three feeders is presented in Appendix D.

3.3.1 Feeder QS1 – Accounting for Coordination Loss

The testing of PV induced protection violations described in the previous section is carried out on the 12kV, 7.4MW peak load distribution feeder named QS1. The farthest bus in this feeder is 11.9km from the substation. A map of the feeder is shown in Figure 3.7 along with the locations of the four PDs considered: the substation breaker and three line reclosers, shown as colored triangles. After performing the protection analysis on this feeder, a summary of protection violations due to any fault type or location is compiled and presented in Figure 3.8. Using the PD settings provided by the utility, this feeder sees its first violation at merely 200kVA of PV. With the definition provided in Section 3.2.3, this circuit has a hosting capacity (HC) of 100kVA at the resolution of PV sizes tested. This low HC is due to a nearly immediate onset of coordination violations at several PV placement locations, as indicated by the red line in Figure 3.8. The black starred line represents any violation. However, it is next shown that this poor result is due to this feeder already being in violation of protection as defined in this research.

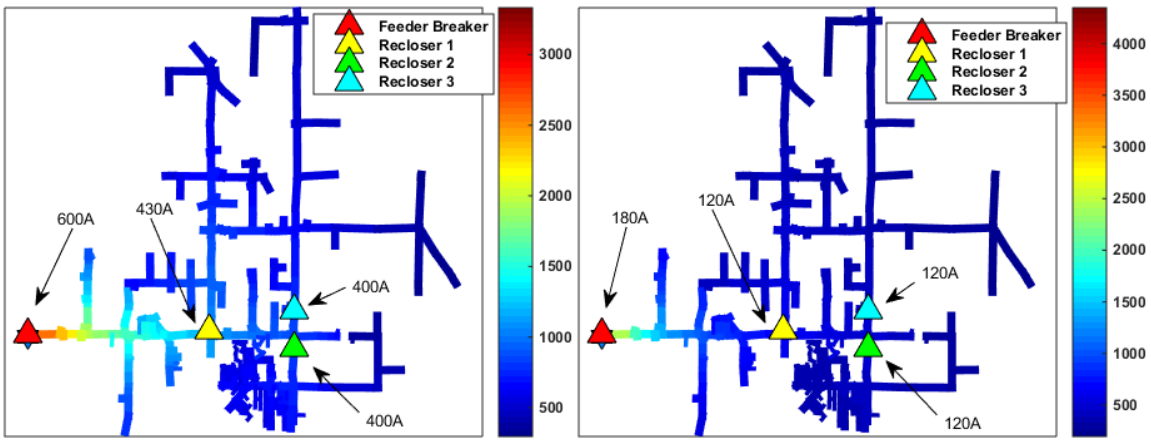

Figure 3.7. Feeder QS1 with the breaker and recloser a) minimum phase pickup current, and b) minimum ground pickup current. The lines are colored by the a) phase current for a 3LG fault and b) zero-sequence current for a 1LG fault at the bus.

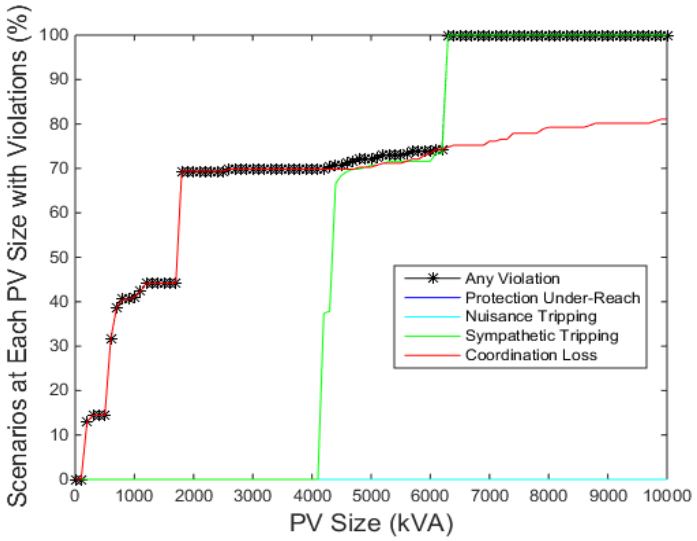

Figure 3.8. Feeder QS1 PV installation locations with violations broken down by type using original protection device time-current curves provided by utility.

To investigating the cause of the coordination issues seen in Figure 3.8, the red line indicating the occurrence of any coordination violation per PV placement is broken up by fault type in Figure 3.9. The red line in this figure, representing coordination loss due to 1LG faults, is the initial cause of coordination loss. This indicates that at nearly zero PV size, 1LG faults are will cause the substation breaker to trip before a recloser. The reasoning for this is clear in Figure 3.10, which colors each bus corresponding to which PD trips first for a 1LG placed there. However, for buses near the ends of the feeder, there are buses for which the substation breaker trips first. This is

already in violation of coordination issues since faults occurring at these buses will cause the entire circuit to lose power rather than just one branch. The reason for this is found in the TCCs provided with the utility model of this feeder, shown in the left plot of Figure 3.11. The substation breaker TCC intersects the reclosers TCCs, meaning some fault currents will pick up the breaker before the reclosers. Introducing almost any size PV system simply moves more buses into the region of the TCC graph for which the breaker picks up first. This existing violation must first be rectified to get an accurate representation of how PV current causes protection violations. To fix the coordination of the TCCs, the time scale of the breaker TCC is increased gradually until no base case coordination issues exist, and then a small extra buffer is given. After this process, the new TCCs are presented in the right plot of Figure 3.11.

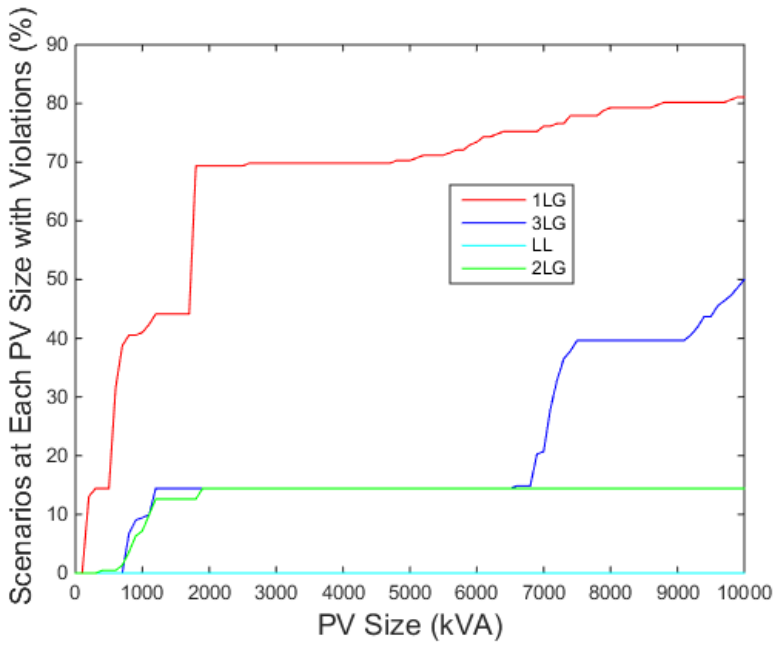

Figure 3.9. PV installation locations causing coordination violations per PV size, broken down by fault type.

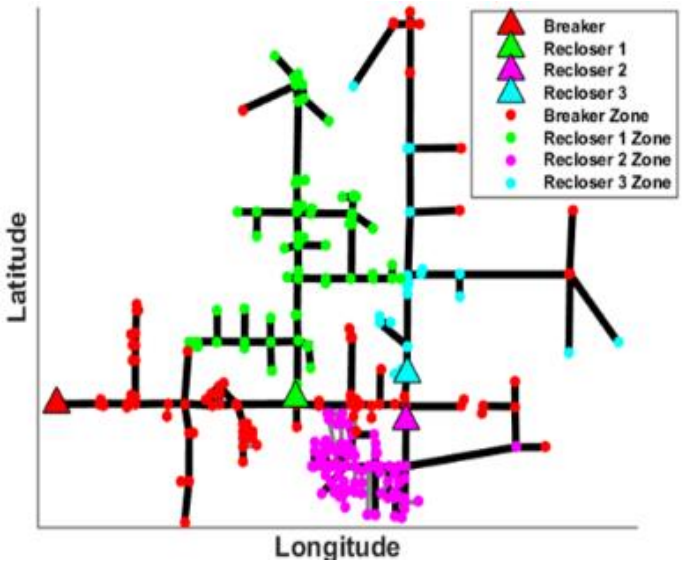

Figure 3.10. Base case (no PV) protection zones, color coded by first PD to pick-up.

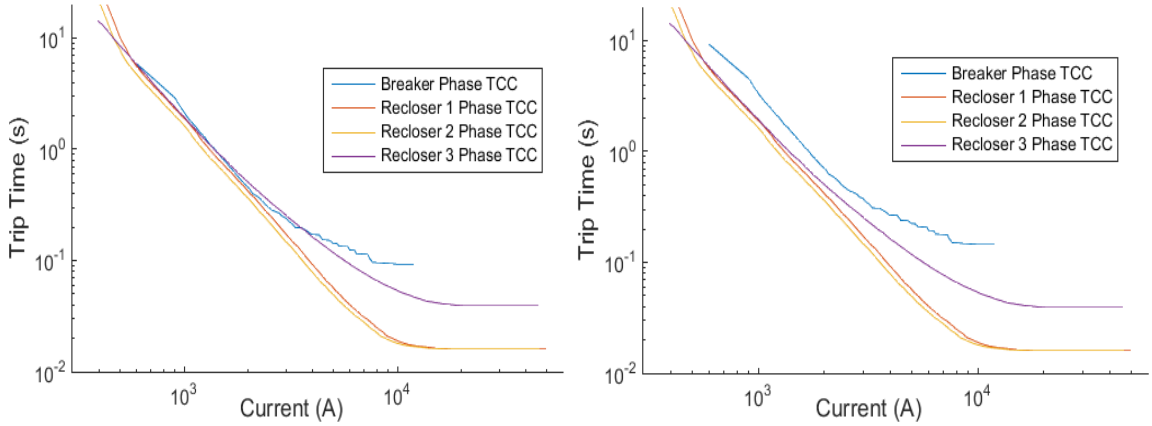

Figure 3.11. (left) Feeder QS1 PD TCCs as provided by utility. (right) PD TCCs after scaling breaker pick-up time upwards until no base case coordination violations exist.

Running the protection analysis again, results in the summary of protection violations shown in Figure 3.12. Now, not only are all of the coordination violations gone, but scaling up the breaker TCC did not result in any new violations occurring, leaving only the same sympathetic tripping issues as before. These violations occur when the PV system reverses current through the PDs for a fault placed in the substation.

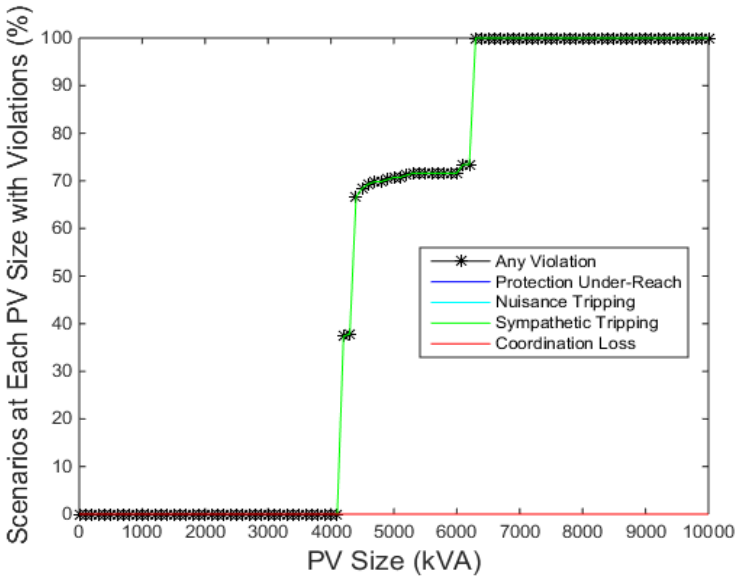

Figure 3.12. Feeder QS1 PV locations with violations broken down by type using corrected PD TCCs.

To get a sense of what is causing the remaining violations, the fault current changes due to increasing PV system size as seen be a recloser are shown in Figure 3.13. This figure is zoomed in to show just the currents below the minimum pick-up of Recloser 3 due to a 3LG fault placed anywhere in the circuit with a PV system placed just downstream of Recloser 3. The circles inside the blue lines indicate the actual PV sizes tested, with the lines representing the least-squares interpolation. The only lines that can be seen in the region shown in this figure are for faults that are placed upstream of recloser, since only these faults will have zero current with PV at 0kVA and will increase with PV size. These are the changes in fault current that will result in reverse-current tripping on the non-directional reclosers. However, most of these lines will not cause a nuisance trip violation due to another device operating first. Only one line in this plot corresponding to a fault in the substation is considered for sympathetic tripping, where the timing of the other breaker is assumed to be unknown. The current feeding the sympathetic tripping fault corresponds to the 4100kVA PV size, as indicated in Figure 3.13. This violation is for only one PV placement and represents a step increase of 0.4% in Figure 3.12. The remaining violations occur due to all the other PV placements downstream of the reclosers, as shown in Figure 3.14. This figure shows the maximum PV size allowed at each bus before a sympathetic tripping

violation occurs. The buses downstream of the reclosers allow for smaller PV than the buses only downstream of the breaker due to the lower minimum trip setting of the reclosers. But, the further downstream from the reclosers the PV system is placed, the less reverse current it will supply for faults upstream of the recloser, resulting in slightly larger PV sizes allowed.

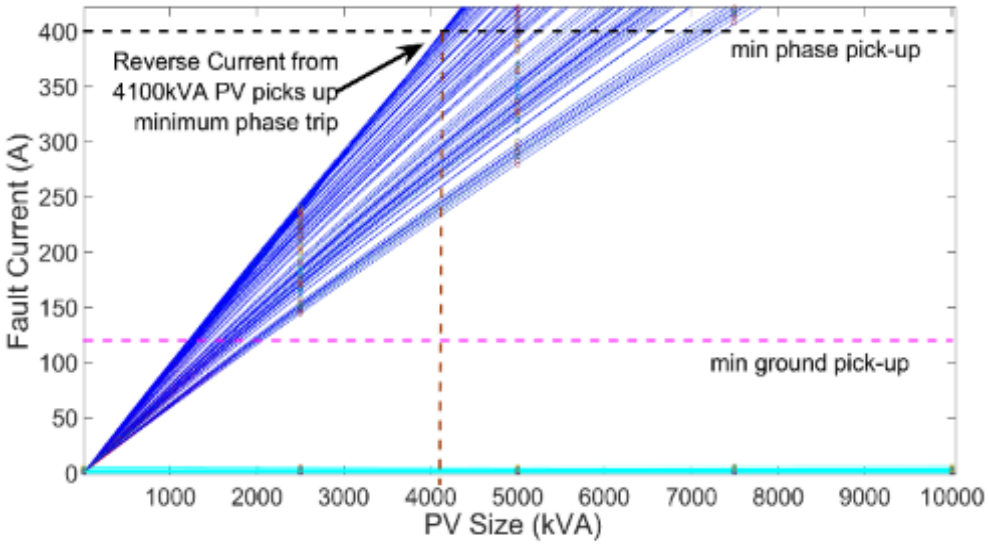

Figure 3.13. All 3LG fault current measured by Recloser 3, zoomed in on area where reverse current meets the minimum pick-up level.

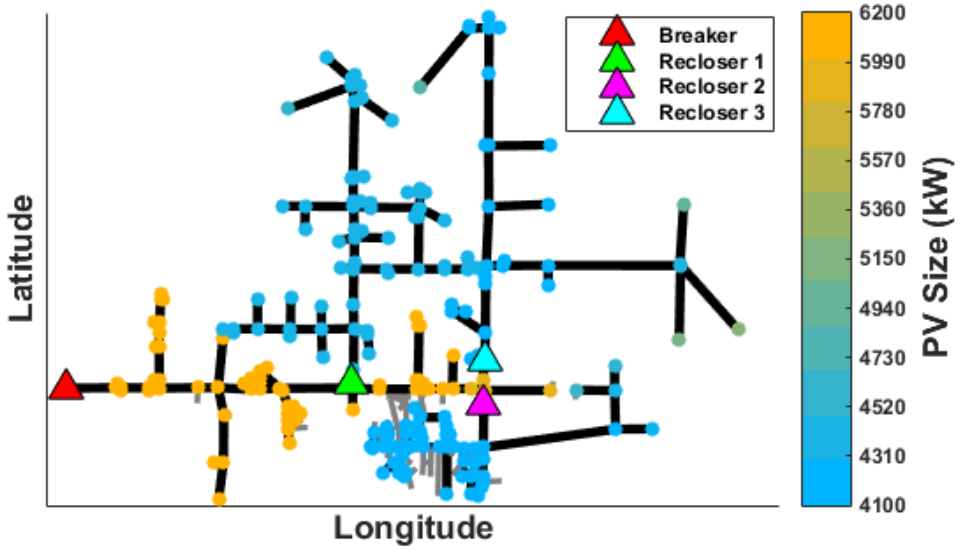

Figure 3.14. Maximum PV size allowed at each viable PV placement bus in feeder QS1 due to sympathetic tripping violations.

3.4.2 Feeder QL1 – Accounting for Nuisance Tripping

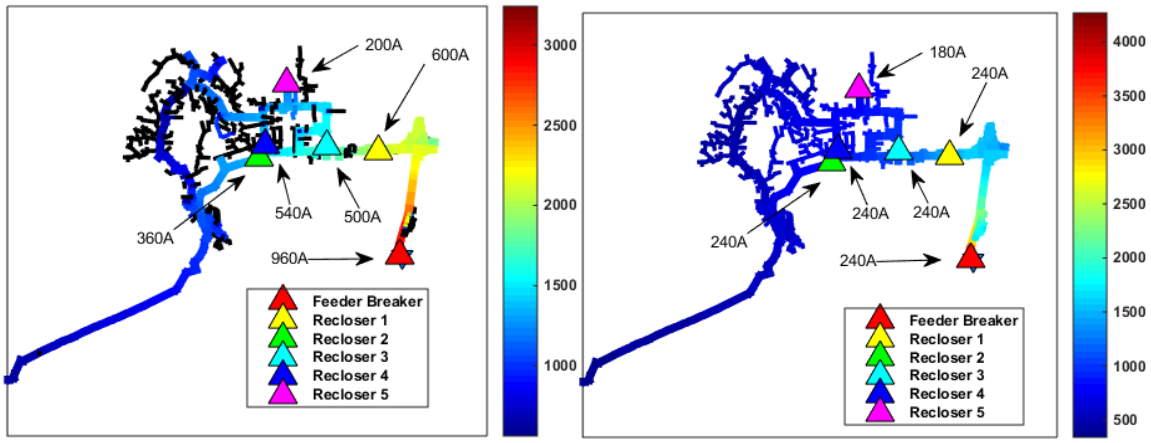

Figure 3.15. Feeder QL1 with the breaker and recloser a) minimum phase pickup current, and b) minimum ground pickup current. The lines are colored by the a) phase current for a 3LG fault and b) zero-sequence current for a 1LG fault at the bus.

The QL1 feeder is in the 20kV class of feeders, so PV interconnections are tested up to 15MVA rather than the 10MVA used in the 12kV feeder class. It has a peak load of 18.63MW and the furthest bus is 12.6km from the substation. The protection violations that occur in this feeder are summarized in Figure 3.16. There are no coordination issues or under-reach violations for this feeder. Again, sympathetic tripping is the main limit of the feeder's HC with the first violation occurring at 3500kVA. The many steps in this violation are due to there being five reclosers distributed throughout this large feeder, each with a different pick-up current.

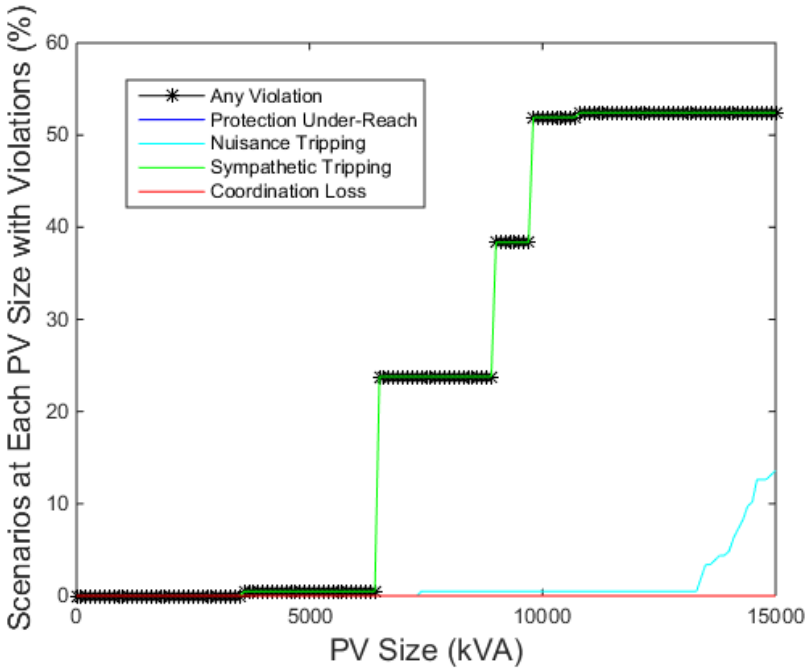

Figure 3.16. Feeder QL1 PV installation location protection violation summary.

The nuisance tripping violations here are due to reclosers operating on reverse-current from a PV feeding a fault elsewhere in the circuit, not in an upstream PD's zone. Since the recloser must operate first for it to be a violation (otherwise the fault would clear before any trip occurs), violations only occur when a large enough PV is downstream of a recloser with a low setting. This is verified in Figure 3.17. Nuisance tripping only occurs when the PV is placed downstream of an end-of-line (EOL) recloser (Reclosers 2 and 5). Only buses limited by nuisance tripping are colored in Figure 3.17, all of the other uncolored buses can host over 15MVA of PV without causing nuisance tripping in their upstream PD. The overall LHC limitations per bus are shown in Figure 3.18. These are all limited by sympathetic tripping, and it shows that the feeder is roughly split into three regions of the amount of allowable PV due to the feeder topology and the recloser locations and settings.

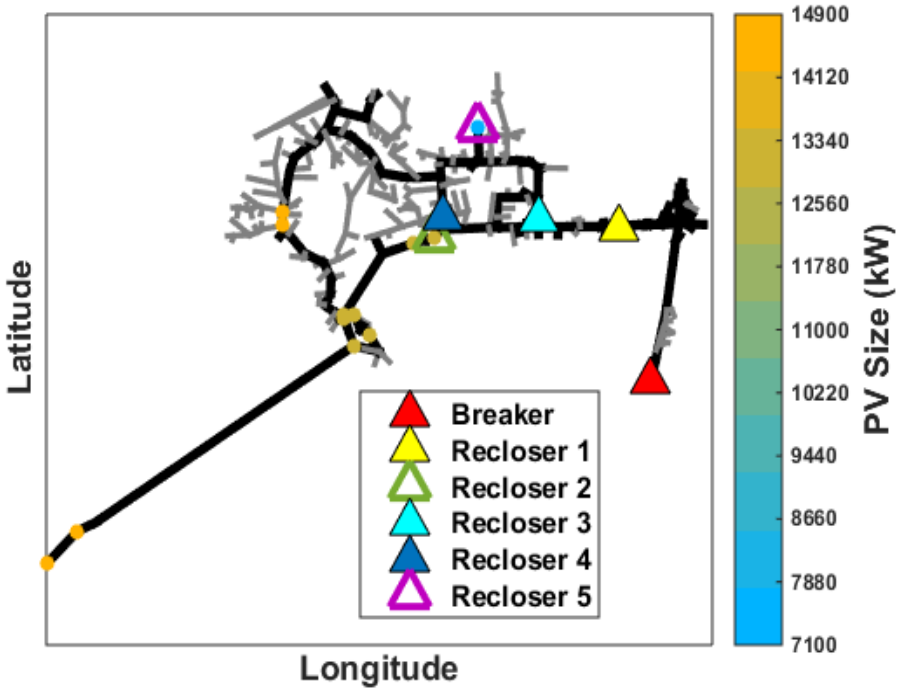

Figure 3.17. Maximum PV size allowed at each viable placement bus in feeder QL1 due to nuisance tripping.

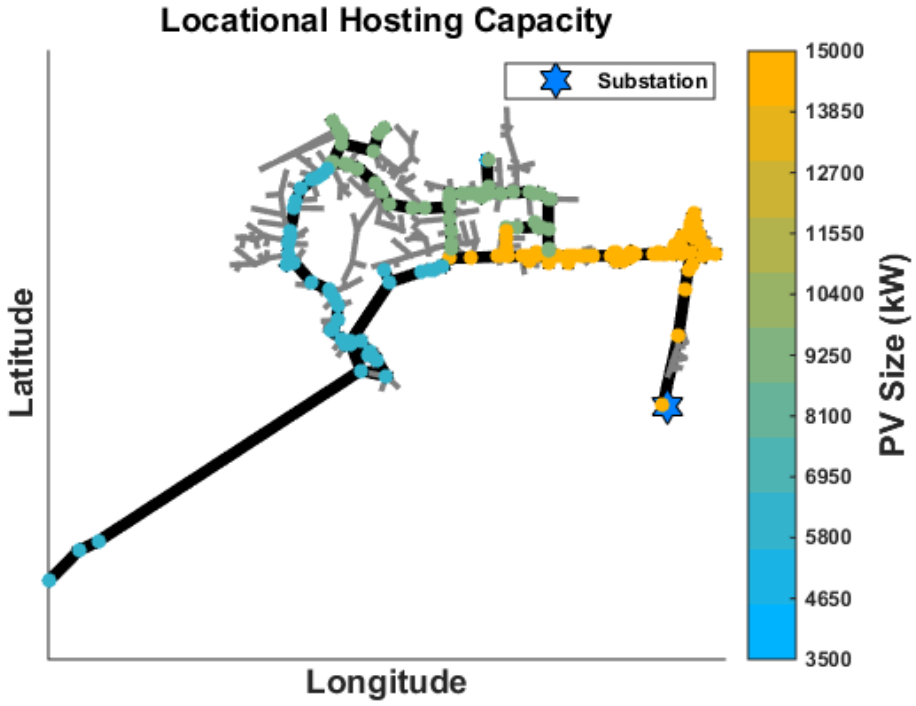

Figure 3.18. Maximum PV size allowed at each viable PV placement bus in feeder QL1 due to any protection violation.

3.4.3 Feeder QW1 – Demonstrating Under-Reach

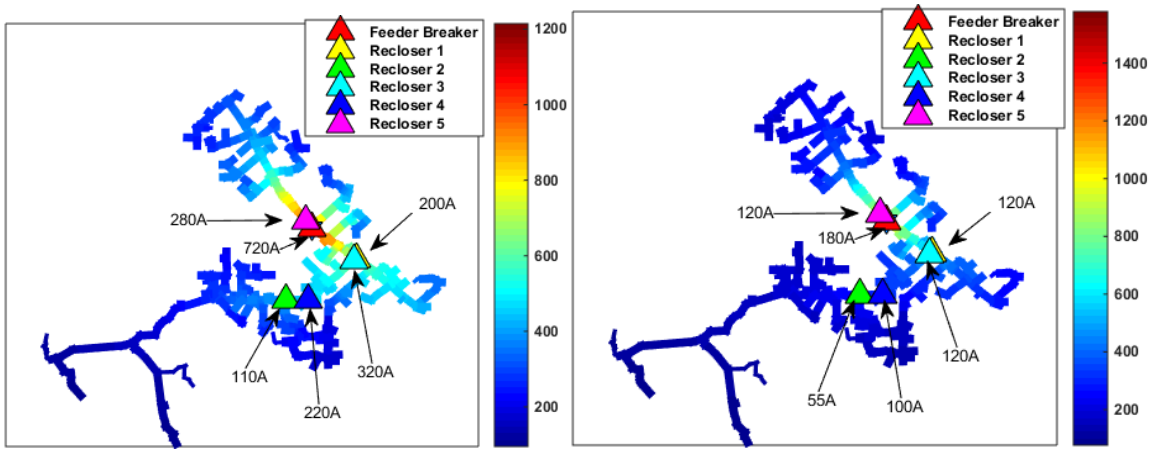

Figure 3.19. Feeder QW1 with the breaker and recloser a) minimum phase pickup current, and b) minimum ground pickup current. The lines are colored by the a) phase current for a 3LG fault and b) zero-sequence current for a 1LG fault at the bus.

Feeder QW1 is a 12kV class feeder with 5 reclosers. It has a peak load of 8.44MW and its furthest bus is 27.6km from the substation. It is distinct from the other feeders in that it has comparable high impedances to its furthest buses, making it an electrically weak circuit. For this reason, the circuit reduction selected much fewer buses for the reduced feeder model of QW1 than the other feeders so that faults could be placed without causing numerical instability in the power flow solution. The map of the reduced circuit, its PD locations, and baseline protection zones is shown in Figure 3.20. There are buses at the end of the feeder that again trip the substation breaker before the appropriate recloser. For this reason, the breaker TCCs are scaled up on the time axis.

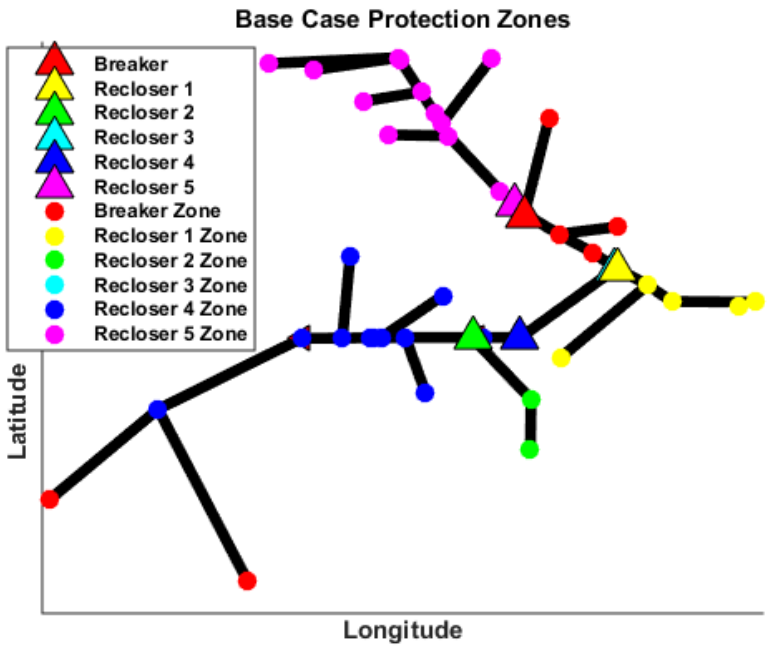

Figure 3.20. Feeder QW1 baseline protection zones colored by first PD to trip.

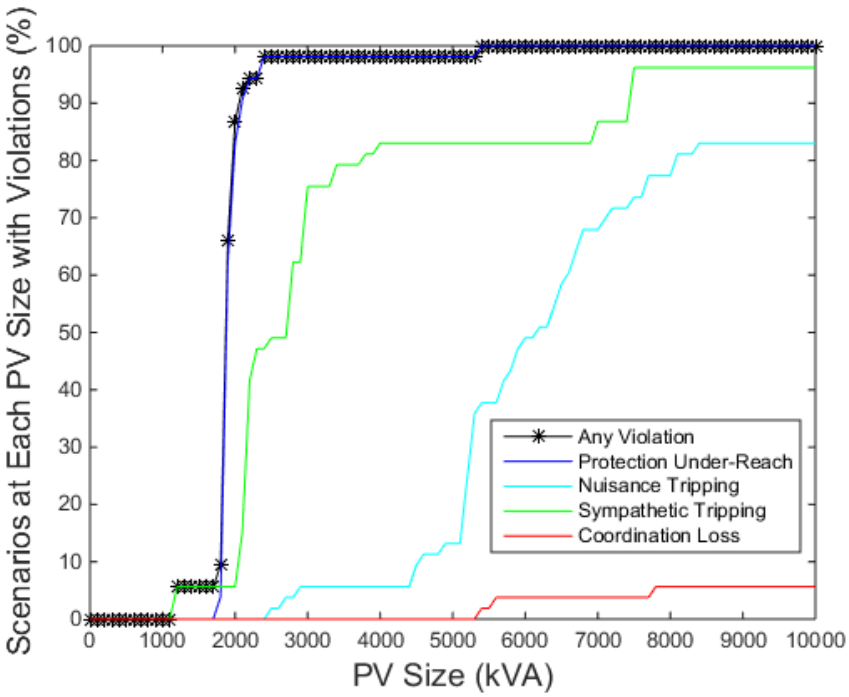

Figure 3.21. Feeder QW1 PV installation location protection violation summary.

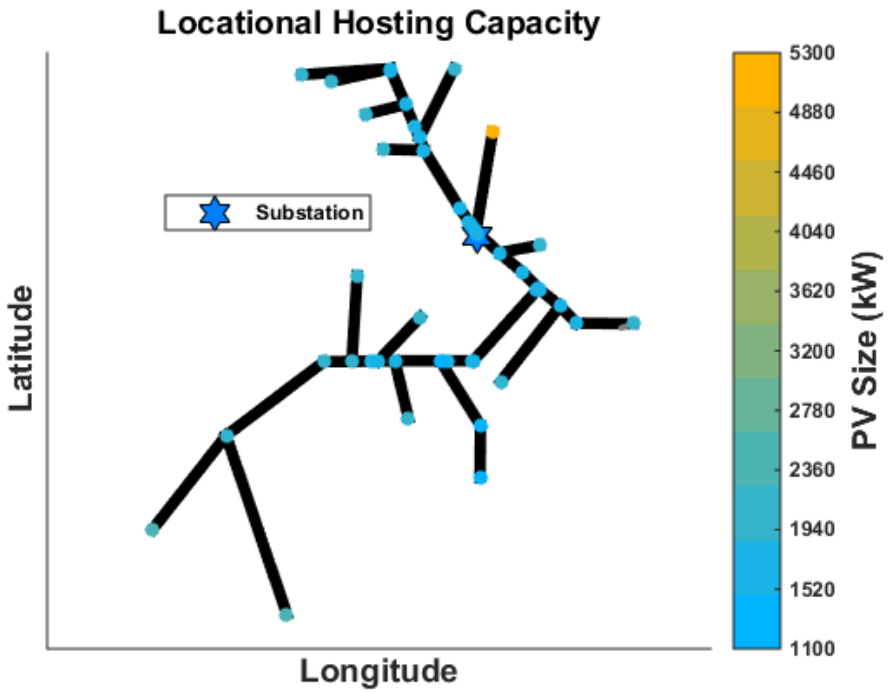

Figure 3.22. Maximum PV size allowed at each viable PV placement bus in feeder QW1 due to any protection violation.

3.5 Predicting Protection Violations

This section presents preliminary research into identifying when protection violations due to PV occur on a feeder analytically rather than with the exhaustive search technique.

3.5.1 Predicting Sympathetic Tripping

After modifications to the PD TCCs to account for preexisting issues, sympathetic tripping was always the first cause of PVs to violate protection equipment. Since the largest fault-induced reverse current produced by the PV is due to 3LG faults, which are also the simplest to analyze, this section will propose a simple heuristic method for determining the likely HC limitations due to sympathetic tripping.

Since the sympathetic tripping test places a short-circuit near the source, it can be assumed that the PV size that will produce enough reverse current to pick up the nearest upstream PD will not be large enough to recovers its PCC voltage past 0.5 pu. Therefore, based on (8), the PV current can be assumed to be saturated at 2 pu of its rated value when causing this violation. Using the

same notation as Section 3.2.3, the set of violated sympathetic tripping buses can be approximated as below in (3.9). Here, I_m denotes the pickup current of PD m, V_n^* is the nominal voltage of the PV interconnection bus n, and B_m is the set of buses downstream of PD m.

$$V_{ST}(P_{PV}) \approx \{(n \in B_m)\}, s.t. \ \frac{2P_{PV}}{3V_n^*} \geq I_m \tag{3.9}$$

Using equation (3.9), the sympathetic tripping violations for feeder QL1 are estimated and shown against the actual violations in Figure 3.23. There is very little error between the percent of violations at the appropriate PV size between the simulated and estimated curves, thus validating this approach.

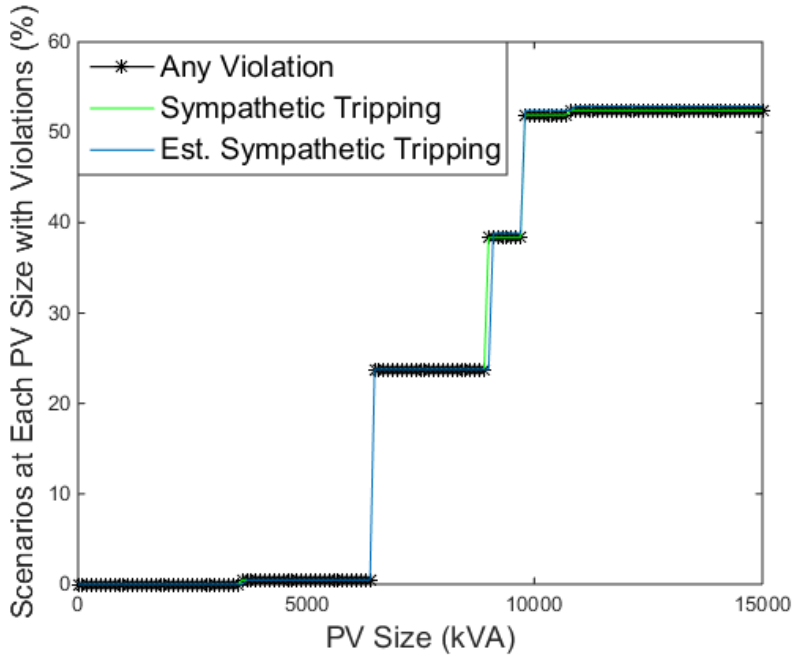

Figure 3.23. Actual and estimated sympathetic tripping for feeder QL1.

3.5.2 Existence of Protection Under-Reach

The under-reach violation is not present in most of the distribution feeders tested in Section 3.3. This is mainly due to the large zone of over-reach that exists for the PDs in these feeders. Due to the balanced-power PV system model used, under-reach is most likely to occur in 3LG faults. For under-reach to occur, the PV system must reduce the fault current seen by a PD which covers

the end-of-line (EOL). This is most likely to occur for the 3LG fault that produced the minimum current in the EOL PD's zone. Then, the PD with the lowest ratio of minimum fault current to phase pick-up ratio will experience under-reach first. A summary of the EOL PD in each feeder with the smallest ratios of fault current to phase pick-up is given in Table 3.2. Feeder QW1 is not included because it has under-reach violations in the base case.

Table 3.2. Summary of end-of-line (EOL) PDs' minimum 3LG fault current and phase pick-ups.

Test Circuit	kV	EOL PD Pickup (A)	Min 3LG I_{Fault} (A)	Min. Ratio of Fault:Pickup
QS1	12	400	866	2.16
QL1	20	360	1665	4.63
QL2	12	720	2066	2.87
QN1	20	300	3174	10.58
QB1	12	360	1808	5.02

The most likely feeder of those listed in Table 3.22 to experience under-reach is QS1 since it requires the least amount of decrease in fault current to bring its lowest current fault below its pick-up level. If the PV system is between the substation and the fault, as shown in Figure 3.24, as PV system size increases, the current sensed by the PD should decrease.

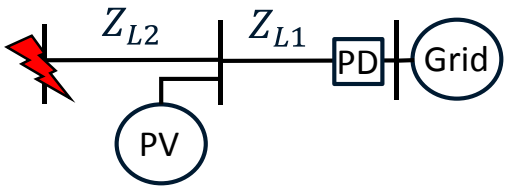

Figure 3.24. Three-bus network for demonstrating change in fault current through a PD due to PV.

If the fault, PV system, lines, and grid connection are all assumed to be balanced in Figure 3.24, only the positive-sequence network needs to be solved to calculate how the current measured by the PD changes as a function of PV size. Treating the PV as a current source and the fault as a bolted-fault, solving KVL and KCL presents the relationship in (3.10).

$$I_{PD} = \frac{V_S}{Z_{L1} + Z_{L2}} - \frac{Z_{L2}}{Z_{L1} + Z_{L2}} I_{PV} \tag{3.10}$$

This makes sense since the first term is the short-circuit current based on the line impedances and the source voltage, V_S, and the second term is simply a current divider based on the PV system output current, I_{PV}. If I_{PV} increased linearly with PV system size, then we would expect a linear decrease in fault current. In the case for feeder QS1, to reduce the fault current by the 466A necessary to produce under-reach, we would expect to see a violation at 9.7MW if PV system output current increased linearly with PV system size. This is just within the range of PV sizes tested and yet no under-reach occurred in simulation. To determine this size under-reach occurs in QS1, the range of PV system sizes tested is increased and only the minimum 3LG fault current for the EOL recloser is plotted in Figure 3.25. The last phase of the recloser to drop below its pick-up of 400A occurs at a PV system size of 13.0MW, which is outside of the range originally tested for this feeder. This is due to the slightly nonlinear change in fault current as a function of PV system size, which is due to the fact, from (8), that PV system output current is not a linear function of PV system size.

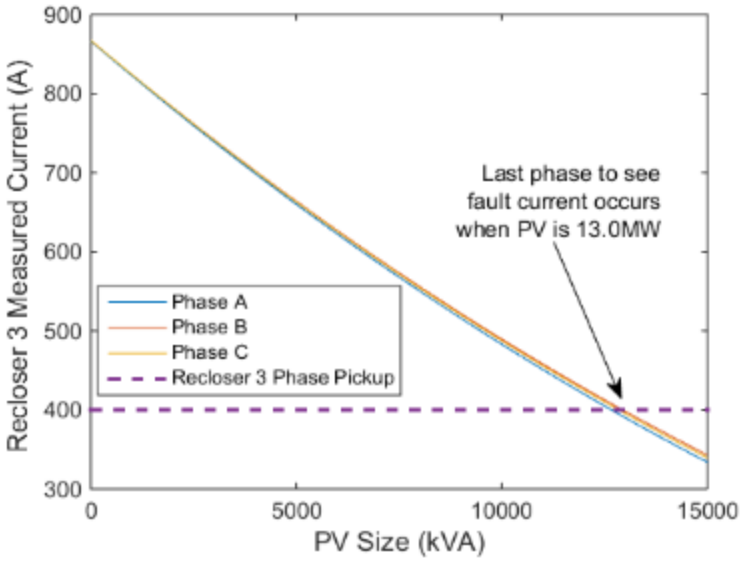

Figure 3.25. Minimum 3LG fault current seen by EOL recloser in QS1 as a function of PV size.

Plugging in just the unsaturated region of (2.3) into (3.10) yields:

$$I_{PD} = \frac{V_S}{Z_{L1} + Z_{L2}} - \frac{Z_{L2}}{Z_{L1} + Z_{L2}} \frac{P_{PV}}{V_{PV}} \tag{3.11}$$

From Figure 3.24 it is known that $V_{PV} = V_S - Z_{L1} I_{PD}$, or the voltage drop from the source across Z_{L1}. Plugging V_{PV} into (3.11) and results in I_{PD} as a quadratic function dependent on P_{PV}.

$$\frac{Z_{L1}}{V_S} I_{PD}^2 - \left(1 + \frac{Z_{L1}}{Z_{L1} + Z_{L2}}\right) I_{PD} + \left(\frac{V_S}{Z_{L1} + Z_{L2}} - \frac{Z_{L2}}{Z_{L1} + Z_{L2}} \frac{P_{PV}}{V_S}\right) = 0 \tag{3.12}$$

It is important to realize that all variables in (3.12) are complex phasors and the value of interest is the magnitude of current the PD sees, $|I_{PD}|$, which in itself is the solution to a nonlinear equation in the presence of line reactance. Therefore, analyzing the current seen by the PD can be investigated easiest by solving (3.12) with some typical values from feeder QW1, which is the only feeder to see under-reach in those tested.

In Figure 3.26, $|I_{PD}|$ is plotted as a function of P_{PV} by solving (3.12) at various distances down a line of total impedance $Z_L = 10 + j10\Omega$ with $V_S = 12kV$. With the PV placed at the fault, 100% down the line, $Z_{L2} = 0$, therefore the term in (3.12) which is a function of P_{PV} is also zero, so fault current is constant as a function of P_{PV}. With the PV placed at the substation, 0% down the line, $Z_{L1} = 0$, therefore the quadratic term falls out and we get the seemingly linear relationship:

$$I_{PD} = \frac{V_S}{Z_{L2}} - \frac{P_{PV}}{V_S} \tag{3.13}$$

However, since these are phasor quantities in (3.13), the current seen by the PD is actually more complex. Using the rectangular form of impedance, $Z_L = R_L + jX_L$, we get:

$$|I_{PD}| = \sqrt{\left(\frac{V_S R_{L2}}{R_{L2}^2 + X_{L2}^2} - \frac{P_{PV}}{V_S}\right)^2 + \left(\frac{V_S X_{L2}}{R_{L2}^2 + X_{L2}^2}\right)^2} \tag{3.14}$$

The current seen by the PD due to (3.14) will only be linear for a purely resistive circuit. As seen in Figure 3.26, the PV placed at the substation actually supplies the fault and reverses current the quickest. Figure 3.26 also shows the maximum decrease in fault current, which is most likely to cause under-reach, occurs for a PV placed halfway down the line. This is not a very intuitive

result since it implies the PV feeds a greater portion of the fault as it gets closer to it and then none at all.

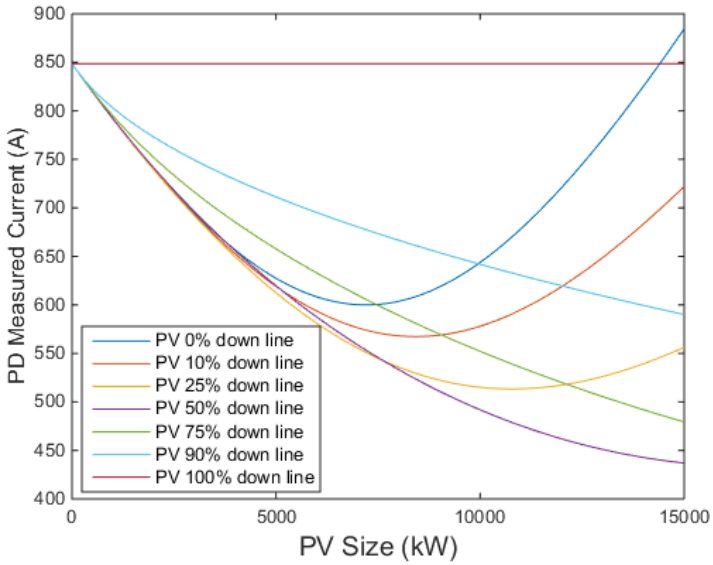

Figure 3.26. Current magnitude seen by PD as a function of PV size at various distances down the line using analytical solution.

The problem with this analysis lies in ignoring the current limitation set on the PV system in (2.3). Accounting for this saturation in (3.11) results in a discontinuous, nonlinear system that is easiest solved iteratively. The resulting current magnitude seen by the PD as a function of PV system size is shown in Figure 3.27. Now, the maximum amount the PV systems decrease the current seen by the PD is the same amount, regardless of PV location, just occurring at different sizes. This makes sense for how a PV system would behave in practice. Figure 3.27 also shows the PV system closest to the source will decrease current seen by the PD to its minimum value at the lowest size. With this knowledge, we can place a PV system at the substation and determine the impedance and X/R ratio to the fault that results in the largest decrease in current. In Figure 3.28, the decrease in measured current is shown for a 1MW PV system placed at the substation under various impedances to the fault. Only net decreases in current are shown.

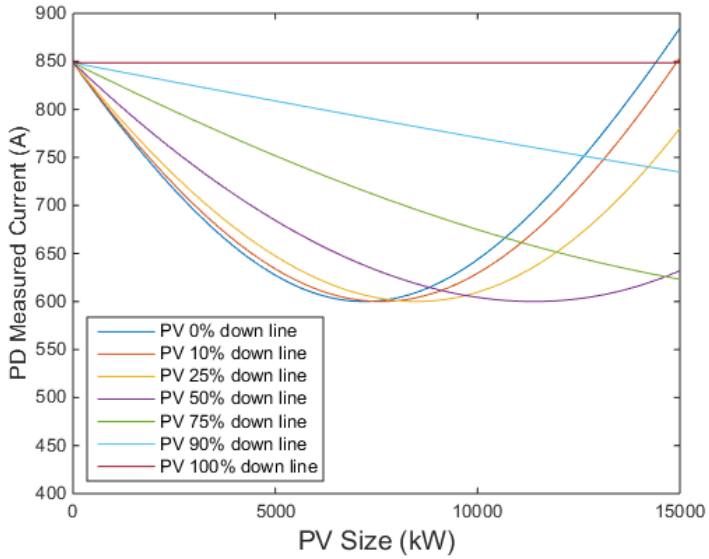

Figure 3.27. Current magnitude seen by PD as a function of PV system size at various distances down the line using a current-limited PV system model in simulation.

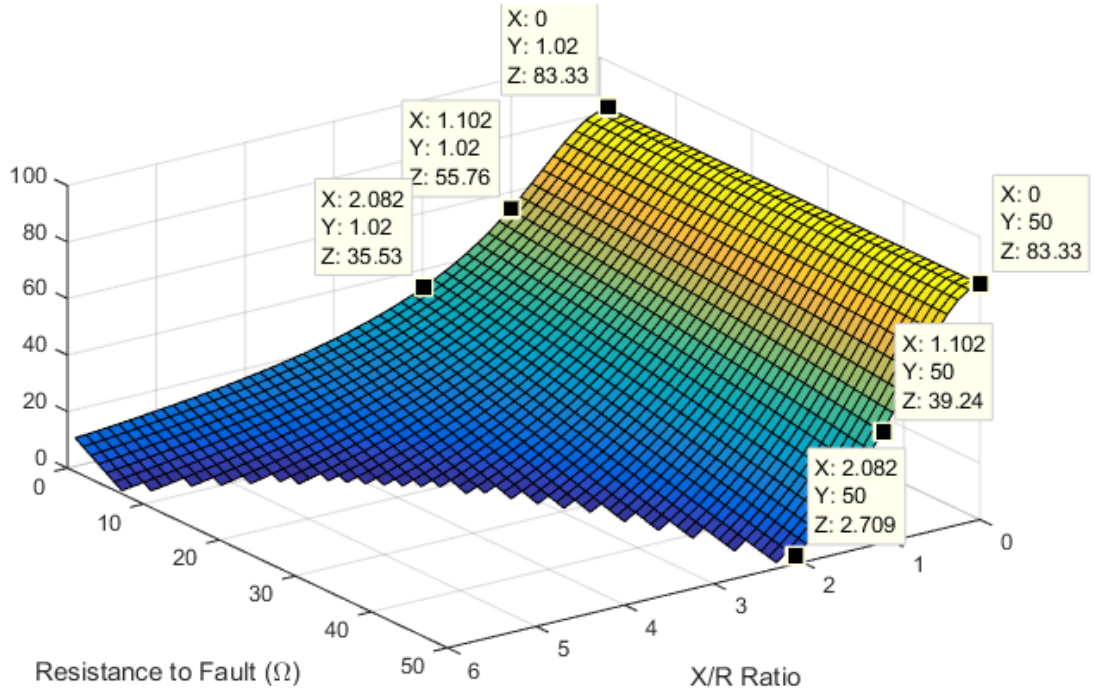

Figure 3.28. Decrease in PD measured current (A) for a 1MW plant placed at the substation for various 3LG fault distances.

With a purely resistive line, the current decreases the most regardless of the distance to the fault. This will of course not be true if the PV is large enough to completely supply the fault and

begin back-feeding to the substation. However, the shape of Figure 3.28 simply scales with PV system size. The higher the X/R ratio to the fault, the more current will continue to flow through the PD in order to supply the reactive current of the fault. However, as the line impedance changes, so too does the fault current magnitude. Thus, low impedance regions with maximum fault current decrease in Figure 3.28. These regions also have larger fault current in the base case, making it difficult to say whether under-reach occurs. This means the most likely cases for under-reach are high impedance faults with very low X/R ratios.

The regions where under-reach actually occur for a minimum trip level of 500A are plotted in Figure 3.29 for PVs of size 1MW and 5MW. Each point indicates that a fault at that impedance failed to be detected by the PD due to the presence of the PV system. The color of the point indicates how much PD measured current decreased relative to the base case, similar to Figure 3.28. In the left plot, it is shown that it is possible for small PVs to cause under-reach for typical X/R ratios, however, only under *very* particular impedances, making it extremely unlikely. In fact, this curve of particular impedances shifts to lower impedance levels for high minimum pick-ups and to higher impedance levels for lower minimum pick-ups. Increasing the PV size to 5MW increases the area of impedances that will cause under-reach, however, only a fraction are within the range of typical X/R ratios seen in distribution networks. Again, as minimum trip values increase, this region will shift to lower impedance values. Increasing the PV size much further will shift the under-reach region below practical X/R ratios. The conclusion here is that there is a very small cross-section between any given fault impedance, PV size and location, and PD pick-up value for there to be under-reach. This makes sense since the impedance to the fault has to be such that the base-case current is large enough to pick up the PD with no PV, but not so large that the PV could not decrease it past the pick-up. Also, the reactance has to be low enough for the PV to significantly reduce the absolute value of the fault current.

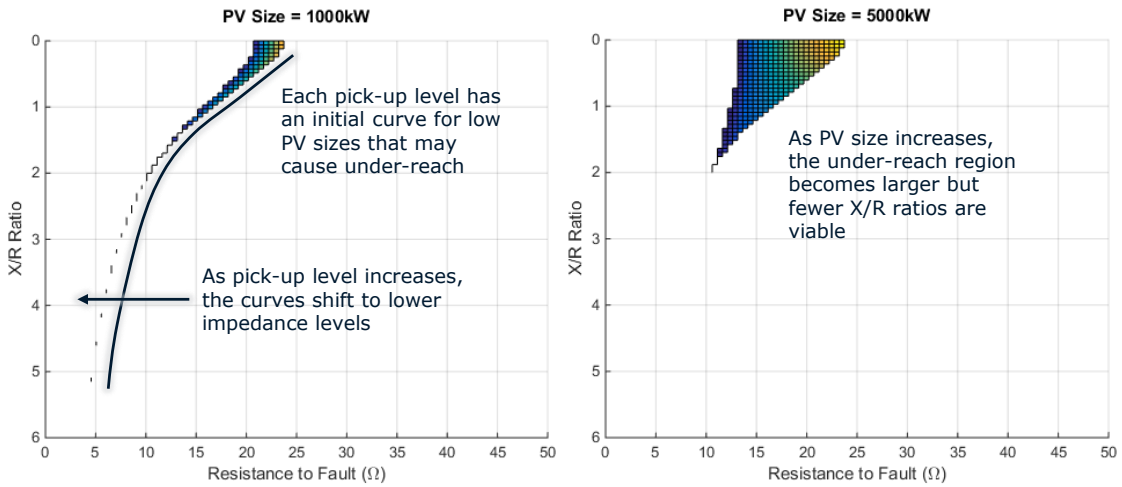

Figure 3.29. Regions of impedance that cause under-reach for a 500A minimum pick-up for PVs of size 1MW (left) and 5MW (right).

Using the above analysis for the pick-up values of each PD in the feeders that do not get under-reach reveals that none of the buses downstream of the PDs have impedances that fall within the range that will cause under-reach. However, feeder QW1, which has under-reach in its base case, has several buses downstream of a recloser that fall within the range of impedances that show they will cause under-reach from the above analysis. The next step in this analysis is to then predict which buses, based on their impedance, are at risk of causing an under-reach violation and at what size of PV.

3.6 Discussion and Conclusions

3.6.1 Discussion of Coordination Loss and Nuisance Tripping

The protection issues that arise the least frequently in the analysis of the six feeders tested in Section 3.4 are coordination loss and nuisance tripping. This subsection discusses why this is the case and why these issues can be disregarded for the most part.

First, as mentioned several times in Section 3.4, coordination loss can only occur when TCCs from different PDs are intersecting. While this does occur in the protection settings provided in these real-world feeders, the solution is relatively simple. Most modern breakers and reclosers are microprocessor based and can simply have their TCCs scaled along the time axis. Even older

electromechanical relays have several options for scaling TCC time axes. Although not negligible, the cost to mitigate this issue is only in engineering time. Furthermore, this coordination loss is only a major limiting factor of PV interconnections if the problem is pre-existing or nearly existing in the base case.

Second, based on necessary assumptions made about known or unknown protection settings, nuisance tripping violations will always occur at an equal or larger PV size than sympathetic tripping. This makes testing for nuisance tripping violations redundant, as they are both related to reverse current flow through PDs. Additionally, the designation of nuisance tripping, as defined in this research, as a violation may be subject to debate. Since nuisance tripping is defined as tripping an additional PD first from PV reverse current, the fault will still be appropriately cleared by the PD, and incorrectly tripped PD with the PV will reclose, reenergizing the part of the feeder with only a momentary outage. These momentary outages are not included in typical reliability metrics for distribution companies.

3.6.2 Discussion of Sympathetic Tripping

In all feeders tested, sympathetic tripping was the first limiting factor for size of PV installation before causing any violation. However, the assumptions that had to be made to undertake this research play a large part in the size of PV which cause sympathetic tripping violations and these sizes should be considered as very conservative limitations. First, there is was no knowledge of the protection devices on the feeder being faulted for the sympathetic tripping tests. Thus, the worst-case had to be assumed that the protection had much slower TCCs than those upstream of the PV, or essentially that there was a failure of protection on the adjacent feeder. If the protection of the adjacent feeder were to be modeled similar to the PV system's feeder breaker, the timing could be considered and sympathetic tripping would not cause violations until very large PV sizes, similar to nuisance tripping. Furthermore, the PV sizes at which nuisance tripping occurs are also conservative values due to the fault current tests being performed under no-load conditions.

3.6.3 Summary of All Feeder Hosting Capacities

A summary of the hosting capacities as limited by protection violations of the feeders presented in the previous subsections is provided in Table 3.33. With this limited number of feeders, it is hard to discern any trends. However, past research has shown that HC is limited by the voltage class of the feeder, which is the case for feeder QB1. Feeders that are very close to producing a violation without PV, such as feeder QW1, also have limited HC. In general, it can be seen that the average LHC exceeds the feeder HC, which is to be expected. In the highest voltage class cases (feeders QL1 and QN1) the hosting capacities of most buses are several times greater than that of the first bus to violate.

Table 3.3. Summary of feeder HC and average LHC as limited by protection issues of each feeder tested.

Feeder Name	**kV**	**HC (MW)**	**Limiting Protection Issue**	**Avg. LHC (MW)**
QS1	12	4.1	ST	4.8
QL1	20	3.5	ST	11.3
QL2	12	7.4	ST	7.4
QN1	20	5.3	ST	12.2
QB1	4	1.2	ST	1.37
QW1	12	1.1	ST	1.88
Avg.		**3.77**	**ST**	**6.49**

3.7 Summary

This chapter has described the potential limitations to PV system installation sizes based on whether the system interferes with distribution overcurrent protection. Of the feeders tested, it was found that PV systems of 1.1 MW and below will not cause problems with distribution network protection. The next step in the research is to evaluate the other impacts that a PV system could have on a distribution network over time, such as increased voltage violations. The next chapter investigates these other impacts using a 1 MW PV system, which is below the lowest size found to be of concern to protection schemes.

4. PARAMETER SETTINGS FOR PROPOSED ADVANCED INVERTER CONTROL STRATEGIES

4.1 Introduction and Background

The previous chapter investigated how PV systems may interfere with distribution overcurrent protection if they are too large. This chapter investigates what other impacts a PV system that is not large enough to impact protection may have on the network. Then, several advanced PV inverter control strategies are investigated to mitigate these impacts. A parametric study is performed to identify the optimal performance of each control type at different PV installation locations.

With the increasing adoption of PV generation in distribution networks, utilities are becoming ever more cautious about the impacts PV may have on network operation and maintenance. Research has shown that PV installation sizes must be limited to prevent them from causing voltage deviation and line overcurrent violations [1, 2, 69]. It has also been shown that the variability of PV generation can have a negative impact on the operation of voltage regulators and switching capacitors [3,70]. A PV system's impact on voltage regulating equipment also affects whether or not line voltages remain within ANSI limitations. The interaction between the predicted variability of a potential PV installation and existing voltage regulating controls must be studied using quasi-static time-series (QSTS) simulations. An interconnection request can be denied if a study indicates a significant increase in the operation of network equipment or voltage deviations.

However, it has also been shown that the PV system's grid-tie inverter can be utilized to ensure the PV system's variability does not cause a significant negative impact to the distribution network. Specifically, so-called "advanced" or "smart" functionalities in modern inverters have been proposed to this end [6, 46]. Since there is an increasing number of PV inverter manufacturers, a standard set of control functions is being proposed by the California Public Utilities Commission (CPUC) that all inverter manufacturers must provide in order to be approved for use on California distribution networks. Advanced inverter functions can refer to a number of hardware and software capabilities, from the ability of the inverter to transmit data and receive new operating set-points to the ability to provide a certain amount of reactive power or curtail the power output of the PV system to desired

level. Although there are currently no recommended uses for advanced inverter controls, these standard functions will provide utilities the flexibility to select the PV system behavior that best suits any given scenario.

The problem that is addressed by this research is that the advanced inverter functionalities, and in particular the advanced inverter controls which dictate the real and reactive power output of the PV system based on local measurements, may not improve the impact of the PV system on the distribution network. In fact, this research demonstrates that there are certain control settings that result in the PV system causing more problems than if it had no advanced inverter controls at all. Some poor settings may be obvious, such as instructing the PV inverter to output a large amount of capacitive vars while at high line voltages, thus causing more over-voltage scenarios. However, situations such as the injection of a certain amount of reactive power during a period of highly variable irradiance and the impact it has on voltage regulator tap changes are less obvious and must be simulated. Also, based on the interconnection location, the PV system may have an overall positive impact on the network and thus not warrant certain control types.

The goal of this research is to determine the appropriate advanced inverter control parameters that will provide an overall improvement in the operation of the distribution network compared to the PV under "legacy" control, or simply outputting all real power available to it at unity power factor. Only those advanced inverter controls that can be simulated in a QSTS simulation are studied in this investigation. These controls are summarized in the following section along with the other QSTS simulation details.

4.2 Modeling Advanced Inverter Functions

4.2.1 Advanced Inverter Functions Considered

This section lists the advanced inverter control types considered in this research, briefly describes them, and indicates which variable parameters are to be considered. Six advanced inverter controls are selected from the set under consideration by CPUC in [7] based on their ability to be simulated in the OpenDSS QSTS simulation environment. For each of the control's

parameters, the units are given in parentheses and the range of parameters considered is given in brackets. The parameters have been selected and defined to minimize the total number of parameters necessary to define the control action. This is due to the fact that each additional parameter increases the dimensionality of the problem and thus geometrically increases the computation time required. At the end of this section, the network metrics used to determine the successfulness of each control are described. Time-series demonstrations of each control type for an example set of parameters can be found in Appendix F.

4.2.1.1 Ramp-Rate Control

This function limits the up-ramp of the PV systems to a fixed rate over time. The down-ramp is not limited since the PV system cannot store energy. A lower ramp-rate limit parameter value in this case means there is a greater amount of PV power curtailment due to output limiting. At the lowest parameter value tested, the PV will only be allowed to increase its output level by a tenth of its rating in an hour.

Parameters:

- Ramp-rate limit ($P_{PV,p.u.}/hr$) [0.1 – 1.5]

4.2.1.2 Fixed Power Factor Control

This function sets the inverter to operate at a constant power factor. This means as the PV real power output increases, the reactive power output increases proportional to the power factor. Only lagging (negative) power factors are considered to prevent voltage rise associated with PV system output. However, if the inverter is not large enough it will only output the reactive power available to it and not curtail the real power.

Parameters:

- Power factor (pf) [(-0.99) – (-0.7)]

4.2.1.3 Volt/Watt Control

This function controls the PV inverter using a similar voltage-based droop curve as in Figure 2.3, but curtails the real power output as voltage becomes too high, rather than dispatch vars which are kept at zero. Since it operates only in the region of $V_{p.u.} > 1.0$, the deadband starts at nominal and the PV output is curtailed based on the steepness of the slope past that.

Parameters:

- Volt/Watt slope ($\Delta P_{p.u.}/\Delta V_{p.u.}$) [5 – 100]
- Deadband width (V_{pu}) [0-.04]

4.2.1.4 Watt-Triggered Power Factor Control

This function is similar to the previous except the power factor becomes more lagging as the real power output increases based on a defined slope. This means as the real power ramps from zero to peak output, the power factor changes from unity to a maximum lagging value, the target power factor at rated output. Again, the real power output is prioritized if the inverter is not large enough to supply the necessary vars.

Parameters:

- Target power factor (pf) [0.7 – 0.99]
- Deadband width ($P_{PV,p.u.}$) [0.9 – 0]

4.2.1.5 Watt-Priority Volt/Var Control

This function outputs reactive power from the PV grid-tie inverter based on a droop slope with a deadband around nominal voltage, such as in Figure 2.3. The vertical axis for this control is available reactive power, or $Q_{avail} = \sqrt{S_{inv}^2 - P_{PV}^2}$, where S_{inv} is the rating of the inverter and P_{PV} is the real power available to the PV system from the irradiance. This control outputs all available real power before dispatching reactive power based on the measured local voltage.

Parameters:

- Volt/Var droop slope ($\Delta Q_{avail,p.u.}/\Delta V_{p.u.}$) [5 – 100]
- Deadband width (V_{pu}) [0 – 0.04]

- Target voltage (V_{pu}) [0.98 – 1.03]

4.2.1.6 Var-Priority Volt/Var Control

This function outputs reactive power from the PV grid-tie inverter similar to the previous control, but instead limits the real power based on the reactive power needs, or $P_{PV} = \sqrt{S_{inv}^2 - Q_{Volt/Var}^2}$. In this case the vertical axis of the Volt/Var droop curve in Figure 2.3 is the full rating of the inverter. This control curtails the real power output of the PV if there is not enough inverter capacity to provide enough vars to regulate voltage based on the droop curve.

Parameters:

- Volt/Var droop slope ($\Delta Q_{avail,p.u.}/\Delta V_{p.u.}$) [5 – 100]
- Deadband width (V_{pu}) [0-.04]
- Target voltage (V_{pu}) [0.98-1.03]

4.3 Analysis Methodology

This section presents the methodology used to simulate PV inverters in quasi-static time-series (QSTS) simulations. The simulation platform is OpenDSS, which is operated via Matlab in conjunction with the Sandia GridPV toolbox [8].

4.3.1 Weekly Irradiance, Load Selection, and Base Case Simulation

To analyze the controls described in the previous section, a time-series simulation is run to evaluate how fluctuations in load and irradiance affect the controls and thus the impact of the PV system on the network. Since the inverter's internal control loops are assumed to be stable and converge faster than the 1-minute load and irradiance data used, a QSTS simulation is appropriate. A year of substation SCADA data collected at 1-minute resolution is allocated to model the variations in feeder load throughout the year. Irradiance data from the University of California San Diego is used to model a fixed-tilt PV system with appropriate smoothing for a large central plant [9]. A representative week of irradiance data is selected and paired with a representative

week of load to use as a basis for the QSTS analysis. The representative week is chosen by identifying the week of load that minimized the square of the error between its load duration curve (LDC) and the yearly LDC, as shown in Figure 4.1. This process results in the load and irradiance data shown in Figure 4.2, which are used as the basis for the QSTS analysis for this feeder. This procedure is done for both feeders tested, which are described in the next section. The reactive power measurements in Figure 4.2 are assumed to be bad data due to their shape and have therefore been discarded. The real power curve is allocated to each network load which are then held at a given power factor.

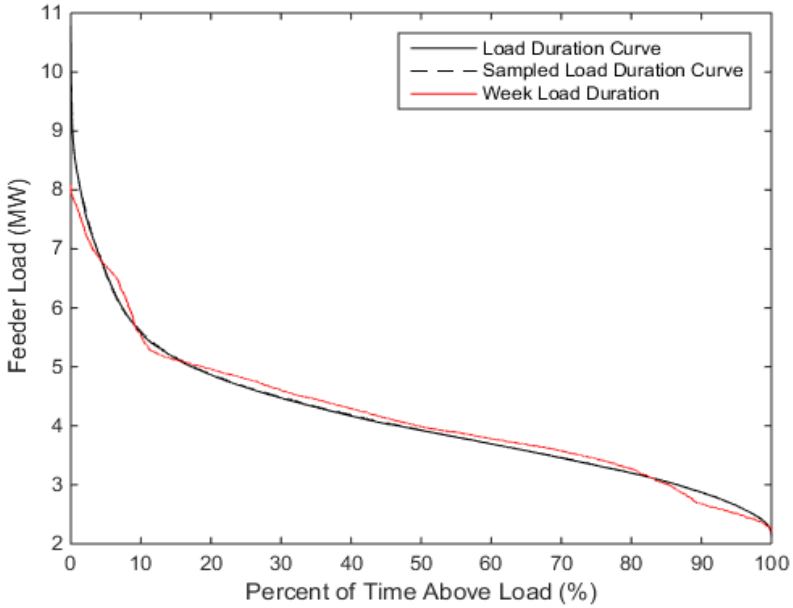

Figure 4.1. Weekly load selected for QSTS simulation's LDC selected as the least-square-error of the yearly data's LDC.

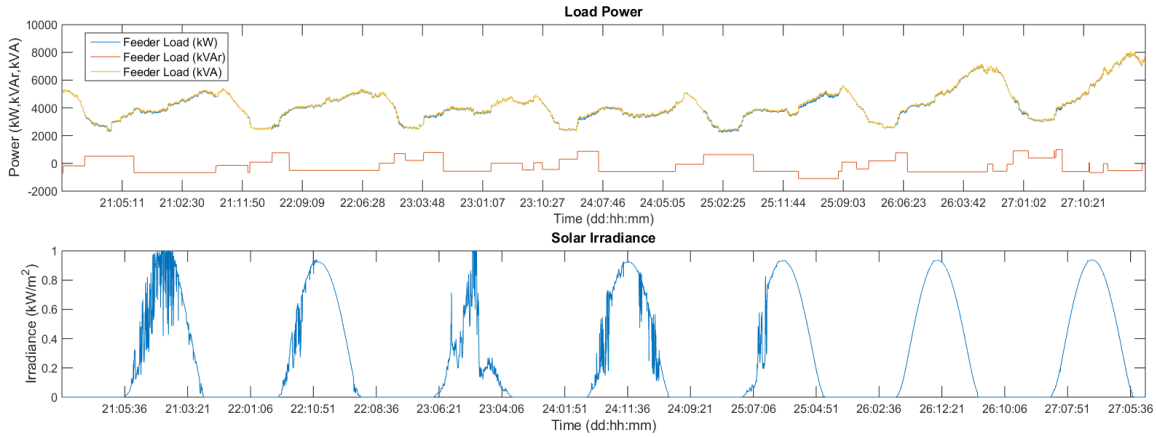

Figure 4.2. Weekly 1-minute resolution load and irradiance data selected for QSTS simulation to be representative of year.

The left plot of Figure 4.3 shows how the voltage of a bus near the end of the feeder fluctuates due to the load profile from Figure 4.2. The load is unbalanced and causes the voltage to sag significantly below nominal. The voltage even violates the ANSI low-voltage limit for several hours during the last two days. In the right-hand plot, a 1 MW PV system with no advanced inverter controls is added to follow the irradiance data from Figure 4.2. The voltage has much greater variability and violates the ANSI high-voltage limit many times. The goal of this research is to apply a control to the inverter of this PV system to mitigate these adverse voltages.

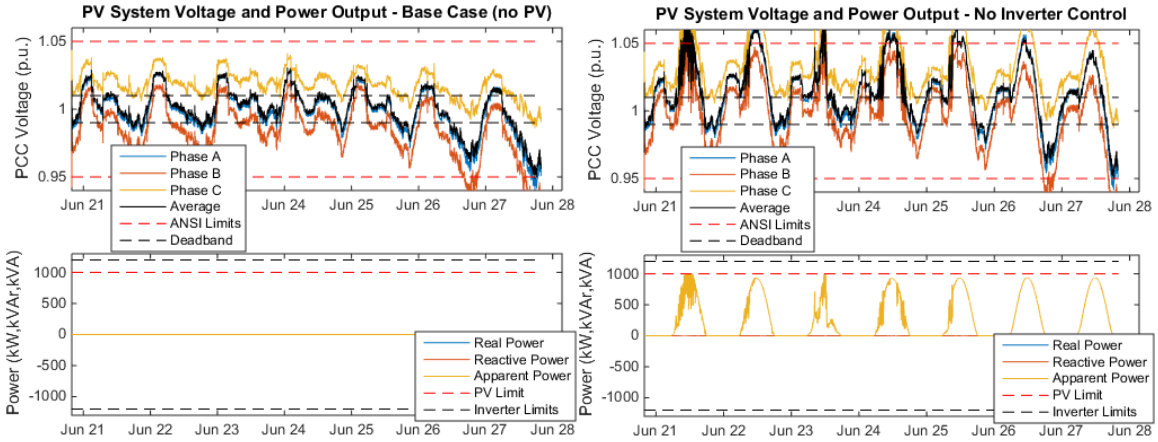

Figure 4.3. (left) Weekly simulation of end-of-feeder bus voltage and PV generation in the case of no PV and (right) with 1MW PV.

4.3.2 Feeder Models Used in Analysis

Two distribution feeder models are used in this research to study the impact of the advanced inverter control types and their settings. The details of these two feeders are described below.

4.3.2.1 Feeder CO1

Feeder CO1 is a 12 kV rural network with a peak load of 6.41 MW. Its farthest bus is 21.4 km from the substation. The feeder has one voltage regulator with a 15-second delay, 3 switching capacitors that switch on voltage, and two capacitors that switch on time. The locations of these devices are shown in Figure 4.4 along with the voltage levels at peak load with no PV. The load profile selection for this feeder was covered in Section 4.3.1, as shown in Figure 4.1. This results in the load and time-matched irradiance curves shown in Figure 4.2. The following results use this week of data in each QSTS study. Each control type described in Section 4.2.1 is tested at 20 PV locations using a 1 MW PV system with a 1.1 MVA inverter.

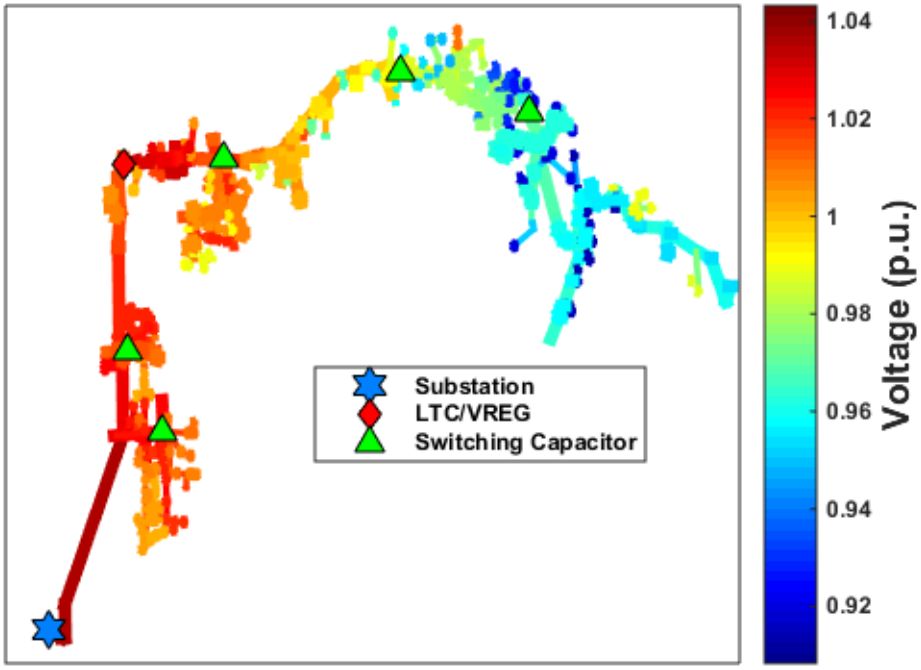

Figure 4.4. Feeder CO1 circuit topology with lines colored by voltage level at peak load.

4.3.2.2 Feeder CS1

Feeder CS1 is a 12 kV agricultural feeder with a peak load of 9.23 MW. The farthest bus is 11.9 km from the substation. The feeder has two voltage regulators on 45-second delays and six switching capacitors that switch on either time, voltage, or temperature. The locations of these devices are shown in Figure 4.5 along with the voltage levels at peak load with no PV. The LDC fitting to find the most representative week of load is presented in Figure 4.6. As before, the red line shows the LDC of the week of load that closest matches the LDC of the yearly load data, represented by the black lines. To clarify, the dashed line is a one-week down-sample of the solid one-year line used to approximate what the desired week's LDC should look like. The load profile for Feeder CS1 does not have a continuous week that matches the year's LDC as well as Feeder CO1. The closest week of load that approximates the year's LDC is shown in the time domain in Figure 4.7. The same irradiance profile as Feeder CO1 is used on the PV system.

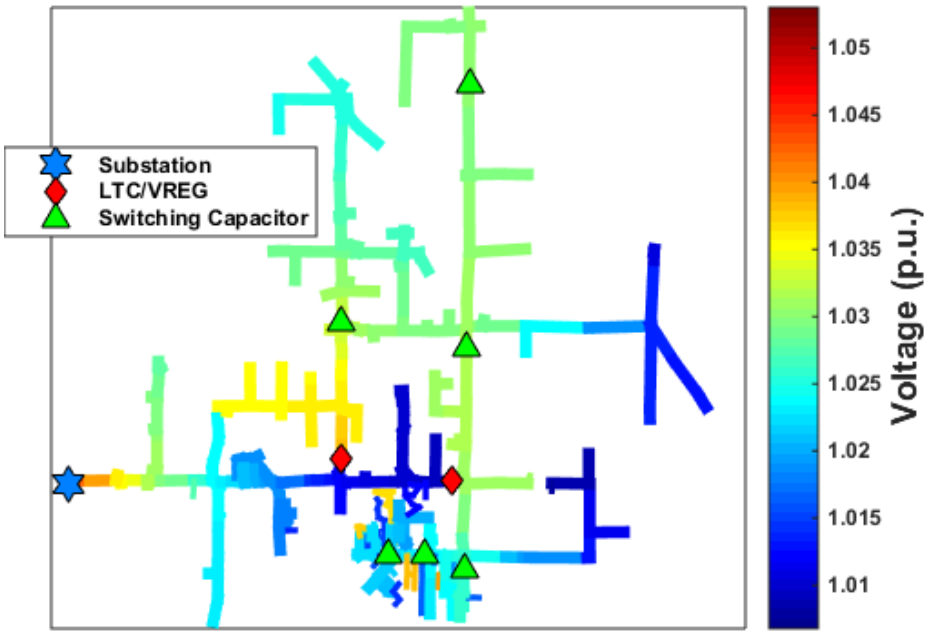

Figure 4.5. Feeder CS1 circuit topology with lines colored by baseline voltage level.

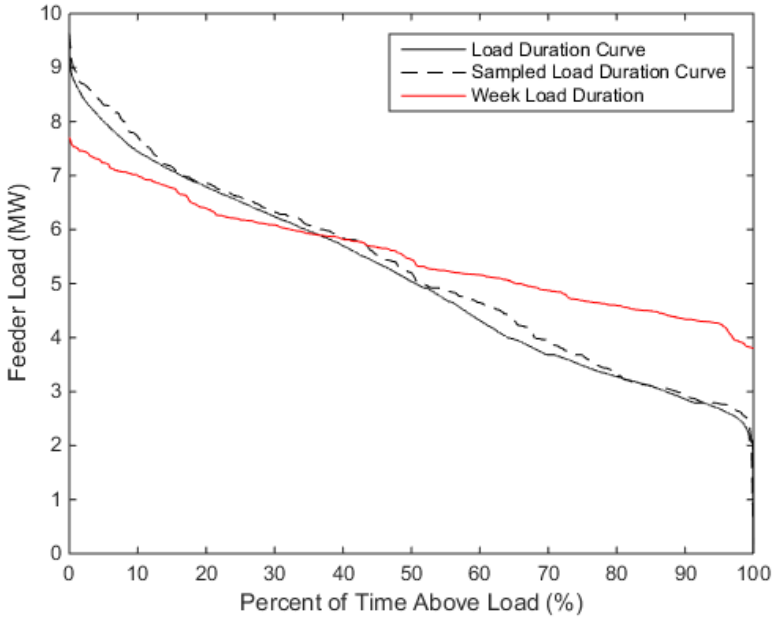

Figure 4.6. Week of load selected for the QS1 feeder by minimizing the error of its LDC to the year of load.

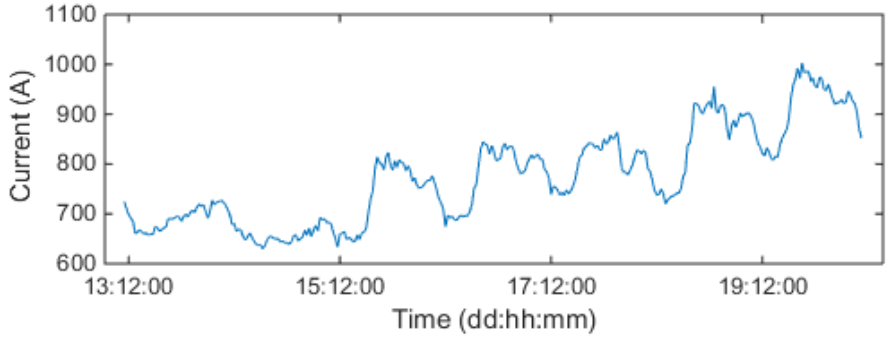

Figure 4.7. Load profile to be normalized and applied to each load in QS1 feeder.

4.3.3 Network Metrics Considered

Below is a list of each network measurement to be quantified over a time-series simulation that will gauge the success of each control described above at mitigating the negative impact of PV. Each metric is measured for the base case of PV at unity power factor and individually for each type of advanced inverter control.

- Time over-voltage (OT) – total simulation time during which any bus is over $1.05V_{pu}$.
- Time under-voltage (UT) – total simulation time during which any bus is under $0.95V_{pu}$.

- Regulator tap changes (TC) – sum of all voltage regulator tap changes that occur during the simulation.
- Capacitor switches (CS) – sum of all capacitor bank switching operations that occur during the simulation.
- Network losses (L) – sum of all line and equipment losses incurred on the network during the simulation in kWh.
- PV power curtailed (PC) – total PV power curtailed by the control during the simulation.
- PV vars generated (VG) – total reactive power generated by the PV inverter due to the advanced inverter control during the simulation, which may incur a cost to the customer.

4.3.4 Scoring Positive or Negative Controller Impacts

The previous section concluded that controller parameters cannot be universally deemed good or bad for improving a PV's impact on a distribution network. This section describes the method by which the metrics resulting from advanced inverter controls are deemed positive or negative overall. Each vector of metrics, $\boldsymbol{m}$, refers to the network metrics described in Section 4.3.3. The procedure is described in the following steps for any given control type:

1. Solve a base case QSTS with no PV, and record base metrics, $\boldsymbol{m_b}$
2. Place PV at interconnection location
3. Solve QSTS with no PV control, record metrics, $\boldsymbol{m_{nc}}$
4. Set inverter controller with parameter combination i
5. Solve QSTS with PV control, record metrics, $\boldsymbol{m_i}$
6. Find difference in metrics solely due to controls:

$$\Delta \boldsymbol{m_i} = (\boldsymbol{m_i} - \boldsymbol{m_b}) - (\boldsymbol{m_{nc}} - \boldsymbol{m_b})$$

7. Apply relative importance weight to metrics: $\Delta \boldsymbol{m_i^w} = \boldsymbol{w} \cdot \Delta \boldsymbol{m_i}$
8. Repeat steps 4-7 for all parameter combinations
9. Repeat whole procedure for all interconnection locations

Due to the formulation in Step 6 above, if a particular set of parameters has improved a particular metric, its value will be negative. That is to say the no-control case will have resulted in more negative impact metrics relative to the base case than the control case, or the control has improved the impact of the PV. Thus, once all control parameters are tested at a location, the ideal range of parameters can be identified by finding the largest continuous range of parameters that result in $\Delta \boldsymbol{m}_i^{\boldsymbol{w}} < 0$. The procedure for finding this range is covered in Section 3.3. In this research, the weighted change in metrics is defined below in (1) based on the metrics and symbols defined in Section 3.2.1.

$$\Delta \boldsymbol{m}_i^{\boldsymbol{w}} = w_1 * OT + w_2 * UT + w_3 * TC + w_4 * CS + w_5 * L - w_6 P_{PV} - w_7 Q_{PV} - b \qquad (4.1)$$

In (4.1), b is a scalar bias that may be changed between control types to achieve a desired level of network improvement. In this research, the weight vector is $\boldsymbol{w} = [\,2\ 2\ 3\ 3\ 0.1\ 3\ 0.1]$. These weights indicate the relative importance of each metric, which are described in Section 4.3.2. Therefore, with this weighting the equipment operations are the most important network metrics and real power curtailment is the most important control cost. This weighting is necessary since slight improvements in voltage deviations and losses should not be scored as positive improvements if there is an increase in equipment operations. Here, the majority of metrics need to be improved for the control to be deemed successful. The PV power curtailed and vars generated are not included here because they directly contradict the $\Delta \boldsymbol{m}_i^{\boldsymbol{w}} < 0$ threshold. Instead, once parameter ranges that lead to net improvements are identified, the absolute value of $\Delta \boldsymbol{m}_i^{\boldsymbol{w}}$ can be compared to $PC_i + VG_i$.

4.3.5 Approximations Made to Reduce Computation Time

The parameter identification procedure laid out in Section 4.3.4 is an exhaustive search of the parameter space for each control type. An exhaustive search is necessary due to the discrete,

discontinuous, and nonlinear nature of the solution space of $\Delta \boldsymbol{m}_{\boldsymbol{i}}^{\boldsymbol{w}}$. However, this means as the dimensionality of the parameter space increases, the computation time increases geometrically. For example, if fixed power flow control is tested at a parameter granularity of 10, then only 10 QSTS simulations need to be performed for each PV interconnection location, in addition to the no-control case. However, for the two-parameter volt/watt control, 100 QSTS simulations need to be performed, and for the three-parameter watt-priority volt/var control, 1000 QSTS simulations need to be performed to span all unique parameter combinations. With such a large number of simulations necessary for even this rough parameter identification to within one tenth of each parameter's range, certain approximations need to be made.

The first approximation has already been alluded to in Section 4.3.1: only one week of load and irradiance data is simulated in the QSTS rather than an entire year. A representative week of load is selected by minimizing the error between the yearly LDC of the feeder and the LDC of the week selected. A representative week of irradiance data is then matched to the week of load selected.

The second approximation is the time step size used in the QSTS. Figure 4.8 shows the percent change in the two most time-sensitive metrics, regulator tap changes and capacitor switches, at various time steps. The highest resolution data available has a time step of one second and each increase from this changes the total number of tap changes and switches recorded. But, the changes are on the same order of magnitude between the time steps, meaning an approximation of how the network will change due to each control type can still be made.

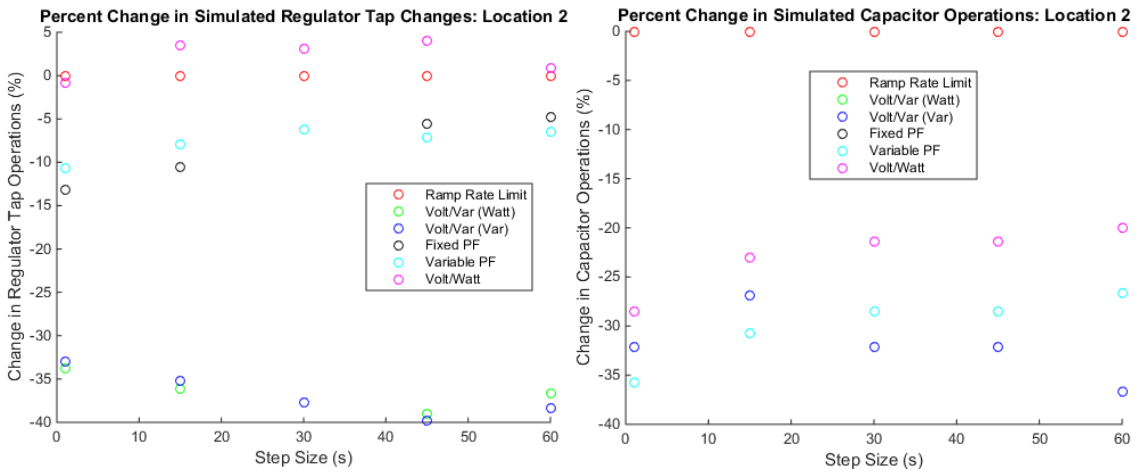

Figure 4.8. Percent difference in tap changes (left) and capacitor switches (right) using different simulation time steps under the various control types.

Furthermore, for similar results, the QSTS computation time required decreases exponentially for each increase in time step size. This trend is demonstrated in Figure 4.9. The worst-case scenario in this figure is the var-priority volt/var control, which must communicate over the COM interface between Matlab and OpenDSS several times each time step. This control takes over 10 minutes to calculate the one-week QSTS simulation at one-second time steps. At one-minute time steps, the one-week simulation takes less than 10 seconds. Therefore, in order, to simulate the large number of QSTS simulations required by an exhaustive search of the parameter space (as previously described in this section) in any reasonable amount of time, a step size of one-minute is used in each QSTS simulation in this research.

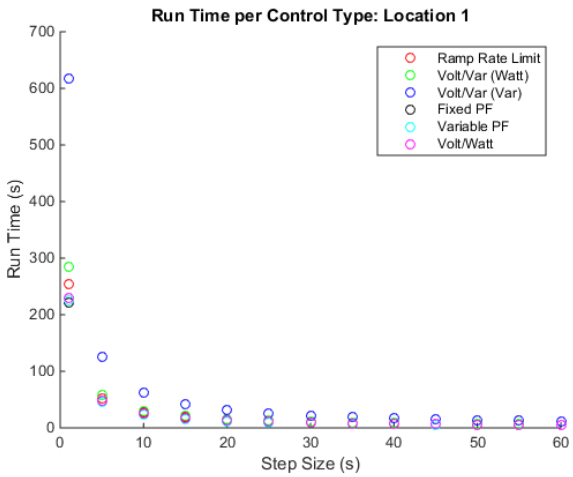

Figure 4.9. Computation time of each control type per data step size.

The third approximation is the use of reduced order network models. Extraneous elements such as short network branches, secondary networks, and clustered loads are aggregated to provide a similar voltage profile on a much smaller network. The reduction process is described in [8].

4.3.6 Search Algorithm to Find Optimum Settings per PV System Location

The algorithm to find the optimum range of control parameter settings depends on the number of parameters in the controller. In the simplest case, for a single parameter, the region $\Delta \boldsymbol{m}_i^{\boldsymbol{w}} < 0$ directly corresponds to an array of parameters. The "search" in this case simply verifies that all parameters that satisfy the $\Delta \boldsymbol{m}_i^{\boldsymbol{w}} < 0$ requirement are continuous.

The problem becomes more challenging in two or more parameter dimensions. Starting with two parameters and using volt/watt control as an example, the solution space of $\Delta \boldsymbol{m}_i^{\boldsymbol{w}}$ can be visualized as a surface, as in Figure 4.10. It is clear from this figure that the solution space is indeed nonlinear and discontinuous, making an analytical solution to the optimum parameter set difficult. The axes of this surface are the two parameters of volt/watt control: the slope of the PV curtailment due to PCC voltage and the deadband at which the control begins. The values in this space that correspond to the net score of the objective function and the control action. Net negative values represent control parameters that balance PV curtailment equally with an overall improvement of network parameters.

Only these negative values indicating good parameter combinations are shown in Figure 4.11. Now it becomes clear that finding a range of both parameters that encompasses the most improvement is not straightforward. The goal of finding the largest parameter ranges that only include good metric scores is equivalent to finding the largest rectangle that encompasses only colored blocks in Figure 4.11. To achieve this, an image processing tool called "FindLargestRectangle" is employed in Matlab. This function uses an optimization algorithm to maximize a rectangle in a Boolean bitmap image. In this case, the "image" used is the solution space from Figure 4.11, with negative values set to 1 and positive values set to 0. The largest

rectangle, or largest intersecting range of acceptable control parameters, is highlighted over the entire surface in Figure 4.12.

This entire procedure is replicated for a PV interconnection placed midway down the feeder and the results are shown in Figure 4.13. Comparing the two resultant rectangles, it can be seen that the PV interconnection location has a large impact on the range of viable control parameters. This result indicates multiple PV interconnection locations should be tested to get a sense for the appropriate control parameters to use.

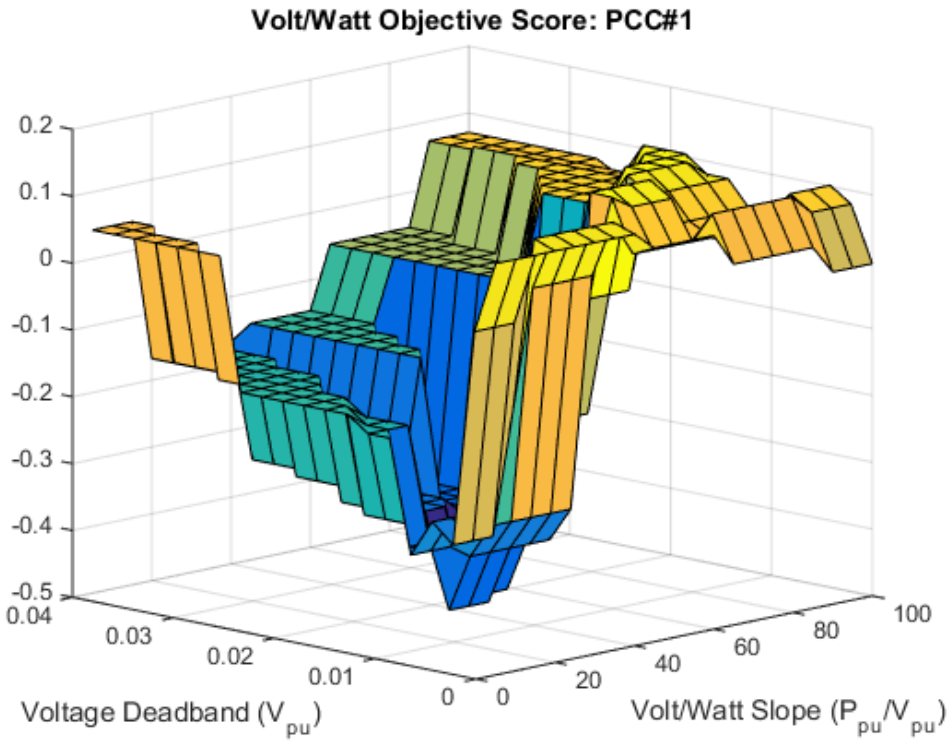

Figure 4.10. Solution space to the weighted objective function for volt/watt control at a given PCC.

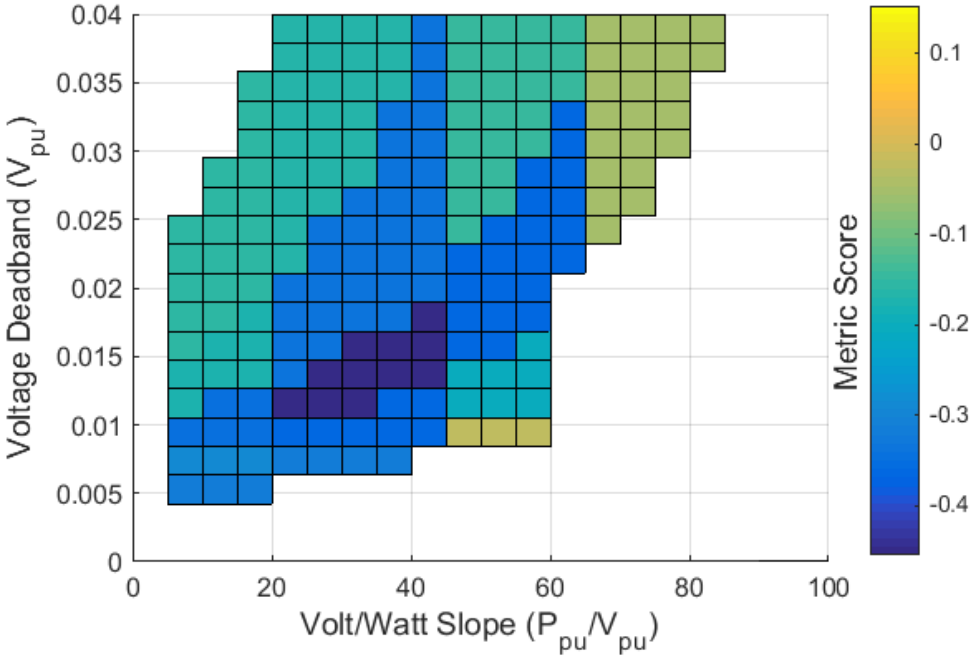

Figure 4.11. Volt/watt optimization solution space resulting in net-negative values.

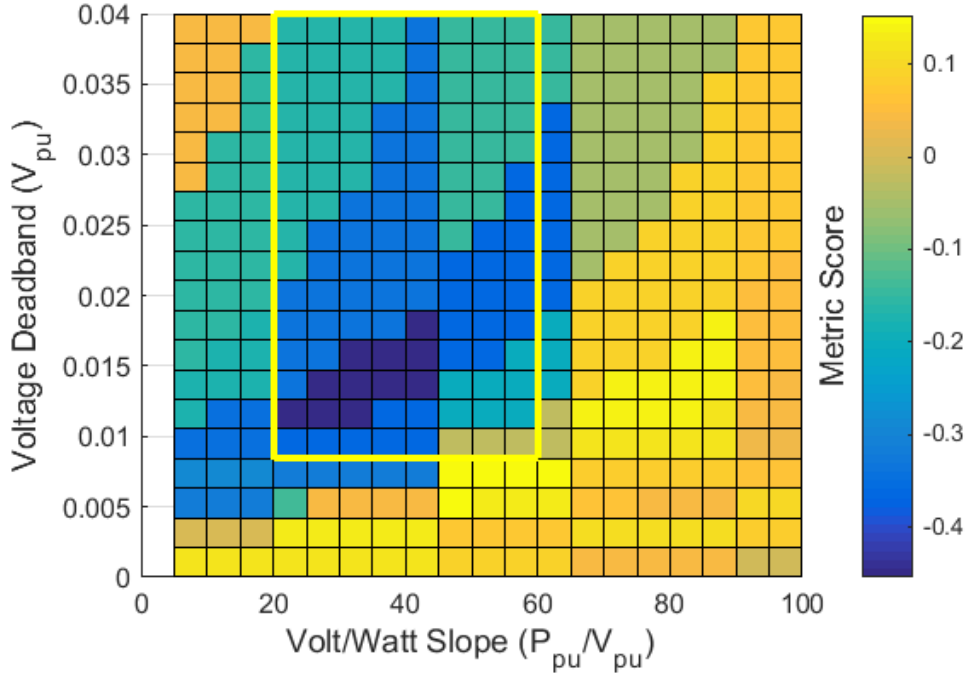

Figure 4.12. Largest range of parameters corresponding to net improvement due to Volt/Watt control at a PV interconnection at the end of the feeder.

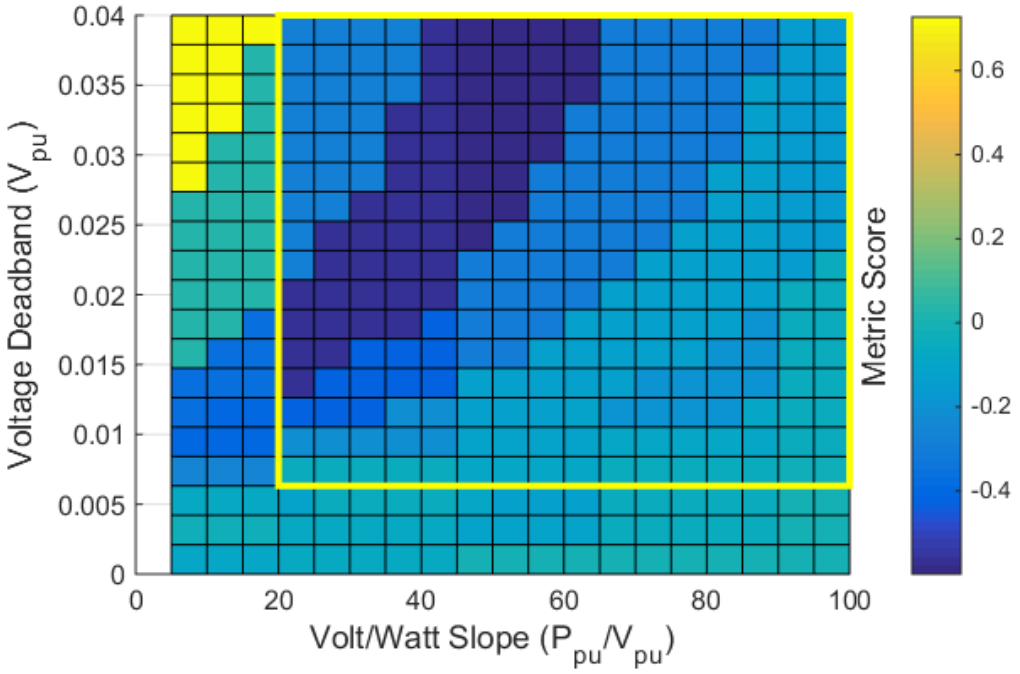

Figure 4.13. Largest range of parameters corresponding to net improvement due to Volt/Watt control at a PV interconnection midway down feeder.

To find the optimum range of parameters in the controllers with three parameters (i.e. both volt/var controls), the methodology for the two-parameter case is applied to the two-dimensional solution space corresponding to each discretization of the third dimension. For any particular range of the third dimension parameter, the good values that span the entire third-dimension's range as well as the other two parameter dimensions are found by multiplying all the Boolean two-dimension solution spaces together. Then, the volume of the space that spans all three parameter dimensions is summed for every possible range in the third parameter dimension. The largest volume is kept and this represents the optimum set of parameters in all three parameter dimensions.

4.4 Advanced Inverter Control Type Performance

This section presents the detailed results of each control type being run on one of the two feeders described in Section 4.3.2.

4.4.1 Inverter Ramp-Rate Limiting

By simply limiting the rate at which the PV system is allowed to achieve a higher power output level, some of the adverse impacts on network metrics may be avoided at the expense of a slightly lower PV energy production. The impact on the various metrics and the amount of PV being curtailed at different rate limits is shown in Figure 4.14. Each of the colors represents one of the 20 different interconnection locations on feeder CO1. From the top plots, a general trend of improvement with increased ramp-rate limiting can be seen in tap changes on the left and capacitor switches on the right. However, only certain interconnection locations see improvements whereas interconnections at several locations appear to result in increased switching when the ramp rate is limited. The total amount of PV generation curtailed by each ramp rate is shown in the bottom-right plot. The bottom-left plot shows the network losses, which generally increase with more curtailment since the PV is offsetting certain network current flows. Over-voltage violations, shown in the middle-left plot, generally decrease with more curtailment as expected. Under-voltage violations interestingly improve somewhat consistently when PV is placed at certain buses and this improvement is hampered by the curtailment.

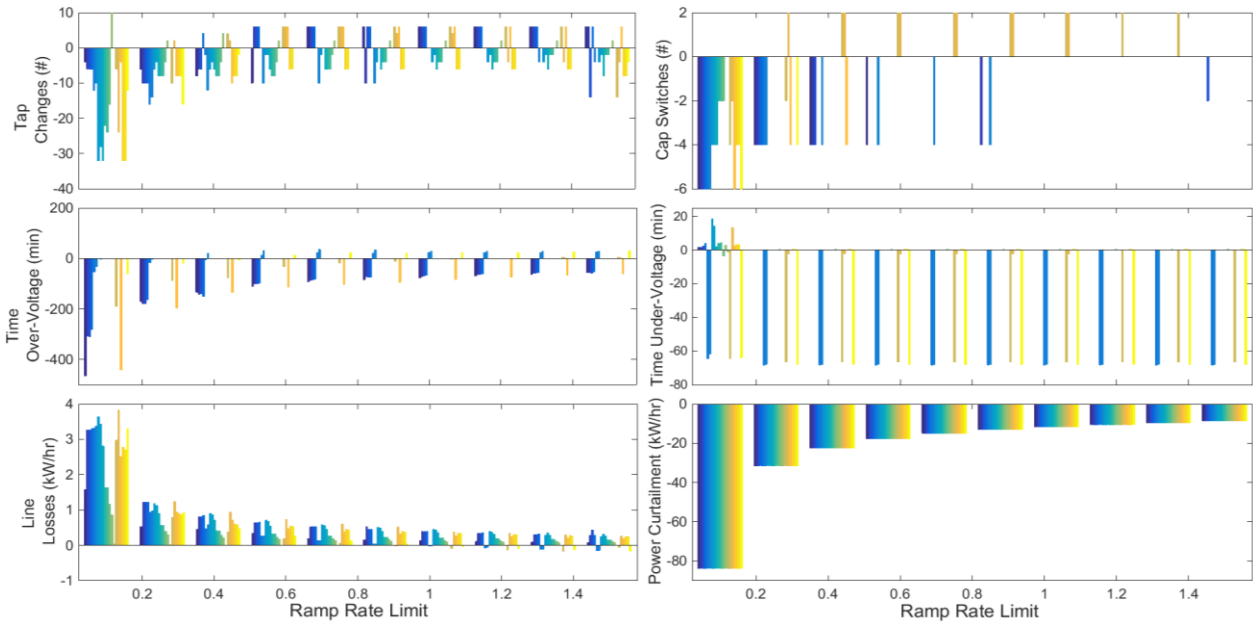

Figure 4.14. PV power curtailment and five network metrics as impacted by inverter ramp-rate limiting for 20 locations (different colors) on feeder CO1.

Due to the conflicting nature of some of the metrics shown in Figure 4.14, it is useful to get a sense of the overall improvement gained by the control at each location and setting. In Figure 4.15, each network metric (not including control action cost) is normalized to its minimum (best) value and summed together. The first thing to note in Figure 4.15 is that the positive green values are indicative of one particular PV location showing no overall improvement for any of the control's parameter values. In other words, at this location the PV system alone always has a better impact on the network without ramp-rate limiting. The second thing to note is that there is a general trend of more overall improvement with increased curtailment. This is expected since, unless the PV actually improved the system, the more PV is curtailed the closer the system returns to its baseline metrics. This is why a weighted objective score including the cost of the control is necessary. In Figure 4.16, the objective function in (4.1) is used to weigh control cost against network improvement. In this case, the settings that only slightly limit the ramp-rate of the PV perform slightly better than the other more aggressive control settings. This indicates that the improvements gained by limiting PV ramping are not significant compared with the cost of curtailment using these metric weights.

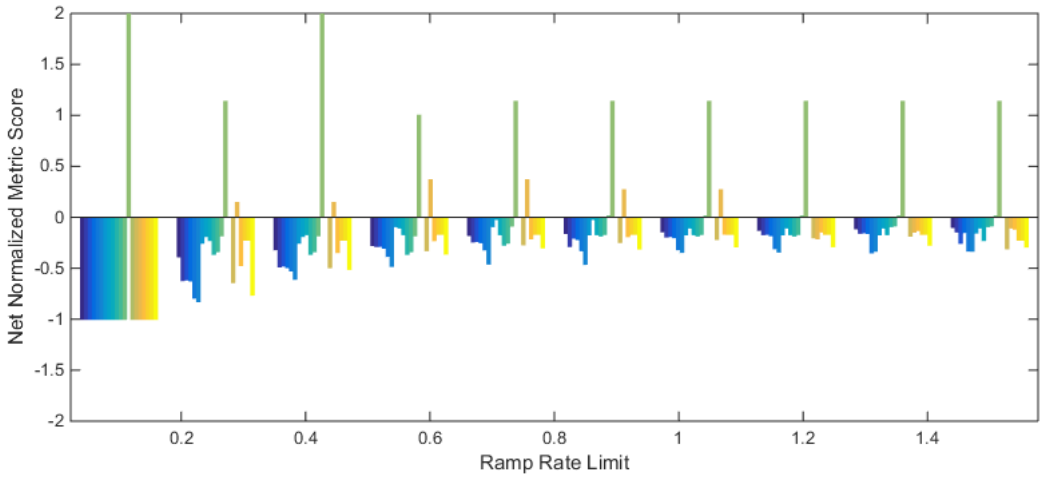

Figure 4.15. Sum of normalized metrics per ramp-rate limit.

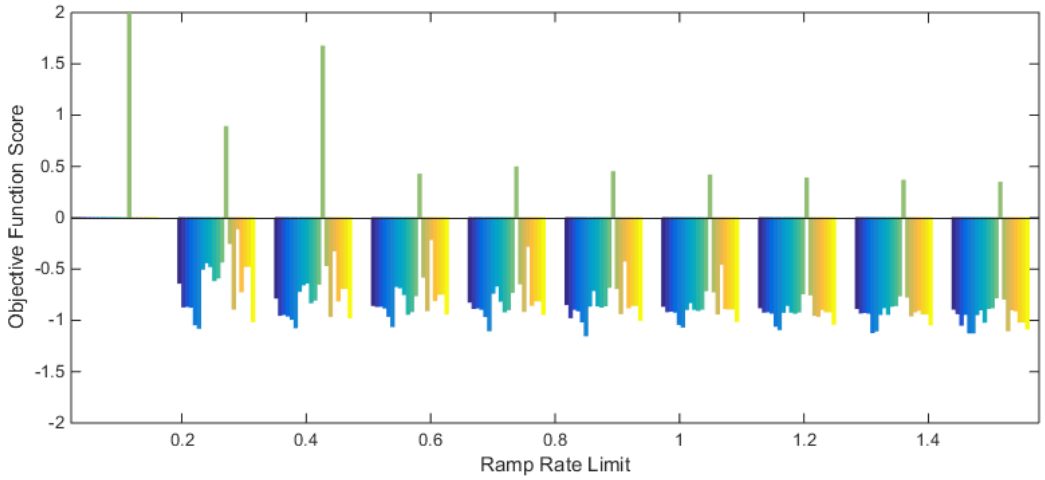

Figure 4.16. Weighted objective function (4.1) score per ramp-rate limit.

4.4.2 Constant Power Factor Control

With the inverter set to a constant power factor, the change in the base case of the five network metrics and the control action are shown in Figure 4.17. Each grouping of bars represents the net change from the no-control case for one particular control setting at all 20 interconnection locations in feeder CO1, where the locations are shown as different colors. The top-left plot shows that the reduction in tap changes peaks in general across the feeder at 0.9 power factor and at 0.8 power factor but as the power factor decreases further there are several interconnection locations that begin to see more tap changes due to the control. Capacitor switching displays a similar behavior in the top-right plot, except several of the power factors perform equivalently well. As expected, the number of over-voltages shown in the middle-left plot improves with increased reactive power absorption. However, this improvement plateaus around 0.85 power factor. Conversely, the number of under-voltage violations becomes worse as more vars are absorbed by the PV inverter, as shown in the middle-right plot. This is an indication of why an objective function is necessary to rate the control action, as some metrics may change in different directions. In the bottom-left plot, losses can be seen to increase in general as the inverter injects more reactive current into the network, which is to be expected. Lastly, the bottom-right plot shows the control action used by

the inverter. In this case, it is the vars generated by the PV inverter, which of course increase with decreased power factor.

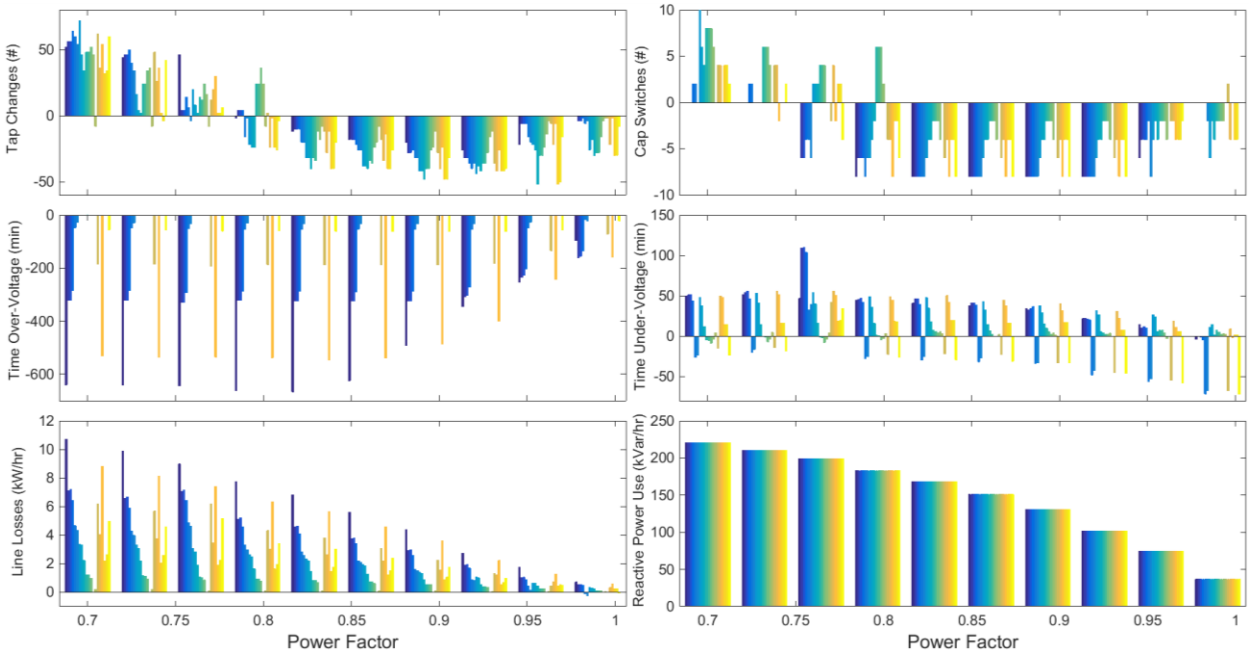

Figure 4.17. Inverter control action and five network metrics as impacted by inverter constant power factor settings and PV interconnection location on feeder CO1.

Again, due to the conflicting nature of some of the metrics, the sum of the normalized improvements is used and displayed in Figure 4.18. Here it can be seen that across all locations a constant power factor between 0.9 and 0.95 shows the largest overall improvement. This finding is echoed by the objective scores, which are displayed in Figure 4.19. The upper and lower boundaries that correspond to the widest range of good power factors settings at each location are shown per their interconnection location on the network maps in Figure 4.20.

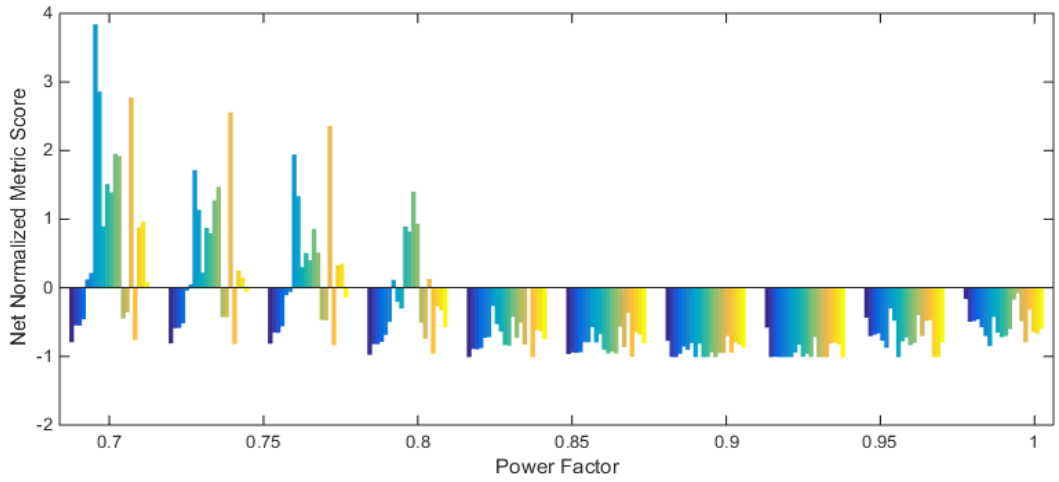

Figure 4.18. Sum of normalized metrics per inverter power factor.

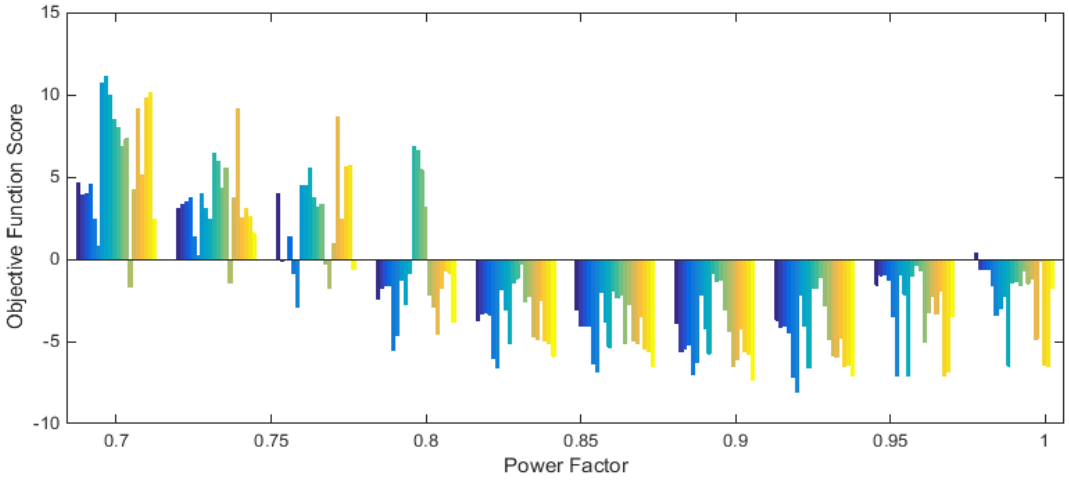

Figure 4.19. Weighted objective function (4.1) score per inverter power factor.

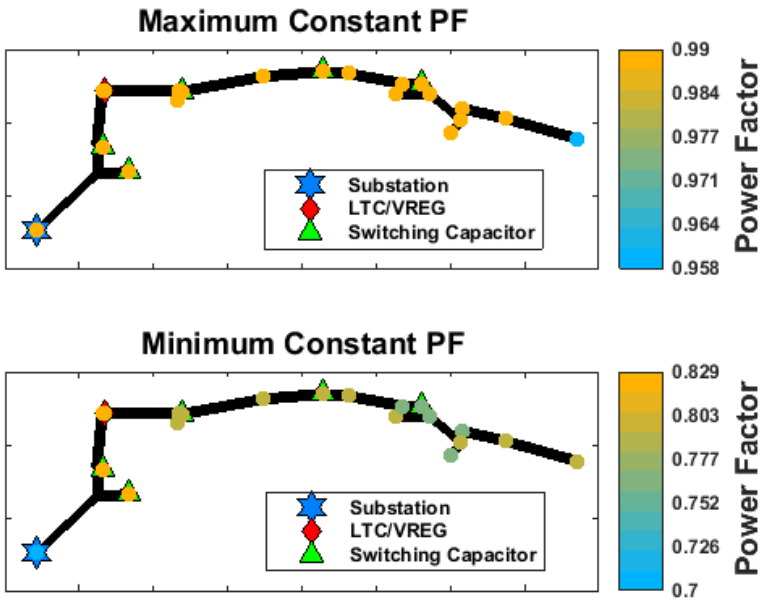

Figure 4.20. Upper and lower boundaries on power factor settings per interconnection location in feeder CO1 based on the metric weighting function (4.1).

4.4.3 Volt/Watt Control

For a two-parameter control, such as Volt/Watt, the network metrics become more difficult to visualize individually. The sum of the normalized network metrics for each unique combination of the two control parameters, at all interconnection locations, is presented in Figure 4.21. As with the ramp-rate limiting control before, there is a general trend of improving network conditions the more aggressive the controller curtails the PV. This is expected since more curtailment will mitigate any PV-induced issues. However, in this case the amount of improvement is more variable with PV location since the control relies on the local voltage, which has a strong or weak dependence on the PV output.

The objective function score (1) of each parameter pair at each PV location is presented in Figure 4.22. In this case, since the score of each control is now penalized for the amount of PV power curtailed, the most aggressive control parameters (high slope and low deadband) no longer register the minimum scores. It is clear that since there is almost a direct trade-off between the effectiveness of the control action and its cost that the best parameters to use should be somewhere

in the middle of the ranges considered. However, the increased variability due to PV location makes it difficult to draw an overall conclusion.

Rearranging the data from Figure 4.22 to represent the control parameter surfaces such as the one in Figure 4.12, yields the set of twenty surfaces (one for each location) in Figure 4.23. Orange and yellow regions indicate a poor control response and green to blue regions indicate a good response. However, this continuous color scale applied across all locations makes it difficult to distinguish the boundary between good and bad parameter sets. Instead, a threshold can be chosen, as in Figure 4.11, under which there is an acceptable improvement in network conditions for the associated control cost. In Figure 4.25, a threshold of -1.0 is set and the yellow regions indicate the parameter sets that achieve at least this level of improvement against control cost. For most interconnection locations, there are a broad range of acceptable parameters. However, several regions have much narrower ranges. There is even an outlying location, represented in pale green, in which no set of parameters achieved an improvement below the given threshold. This is a location where Volt/Watt control of any kind would not be practical, indicating the presence of the PV may actually improve the overall network conditions when placed there.

The method described in Section 4.3.6 is then used to find the largest range of parameters that meet the minimum threshold required of the objective function for each of the subplots in Figure 4.25. The upper and lower bounds of these areas are then plotted in Figure 4.26 and Figure 4.27 per PV interconnection location in feeder CO1. Figure 4.26 shows the minimum and maximum Volt/Watt slope settings that can be used at each PV location and still achieve the objective function goal. Figure 4.27 similarly shows the upper and lower Volt/Watt deadband settings to achieve this goal. As expected from the plots in Figure 4.25, many of the locations can set the control parameters loosely and still achieve the desired goal. This also depends on the weights given to the objective function (4.1) and the scalar bias. If, for instance, the weight of the PV curtailment control action is increased, then more aggressive control parameter sets will fall above the bias. Figure 4.26 indicates that the upper bound of the controller slope is dependent on

interconnection location, but not the lower bound. Similarly, the lower bound of the size of the deadband is location dependent, as seen in Figure 4.27.

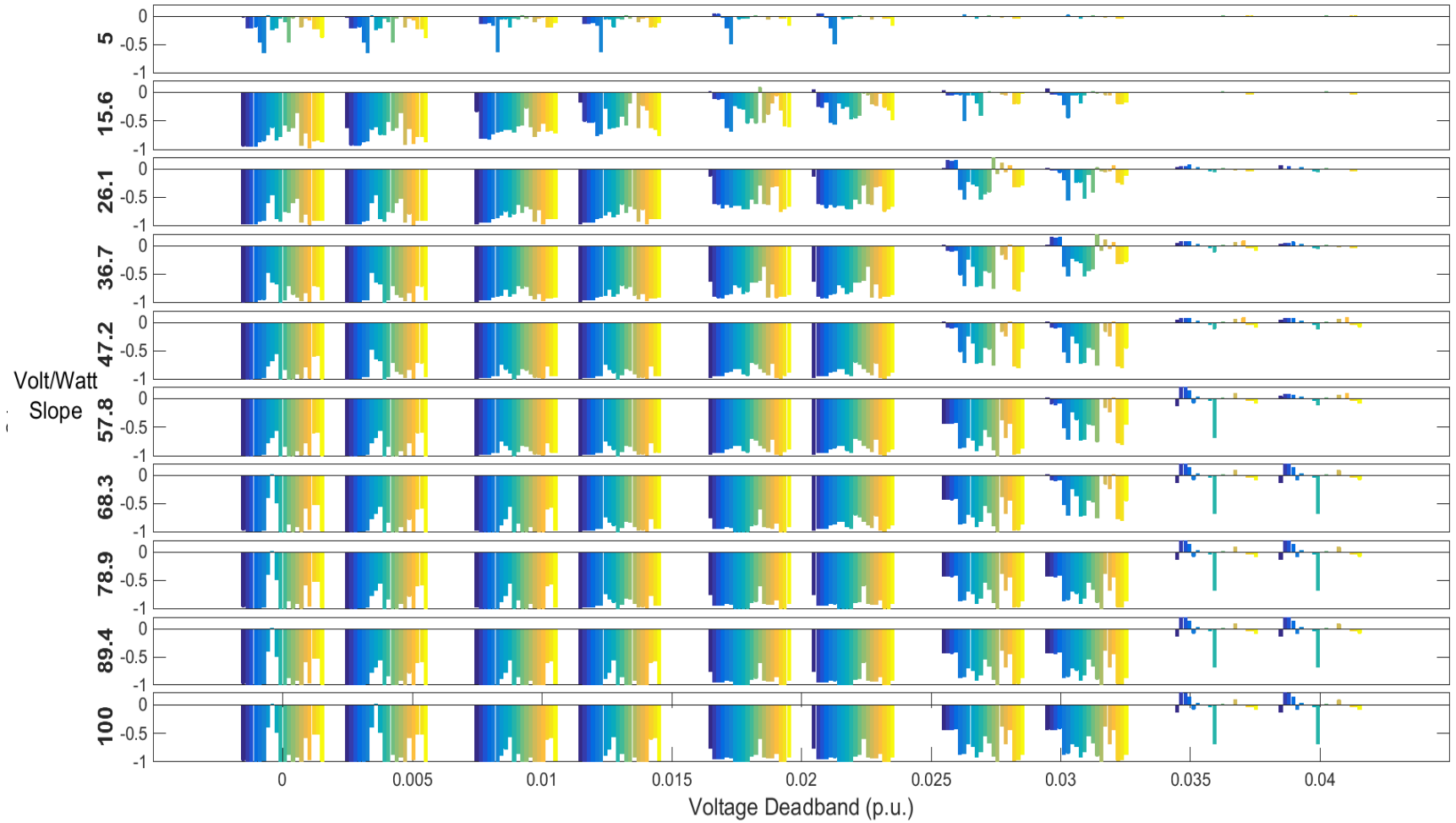

Figure 4.21. Sum of normalized network metric scores for each Volt/Watt control parameter at all PV locations.

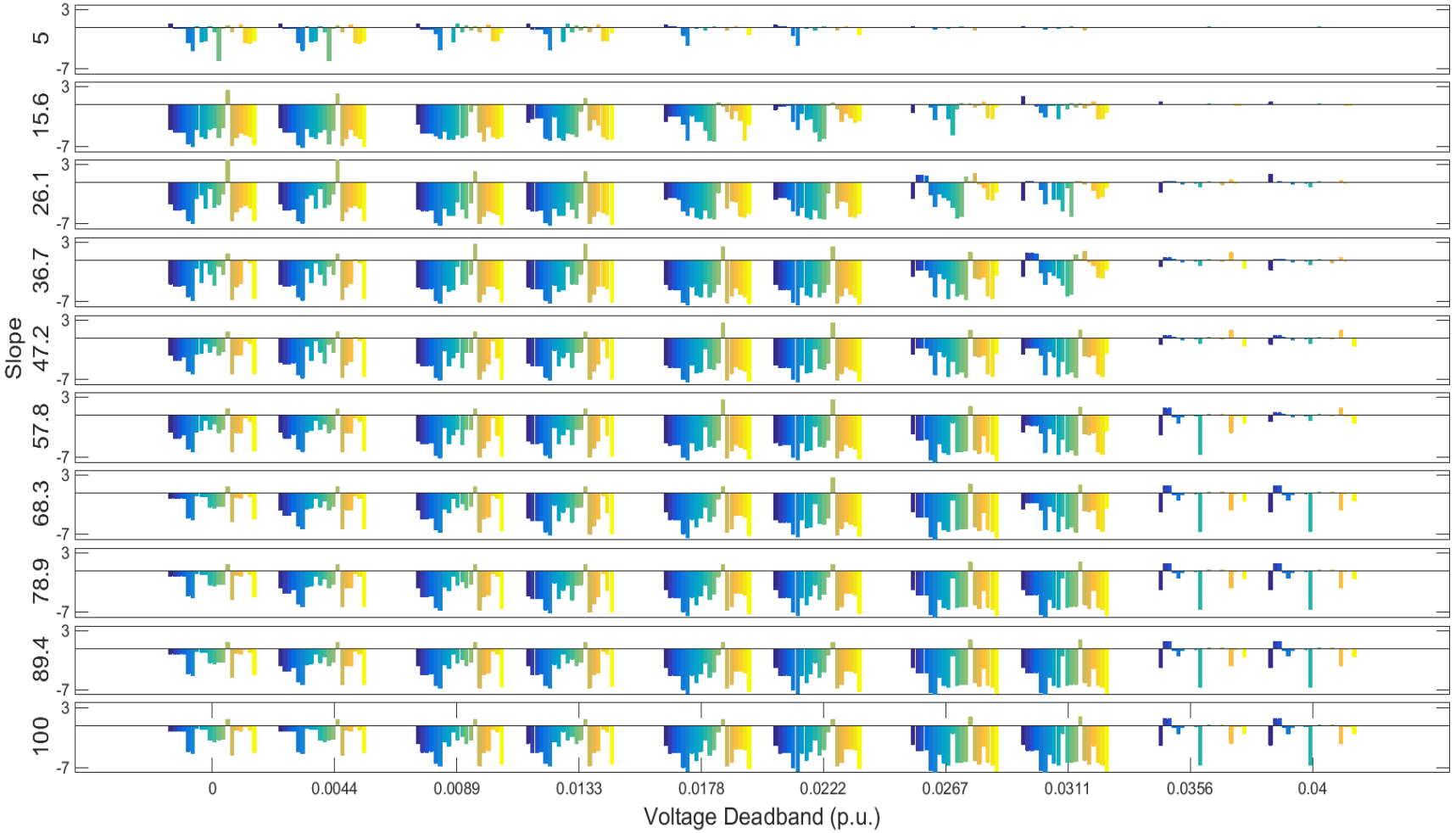

Figure 4.22. Objective function score for each set of Volt/Watt control parameters at all PV locations.

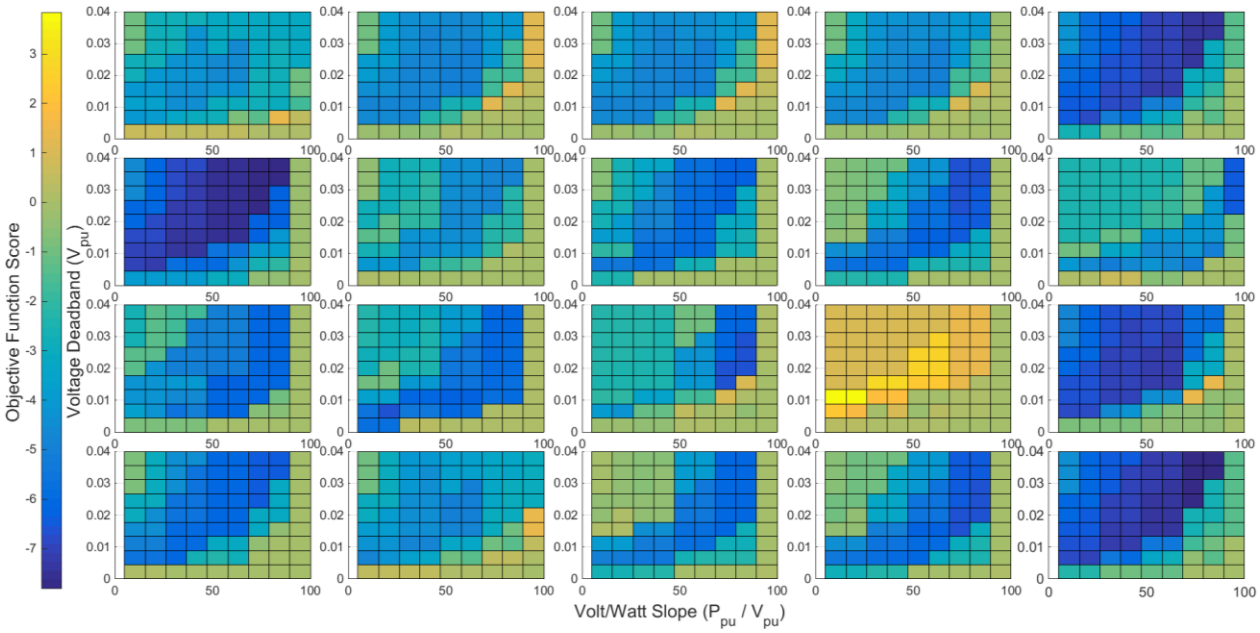

Figure 4.23. Volt/Watt control objective function score surfaces at each PV location.

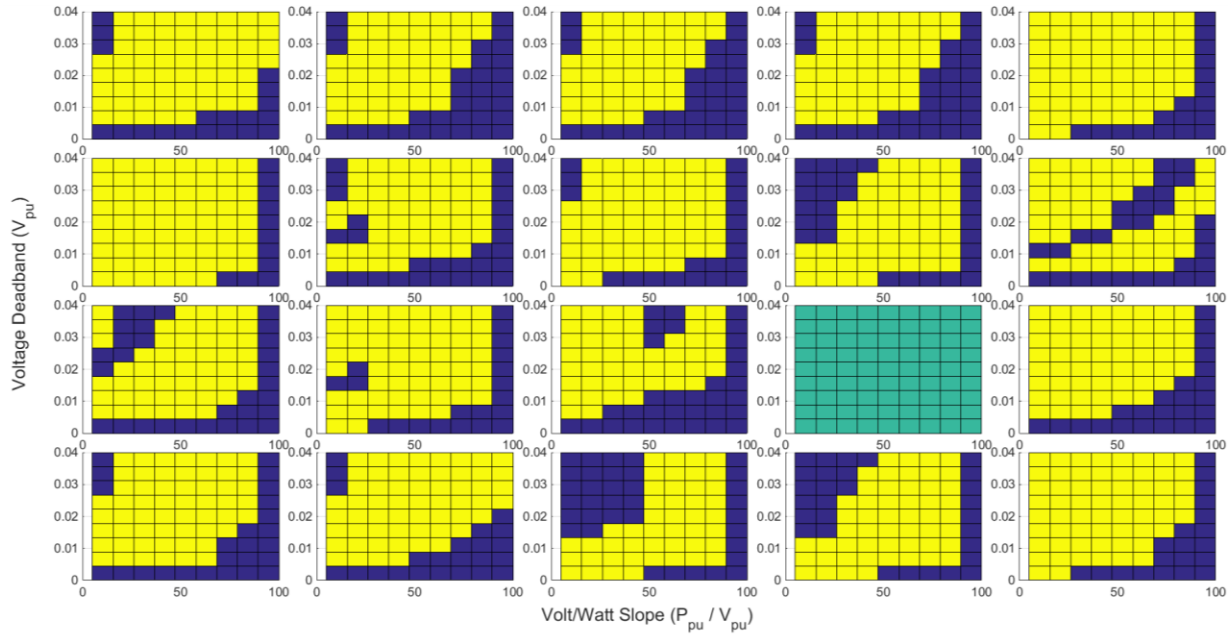

Figure 4.24. Control parameter regions in yellow that improve the network metrics more than the Volt/Watt control action used with no objective score biasing.

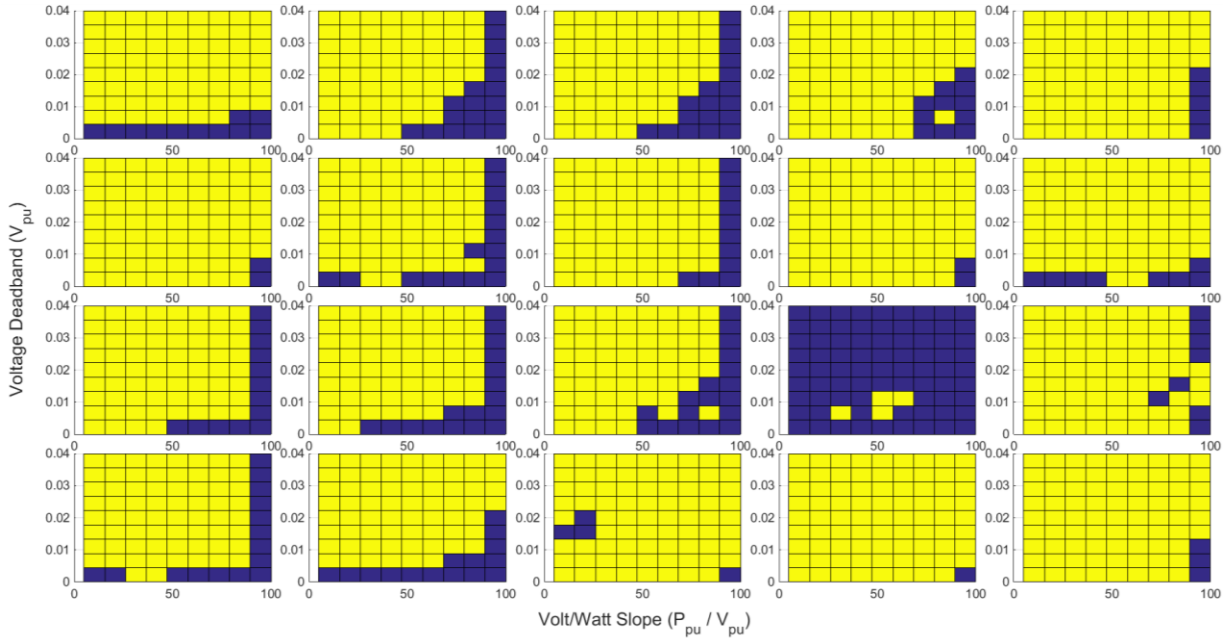

Figure 4.25. Control parameter regions in yellow that improve the network metrics past a bias of -1.0 added to (4.1) to highlight the impact of of the Volt/Watt control action used.

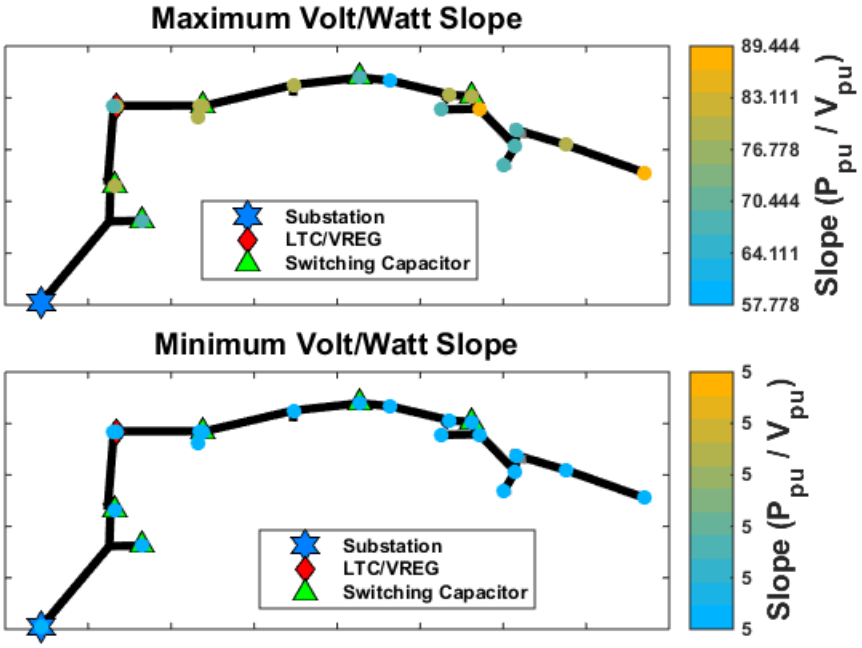

Figure 4.26. Volt/Watt slope upper and lower boundaries for feeder CO1 based on objective score.

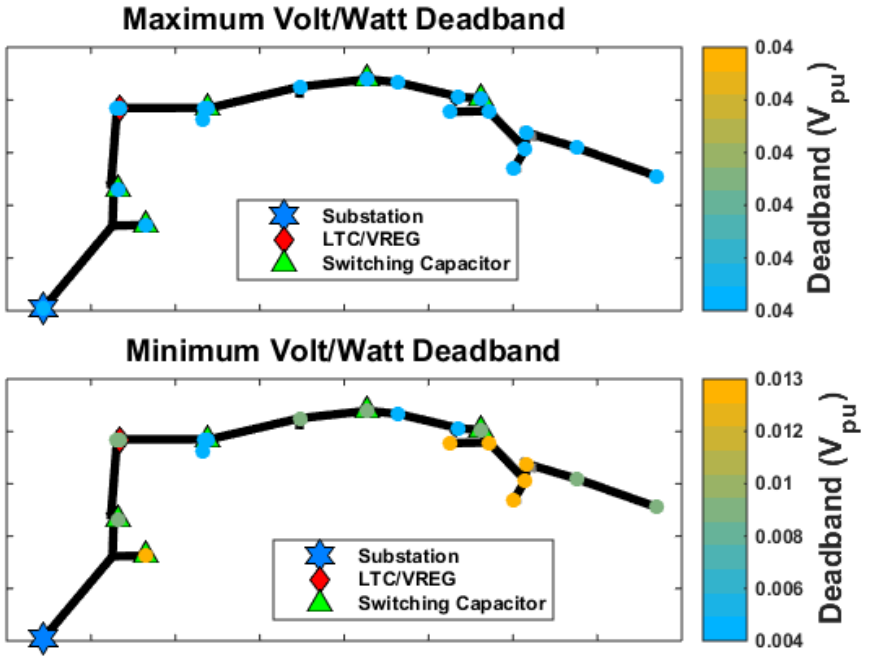

Figure 4.27. Volt/Watt deadband upper and lower boundaries for feeder CO1 based on objective score.

4.4.4 Watt-Triggered Power Factor Control

For watt-triggered power factor control, the inverter increases its var absorption based on its real power output. Figure 4.28 shows how the normalized network metrics vary with the two parameters that determine this control action: the target power factor at full rated output and the deadband of output power at which the control begins. While low deadband values will cause more overall control action, high deadband values will cause more aggressive var compensation. For this reason, the control settings in Figure 4.28 with low target power factors and high deadbands cause sharp changes in the network, resulting in more regulator and capacitor switching and under-voltages. Lower power deadband settings improve the network parameters more in general, at the cost of more reactive power use and increased network losses.

This cost only slightly skews the objective function scores to higher deadband settings since these metrics have low weights, as seen in Figure 4.29. A bias of 0.5 is added to (4.1) to compensate. The parameters that minimize the objective function are highly dependent on

interconnection location with this control. Some interconnection locations have few control parameter combinations that give an overall improvement that outweighs the control cost, so in this case a positive bias of 0.5 is added to the objective function (4.1). This dependence can be seen clearer in Figure 4.31, which shows the control parameter regions that achieve a net improvement past the bias in yellow for each PV interconnection location. The upper and lower bounds of the control parameters that maximize these regions are shown in Figure 4.32 for target power factor and Figure 4.33 for power deadband. The value of the target power factor is more location dependent on its upper bound because generally more var compensation will give greater overall network improvement with the chosen weights.

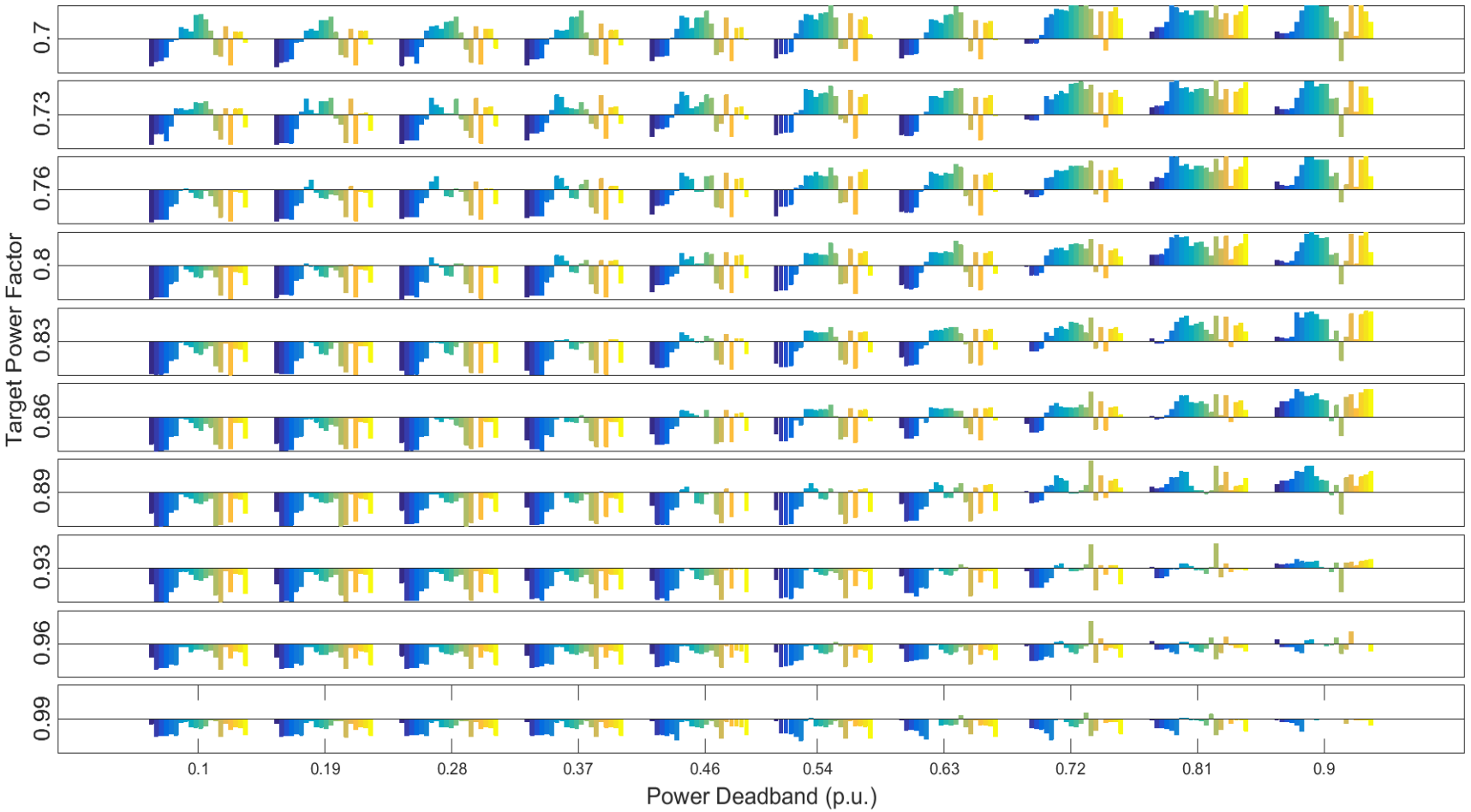

Figure 4.28. Sum of normalized network metric scores for each watt-triggered power factor control parameter at all PV locations.

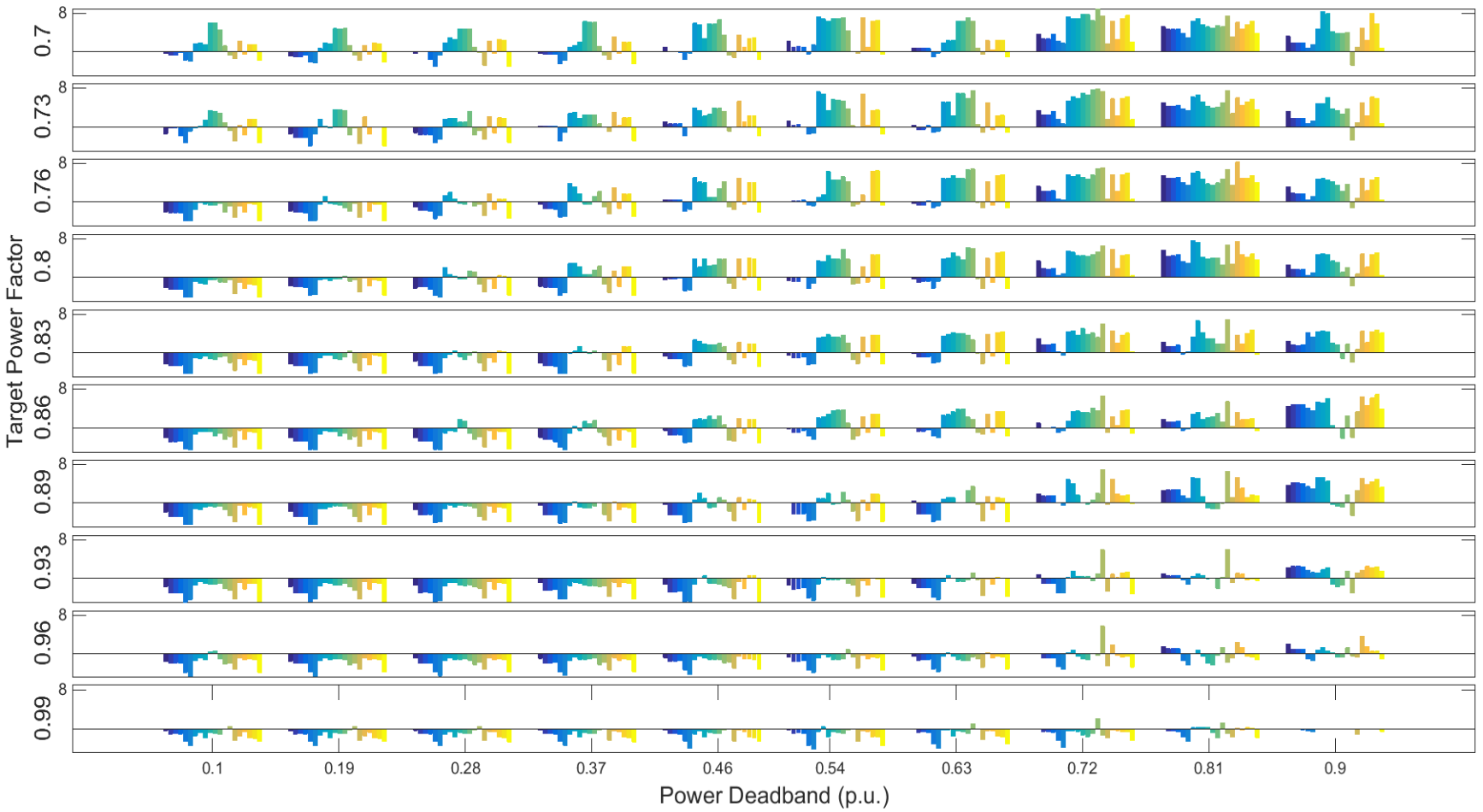

Figure 4.29. Objective function score for each set of watt-triggered power factor control parameters at all PV locations.

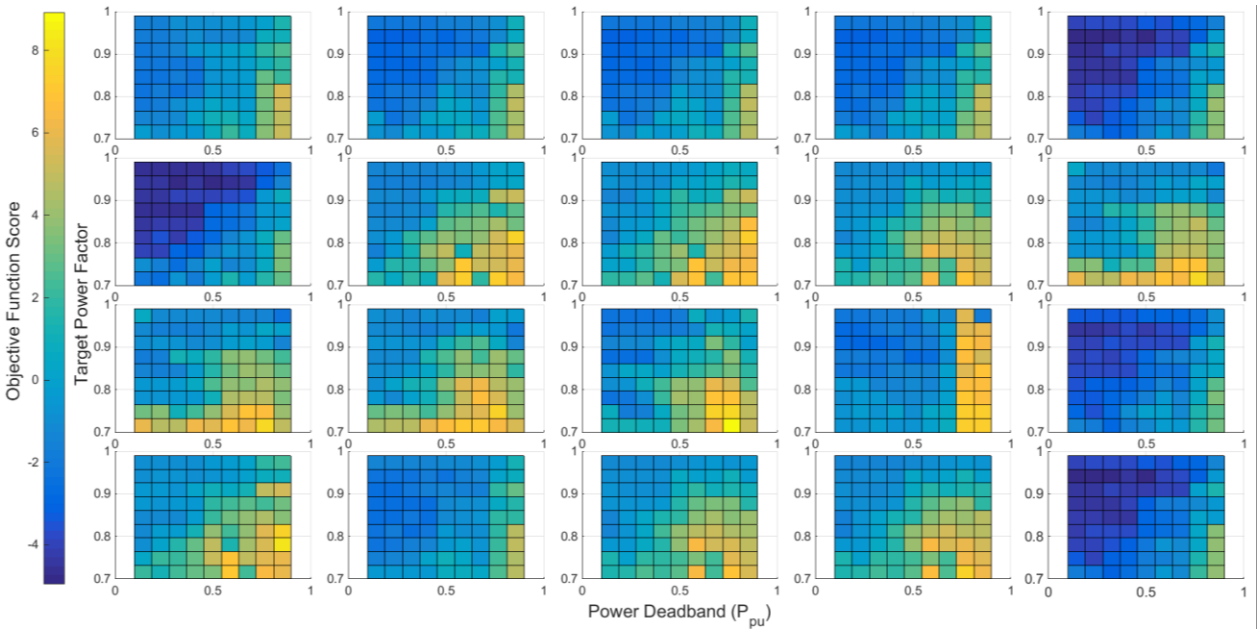

Figure 4.30. Watt-triggered power factor control objective function score surfaces at each PV location.

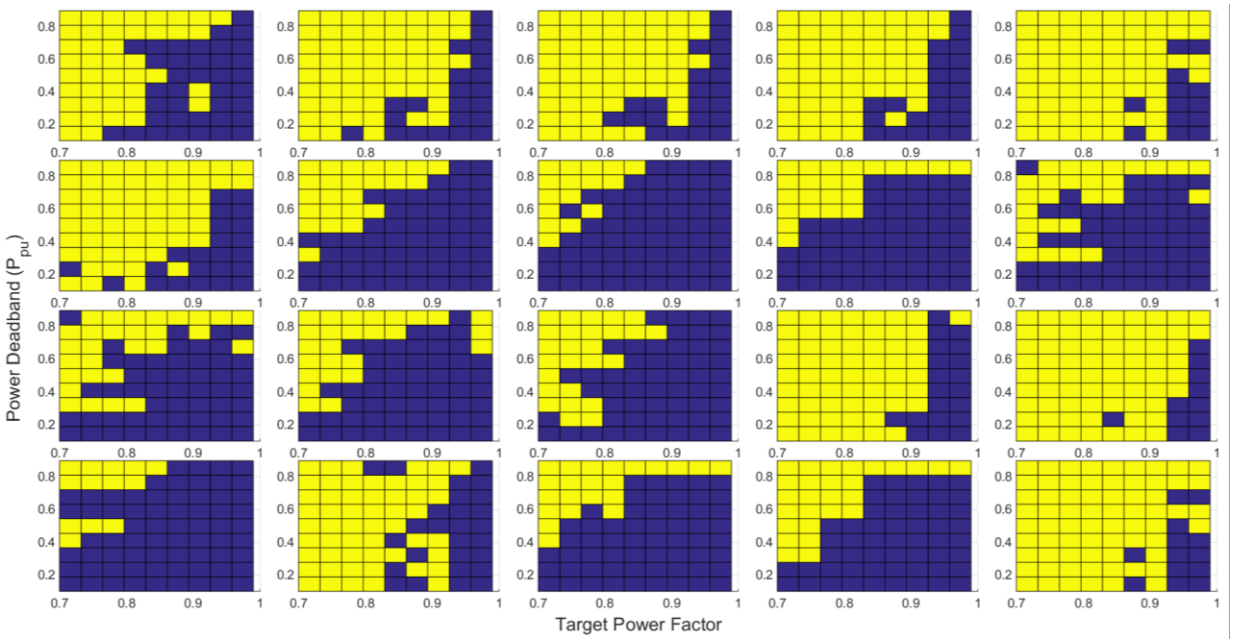

Figure 4.31. Control parameter regions in yellow that improve the network metrics using watt-triggered power factor control with a bias in (4.1) of 0.5.

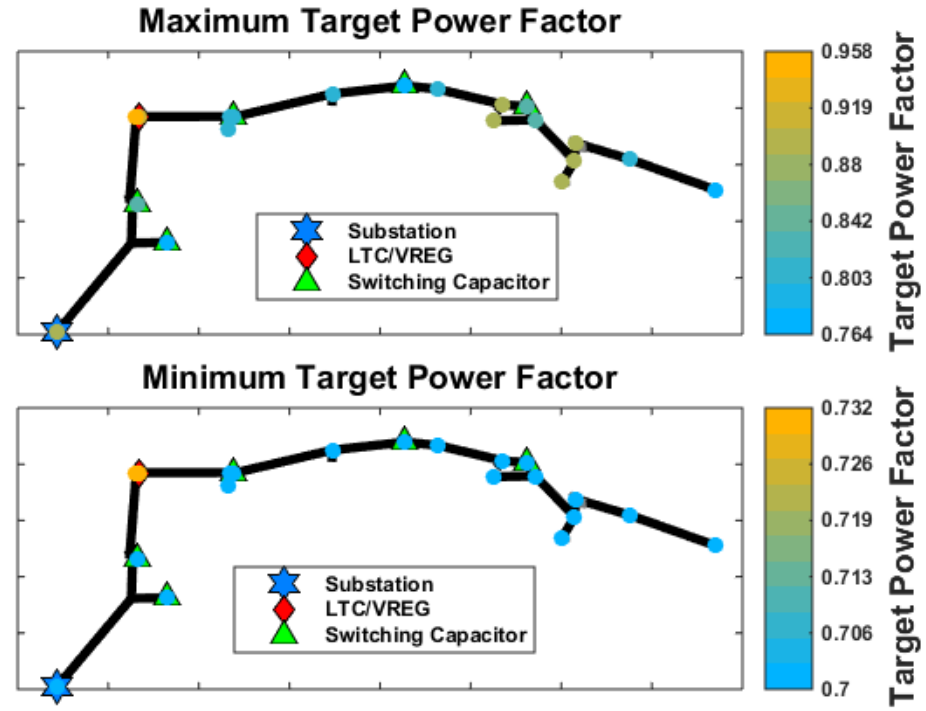

Figure 4.32. Upper and lower bounds of target power factor for watt-triggered power factor control for each PV interconnection in feeder CO1.

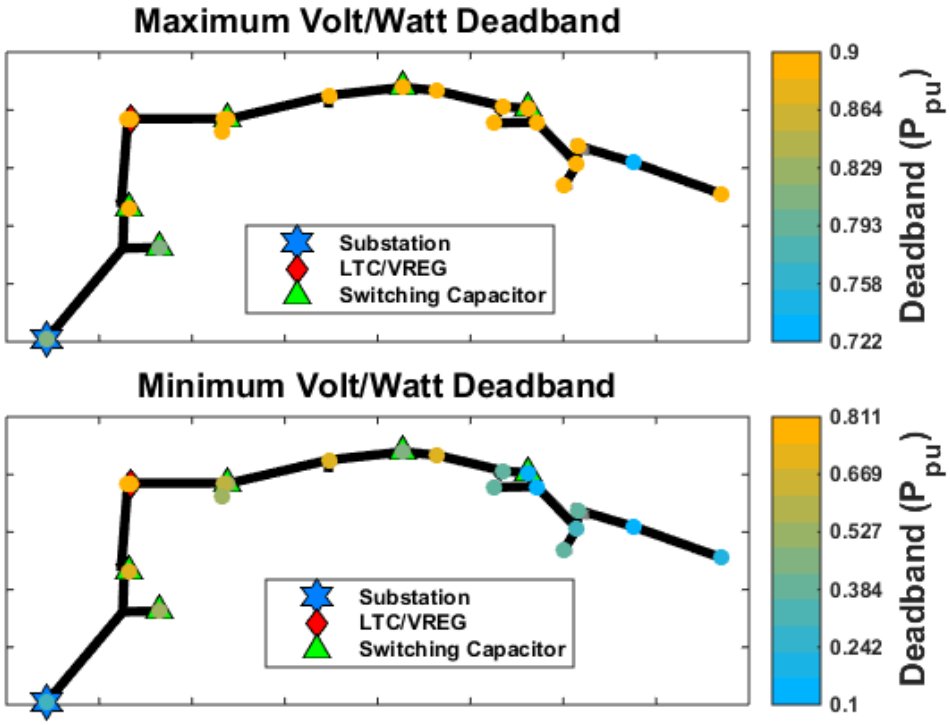

Figure 4.33. Upper and lower bounds of PV power output deadband for watt-triggered power factor control for each PV interconnection in feeder CO1.

4.4.5 Watt-Priority Volt/Var Control

Unlike the other advanced inverter controls, Volt/Var control has three parameters that may be set. This makes it difficult to visualize how the parameters impact the network metrics due to the extra dimension. This control is applied to 20 locations in feeder CS1. The normalized network metrics at each control parameter combination across the feeder is shown in Figure 4.34. Each of the 100 plots in this figure has a horizontal axis that represents that variation of the nominal voltage parameter. The slope parameter is then varied vertically across plots and the deadband parameter is varied horizontally across plots (viewing the figure in a landscape format). The best performing parameters are then those that produce the most negative bars across all locations, which are differentiated by color. The general trend is that network metrics improve as the Volt/Var curve slope is increased but at some point a deadband must be added to gain more improvements. Increasing the deadband of the curve too high will prevent the controller from acting enough. Therefore, the best improvements are seen at a high Volt/Var slope, say greater than $50Q_{pu}/V_{pu}$, with a deadband with a width less than $0.02V_{pu}$ but greater than $0.01V_{pu}$. In this range, using a nominal voltage around $1.0V_{pu}$ will see the greatest improvements across the feeder.

The objective function surfaces per location are too difficult to display with more than two control parameters, but the ranges of good parameter settings can still be found by the same method described in Section 4.3.6. The range of good Volt/Var slope values per interconnection location on feeder CS1 is shown in Figure 4.35, deadband ranges are shown in Figure 4.36, and nominal voltage ranges are shown in Figure 4.37.

Figure 4.34. Normalized metric score for various Volt/Var controls applied at 20 locations in feeder QS1.

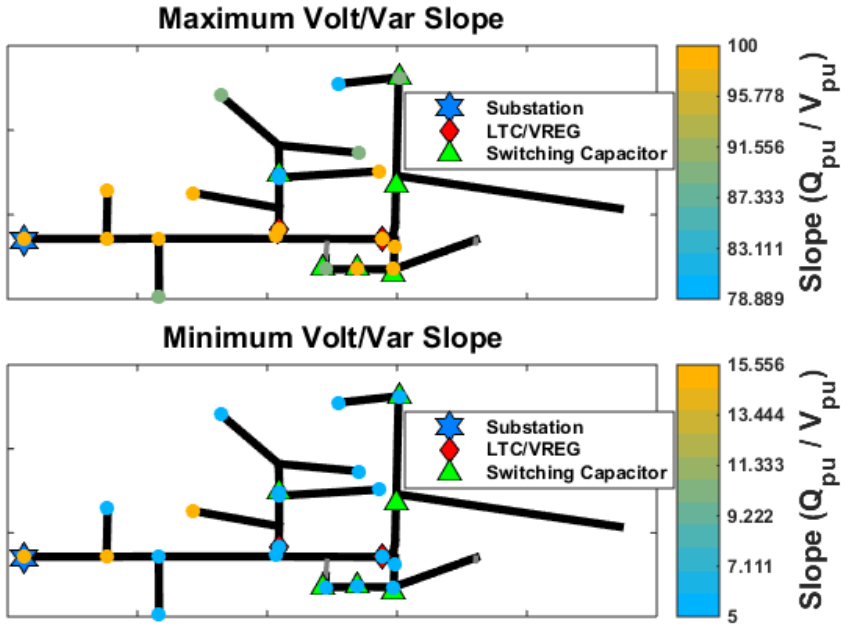

Figure 4.35. Upper and lower bounds of Volt/Var slope for Volt/Var control for each PV interconnection in feeder QS1.

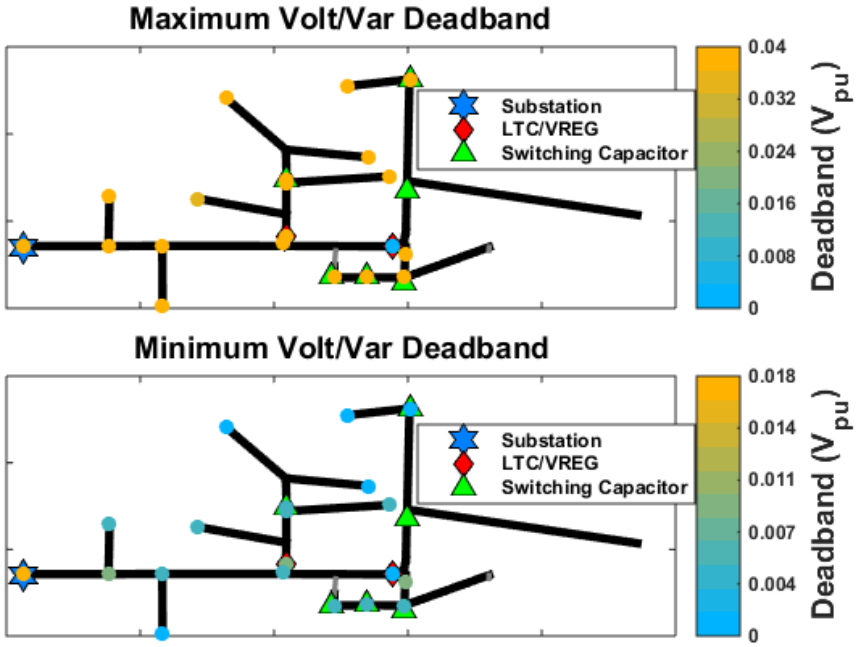

Figure 4.36. Upper and lower bounds of voltage deadband for Volt/Var control for each PV interconnection in feeder QS1.

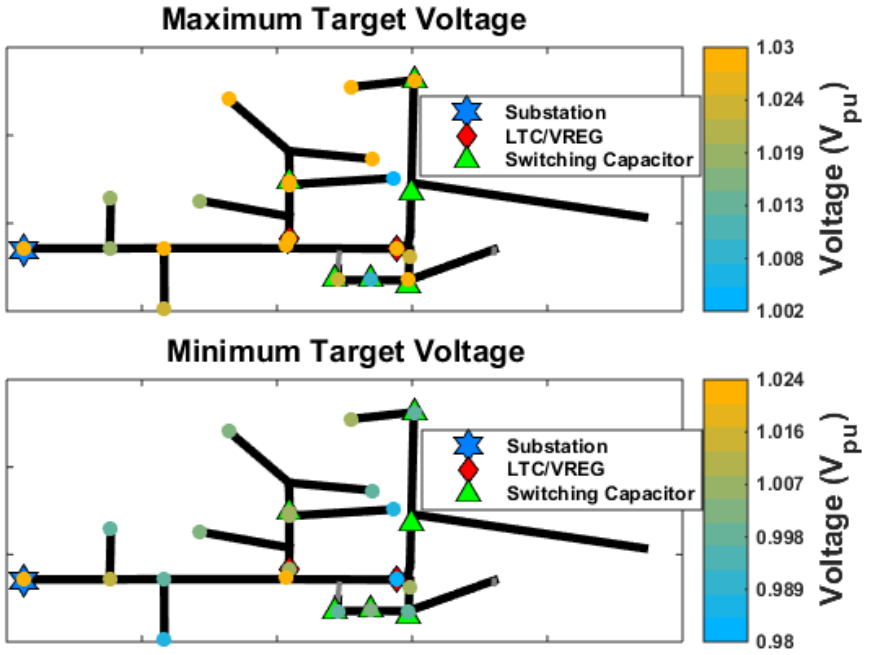

Figure 4.37. Upper and lower bounds of target nominal voltage for Volt/Var control for each PV interconnection in feeder QS1.

4.4.6 Var-Priority Volt/Var Control

Unfortunately, there are no parametric simulation results for the var-priority volt/var control type. At the time of running these simulations, a var-priority volt/var mode did not exist in the OpenDSS platform and the var-priority controls demonstrated in Appendix F are executed by communicating between OpenDSS and Matlab iteratively. This process slows down the simulation of each one-week QSTS, as seen in Figure 4.9, compared with the other control types. Since this control type also has three parameters, running a comparable parametric study on it would have taken months to complete, which is impractical for the time allotted this research.

4.5 Generalized Control Settings for Example Feeders

This section presents the method for finding the set of parameters for each control type that work well across all interconnection locations studied in the two feeders presented in Section 4.3.2. Each feeder has 20 interconnection locations, except for technical reasons Feeder CO1 only tested

the impact of Volt/Var control at four locations. To find the control settings that work well at any general location in a feeder, the binary network improvement mask, such as those shown in Figure 4.24, is found for the entire feeder. This is accomplished by applying the AND operator to all binary masks, which each represent an interconnection location, to get one binary mask for the entire feeder. Then, the same procedure presented in Section 4.3.6 is applied to find the largest area of parameter ranges that will work for the entire feeder. The general control setting ranges that work on the two feeders tested are presented below for each control type in Table .1 through Table 5.

Table 4.1. Ramp rate limit control parameter ranges that work across all tested locations per feeder.

FEEDER	RAMP RATE (P_{pu}/h)
CO1	0.33 – 1.5
CS1	0.137

Table 4.2. Constant power factor control parameter ranges that work across all tested locations per feeder.

FEEDER	PF
CO1	0.83 – 0.96
CS1	0.80

Table 4.3. Volt/Watt control parameter ranges that work across all tested locations per feeder.

FEEDER	SLOPE (P_{pu}/V_{pu})	DEADBAND (V_{pu})
CO1	5.0 – 36.7	0.018 – 0.04
CS1	26.1 – 36.7	0.01

Table 4.4. Watt-triggered power factor control parameter ranges that work across all tested locations per feeder.

FEEDER	PF	DEADBAND (V_{pu})
CO1	0.70	0.72
CS1	0.86 – 0.96	0.72 – 0.90

Table 4.5. Volt/Var control parameter ranges that work across all tested locations per feeder.

FEEDER	SLOPE (P_{pu}/V_{pu})	DEADBAND (V_{pu})	NOMINAL VOLTAGE (V_{pu})
CO1*	15.5 – 100	0 – 0.022	0.997 – 1.03
CS1	15.5 – 47.2	0.018 – 0.027	1.019 – 1.03

**Represents the parameters the work well across only four test locations.*

4.6 Conclusions

This chapter has presented a parametric study of various proposed advanced inverter control types acting on realistic distribution feeder models over a one week time-domain simulation. Several measurable network quantities are identified to be used as metrics to determine the effectiveness of each control. A weighted objective function is then used to score the combination of metrics against the perceived cost of control. Each control type investigated has between one and three parameters that define its time-domain behavior. These parameters are varied within a pre-determined discretized range to study how the different possible controller behaviors affect the objective function. Additionally, the PV system is tested at various locations around the distribution feeder model to study how the interconnection location impacts the effectiveness of each control type. Several approximations are made in the study to reduce its computational burden. After all the parametric studies are complete for a feeder, the largest range of parameters that satisfies the objective function is determined for each location tested, as well as those parameters that will work satisfactorily at all locations.

The first control type investigated is simply limiting the amount by which a PV system can ramp up its output to prevent problems caused by rapid irradiance transients due to clouds. Decreasing the ramp-rate limit exponentially increases the amount of PV power curtailed. Of course the greatest improvements in PV-induced network issues correspond to the highest curtailment levels, which is why power curtailment is included in scoring a control's effectiveness. The curtailment of PV power is uniform per interconnection location, but the improvements gained are highly variable between locations. This is where a careful selection in the trade-off between acceptable curtailment and desired improvement is necessary to tune the control. For the weights used in this study, the slightest curtailment of $1.5P_{pu}/h$ scores the highest in general. However, one interconnection location does not gain any improvement with this type of curtailment.

Similar results are seen in the other curtailment control type: volt/watt control. Although there are two parameters that define this control, in general, the lower the deadband and steeper the control slope, the more the PV system will be curtailed and the more problems will be mitigated. Again, the weights are carefully selected to balance curtailment with network improvements such that the lowest objective scores across the feeder can be found around $0.02V_{pu}$ deadband and $50P_{pu}/V_{pu}$ slope. Again, the ideal parameter ranges are highly dependent on the location and certain locations result in much smaller ranges. In particular, the locations near the substation benefit most from steep slopes with large deadbands, whereas the locations near the end of the feeder benefit most from shallow slopes with shorter deadbands.

Arguably, the more interesting results are achieved with the advanced inverter controls that employ reactive power. This is because use of PV inverter reactive power capabilities are typically not viewed as negatively as real power curtailment, but there is not as clear of a connection between increased var output and decreased PV-induced issues. The simplest form of var control is constant power factor. Interestingly, the network improvements increased with lower power factor (more var output) up to 0.89 lagging before falling off and actually starting to increase overall network problems at around 0.8 lagging power factor. Watt-triggered power factor control is much more variable between interconnection locations. This is likely due to the fact that the PV system real power output impacts the network much differently between interconnection locations. Also, if the reactive power control is triggered sooner, it generally has a better overall improvement. Large deadbands result in steeper var slopes, which in turn leads to negative interactions with existing voltage controllers. Lastly, volt/var control is much more difficult to generalize due to the additional parameter dimension. However, it is the control that has the most overall improvement at the largest number of parameters. Only the steepest control slopes with the smallest deadbands, which correspond to the most aggressive control behaviors, actually result in more negative impacts on the network. In general, keeping a gradual slope around $50.0Q_{pu}/V_{pu}$ with a deadband with a width of at least $0.01V_{pu}$ seems to lead to the most improvements across the feeder. After

that, it seems larger deadband settings correspond positively to lower nominal voltages, and vice versa.

In general, since there is an inherent conflict between control action and network improvements, the weighting and biasing of the objective function significantly impacts the results. The parameter ranges presented in this chapter are skewed by different weights and biasing. Additionally, it has been shown that the interconnection location of the PV system plays a significant role on the impact an advanced inverter control may have. This is corroborated by past research that has shown that the PV interconnection location can largely determine if it will cause any negative impact at all on the feeder.

4.7 Summary

This chapter has described the impacts that a large PV system has on various distribution network metrics over time, such as voltage levels, equipment operations, and losses. Several advanced inverter control strategies have been investigated to mitigate these negative impacts. However, the performance of each control type over time depends on how certain parameters in the control are set. Thus, a parametric study has been performed to find the ranges of control parameter settings for each control type that optimize the performance of the controls. The next step in the research is to evaluate how advanced inverter controls perform on multiple PV systems interconnected in the same distribution network and this is described in the next chapter.

5. COMPARISON OF CONTROL STRATEGIES TO IMPROVE PV-INDUCED VOLTAGE VIOLATIONS

5.1 Introduction

The previous chapter studied the performance of advanced inverter controls to mitigate negative impacts to the distribution network caused by a single large PV installation. To study how advanced inverter controls may interact, this chapter focuses on the application of advanced inverter controls to a large number of highly distributed PV systems in a realistic distribution network. To effectively study the time-dependent and unpredictable nature of PV, a full year of irradiance and load data is studied. The goal of this research is to study how advanced inverter controls can be used to mitigate the rise in network voltage caused by a large amount of PV distributed throughout a distribution feeder. The PV systems are distributed to every load in the network and sized proportional to their local load. A sufficient amount of PV generation is placed on the network to ensure over-voltage is a legitimate problem during daytime periods throughout the year. Several PV inverter control strategies are compared that will either curtail the real power output or provide reactive power support based on network conditions. The goal of each control strategy is to mitigate all over-voltage violations caused by PV. Both controls that only utilize local measurements and those that require a robust communication network are tested. If applicable, each controller has its parameters adjusted over a sample time period so that the controls are fairly compared. In addition to their ability to mitigate over-voltages, the controls are compared based on the amount of control action used, either power curtailed or vars produced, and the fairness of how the control action is applied across the population of PVs in the network.

5.2 Control Types Explored

5.2.1 Zero Current Injection

The simplest control strategy implemented mitigates potential voltage issues caused by PV power injection by not permitting the PV systems to inject current into the distribution network. This zero current injection (ZCI) control resolves this particular problem caused by PV systems by simply not allowing it to occur and it is the most conservative approach investigated. This control is used as a benchmark to compares the more sophisticated control types.

5.2.2 Local Voltage-Based PV System Curtailment

Using only locally available measurements, the output of each PV system can be curtailed based on the PCC voltage of its respective phase. To maintain smooth control operations, the curtailment is typically performed as a ramping down of active power output beginning at some measured voltage, v_1, as shown below in Figure 5.1. If voltage continues to rise, the inverter will continue to ramp down its output until it is completely curtailed at measured voltage v_2. This type of control curve is called a "Volt/Watt droop". The theory behind this control is similar to the "frequency droop" curve applied to automatic governor control whereby the speed of a generator is proportional to frequency rise, thus setting generator speed inversely proportional to change in frequency will result in a new stable operating point. Here, change in PCC voltage is close to being linearly proportional to PV power output, so if all PVs apply this control, a new stable operating point should be reached. However, the slight nonlinearity of the relation between PCC voltage and PV power output makes it difficult to precisely determine the voltages v_1 and v_2 that define the curve. For this reason, these parameters will be tuned experimentally to find the curve that best mitigates over-voltages. To ensure the control begins to curtail its

power output at v_1, the $P_{set,pu}$ axis in Figure 5.1 is normalized to the real power available to the PV at that point in time, not the constant rating of the panels.

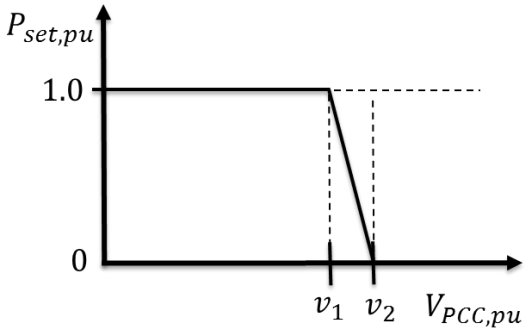

Figure 5.1. Volt/Watt droop curve used for local PV power curtailment.

5.2.3 Local Voltage-Based Var Control

A PV grid-tie inverter can supply reactive power to the grid to help regulate the line voltage by phase shifting the current it injects with respect to the voltage at its PCC. However, the capability for the inverter to provide vars is limited by its rating. In this work, it is assumed that the inverter is rated equivalent to the maximum power point its PV panels are capable of achieving, P_{MPP}. Neglecting non-idealities, the amount of reactive power available to the inverter is represented by the diagram in the Figure 2.1. Here, the radius of the circle represents the rating of the inverter and the red dashed lines indicate the range of reactive power capability for the hypothetical level of PV output power shown. The reduced power level can either be due to the PVs panels operating below P_{MPP} due to lack of rated incident irradiance or due to active curtailment from a control, such as Volt/Watt. PV panels are seldom operating at P_{MPP}, so there is typically some reactive power available to the inverter.

The var limits from Figure 2.1 determine the per-unit scale of the Volt/Var curve shown earlier in Figure 2.3, which dictates how the inverter outputs its available reactive power based on the voltage measured at the PCC. Again, this means the $Q_{set,pu}$ axis in Figure 2.3 is normalized to the amount of reactive power available at each point in time, not the inverter's rating. Similar to Volt/Watt, a negative droop curve is employed to supply the

proper vars that will regulate the PCC voltage towards its nominal value. A deadband is used to prevent oscillation around the nominal network voltage. The curve is thus defined by the four points along the voltage axis that determine where the output will saturate and where the deadband exists, $\boldsymbol{x} = [x_1\ x_2\ x_3\ x_4]$.

5.2.4 Centralized Fair Curtailment Dispatch

The previous two control methods assume that no communication network exists to assist in controlling the PV inverters, so they must rely on local measurements only. In an advanced distribution network, PV inverters may be able to communicate through a sufficient communication network with a centralized controller that is also linked to other sensors and meters in the system. Such a centralized controller could have knowledge of all network voltages and could strategically dispatch control signals to the specific inverters that would be best suited to mitigate over-voltage violations. However, simply controlling those inverters that will mitigate over-voltages first may unfairly target a few PV installations on the network. With a centralized approach, knowledge of each inverter in the network means that fairness of the control can also be taken into consideration in the control algorithm itself.

The first centralized method is investigated to see how well inverters can mitigate over-voltages by curtailing them all by an equal proportion at each time step. To this end, a regulator is established that determines the percent each PV should curtail from its available power at time instant *k* based on the deviation of the maximum voltage in the network from a desired voltage limit, V_{lim}.

$$\alpha(k+1) = K_\Phi \alpha(k) + K_R(\max(V_i(k)) - V_{lim}) \tag{5.1}$$

The curtailment ratio α in (5.1) is dispatched to each inverter at each discrete time step, *k*. An inertia gain, K_Φ, can be adjusted to weight the importance of the past step. The speed of this regulator can be set by the gain K_R, which must be tuned depending on the rate at

which the signal is dispatched to the PV. Since this is a discrete controller with physical constraints, there is an upper limit to K_R beyond which the control will oscillate between saturated states. This upper limit is proportional to the rate at which the control updates and the rate at which the inverters respond. When inverter *i* receives the curtailment ratio α, it sets the inverter's power reference signal as a function its maximum power point power, P_{MPP}, and the local irradiance at that time step $I_i(k)$.

$$\begin{aligned} P_i(k) &= \alpha(k) P_{i,max}(k) \\ P_{i,max}(k) &= I_i(k) P_{MPP,i} \end{aligned} \tag{5.2}$$

5.2.5 Centralized Dispatch via PV Voltage Sensitivities

This approach takes into consideration the linear approximation of voltage change in the network due to curtailment of each individual PV system. A first-order approximation assumes the change in network voltage can be found via (5.3).

$$\Delta \boldsymbol{V} = \boldsymbol{A}\Delta \boldsymbol{P} + \boldsymbol{B}\Delta \boldsymbol{Q} \tag{5.3}$$

The matrices $\boldsymbol{A}$ and $\boldsymbol{B}$ are the so-called sensitivity matrices [27] that relate change in PV system real power output $\Delta \boldsymbol{P}$ and reactive power output $\Delta \boldsymbol{Q}$ to change in network voltage. There are several approaches to finding the sensitivity matrices for a given distribution of PVs in a network. One method is to take a first-order linearization of the system equations. If the network equations are of the form $f(V, P, Q) = 0$, then the sensitivity matrices would be the Jacobian related to each PV input:

$$\begin{aligned} \boldsymbol{A} &= \frac{\boldsymbol{\partial V}}{\boldsymbol{\partial P}} \\ \boldsymbol{B} &= \frac{\boldsymbol{\partial V}}{\boldsymbol{\partial Q}} \end{aligned} \tag{5.4}$$

However, it is difficult to formulate the network equations in this form for an unbalanced, three-phase system. Often, power-flow software does not expose these sensitivities to the user and a practical approach is to utilize the power-flow solution to

directly obtain the change in network voltages due to curtailment of PV systems. For this procedure, each PV system j has its output power curtailed by a percentage of its per-unit rating, Δp, such that $P_j = P_{j0} - \Delta p$. The columns of the real power sensitivity matrix can then be populated with the resulting difference in voltage from the zero-curtailment case, $\boldsymbol{V_0}$. The control presented next in this research only focuses on real power curtailment, so it is not necessary to derive the $\boldsymbol{B}$ matrix.

$$\begin{aligned} \boldsymbol{A} &= \left[\boldsymbol{a_1}\ \boldsymbol{a_2} \dots \boldsymbol{a_j} \dots \boldsymbol{a_n}\right] \\ \boldsymbol{a_j} &= \boldsymbol{V_j} - \boldsymbol{V_0} \end{aligned} \tag{5.5}$$

The optimum (minimum) amount of power curtailment that mitigates all over-voltages for the measured system state $\boldsymbol{V}$ is then the solution to the following linear programming problem:

$$\begin{aligned} &\min_{\Delta P_j} \sum_{j=1}^{n} \Delta P_j \\ &s.t.\ \begin{cases} \boldsymbol{A}\Delta\boldsymbol{P} \le 1.05 - \boldsymbol{V} \\ \boldsymbol{p_{min}} \le \Delta\boldsymbol{P} \le \boldsymbol{p_{max}} \end{cases} \end{aligned} \tag{5.6}$$

The first line in (5.6) assures that the curtailment is minimized; the second line assures that the curtailments bring the over-voltage values within the nominal voltage range, and the last line assures the curtailment values are valid. Due to the last line, the state of curtailment must be recorded and passed between dispatch solutions. Additionally, there is no guarantee for any given system state $\boldsymbol{V}$ that there exists a change in PV system power outputs, $\Delta\boldsymbol{P}$, that satisfies the constraints, even if all PVs are curtailed. This may seem counter-intuitive at first if the network over-voltages are caused by the PV real power injection and should therefore be fully mitigated if the PV are fully curtailed. However, this optimization does not take into consideration the state of the voltage regulators since in this work it is assumed that they can neither be measured nor controlled. Without taking the regulator controls into consideration, the dispatch solution provided by (5.6) will tend

to oscillate. Under these restrictions, an optimization of (5.6) cannot provide the inverter power dispatches, so another approach must be taken.

To account for the action of the voltage regulators, a smoothing approach is developed by integrating the desired curtailment of all inverters, $\Delta \boldsymbol{P}$**,** at each time step within their physical limits. Thus, the curtailment of each inverter, ΔP_j, becomes a state variable to be updated and passed between time steps and then dispatched to the PV at the appropriate interval. The time step *k* represents either 1-minute or 5-minute dispatch to the PV in the later simulations, based on assumed restrictions in the communication network. The curtailment vector is updated by the inverse sensitivity matrix times the desired change in voltage and a tunable gain K_A, as shown below in (5.7).

$$\begin{gathered} \Delta \boldsymbol{P}(k+1) = \Delta \boldsymbol{P}(k) + K_A \boldsymbol{A^{-1}}(\boldsymbol{V}(k) - V^*) \\ s.t\ \ (-1 \le \Delta \boldsymbol{P}(k) \le 0) \\ |\Delta \boldsymbol{P}(k+1) - \Delta \boldsymbol{P}(k)| \le \Delta P_{lim} \end{gathered} \tag{5.7}$$

The inequality constraints in (5.7) are added to keep the control actions bounded to physical constraints. The 2nd line in (5.7) represents the fact that an inverter cannot curtail or produce more power than that flowing through it. To prevent oscillations between controllers, the amount each PV can ramp between iterations is limited to 20% of its rated power per minute, which is achieved by setting $\Delta P_{lim} = 0.2$ in the 3rd line of (5.7). The desired voltage to regulate to in (5.7), V^*, is initially set to the ANSI limit of 1.05, however, this value can be reduced to account for inaccuracies of the linear approximation and mitigate any remaining voltage violations. In addition to V^*, the control in (5.7) can be tuned by the gain variable K_A and the power change limiter ΔP_{lim}.

5.3 Baseline Feeder and PV Simulation

5.3.1 Feeder Characteristics

A real distribution feeder is modeled in OpenDSS to test the PV controls. The circuit, designated Feeder CO1, is a rural 12 kV distribution feeder consisting of 2970 medium- and low-voltage buses and 2569 lines servicing 1447 loads through 401 service transformers. A map showing the layout of the feeder topology and the existing voltage regulating devices is shown in Figure 5.2. The furthest bus is 21.4 km from the substation. There is one three-phase voltage regulator on the feeder backbone about 6 km from the substation and five switching capacitors. The coloring of the lines in Figure 5.2 represents the relative line voltages and demonstrates how voltage drops with distance from the substation and voltage regulator. The line thickness represents the current flow in the lines. These plots were created with the GridPV Matlab toolbox [71],[26]. The feeder has a peak load of 6.41 MW and operates at a power factor of 0.917 at peak load. The minimum load within the year of data simulated is 20.1% of the peak load, or 1.29 MW. To simulate the variation in load over the course of the year, the average of the three substation SCADA phase current measurements is taken and then normalized to create a multiplier time series that varies between [0.201, 1.0]. The reason the average of the three phases is used is because the correct phasing of the loads and measurements could not be verified. This time series has one-minute resolution and is allocated to all loads in the network since only the substation aggregate measurements are available. The loads remain at their individual constant power factors during the simulation.

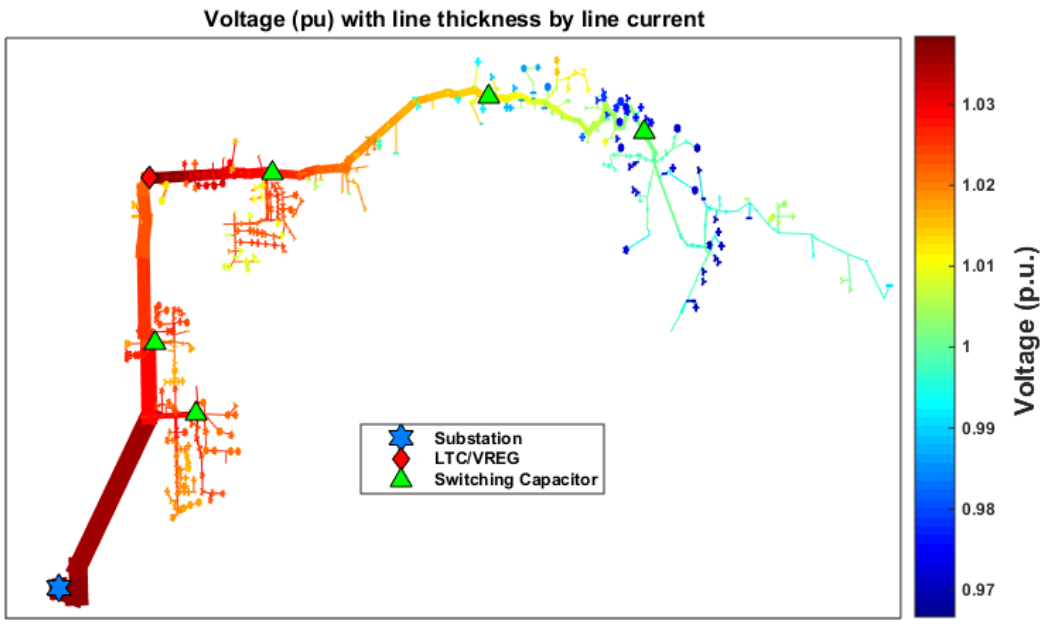

Figure 5.2. Map of Feeder CO1 with line thickness representing current magnitude and color representing relative voltage level.

The baseline voltage profile of the feeder simulated over the course of a year without any PV results in numerous under-voltage violations, as depicted in Figure 5.3. In this figure, the amount of time each load phase in the feeder spends in a voltage violation is shown. A bus is in violation if its voltage is outside the ANSI Range-A $0.95 \leq V_{pu} \leq 1.05$ limits on a moving 10-minute average. Over-voltage violations are shown in the top plot and rarely occur without PV. The node number roughly corresponds to increasing distance down the feeder. Under-voltage violations are shown in the bottom plot and occur at numerous loads, especially towards the end of the feeder. The nodes with the most under-voltage violations are only in violation roughly 3% of the year. However, since adding PV to the network will only improve the under-voltage conditions of the network, unless the voltage regulator has load drop compensation [27], from this point on only over-voltage violations will be considered as a goal for improvement by the control of the PV inverters.

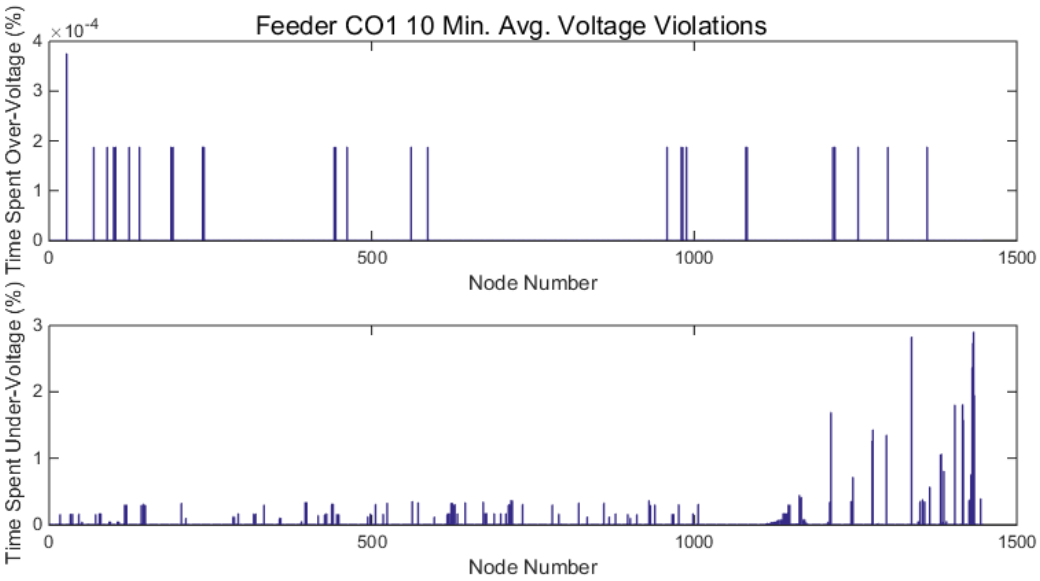

Figure 5.3. 10-minute average ANSI voltage violations in a year with no PV placed on the feeder.

In total, 2079 single-phase PV systems are placed on the feeder, one at each load, as shown in Figure 5.4. The lines in this figure are color-coded by the voltage level, which is not in violation for the snapshot of load and irradiance shown here. Each PV system is sized to represent 60% of the peak value of the local load to which it is connected. This is equivalent to 250% of the minimum daytime load within the year, which means there will be reverse power flows and voltage rise. The average per-phase PV system is 1.74 kW at its peak power, P_{MPP}, which occurs at irradiance equal to $1000\ W/m^2$. The total rated output of all PVs in the network is 3.62 MW.

The voltage profile plots in Figure 5.5 demonstrate the voltage-rise effect of the PV during a period of low load and high irradiance. The bottom three lines without yellow stars are the voltage profiles of the three feeder phases without PV at this load level. The top three lines are the same load level with PV added at the locations indicated with a yellow star. The fact that voltage rises with distance from the substation rather than sagging is an indication that the PVs are reversing current through the lines. Since PV is installed proportionally at each load, this means that the PV are back-feeding the substation in this

figure. The next section will discuss how the PV systems behave during the time-series simulation.

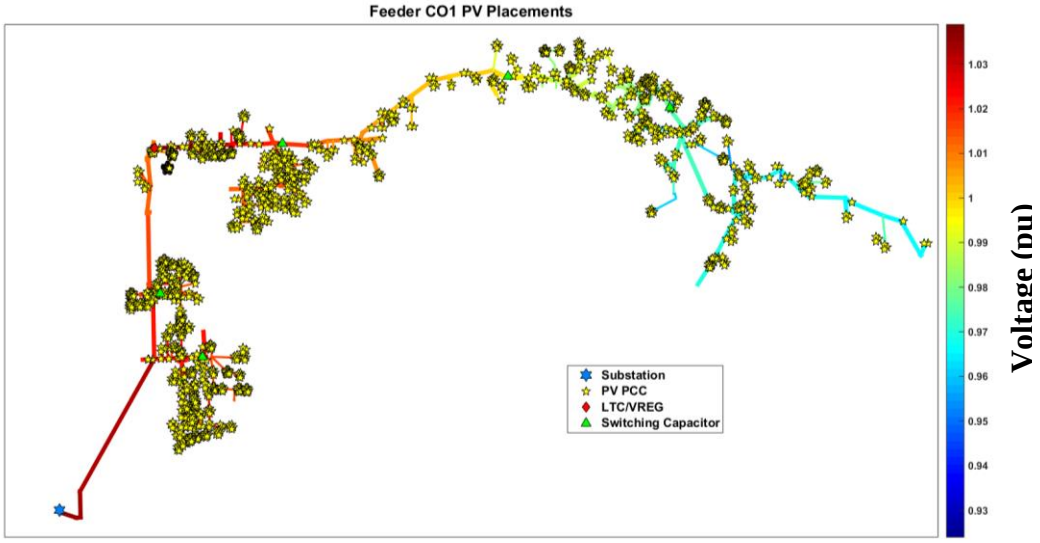

Figure 5.4. Map of feeder CO1 with PV placements indicated and lines colored by per-unit voltage.

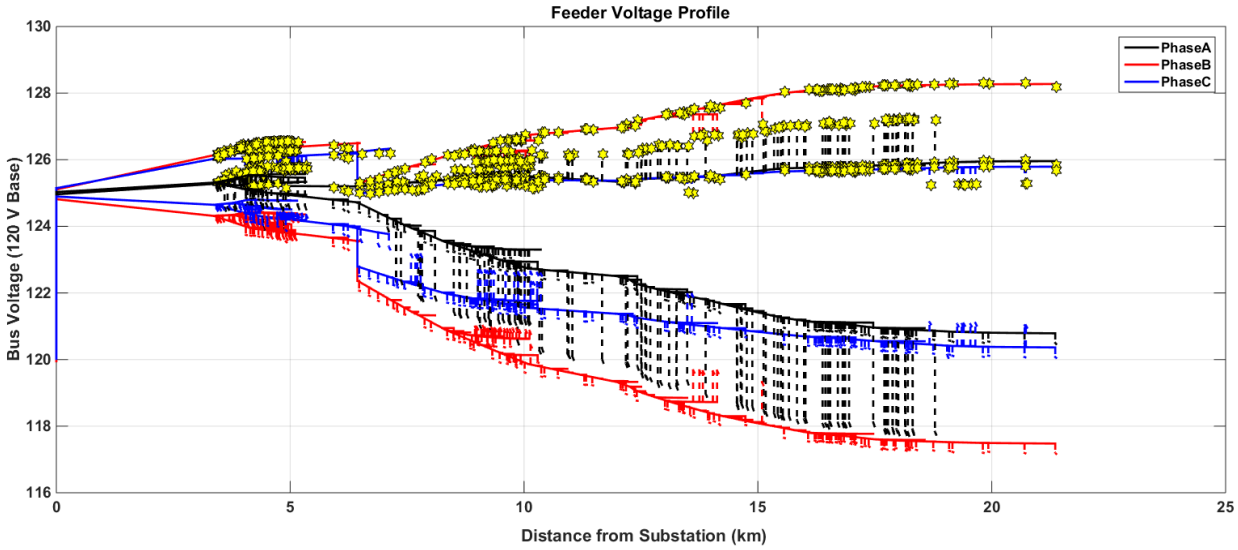

Figure 5.5. Feeder voltage profile at minimum load without PV and with PV, represented as yellow stars.

5.3.2 Distributed Irradiance Profiles

To properly investigate the interaction between the controls of multiple PV systems, they cannot be given the exact same input irradiance signal. In practice, moving clouds cause PV systems to have different amounts of available power from their neighbors. To

simulate this transient effect, an irradiance profile for the entire year is created that is time-shifted based on the velocity of the clouds and the spacing of the PV installations. To achieve this, historical daily cloud speeds are matched to the irradiance data and clouds are assumed to move west to east across the feeder. Then, a time offset of cloud-arrival times is calculated for each load transformer. Figure 5.6 shows the time offsets for each transformer for a cloud speed of 11.4 m/s. To create simulated irradiance time series for each transformer, 1-year of global horizontal irradiance (GHI) measured in Albuquerque, NM is time-shifted by the appropriate time offset, as seen in Figure 5.7, which shows the simulated GHI for a transformer with a 7 minute time offset. The GHI measurements are translated to plane of array irradiance for south-facing fixed-latitude-tilt PV systems. To convert this simulated irradiance to PV DC power available to inverters, DC de-rates of 6% due to soiling, wiring, and mismatch losses are assumed.

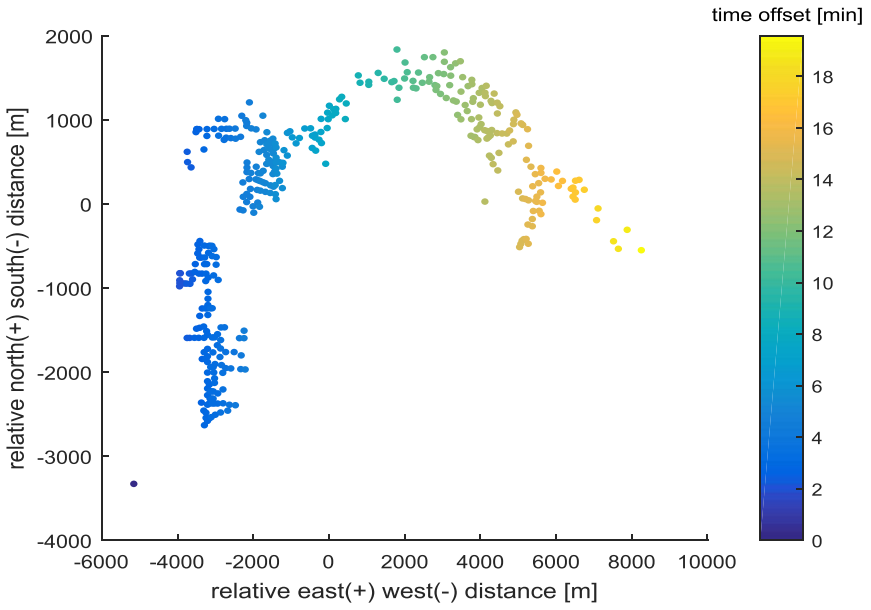

Figure 5.6. Irradiance time offset used per load transformer in the feeder based on historical wind speeds.

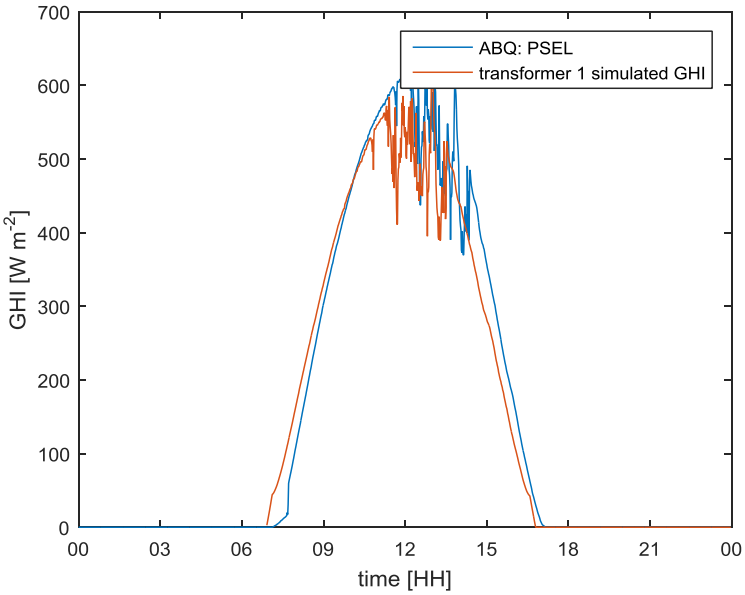

Figure 5.7. Example of the time-shifted global horizontal irradiance (GHI) compared with original data (blue).

5.3.3 Interfacing the Matlab Simulation with OpenDSS

This section briefly describes how the simulation and controls are run in the Matlab and OpenDSS platforms. The simulation is run in a Matlab script that stores parameters, performs some control actions, and inputs and compiles results. The Matlab script interfaces with OpenDSS through a COM interface to run power flow solutions. The feeder model is loaded into OpenDSS and Matlab tells OpenDSS where to place PV systems and how to control their inverters. It is preferable to use OpenDSS's built-in inverter controls as they perform iterations faster. Both Volt/Watt and Volt/Var controls are implemented with OpenDSS's built-in controls. The ZCI control and both centralized approaches are performed in Matlab. For these controls, at each time step Matlab receives the network voltages and powers and based on the control type determines the power output of each PV system. It then directly edits the PV systems in OpenDSS through the COM interface to reflect the control actions and solves the next time step. Since the simulation is a time-

series, the ZCI method predicts what the current time-step control should be and the centralized methods use continuous curtailment states updated by the previous solution.

5.3.4 Impact of PV Systems with No Advanced Inverter Controls

In this case the feeder is simulated by using the year of spatially dispersed irradiance profiles applied to the appropriate PV system. The yearly real and reactive power demand for the feeder are shown in Figure 5.8 both in the baseline case without PV and with PV systems. This results in a total of 6.76 GWh of power generated by PV throughout the year, an average of 3.25 MWh per PV. There is much overlap in the plot due to the diurnal nature of the PV generation, so to get a sense of how much the PV impacts the base load, a zoomed-in segment around the yearly minimum load is also provided. It can be seen in the zoomed-in segment that there are times when the PV systems reverse current and begin injecting power into the transmission system.

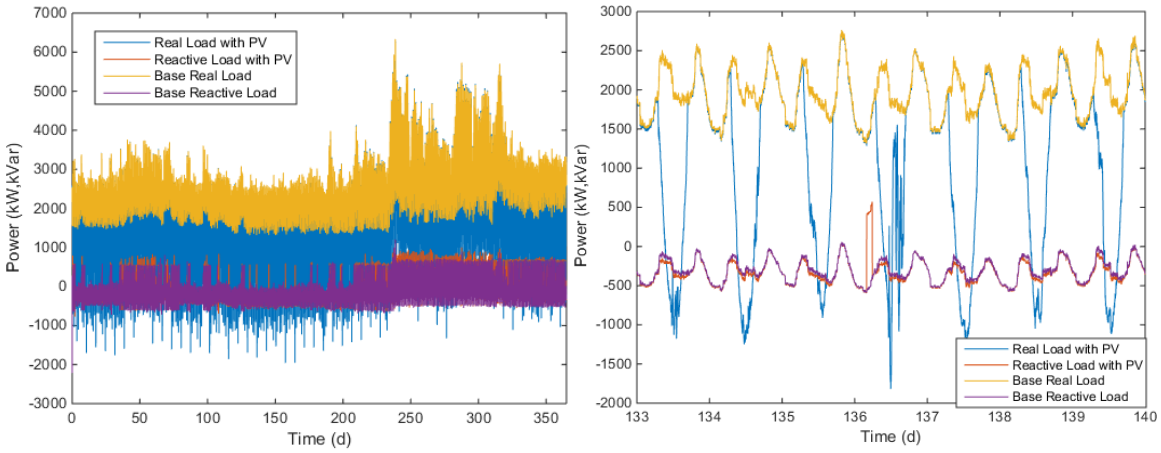

Figure 5.8. Yearly feeder real and reactive load with and without PV (left) and a zoomed-in segment (right).

The 10-minute average voltage violations due to this amount of PV are shown in Figure 5.9. As expected, the under-voltage violations are largely mitigated due to the voltage rise caused by the PV. However, this results in a large amount of 4,784,242 one-minute violation periods in total across the feeder. Considering the feeder to be in violation if *any*

bus has an over-voltage violation, then the feeder has 18,861 minutes of over-voltage for the year, or 3.59% of the year. The bus with the single most violations has this for 2.74% of the year. These violations are relatively uniformly distributed throughout the feeder, perhaps depending more on PV system size than location.

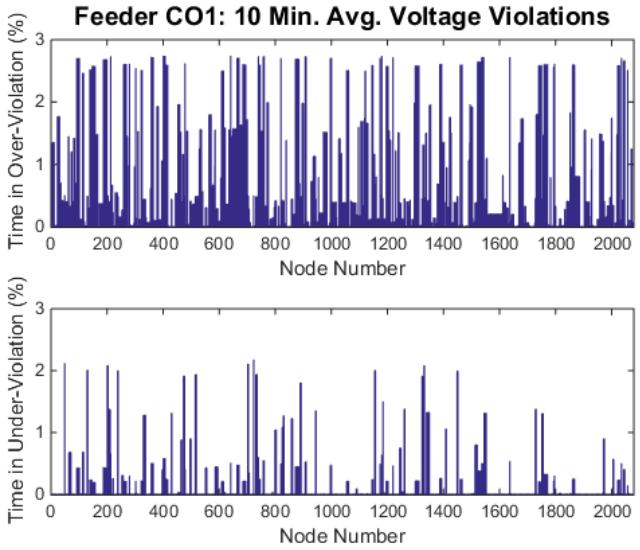

Figure 5.9. 10-minute average ANSI voltage violations in a year with PV placed at each load, sized at 150% minimum daytime load.

Each of the above 1-year simulations at 1-minute resolution takes slightly less than 1-hour to run on a typical 2015 desktop computer. However, once more advanced inverter controls are implemented on each inverter, this simulation time becomes many times larger. Additionally, the appropriate controller parameters are not known. Thus, a subset of the load and irradiance profiles is tested before running the entire year simulation. The one-week period with the single highest number of over-voltage violations in the no-control case is found. Of all the over-voltage violations that occur during the year, most occur just before the middle of the year when the load is relatively low and irradiance values are increasing, as shown in Figure 5.10. The worst week for over-voltage violations starts on the 132nd day of the year and accrues 433,821 minutes of violations across the feeder.

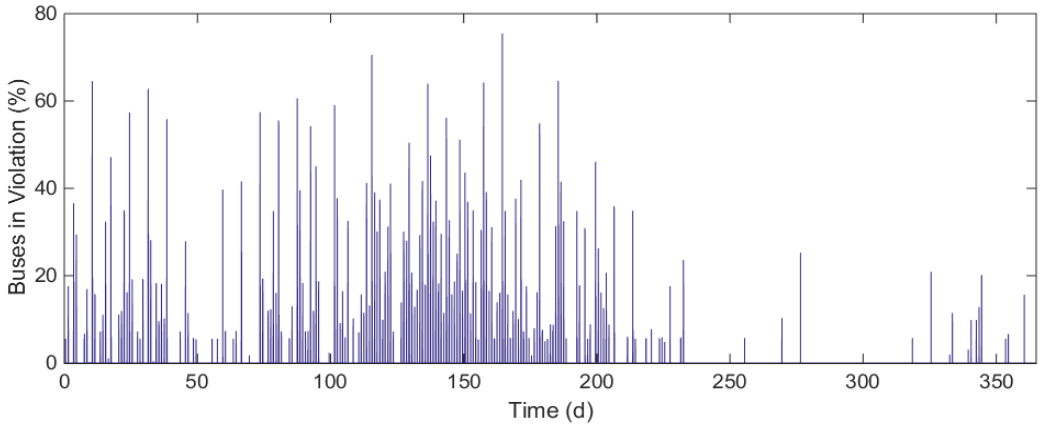

Figure 5.10. Percent of the feeder that is over-voltage any time during a day for one-year simulation.

Simulating this single week, as shown in Figure 5.11, disregards the state of the network leading up to it which slightly skews the results. Due to this there are slightly fewer violations, 413,015 in total. However, this corresponds to the feeder being in violation 13.3% of the time during this week, much greater than the entire year. Also, when eliminating nighttime (59.1% of the sample week), the feeder has a voltage violation 32.5% of the time. Tuning the local inverter controls to improve this single week should approximate the times of best improvement seen over the entire year. Without curtailment, 7.77 GWh are generated during this week from the distributed PV. When tuning the controls, the goal will be to mitigate all voltage violations while minimizing the deviation from this level of PV generation.

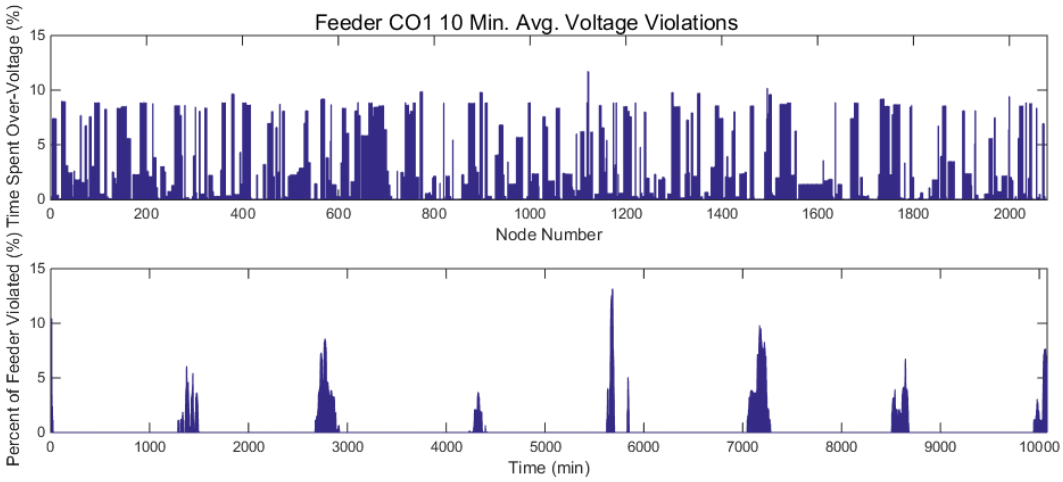

Figure 5.11. Total over-voltage violations during worst week of the year.

5.4 Simulation of Advanced Inverter Controls

5.4.1 Zero Current Injection PV System Control

The first curtailment control strategy investigated is to simply limit the production of the PV to not exceed that of the local load, termed zero current injection (ZCI). The theory behind this approach is that so long as the PV systems do not inject current into the distribution network, there will be no voltage rise. Thus, the inverters are controlled to match, but not exceed, the power consumption of their local load so that the PCC never sees reverse current flow. However, this curtailment strategy can significantly reduce the amount of overall renewable energy produced. Additionally, this is not a standard advanced inverter control being proposed for PV inverters as they do not typically have a means of measuring local load. Figure 5.12 shows the real power local load and the baseline PV generation during worst-case week for over-voltages for a single PV system in the network. During the peak sunlight hours of each day, the PV system outputs more than the local load consumes and should be curtailed under this control strategy. This control action can be seen clearly in Figure 5.13, which shows the total real power flow through the feeder breaker both with and without the ZCI control active. In the baseline case, there is negative power flow through the breaker each day, yet with the control active, the reverse power flow is prevented.

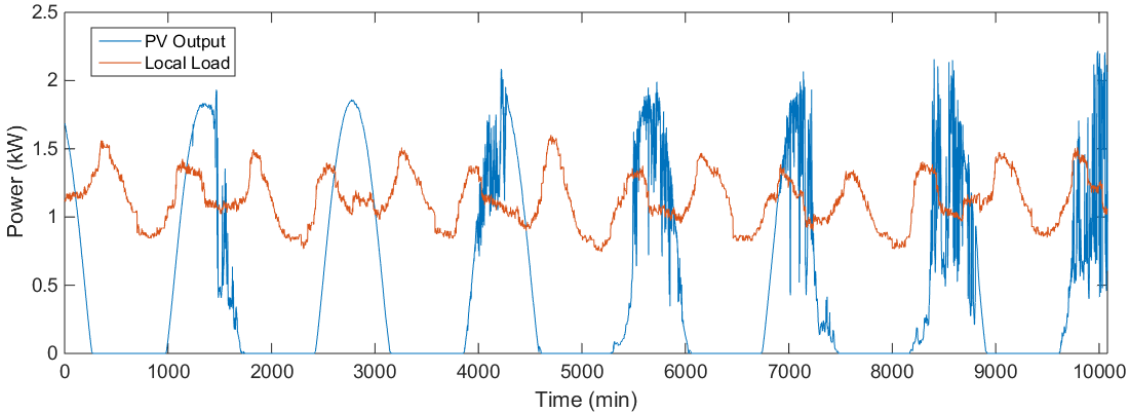

Figure 5.12. Real power load and PV output at first load in feeder during worst-case week.

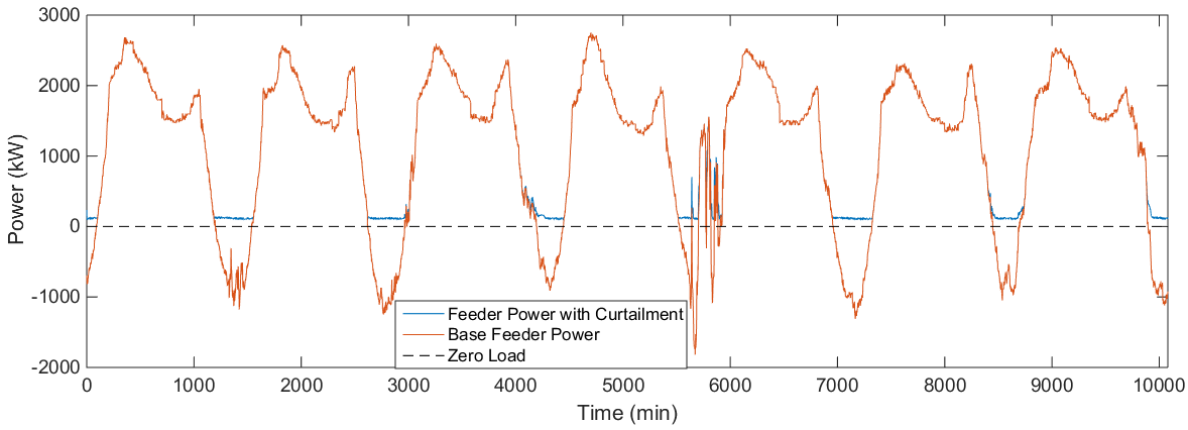

Figure 5.13. Substation power with and without zero-current injection control.

Although the control is commanding the PV systems to match the load during the hours it curtails, there is a small amount of real power still flowing through the feeder breaker. The output of a single PV system under ZCI control is shown in Figure 5.14 to investigate its performance. The inverter matches the load consumption almost perfectly, but there exists a small error. This is an artifact of the QSTS simulation, which uses the irradiance and load time series data to predict what each time step's curtailment should be rather than using measurements. This approach was taken in an effort to speed up the simulation time and results in a relatively consistent error of about 4% between PV and load power during curtailment, as shown in Figure 5.15. The cause of this error is most likely due to simulated load model including a slight voltage dependence where the load consumes more power at higher voltages. The load and PV power do not exactly match because the inverters are controlled to curtail exactly to the universal load multiplier time series, not the measured power of the load from the simulation results. The remaining power consumption by the feeder is shown in Figure 5.13. During times of curtailment, the remaining feeder load is also about 4% of the overall load, confirming the approximation as the source of the error. This slight under-curtailment has a minimal impact on the overall results, however, since the goal of over-voltage mitigation is still achieved.

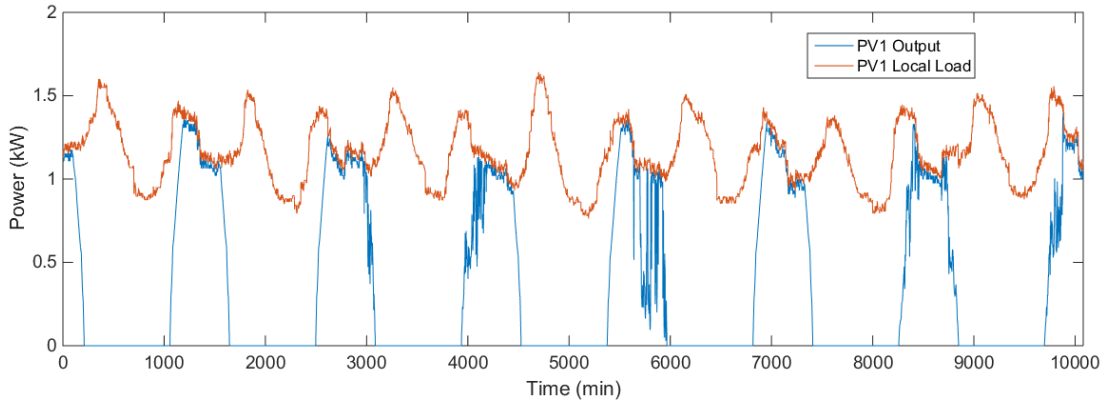

Figure 5.14. Power output and local load of a single PV system under ZCI control.

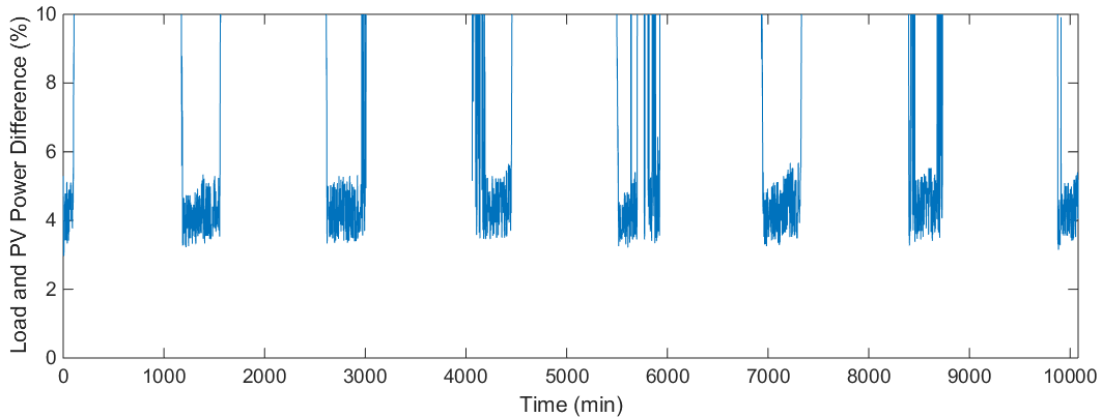

Figure 5.15. Percent difference in PV power output from local load consumption for a single PV system under ZCI control.

The difference in real power output of all PV systems in the network between this control and the baseline case is shown in Figure 5.16. With this control, the peak generating hours of each day are shaved off to match the load.

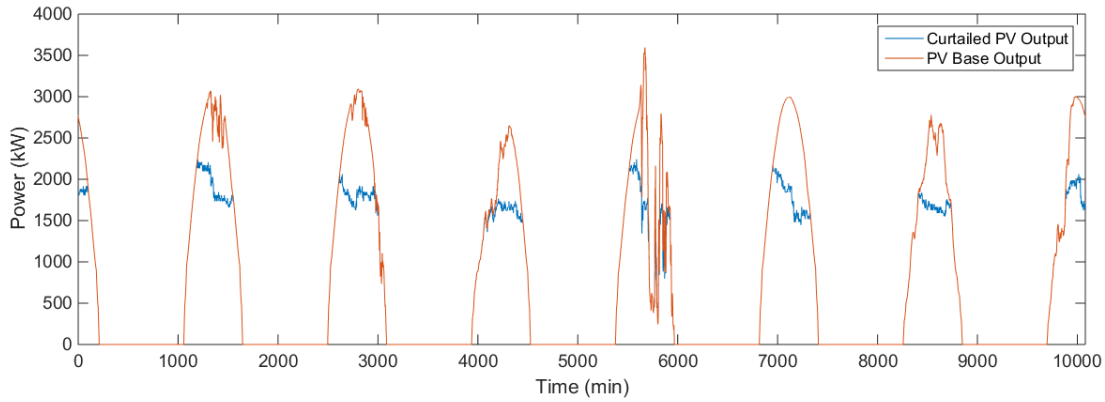

Figure 5.16. Total PV generation over time with and without zero-current injection control.

Using this control strategy, all over-voltage violations are mitigated for the week, but at the cost of reducing a significant amount of PV generation. With this control, a total of 6.09 GWh of energy is generated over the course of the week, a reduction of 21.6% in PV production. These levels of over-voltage improvement and curtailment cost are used as benchmarks to improve upon for more sophisticated control strategies presented in the following subsections. Although the ZCI control strategy curtails a large percentage of PV generation, it does so in a relatively fair manner amongst PV system owners. The distribution of how much each PV system is curtailed from its baseline energy output during the week under ZCI control is shown in Figure 5.17 as the blue line. Each point in this line corresponds to the percent of the total energy a PV system is curtailed due to the control. If the line is flat, it means all PV system owners are equally curtailed relative to the size of their PV system. The "flatness" of the distribution can be measured by the standard deviation of the data. This is a relatively flat distribution with a standard deviation of only 0.75%.

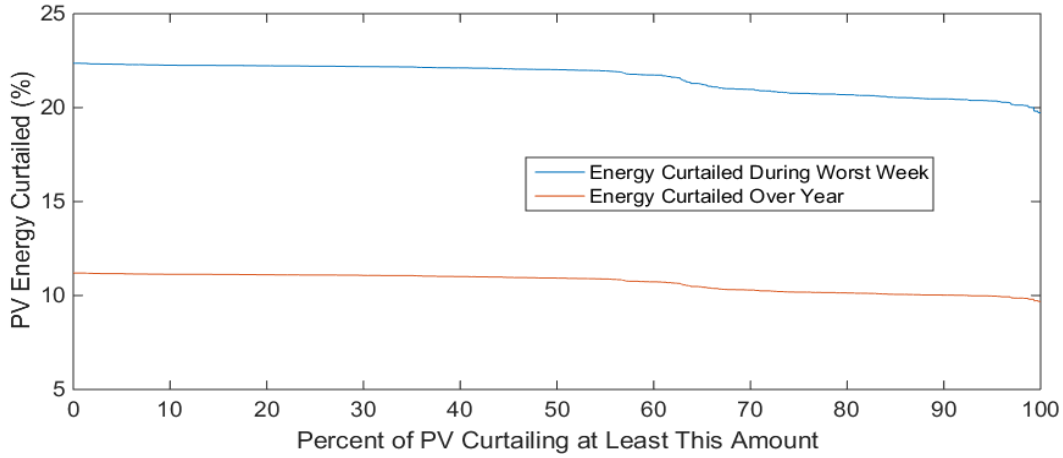

Figure 5.17. Disparity of PV power curtailment using ZCI control during the worst week and year.

The distribution of PV system curtailment for the year is shown as the red line in Figure 5.17. It has a similar shape, but is lower due higher load on average over the year than over the one week period studied. The year has a standard deviation of curtailment of 0.46%. No over-voltage violations occur during the year with ZCI control, an improvement of

100%. But the cost of this improvement is an overall curtailment of 10.73% of the PV systems' potential energy production.

5.4.2 Local Voltage-Based PV System Curtailment

For this section, the Volt/Watt control described in Section 2 is applied to each inverter. The parameter set $\boldsymbol{v} = [v_1, v_2]$ that defines the controller Volt/Watt curve in Figure 5.1 is tuned using the worst week of data in the year. Ten parameter sets are tested using $v_2 = 1.05$ and linearly varying $v_1 = [1.040 \ldots 1.049]$. The performance of each parameter set is summarized in Figure 5.18. The top plot shows the percent of the week the network spent in an over-voltage violation, which should be zero for a successful control performance. The bottom plot shows the percent by which the total PV power generation is curtailed due to each control. As expected, a lower v_1 parameter corresponds to more curtailment, yet the increase in voltage violations as v_1 increases is not readily explained since each inverter should curtail completely by the time the voltage limit is hit locally. These higher v_1 settings correspond to larger controller gains, so one possible explanation is poor interaction between the inverters and other feeder voltage regulation. Alternatively, the QSTS solution may not be converging to a single operating point if the parameters that determine maximum controller rate of change and convergence tolerance are not set properly for these higher gain values. To investigate the cause of these over-voltages further, the time-domain cumulative power outputs corresponding to parameter Sets #5-10 are plotted in Figure 5.19 for a midday time period with some irradiance variability. It is evident that some of the parameter settings are causing the inverters to oscillate between output levels as the irradiance varies. This is an indication that the controls are not achieving a stable operating point. It seems in this case that the larger controller gains associated with the higher v_1 parameter cause the inverter controllers to take steps that are too large between solution iterations and never find the stable operating point.

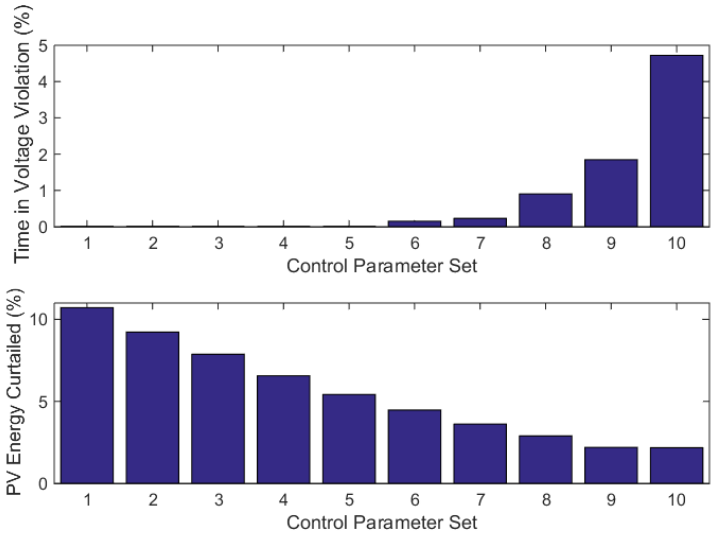

Figure 5.18. Comparison of the performance during the worst week for different local control parameter sets.

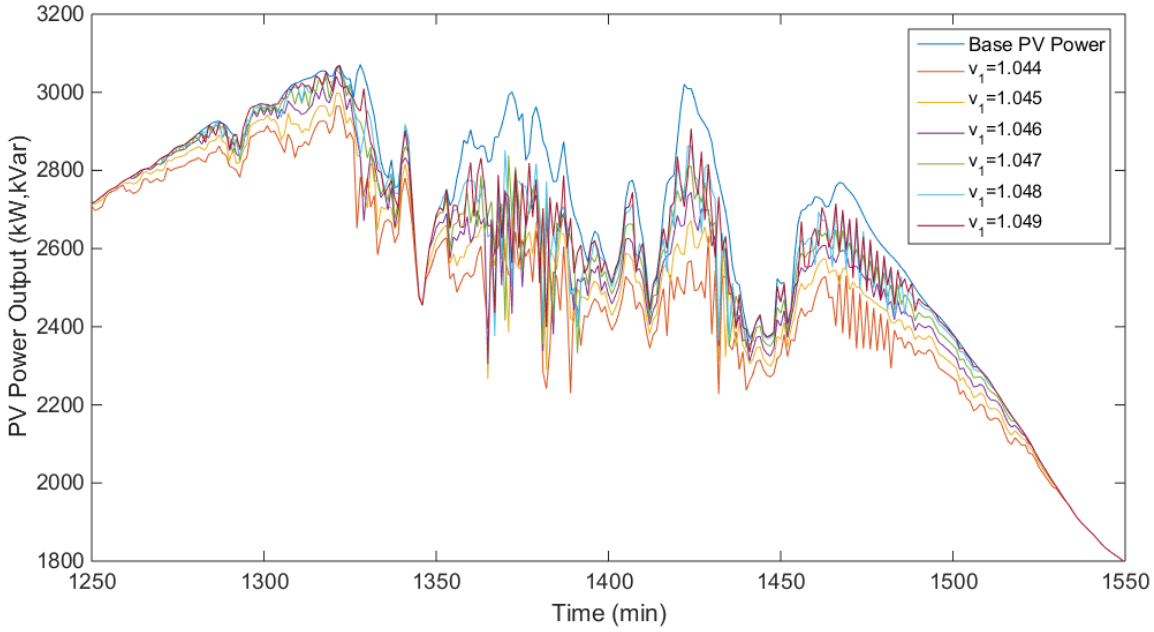

Figure 5.19. Impact of Volt/Watt control parameters on power oscillations due to irradiance.

For this reason, the maximum rate of change in inverter power output between control iterations is lowered in OpenDSS from 40% to 10% of the inverter rating and the tuning procedure is run again. Since the original tuning procedure already discovered that voltage violations are mitigated at $v_1 = 1.044$, only six parameters within the set $v_1 =$

[1.044 ... 1.049] are tested this time. The comparison of the performance of this reduced set of parameters is shown in Figure 5.20. Now all voltage violations are mitigated up to $v_1 = 1.046$ (Set #3), which means even less power needs to be curtailed to mitigate violations with the control working properly.

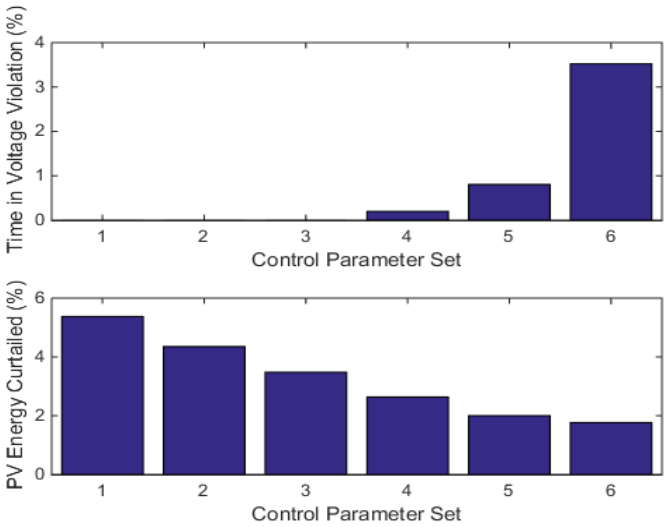

Figure 5.20. Volt/Watt control parameter comparison with lowered maximum power rate of change.

It remains unclear, however, why Sets #4-6 still have voltage violations in Figure 5.20. The same time period as in Figure 5.19 is investigated to see if the inverters are still struggling to find stable operating points at higher gains. As shown in Figure 5.21, it appears that the inverters are no longer oscillating between operating points during periods of highly variable irradiance. In this case, it seems there is another cause for the voltage violations at the highest controller gains. It could be that there are still some inverters that oscillate between stable settings, but the magnitude of the oscillations has been decreased from 40% to 10% and averages out among all PV and is no longer visible. Alternatively, the inverters could be allowed to run at full output so closer to the ANSI limit at the highest settings that only one instance of over-voltage could bring the 10-minute average into violation.

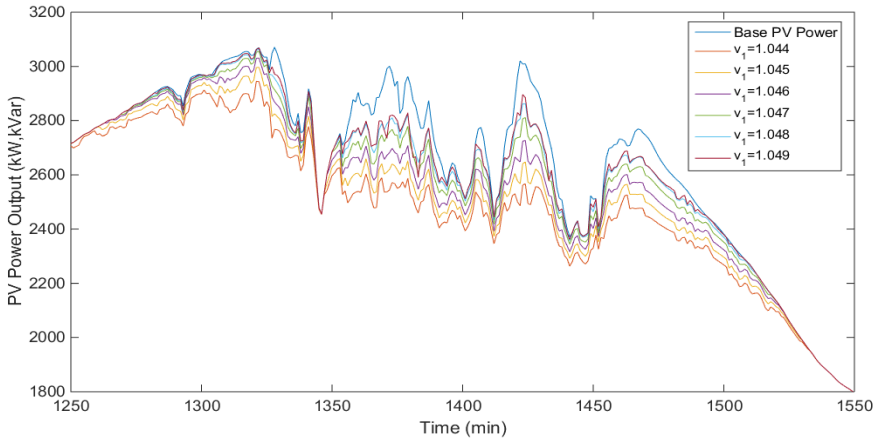

Figure 5.21. Impact of Volt/Watt control parameters on PV system power output with lowered inverter maximum power rate of change.

Since it remains unclear why higher v_1 settings still produce voltage violations, the control parameters are conservatively set at $\boldsymbol{v} = [1.045, 1.05]$ to reduce the chance of incurring over-voltages in the full year simulation. The control's curtailment of the baseline PV system power output during the worst week is shown in Figure 5.22. Over the week, Volt/Watt control with these parameters mitigated 100% of over-voltage violations and curtailed 4.35% of the energy that would have otherwise been generated with no control. This is a much reduced value from the previous local control of zero current injection. However, these improved results are not as fair to all customers as the ZCI approach. The blue line in Figure 5.23 represents the distribution of PV curtailment due to Volt/Watt control during the worst week and it can be seen that a small portion of the PV systems curtail much more than the majority. If the goal is to limit PV system curtailment to 10%, then 17.5% of the customers on this network will curtail more than this value, with the maximum curtailing up to 36.8% of its potential energy production. The PV systems interconnected to the most robust lines do not have to curtail any power under this control, which is why the average curtailment is so low at 4.27%. Although the performance of this control is superior, it introduces the discussion of whether it is better to collectively curtail more power for the sake of fairness.

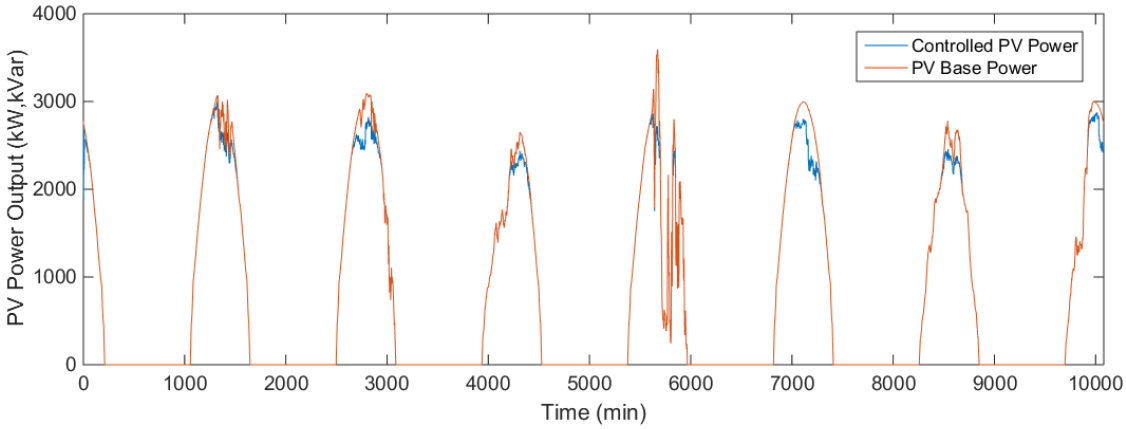

Figure 5.22. Total PV power generation during worst week with tuned Volt/Watt control.

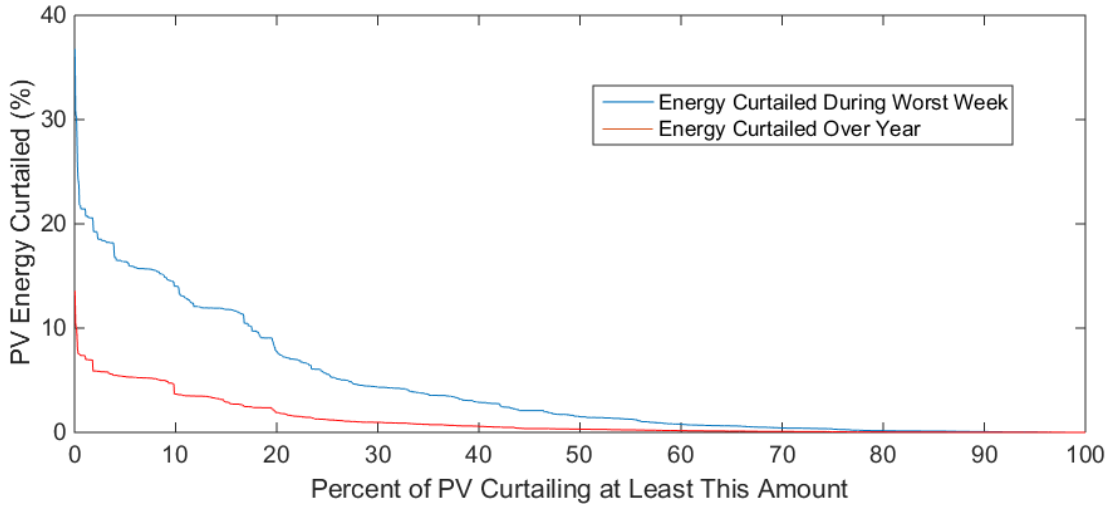

Figure 5.23. Disparity of PV power curtailment using Volt/Watt control during one week and over one year.

Running the entire year with the above tuned controller parameters is also successful in achieving zero over-voltage violations. Also, the relative amount of control action needed is greatly reduced when averaged over the year. To achieve this improvement, the PV systems only need to be curtailed by 0.85% of their cumulative baseline energy output over the year. This represents the amount of energy curtailed by the control that would have otherwise been produced by the PV systems during the entire year. The amount of energy curtailed during each day of the year can be seen in Figure 5.24. However, as with the one-week case, the disparity in the curtailment of the PV systems is large, as shown in

the red line of Figure 5.23. The maximum amount of curtailment seen by a single PV system is 13.57% and the minimum is less than 0.001%. However, the previously stated goal of curtailing less than 10% of available energy is achieved by 99.7% of the PV systems. The standard deviation of the distribution of PV curtailment is 1.81% for the year using this control.

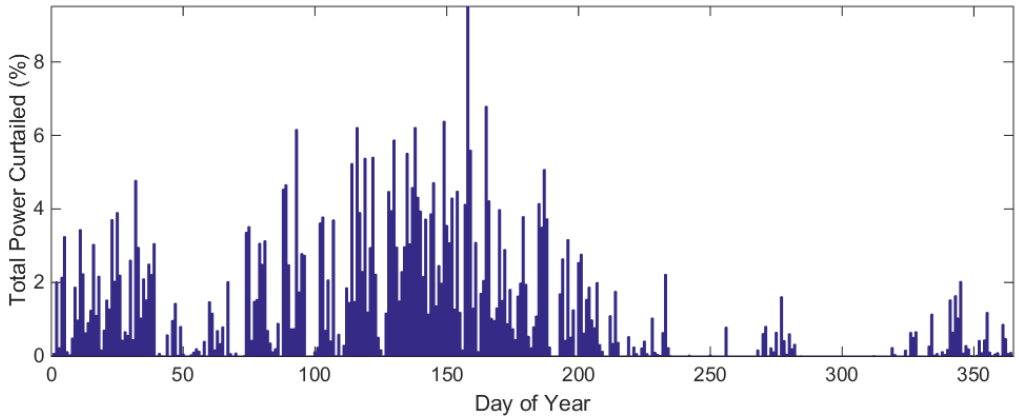

Figure 5.24. Total curtailment of PV energy during each day in the year under Volt/Watt control.

Looking at the curtailment of each PV system based on its location in the feeder in Figure 5.25 highlights the clustering of PV systems facing the highest control costs. The worst-week data is used since it has a larger disparity that will be more visible, but the full year results are similar. Each point represents how much energy the PV system at that location proportionally curtails over the week due to the Volt/Watt control. The highest curtailments occur in a cluster of loads on a lateral branching off near the substation. The next highest curtailments occur towards the end of the feeder, as is to be expected due to the voltage rise effect along the entire feeder.

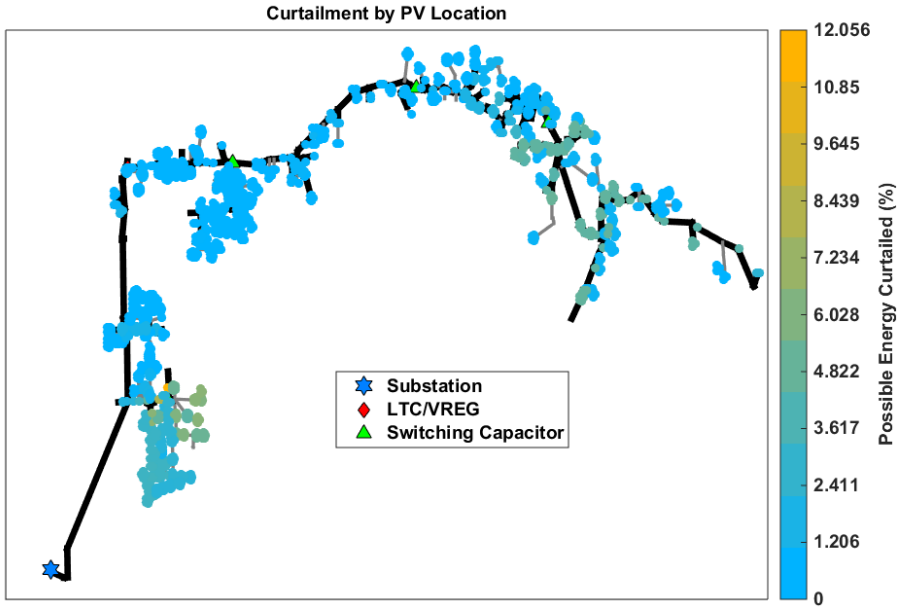

Figure 5.25. Geographic distribution of PV system curtailment in the circuit due to Volt/Watt control.

The curtailment levels do not correspond to the presence of large PV systems, but rather due to existing poor voltage profiles. This is evident in Figure 5.26 where it can be seen that relatively few large PV systems are present in the feeder branch that experiences the worst curtailment. However, the voltage profile of this branch is the worst in the network as it is before the voltage regulator and possibly due to poor control of the local capacitor bank. A zoomed-in plot of this branch in Figure 5.27 shows the PV systems nearest to and downstream of the capacitor curtail the most.

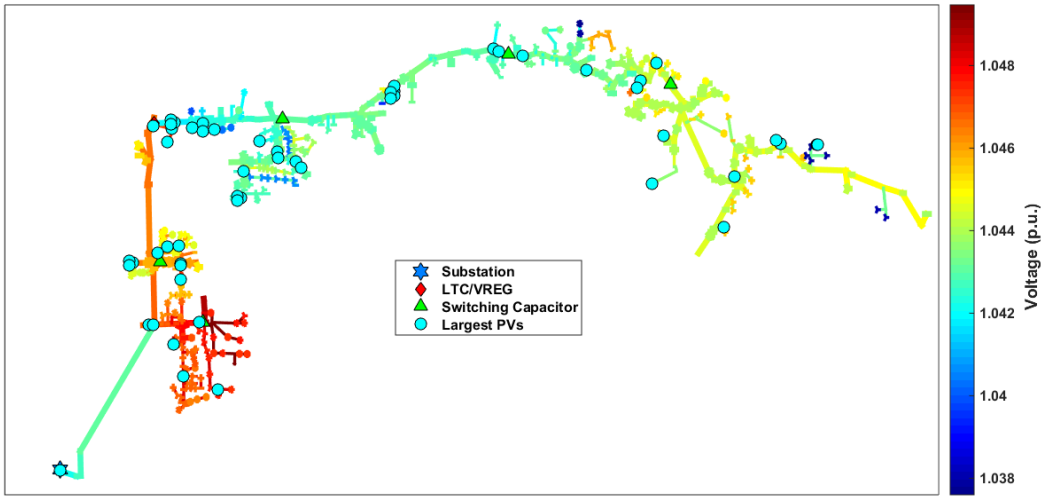

Figure 5.26. Distribution of largest PV systems in the circuit and relative line voltages.

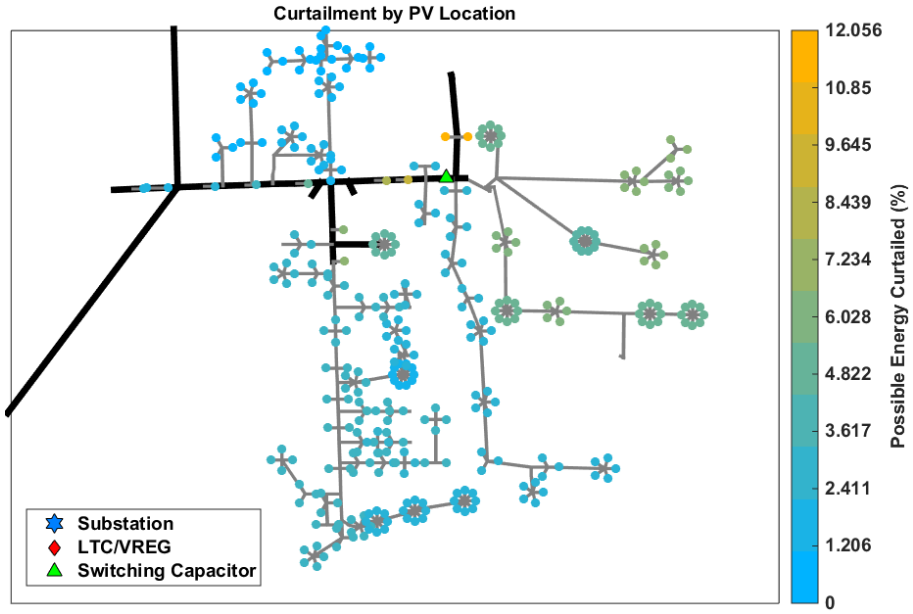

Figure 5.27. Zoomed section of highest curtailment in feeder due to Volt/Watt control.

5.4.3 Local Voltage-Based Var Control

This section demonstrates the effectiveness of implementing local reactive power support on the PV inverter by itself. The control strategy implemented is the Volt/Var control described in Section 2.2. The inverter is assumed to be rated the same size as the PV panels, however, OpenDSS has a convergence problem when setting these parameters equal and implementing Volt/Var control. Therefore, the ratings of the PV inverters in the simulation are increased by 1%. This change does not significantly impact the results.

The time-domain total power output of the PV systems is shown in the top plot of Figure 5.28. The inductive vars are plotted against the real power generated for clarity since it is assumed the vars will always be inductive due to voltage rise. The Volt/Var controller does not affect the real power output of the PV system but absorbs reactive power through the inverter when it turns on. The control does not operate at night because the inverters shut off below 10% real power output. This practice is common as most inverters do not operate efficiently at low power. The subsequent over-voltage violations that occur on the network are shown in the bottom plot of Figure 5.28. The only period of voltage violations

occurs midway through the week. When compared to the top plot, this coincides with a point where the real power output of the PV spikes and is preventing the control from supplying enough reactive power. It may seem as though the inverters are outputting a lot of reactive power, but it should be noted that the PV systems consistently operate below their peak ratings. In fact, looking at all the irradiance multipliers in Figure 5.29 for the week, it is clear that for only a few brief minutes in the week do some PV systems see enough irradiance to provide rated power output. In fact, the period in which the voltage violations occur does not even coincide with one of these times, but still limits the reactive power enough due to the manner in which the profiles are distributed among the PV systems at that point.

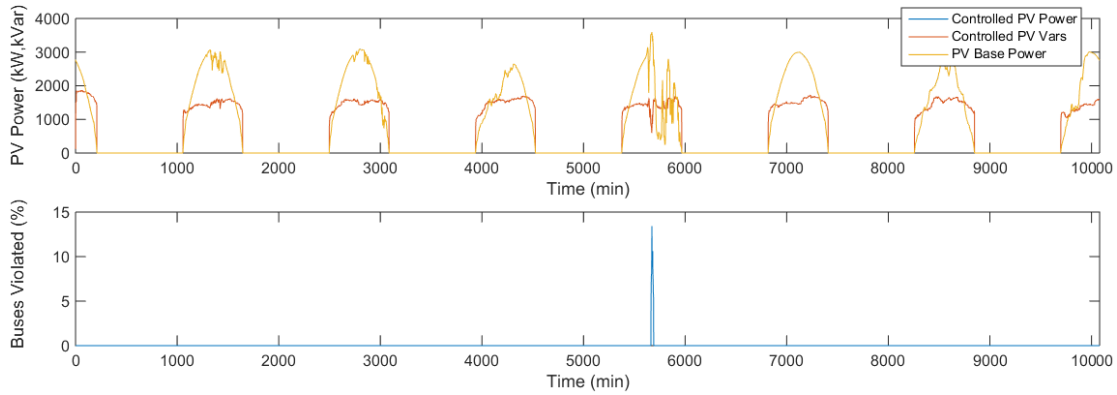

Figure 5.28. (top) PV real and reactive power output during worst week of voltage violations with Volt/Var control. (bottom) Total voltage violations seen on feeder with Volt/Var control.

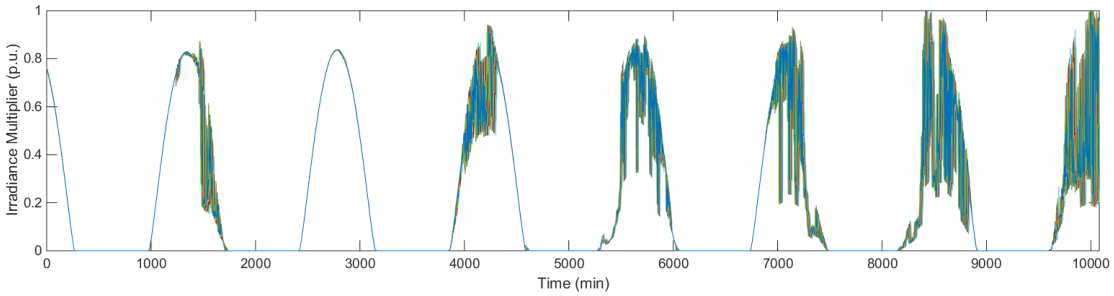

Figure 5.29. All irradiance multiplier time series for worst week of voltage violations.

Even with the time period where the control fails to prevent over-voltages, these results are encouraging. With only Volt/Var control, the feeder is only in over-voltage violation for 28 minutes of the week, or 0.28% of the time, corresponding to an overall reduction in

97.9% of violations. The indication here is that with reactive power support, the PVs should only need to curtail during this 0.12% of the year to mitigate all voltage violations. The results for running the entire year of data are similar with the feeder in violation only 624 minutes of the year, or 0.12% of the time. This represents a 96.7% reduction of the voltage violations seen in the no control case.

5.4.4 Centralized Fair Curtailment Dispatch

5.4.4.1 One-Minute Dispatch

This simulation applies the control strategy discussed in Section 2.3. It leverages a centralized communication structure to gain knowledge of the maximum voltage in the network but dispatches the curtailment signal equally to all inverters as a proportion of their maximum rating. Since there are two distinct control parameters, the sets of control parameters tested do not follow a continuous range as in the local control case. An initial attempt at tuning the centralized regulator gains is made as follows. Parameter Sets 1-5 and 16-20 use an inertia gain of $K_{\Phi} = 1.0$ while sets 6-10 use $K_{\Phi} = 0.9$ and sets 11-15 use $K_{\Phi} = 1.1$ to test this gains impact. Sets 1-15 use a regulator gain of $\mathrm{K_R} = [1\ 5\ 10\ 20\ 30]$ while sets 16-20 use regulators gains of $\mathrm{K_R} = [50\ 60\ 70\ 80\ 90]$ to see if higher values are viable. The results of the different parameter sets are shown in Figure 5.30. The first thing that should be noted from the top plot is that none of the parameter sets were able to completely mitigate all over-voltage violations using this control. It appears that parameter set #15 mitigates most violations at a minimal curtailment cost, however, the fact that slightly lower regulator gains using this same inertial gain curtailed nearly all PV system output is worrisome. Since using this type of control in the QSTS simulation is similar to a discrete control system, using a regulator gain of $K_{\Phi} > 1.0$ may be unstable. The other parameter combinations all have voltage violations above what would be considered a successful control strategy. For this reason, another attempt at parameter tuning is made.

Additionally, the higher set of regulator gains $K_R \geq 50$ can be discarded due to the level of oscillation in the control they cause, as shown in Figure 5.33.

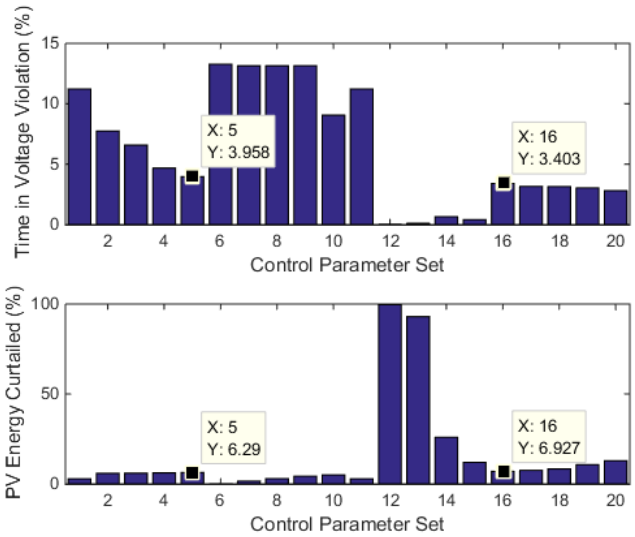

Figure 5.30. Comparison of the performance of an initial set of different central fair control parameter sets.

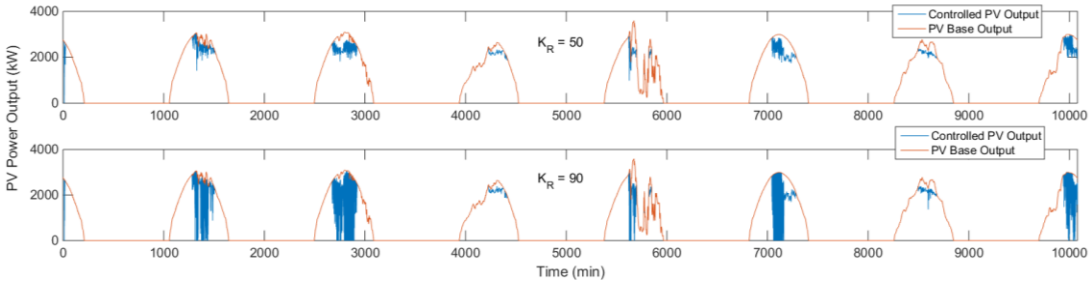

Figure 5.31. Result of increasing regulator gain from lower value (top) to higher value (bottom).

These results bring to light the importance of the voltage limit being regulated to, or V_{lim} in (5.1). Since each voltage violation is a 10-minute average, regulating the PV power outputs to be exactly at the limit means they could spend time above the limit, making averages above the limit a likelihood. For the next tuning attempt, parameter Sets #1-5 use $V_{lim} = 1.049$ and Sets #6-10 use $V_{lim} = 1.048$ and both subsets use the regulator gains of $K_R = [1\ 5\ 10\ 20\ 30]$ and inertia gain $K_\Phi = 1.0$, which were determined to be the more stable of the previous approach. The comparison of the performance of these sets is shown in Figure 5.32.

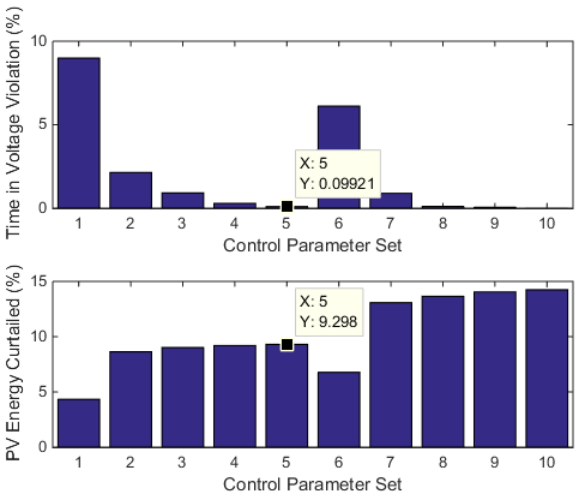

Figure 5.32. Comparison of the performance of the updated central fair control parameter sets.

There is a distinguishable trade-off between the two voltage limits. The parameter sets on the left, corresponding to $V_{lim} = 1.049$ curtail less power, but do a poorer job of mitigating voltage violations, as expected. In both cases, as the regulator gain increases, the number of violations decreases. Both parameter sets #5 and #8-10 are viable, since they are near zero for voltage violations, and since Set #5 represents the minimum curtailment, it should be selected. First, the time-domain performance of these parameter sets is investigated. The top plot of Figure 5.33 shows how the parameter sets corresponding to $V_{lim} = 1.049$ behave during a time of highly variable irradiance and the bottom plot shows the behavior of the sets corresponding to $V_{lim} = 1.048$. The increase in curtailment caused by lower regulator voltage limit is evident in the bottom plot. The regulation action in the top plot, however, seems to have times where it oscillates with more aggressive regulator gains. The oscillations increase with higher gains, but even at the highest gain tested, the magnitude of the oscillations is less than 10% of the cumulative output. This overall impact can be seen in the performance of the control at the parameters over the entire week in Figure 5.34. It should also be noted that these are not dynamic oscillations but rather an oscillating dispatch signal. Therefore, this set of parameters is used for the full year simulation since it results in objectively better performance overall. Over the week, the feeder is in violation 0.10% of the time, which is a 99.2% improvement from the base case.

Across the feeder, the number of violations at buses with PV systems is reduced to 69, an improvement of essentially 100%. The control curtails 9.30% of the energy available to the PV systems to achieve this, but it does it in a fair manner with a disparity in curtailment that has a standard deviation of only 0.57%. The distribution of curtailments during the worst week is represented by the blue line in Figure 5.35.

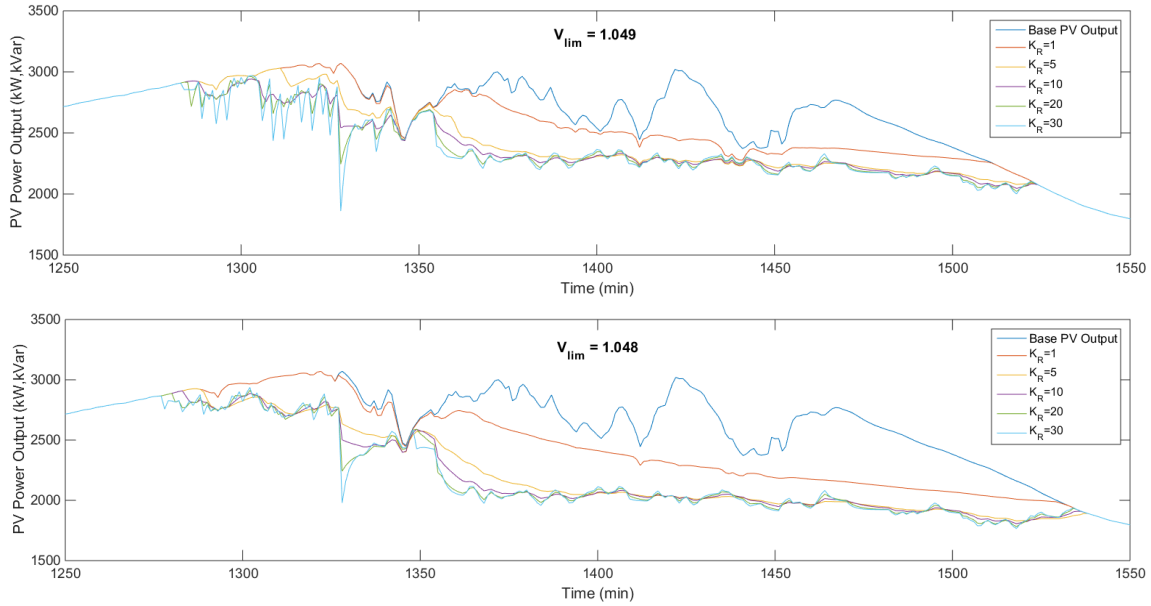

Figure 5.33. Centralized fair curtailment control time-domain performance comparison for (top) V_{lim}=1.049 and (bottom) V_{lim}=1.048.

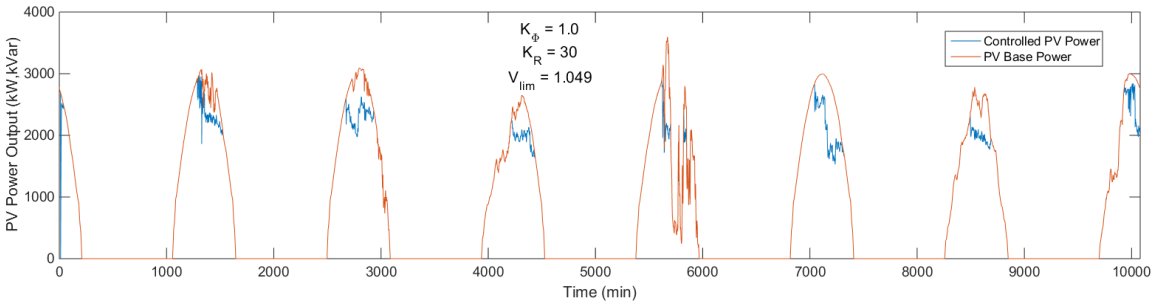

Figure 5.34. PV power output using tuned fair dispatch control parameters during the worst week.

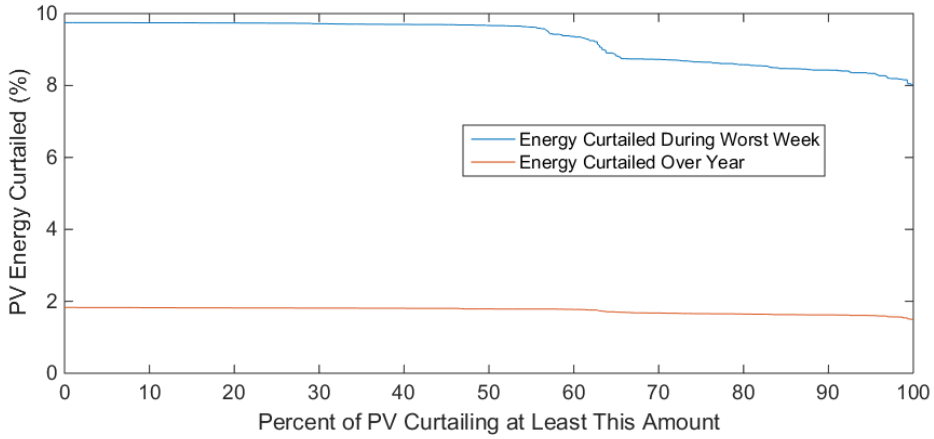

Figure 5.35. Disparity in PV power curtailment using fair centralized dispatch during worst week.

Using the selected controller parameters, the QSTS simulation is run for the full year of data with the centralized fair curtailment control. As expected from the control's performance during the worst week, the control is unable to mitigate all over-voltage violations, but it is able to mitigate most of them. The amount of time per day spent in over-voltage violation throughout the year is shown in Figure 5.36. Only 33 days of the year experience a voltage violation and the feeder is in violation for only a few minutes during those days. Based on how prevalent these violations are throughout the feeder in Figure 5.37, it can be seen that no more than 2% of the buses are ever in violation. The PV power curtailed during each day of the year is shown in Figure 5.38 and the disparity in curtailment between PV systems is shown in Figure 5.35 as the red line. Again, this control type distributes the responsibility of reducing voltage violations fairly among all PV systems. The standard deviation in curtailment between PV systems is only 0.09%. This flat distribution of curtailment can be further visualized by plotting the relative amount each PV system curtails within the circuit map as in Figure 5.39. Although the variation is slight, it is interesting to note the east-west transition in curtailment, which mirrors the irradiance delay imposed in Figure 5.6. Overall the feeder is in violation for 0.02% of the year, corresponding to a 99.3% reduction in time spent in violation. The total number of violations is reduced by nearly 100% of the base case violations to 391 minutes over the

year. The PV systems curtail 1.75% of their total energy production to achieve this result. Given this relatively low curtailment over the year, the control could potentially use the lower $V_{lim} = 1.048$ setting to potentially mitigate all voltage violations over the course of the year.

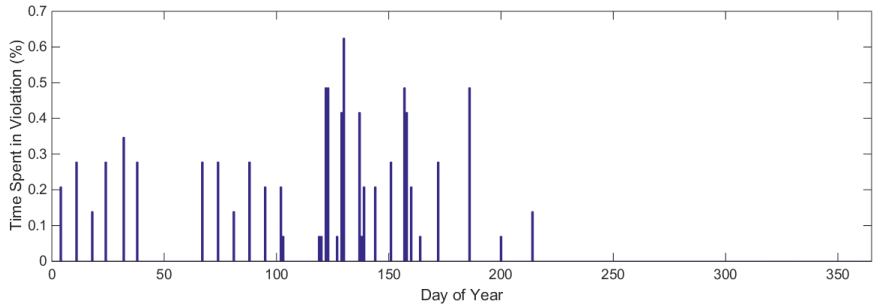

Figure 5.36. Percent of time feeder is in violation during each day of the year under fair curtailment.

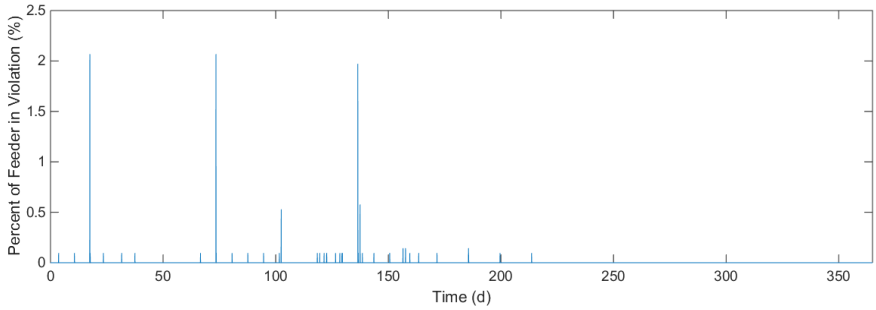

Figure 5.37. Percent of feeder in voltage violation during the year under fair curtailment.

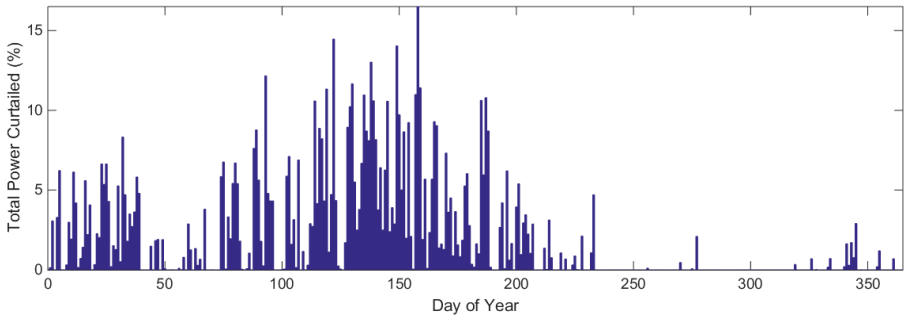

Figure 5.38. Percent of total PV system power output curtailed during each day of the year under fair curtailment.

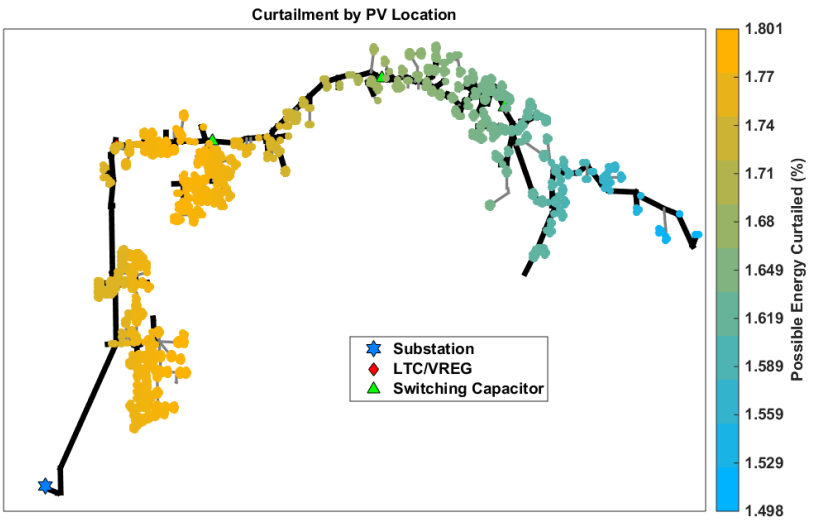

Figure 5.39. Geographic distribution of PV system curtailments in the circuit due to fair dispatch control.

5.4.4.2 Five-Minute Dispatch

It is of interest to increase the time in which the centralized controller is assumed to be capable of dispatching a signal to all inverters to see how this may impact the performance of the control. Due to the previous results, the inertia gain is kept at a constant $K_{\Phi} = 1.0$ with $V_{lim} = 1.049$ and only the regulator gain is adjusted within the set K = [1 5 10 20 30 50 60 70 80 90]. The resulting over-voltage violations and PV system power curtailments at these various gains are compared in Figure 5.40. Based on the consideration that the power curtailment should not exceed 10% of the PV system's base value, parameter sets #4-10 are disqualified. Sets #1-3 are then compared by observing their curtailment behavior during the entire week in Figure 5.41 and for a single day in Figure 5.42. Nothing abnormal stands out from the weeklong simulation, but looking at a single day it is clear that Set #3 shows much more oscillation than the other two. With the next control goal being to minimize voltage violations, Set #2 is chosen to set the regulator gain to $K = 5$ for the five-minute dispatch. As expected, this is lower than the gain selected for the regulator using a one-minute dispatch window.

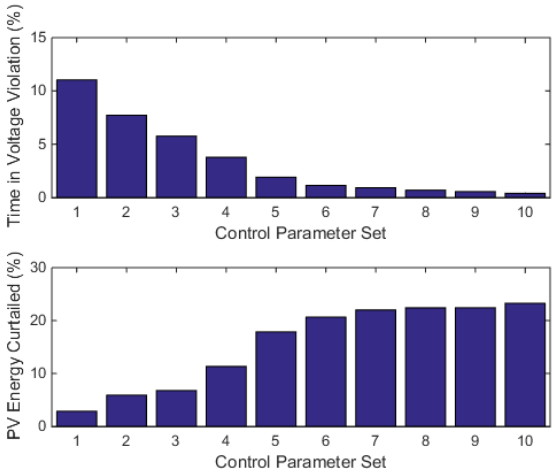

Figure 5.40. Comparison of the performance of different fairly dispatched control parameter sets under five-minute dispatch.

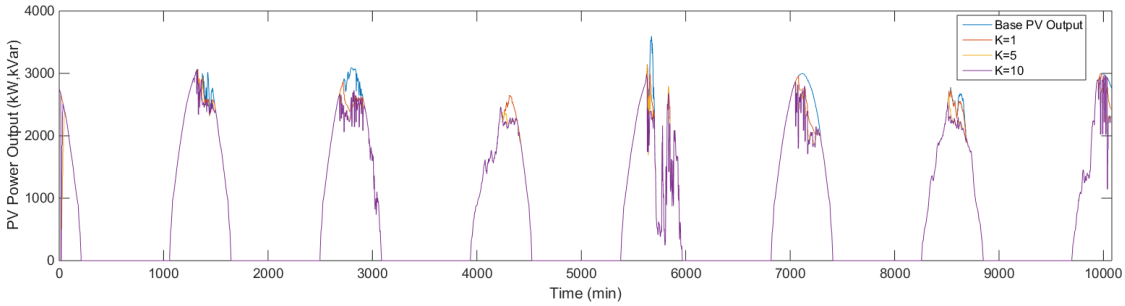

Figure 5.41. Curtailment comparison of three different control parameters for fair dispatch control under 5-minute dispatch window.

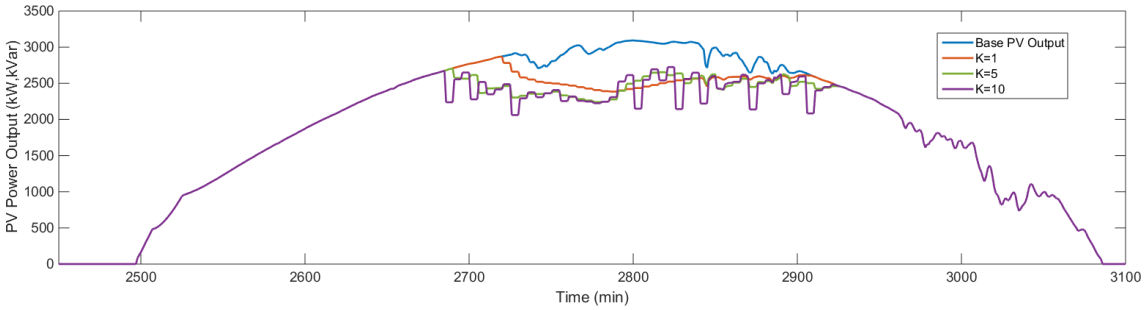

Figure 5.42. Comparison of a single day of fair dispatch control operating with 5-minute dispatches under three different regulator gains.

This control has over-voltage violations for 7.65% of the time, representing a 92.3% mitigation in total voltage violation occurrences and a 41.9% improvement in time spent by the feeder with any violation. The cost of this control is a 5.89% curtailment in total PV system power generation. However, as expected, this control action is evenly distributed

among the PV systems, as shown in Figure 5.43. The standard deviation in the distribution of curtailment is 0.16%. Over the year, a gain of $K = 10$ is used after it is found that $K = 5$ is not aggressive enough during the rest of the year and yields poor results without much curtailment. With the increased gain over the year, the control reduces all violations by 97.6% and the time the feeder spends in violation by 88.4% while curtailing 2.00% of the total PV system energy production. The standard deviation in the distribution of curtailment is 0.05% over the year.

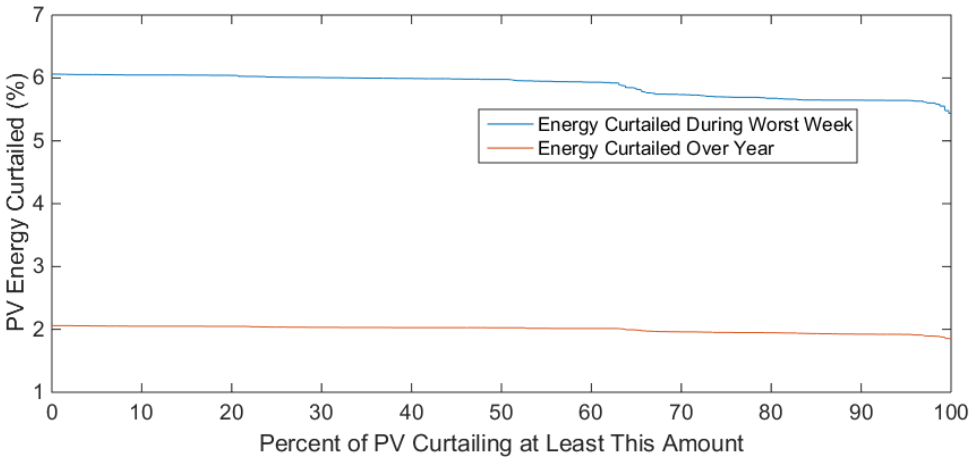

Figure 5.43. Disparity in the amount of power curtailment seen by the PVs under fair centralized control with a five-minute dispatch window.

5.4.5 Curtailment Dispatch via PV Voltage Sensitivities

5.4.5.1 One-Minute Dispatch

This control strategy also assumes real-time measurements from all PV systems are available to the centralized control at one-minute time steps and the controller can dispatch desired power output levels to each individual PV system at some variable time step. The details of this curtailment strategy are presented in Section 2.4. The main difference between this control and the one proposed in Section 2.3 is that fairness in curtailment or control action used between PV systems is not considered a priority. Rather, the main goal of this control is simply to mitigate the PV-induced voltage violations with as little

cumulative curtailment as possible. This is achieved by assuming some knowledge about the distribution network, namely, the sensitivities of the PV systems' power outputs to the network voltages.

A sensible choice for the voltage to regulate to is $V^* = 1.05$, so it remains constant to simplify the controller tuning. Twenty parameter sets are selected to tune the controller. Sets #1-5 and #11-15 use $K_A = 1.0$ and the rest use $K_A = 1.1$ to test how a slightly more aggressive use of the sensitivities will affect the results. Each subset of five parameter sets use the range of change of power limiter $\Delta P_{lim} = [0.1, 0.2, \ldots 0.5]$. A comparison of the different control parameter sets used to tune the regulation of the curtailment parameters is presented below in Figure 5.44. The first thing to note from the top plot is that even though parameter set #13 does completely mitigate all voltage violations, the magnitude of all the other voltage violations is miniscule. In fact, these violations may even be considered negligible when it is considered that the local control that mitigated all voltage violations in tuning still had a few during the entire year simulation. With that said, parameter set #13 achieves this slight improvement at the cost of nearly 50% more curtailment than some of the other sets. For these reasons, parameter set #10 is chosen for the controller tuning, which corresponds to a sensitivity gain of $K_A = 1.1$ and a curtailment change limit of $\Delta P_{lim} = 0.5$. For the worst week, this parameter set had voltage violations 0.05% of the time. This represents an overall violation improvement of essentially 100.0% and a 99.6% improvement in time spent in violation at the cost of curtailing the cumulative PV output by 3.99%. The performance of this controller over the course of the week is shown in Figure 5.45. There is a low amount of curtailment without any visible regulator oscillation. However, the downside of the manner in which this control achieves these improved results is apparent in the plot of PV system power curtailment disparity, represented by the blue line in Figure 5.46 for the week. Under this control, there is a standard deviation of 8.21%

and one PV system owner has the amount of energy they generate curtailed by over 80%. This is by far the least fair of the control types.

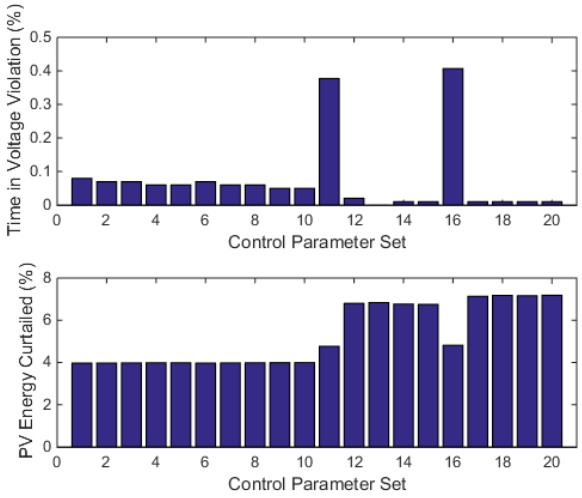

Figure 5.44. Comparison of the performance of different sensitivity-based control parameter sets.

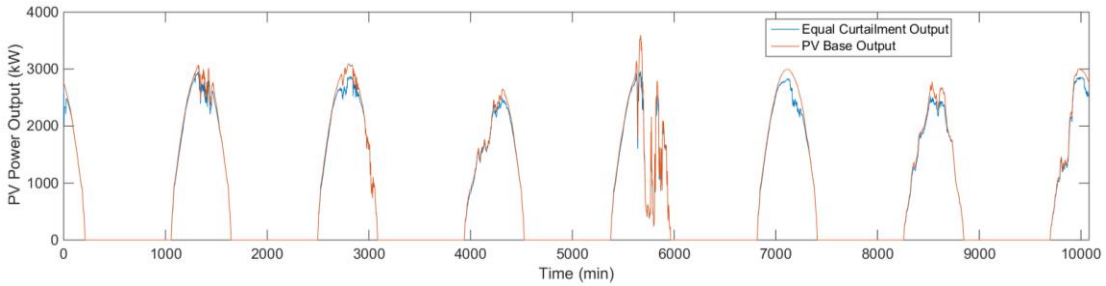

Figure 5.45. Worst week time series PV curtailment using centralized sensitivity-based PV dispatch at 1-minute intervals.

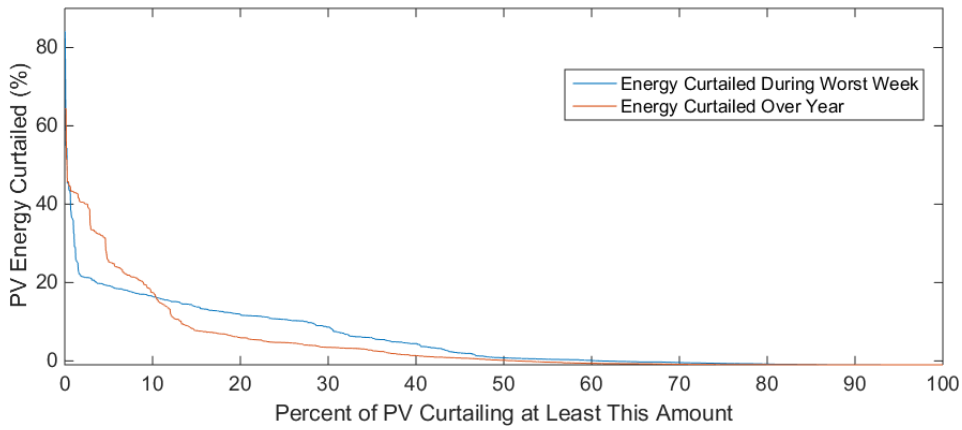

Figure 5.46. Disparity in the amount of power curtailment seen by the PVs under sensitivity-based control.

Over the year, the one-minute sensitivity-based dispatch improves the total number of voltage violations again by nearly 100%. The time spent by the feeder in violation is improved by 99.4% at the cost of 2.46% of the total energy that could have been produced by the PV over the year. However, as indicated by the red line in Figure 5.46, there is even more disparity between the PV system curtailments over the year. The yearly distribution has a standard deviation of 9.78%. This result is at odds with the trends seen in previous control types and warrants further investigation. The distribution of relative curtailments throughout the circuit map for the worst week is shown in Figure 5.47. The PV systems curtailing the most are in the same area here as in Figure 5.25 for the Volt/Watt case, but localized directly around the capacitor, as shown in Figure 5.48. In fact, under the local control, all PV systems in this branch curtail significantly more than the rest of the circuit, but when using the sensitivity-based control, only a few PV system locations must curtail to improve the voltage of the whole branch.

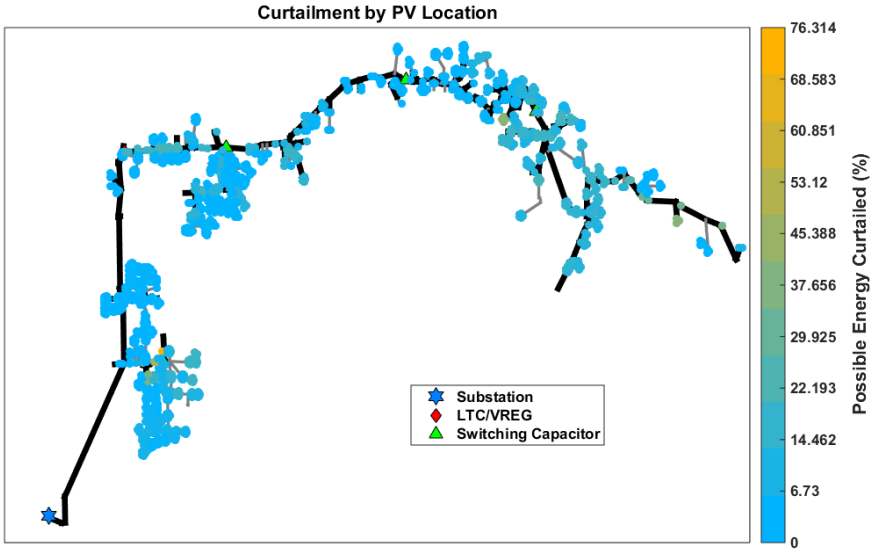

Figure 5.47. Geographic distribution of PV curtailments in the circuit due to sensitivity-based dispatch control during the worst week.

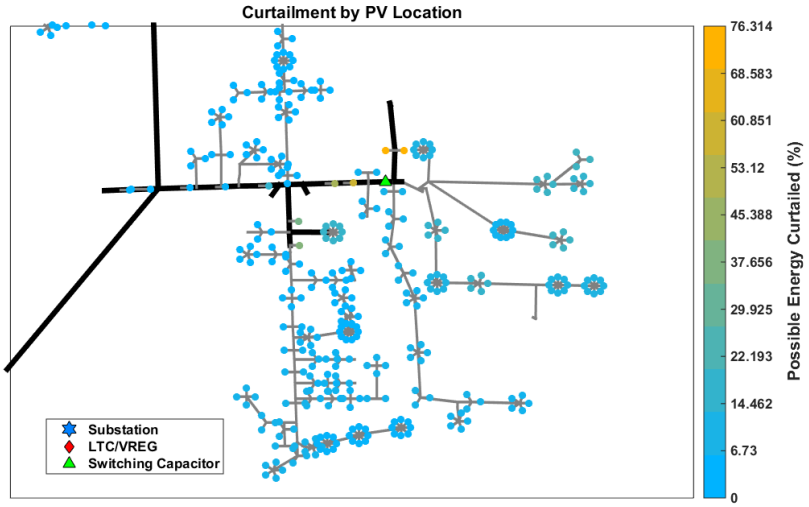

Figure 5.48. Zoomed-in section showing location of PVs curtailing the most due to sensitivity-based dispatch control during the worst week.

To see the difference in the control over the course of the year, the same relative PV system curtailments are plotted in Figure 5.49 using the full year results. The same small group of buses around the capacitor shown in Figure 5.48 curtail relatively more, yet there are also two other areas of the circuit that show large curtailment. The highest curtailment is now a cluster of PV systems that is towards the end of the feeder, but not near any obvious locations that would mitigate voltage rise. This is an interesting result of the sensitivity-based approach because it just so happens that this is a relatively large cluster of PV systems that is well-positioned to improve the voltage profile of the end of the feeder. Therefore this cluster is called on more by the sensitivity matrix to curtail in order improve the overall feeder voltage.

The other area that shows a higher level of relative curtailment over the year than during the worst week is just downstream of the voltage regulator. This section of the feeder is enlarged in Figure 5.50. Here it is clear the PV systems on the feeder backbone directly downstream of the voltage regulator are activated more by the control. This is most likely due to interactions between the inverters, the control, and the voltage regulator that occur

at some points in the year that are not represented during the worst week of over-voltages compared to the base case.

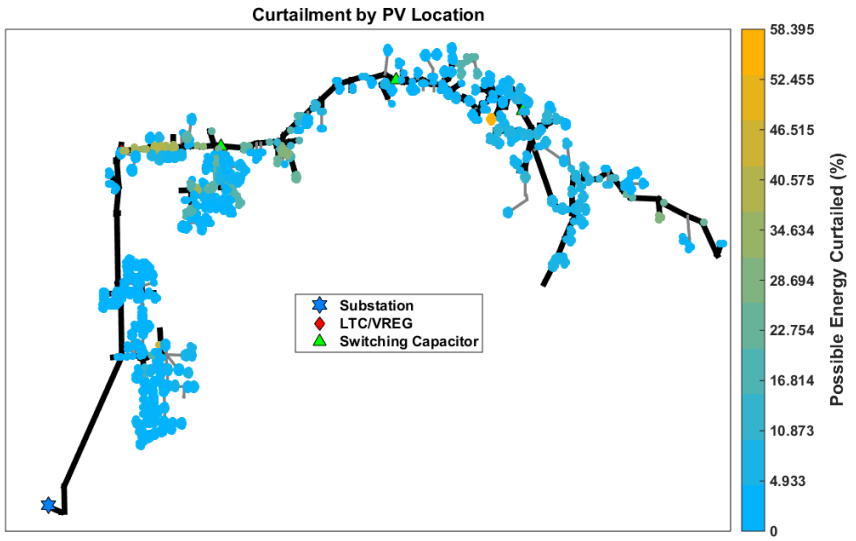

Figure 5.49. Geographic distribution of PV curtailments in the circuit due to sensitivity-based dispatch control over the year.

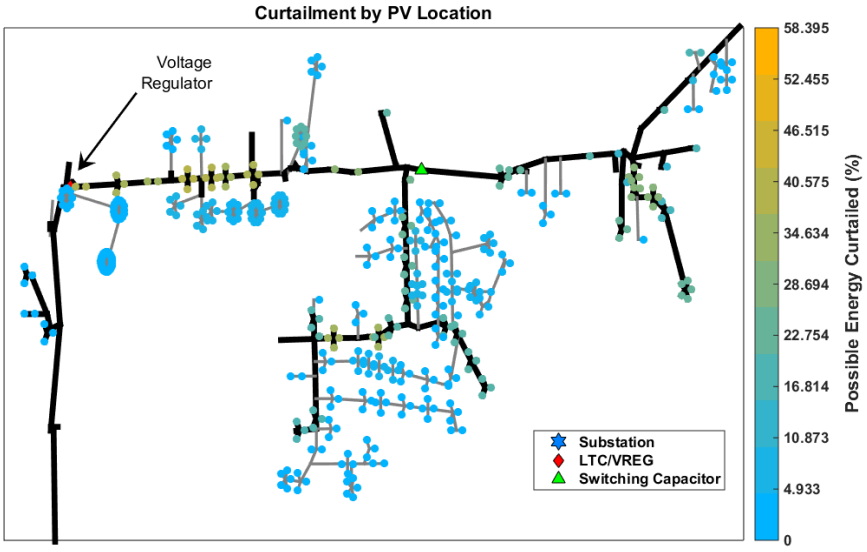

Figure 5.50. Zoomed-in section showing location of PVs curtailing more due to sensitivity-based dispatch control over the year than during worst week.

5.4.5.2 Five-Minute Dispatch

The sensitivity-based control is tuned again under the assumption that the centralized controller can only dispatch signals once every five minutes to all the PV. Since it is assumed a larger dispatch window will require a slower controller to prevent oscillation,

new parameter sets are selected to try. Sets #1-5 have $K_A = 0.9$ and $\Delta P_{lim} = [0.1,0.2, \ldots 0.5]$, Sets #6-15 have $K_A = 1.0$ and $\Delta P_{lim} = [0.1,0.2, \ldots 1.0]$, and Sets #16-20 have $K_A = 1.1$ and $\Delta P_{lim} = [0.1,0.2, \ldots 0.5]$. A comparison in the performance of these control parameters is shown in Figure 5.51. In this instance, it is fairly clear that Set #1 minimizes both voltage violations, power curtailment, and is the least likely to result in oscillations due to its low ΔP_{lim}.

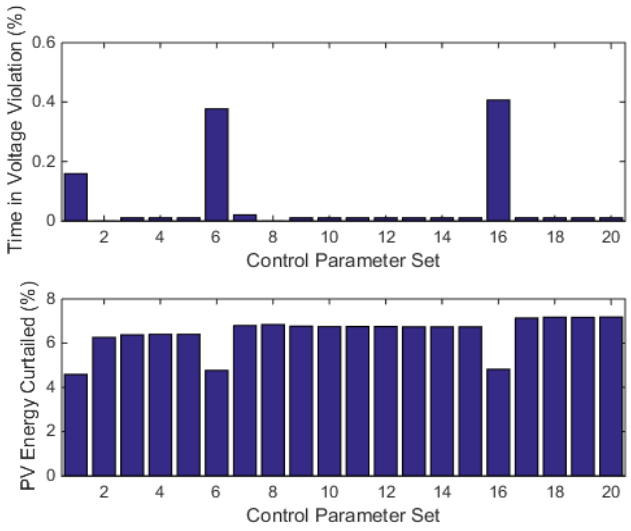

Figure 5.51. Comparison of sensitivity-based five-minute dispatch control parameter set performance.

Using $K_A = 0.9$ and $\Delta P_{lim} = 0.1$, the curtailment profile and remaining instances of over-voltage violations are shown in Figure 5.52. Overall, the controller performs similar to the one-minute dispatch. The overall voltage violations are reduced by 99.8% and the time spent in violation by the feeder is reduced by 98.9%. The PV systems are curtailed 4.58% of their total output.

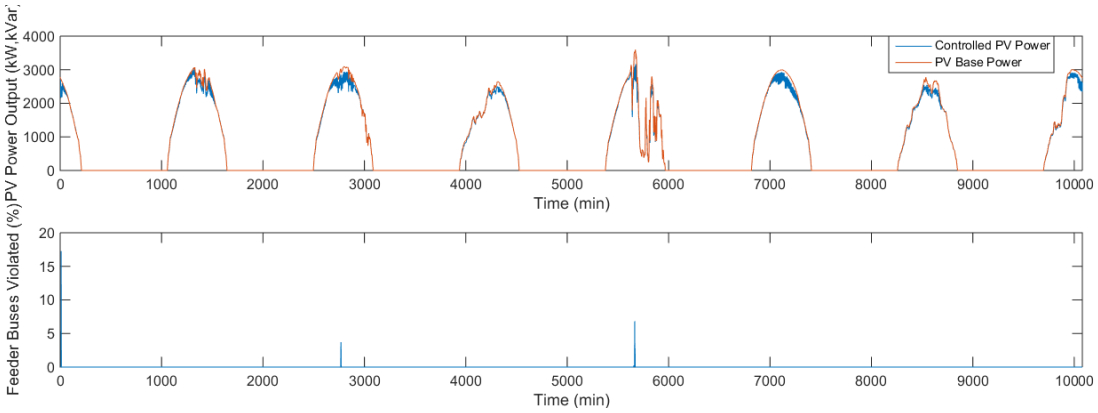

Figure 5.52. PV output power with and without five-minute dispatch sensitivity-based curtailment and remaining voltage violations with control.

However, there are a few major differences between the five-minute dispatch and the one-minute dispatch. The first is the presence of controller oscillations, which are noticeable by the "thick" blue power output lines in Figure 5.52. Zooming in on a single day in Figure 5.53, it is clear that these oscillatory power outputs are indeed the result of controller ringing as the controller is clearly saturating at the ΔP_{lim} value in an attempt to regulate the voltage. The five-minute dispatch is simply too slow to keep up with the changes of the system.

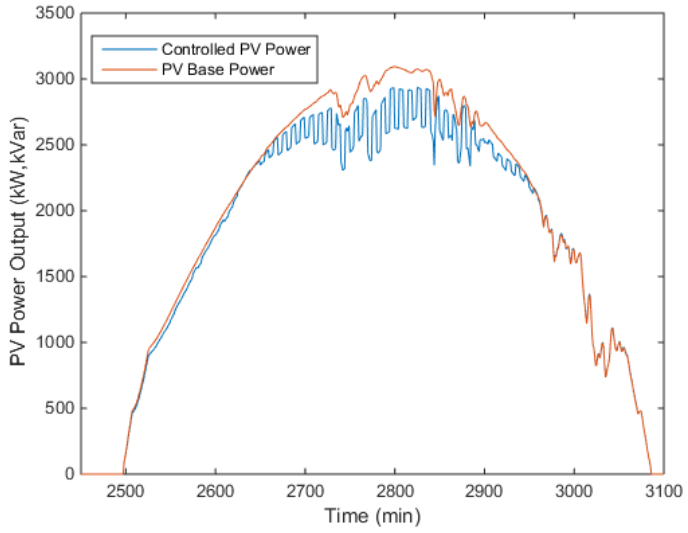

Figure 5.53. Zoomed-in section of a day under five-minute dispatch of sensitivity-based curtailment.

The second major difference is a peculiarity seen in the distribution of PV system curtailments in Figure 5.54. While the overall shape is similar to that of the 1-minute

sensitivity-based dispatch, the presence of negative "curtailment" values is disturbing. This means that several PV systems actually produce more power under this control than in the base case, which is supposed to be the PVs' maximum power output. At face value this appears to be an error in the control. However, the maximum increase is small at 1.00% and may be the result of two things. First, the rating of each PV inverter has been increased by 1% between the baseline run and this control to accommodate reactive power support. Second, each inverter has a cut-in and cut-out value that turns the inverter off if the PV system is not outputting above 10% of its rating, which is common in practice since inverters have poor efficiency at low power output. The result is that at least twice a day during the week, if no curtailment signal is applied, these PV systems will output slightly more than the baseline case. In effect, the result is negligible and any negative values should be considered to be practically zero. Overall there is a standard deviation of 8.23% in the distribution of power curtailment among all PV systems.

Simulating the full year of data with the sensitivity-based control using a 5-minute dispatch has a slightly worse improvement in over-voltage violations. Total over-voltages are reduced by 99.8% and time spent in violation is reduced by 99.2%. This is to be expected from the results of the fair dispatch and it makes sense since the control has fewer actions available to improve the voltage. The amount of energy curtailed is also slightly worse at 2.82%. The disparity in control action is shown as the red line in Figure 5.54 and has a standard deviation of 9.89%, also slightly worse than the 1-minute dispatch case. As with the 1-minute dispatch case, the one-year results have a higher disparity, mainly due to the interaction with some inverters and the voltage regulator.

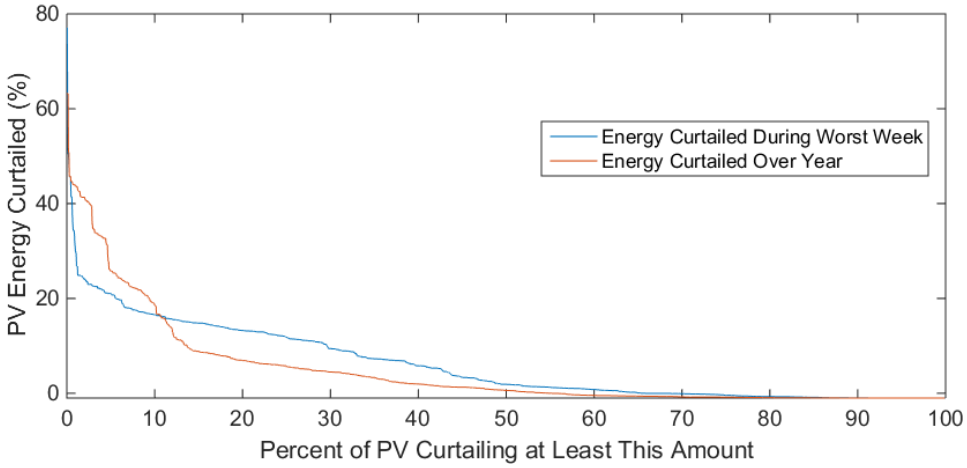

Figure 5.54. Disparity in PV power curtailment using sensitivity-based control dispatched at 5-minute intervals.

5.5 Conclusions

Below in Table 5.1 is a comparison of the different controls presented in Section 5.2 and how they perform during the worst one-week period of voltage violations during the year. The first row of each table compares how each control improves the overall sum of over-voltages at each bus and point in time. The second row compares how each control improves the time in which the feeder spends with an over-voltage violation present at *any* bus. The comparison of how each control performed over the year is presented in Table 5.2. A discussion of the performance of each control type follows.

Table 5.1. Comparison of the performance of the various PV inverter control types investigated during the worst one-week period of voltage violations on the feeder.

Control Type	ZCI	Volt/ Watt	Volt/ Var	Central Fair (1m)	Central Fair (5m)	Sensitivity-based (1m)	Sensitivity-based (5m)
Overall Voltage Issues Mitigated (%)	100.0	100.0	98.7	100.0	91.7	100.0	99.7
Time with Violations Mitigated (%)	100.0	100.0	97.9	99.2	41.9	99.6	98.9
Power Curtailed (%)	21.6	4.35	0	9.3	5.89	3.99	4.58
Curtailment Deviation (%)	0.75	5.69	0	0.57	0.16	8.21	8.23

Table 5.2. Comparison of the performance of the various PV inverter control types investigated during over full year of load and irradiance data.

Control Type	ZCI	Volt/ Watt	Volt/ Var	Central Fair (1m)	Central Fair (5m)	Sensitivity-based (1m)	Sensitivity-based (5m)
Overall Voltage Issues Mitigated (%)	100.0	100.0	98.2	100.0	97.6	100.0	99.8
Time with Violations Mitigated (%)	100.0	100.0	96.7	99.3	88.4	99.4	99.2
Power Curtailed (%)	10.7	0.85	0	1.75	2.00	2.46	2.82
Curtailment Deviation (%)	0.46	1.81	0	0.09	0.05	9.78	9.89

5.5.1 Volt/Watt Control

The Volt/Watt control does a comparable job of mitigating over-voltage violations as the simple method of preventing reverse current injection into the feeder through curtailment (zero current injection). Impressively, the control strategy achieves this while curtailing 94.8% less energy than the zero current injection method.

5.5.2 Volt/Var Control

The application of Volt/Var control is able to mitigate most voltage violations with no curtailment at all. The combination of Volt/Var control with curtailing the PV systems only when necessary should be able to prevent 100% of voltage violations at a minimal level of PV real power curtailment.

5.5.3 Centralized Fair Control

Compared to the local controls, the centralized control types have global network knowledge that allows them to achieve specialized tasks. Specifically, the fair dispatch is able to prevent a large number of over-voltage violations while evenly distributing the

burden of curtailment relative to the size of each PV system. Where the fair dispatch method is able to mitigate a large overall number of over-voltages at a small curtailment, it does a poor job of improving the overall time spent by the feeder in a violated state. Reducing the voltage limit setting in (5.1) should improve the voltage violation mitigation performance of the control but also curtail more energy.

5.5.4 Centralized Sensitivity-Based Control

Unlike the other control types, the centralized control method that makes use of the knowledge of each PV system's impact on the overall network voltage is able to mitigate essentially all over-voltage violations using the least amount of curtailment during the time period when it is tuned. However, when applied to the full year of data, the sensitivity-based method poorly interacts with the feeder's voltage regulator and actually curtails more power than both the fair approach and the local Volt/Watt approach (although the fair approach does not meet the objective of mitigating all violations). This result is unexpected and emphasizes that this control in particular, and possibly others, should take more system measurements into consideration than only over-voltages to make sure the parameters selected do not have adverse effects on the existing voltage controls.

Concerning the dispatch times of both this control and the fair approach, the controls with the larger dispatch windows have the worst results, although not by much. Where the longer dispatch times really suffer is the introduction of power oscillations to the feeder, which is an adverse impact but is difficult to quantify. As with the local control, the centralized dispatch methods can also benefit from reactive power support, either in the form of a direct dispatch or a supporting local control at each PV system.

5.6 Summary

This chapter has described the impact that thousands of highly distributed rooftop PV systems would have on the voltage levels of a distribution network. Several real power

curtailment controls have been considered to mitigate the over-voltage violations. The controls have been tuned and compared by their effectiveness and fairness. A summary of all the research presented in this dissertation and directions for future research are presented in the next chapter.

6. CONCLUSIONS AND SUGGESTED DIRECTIONS FOR FUTURE RESEARCH

The overarching goal of the research presented in this dissertation is to study the physical limitations of installing large amounts of PV generation on distribution networks and how advanced inverter controls may be employed to allow for more PV generation to be installed, while maintaining secure operation of the system. The work in this dissertation covers three main research thrusts that have been detailed in Chapters 3-5. In each chapter, the issues are studied on several large distribution network models of real-world distribution feeders. Each full model studied is unbalanced, includes both medium- and low-voltage networks, spans thousands of buses, and has all existing network voltage regulating controls modeled. The models are studied for one year of input irradiance data with a simulation resolution of either one second or one minute granularity.

6.1 PV System Impact on Protection

In Chapter 3, the impact of a large PV system on existing distribution protection equipment is studied. Exhaustive fault studies are performed for every potential PV interconnection location to determine what size PV system, if any, will interfere with existing overcurrent protection. The studies are carried out in the OpenDSS platform interfaced with Matlab, but the existing PV system models run into convergence issues under fault conditions. Thus, a simplified model for the steady-state fault current injection from a PV system is developed for these studies in Appendixes A and B. Additionally, the simulations are computationally burdensome due to the scale of the networks and combinations of cases. Thus, several approximations are developed to reduce the complexity of the problem in Appendix C.

It is determined that the primary limitation on the amount of PV that may be interconnected is its reverse fault current contribution picking up overcurrent relays. However, the assumptions made in the research are conservative since it is assumed there

is no knowledge of the protection settings on neighboring feeders. Additionally, most modern protection relays on distribution networks have the capability to detect reverse current flow, which could prevent most nuisance and sympathetic tripping issues. Lastly, preliminary research in this dissertation identifies potential cases where PV-induced under-reach may occur, but it is unclear of the prevalence of such cases in actual distribution feeders.

6.2 Tuning Advanced PV Inverter Control Parameters

In Chapter 4, the negative impacts of a single large PV interconnection is studied over varying load and irradiance profiles. Since these studies exist in the time domain and interact with network equipment that has time-dependent states, quasi-static time-series (QSTS) simulations are performed in OpenDSS. Depending on the location of the interconnection, the PV system typically causes increased voltage violations and voltage regulating equipment operations.

A number of advanced inverter controls are investigated for mitigating the issues caused by PV generation. A parametric study is performed on two distribution networks at many interconnection locations to determine how the advanced inverter controls should be tuned to best mitigate PV-induced issues. An objective function is assigned to score controller effectiveness and a map of objective function score versus controller parameters is created. Using this map, the maximum range of control parameters that improves the objective score above a given threshold is found for each PV interconnection location. Performing this procedure at many interconnection locations across a feeder, it is found that the range of advanced inverter control parameters that improve the desired feeder metrics changes significantly between locations.

Finally, the research attempts to find generalized control parameters that improve a PV system's impact on the network if placed anywhere within the network. It is found that the locational dependence of the PV system interconnection limits the range of parameters that

work at any location significantly. In fact, outlying locations must be discarded to find any acceptable parameter range for some control types.

6.3 Interaction of PV Inverter Controls

In Chapter 5, the effectiveness of several advanced inverter controls are compared while implemented on a large number of PV systems uniformly distributed in a realistic distribution feeder model. To investigate the controller interactions over time, QSTS simulations are performed using one year of one-minute resolution irradiance and load data. The irradiance data is spatially dispersed to simulate the effect of moving clouds across the feeder geography. Inverter controls are then implemented to adjust the desired PV system real and reactive power outputs in an effort to mitigate over-voltage violations. The controls are compared on their effectiveness in mitigating over-voltage violations at the cost of curtailing real power or producing vars. The fairness of how the controls are distributed to the inverters is also studied.

The local Volt/Watt control is able to prevent voltage violations while still allowing for reverse power flow without the need for a communication network. The local Volt/Var control is also able to prevent most over-voltage violations without curtailment. Combining the two controls could prevent all over-voltages with minimum curtailment and without the need for a communication network. However, both of these local controls are dependent on their location in the feeder and are therefore not fair to all PV systems in terms of which inverters get controlled more than others.

Introducing a communication network allows for specific objectives to be achieved, namely for the control to be as fair as possible or to use the least amount of power control. However, the parameter selection process for each of the controls does not scale from the subset of time used to tune the controls to the full year. Tuning the controls based only on one set of over-voltage measurements does not take existing voltage controllers into consideration and therefore the controls could not be guaranteed to perform equally well

at all other times. To better select control parameters, the controls could be tuned over the entire time period in question or more metrics should be used in the tuning process, such as capacitor state or regulator tap changes. Additionally, oscillations between inverter controls are observed but not penalized in the tuning process since their negative impact on the network is not quantified.

6.4 Summary of Research Goal Results

In Section 1.4 specific research goals are laid out for the research presented in Chapters 3-5. This section summarizes the key findings of the research with regard to these specific goals.

- The research in Chapter 3 found that the primary limiting factor to the size of a new PV system installation with regard to its impact on network protection is the possibility of the PV system tripping protection devices on reverse current. On average, across the six feeders tested, the maximum size of a new PV system that may be interconnected without impacting network protection is 3.77 MW.
- The research in Chapter 4 found that there is a strong locational dependence on the parameters used to set advanced inverter controls. This locational dependence implies that it is unlikely that there exist a set of general control parameters for all PV inverter advanced controls that work well for any new PV system interconnection in a distribution network. This means that the advanced inverter controls should be tuned per each new interconnection location.
- The research in Chapter 5 found that both local and centralized real-power advanced PV inverter controls are capable of mitigating all over-voltage violations caused by a large amount of highly distributed PV in a distribution network. The research also concludes that local control schemes have comparable performance to centralized methods that leverage communication infrastructure and knowledge of the entire distribution network.

6.5 Future Research

6.5.1 PV System Impact on Protection

Future research in the area of PV impact on distribution protection could continue from the preliminary work done in this dissertation to identify the existence of protection violations analytically. The research presented in Section 3.5 indicates that there exist combinations of fault location, PV size, and protection pick-up currents that may result in an undetected three-phase fault. It is beneficial to utilities to know if these cases exist on their networks. A fast, analytical approach to identifying potential under-reach cases could speed PV interconnection requests by reducing the number of studies that need to be performed by the utility.

6.5.2 Tuning Advanced PV Inverter Control Parameters

To continue the research on tuning advanced inverter controls to improve their performance, further analysis should be made on the additional distribution feeder models. Included in such an analysis should be a review of trends across the feeder models and how these trends correspond to physical aspects of the feeders. The future research could conclude with a study of how these advanced inverter controls can be used to maximize the amount of PV allowed on a distribution feeder before violations occur. The research in this dissertation only investigates a single PV system size, but it is beneficial to know how the implementation of advanced inverter controls may improve the hosting capacity of distribution networks.

6.5.3 Interactions of Advanced PV Inverter Controls

In the area of research on the interactions of distributed PV inverter controls, further research could be conducted on each control type to identify which pairs best with reactive power support. Reactive power support has shown promising results in the research in this

dissertation and could substantially reduce the need for real-power curtailment to prevent over-voltage violations.

Additionally, the research in this dissertation observes power oscillations due to the control types implemented, but network stability is not considered. Future research could quantify network stability as a metric to consider in grading the control types. However, the study of network stability or may require additional data about the feeder dynamics and more time-consuming dynamic simulations.

6.6 Novel Contributions

Several novel contributions in the area of distributed PV system integration have come out of the work done for this dissertation. The work is published or pending publication in several forms. Parts of the work in this dissertation have been included in seven IEEE conference papers, however, the work presented in Chapters 3-5 is published as a series of three reports by Sandia National Labs. The contribution of each report is summarized below.

The work in Chapter 3 is pending publication at Sandia National Labs under the title "Determining the Impact of Steady-State PV Fault Current Injections on Distribution Protection". This work developed a stable steady-state model of a faulted PV system for use in exhaustive fault studies. The work is also unique in being performed on six real-world, large, unbalanced distribution feeder models. Several novel techniques are also developed in this work for reducing the computational burden of an exhaustive fault study.

The work in Chapter 4 is published as an unrestricted Sandia National Labs report titled "Analysis of PV Advanced Inverter Functions and Setpoints under Time Series Simulation". This research is novel in its comparison of five different advanced inverter controls simultaneously using six different metrics. The work is also uniquely performed on two large, real-world distribution feeder models using actual load and irradiance time-

series data. A novel method for performing a parametric study on the performance of advanced inverter control parameters is developed.

Finally, the work in Chapter 5 is also published as an unrestricted Sandia National Labs report titled “Multi-Objective Advanced Inverter Controls to Dispatch the Real and Reactive Power of Many Distributed PV Systems”. This work takes a novel approach to investigate the interactions of PV systems with advanced inverter controls that are completely distributed at each load in a large, real-world, unbalanced distribution network. Two local and two centralized control strategies are compared. The centralized control strategies are novel to this research. Also unique to this work is the comparison of the control types investigated based not just on performance but also fairness to the participating PV systems.

APPENDIX A DEVELOPING A STEADY-STATE FAULTED PV-SYSTEM IN OPENDSS

At the time of this research, the existing OpenDSS PV system model was not recommended for use in faulted networks and testing the model under many different conditions often results in solution convergence issues. Three alternate PV system models are considered in this appendix: an ideal current source, a voltage source behind an impedance, or an equivalent generator. A voltage source behind an impedance is not an ideal candidate since it requires external logic to adjust for different network conditions. A current source is representative of the steady-state behavior of the internal inverter current controls, but does not consider the actions of the MPPT control. The MPPT increases current output as voltage drops at the inverter terminals under fault conditions up to a maximum short-term rating of the inverter, typically 2.0 pu of rated current according to the above literature. For this reason, a current source also requires external logic and multiple power flow solutions to converge to the proper PV current output for each fault condition, which is not ideal. However, a generator model in OpenDSS is able to maintain constant power output within a single power flow solution. The model used must be verified to ensure it is producing the desired currents during network fault conditions. This verification is done using the four-bus, three-line test circuit shown below in Figure A.1. By adjusting the line impedances, this configuration can simulate any relative placement of a fault with respect to the PV at any distance downstream of the grid, which is assumed to be an ideal voltage source.

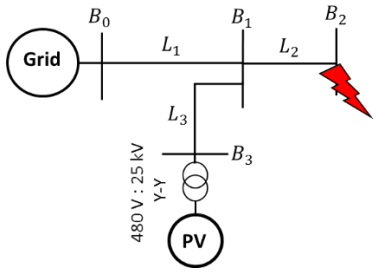

Figure A.1. Four-bus test circuit used to simulate various fault and PV distances from the substation.

A.1 Current-Limited Generator Model

The PV system is first modeled as the OpenDSS Generator Model #7, which is a constant power, current-limited source that approximates an inverter, since this model will produce the fastest solutions per PV and fault placement case. The model parameters are listed in brackets below, followed by a short description.

- [Model: 7] Sets generator to constant power, current limited
- [Balanced: no] Allows unbalanced currents for unbalanced faults
- [Conn: wye] Wye PV connection provides the largest current injection
- [kv: 0.48] Low-voltage rating of grid-tie transformer
- [pf: 1] Operates at unity power factor
- [kw: P_{PV}] Variable size of PV panels
- [kVA: 2.0*P_{PV}] Allows for 2.0 pu rated current
- [phases: 3] Sets to three-phase PV system
- [Vmaxpu: 1.5] Set arbitrarily high to avoid switching to a different generator model
- [Vminpu: 0.5] Will allow 2.0 pu rated current, but no more

To validate that the OpenDSS current-limited generator is an appropriate analog for a PV system using the above settings, its behavior under fault conditions must match what is expected from (2.3). In the test circuit in Figure A.1, L_1 is made large and L_3 small to create a weak connection to the PV. Then L_2 is varied to emulate varying fault severities, which results in various degrees of voltage sag at B_1.

In Figure A.2, the current-limited, constant-power behavior described in (2.3) is validated during balanced three-phase faults. These results are for a 1 MW PV system on a 25 kV network, so the per-phase rated output current of the PV is $I_{rated,MV} = (1 \times 10^6\ W)/(25 \times 10^3 V)/\sqrt{3} = 23.1\ A$ at medium-voltage and $I_{rated,LV} = 1203\ A$ at low-

voltage, interfaced through a Y-Y $25kV{:}\,480V$ transformer. Therefore, each phase is limited to twice these values through the inverter. This output behavior can be seen in the top plots of Figure A.2, where the phase and cumulative currents saturate at their respective 2.0 pu rated current limits for low impedance faults. The cumulative and per-phase current outputs are compared to the 2.0 pu rated current limits for both low- and medium-voltages in the top two plots. The bottom left plot shows how the PCC voltage decreases with lower fault distance. The bottom right plot shows the per phase and cumulative power output of the PV system against its rating. The phase currents are all overlapped due to the balanced network and fault. The current output saturations correspond to the PCC voltage (bottom-left plot) dropping below 0.5 pu as the fault is moved closer to the PV system. The bottom-right plot shows the output power is constant except when the current saturates.

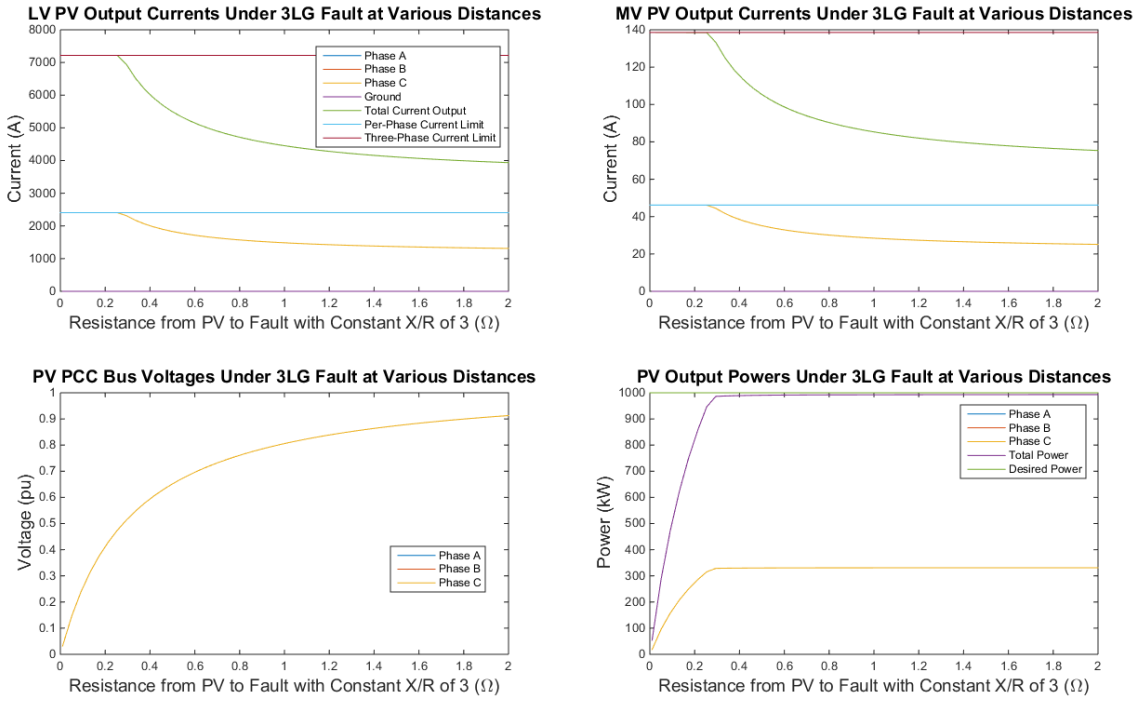

Figure A.2. PV output currents and powers and PCC voltage under various 3LG faults.

Under unbalanced faults, the PV system shows similar behavior as shown in Figure A.3. Here a one-phase fault is applied and only one phase of the PV system increases its current output in response to the sagging PCC voltage. The faulted phase current is the blue

line in the top two plots while the non-faulted phases remain relatively constant. With an unbalanced fault, the PV system also produces ground current, shown in purple. The PCC voltages are shown in the bottom-right plot, where interestingly the non-faulted phases increase in voltage as the faulted phase decreases. One thing to point out in Figure A.3 is that at very low impedances, the ground current has an unexpected increase. In fact, this model is very sensitive to the line parameters while under fault conditions. The next subsection explores the ability of the model to converge while a fault is placed on the network.

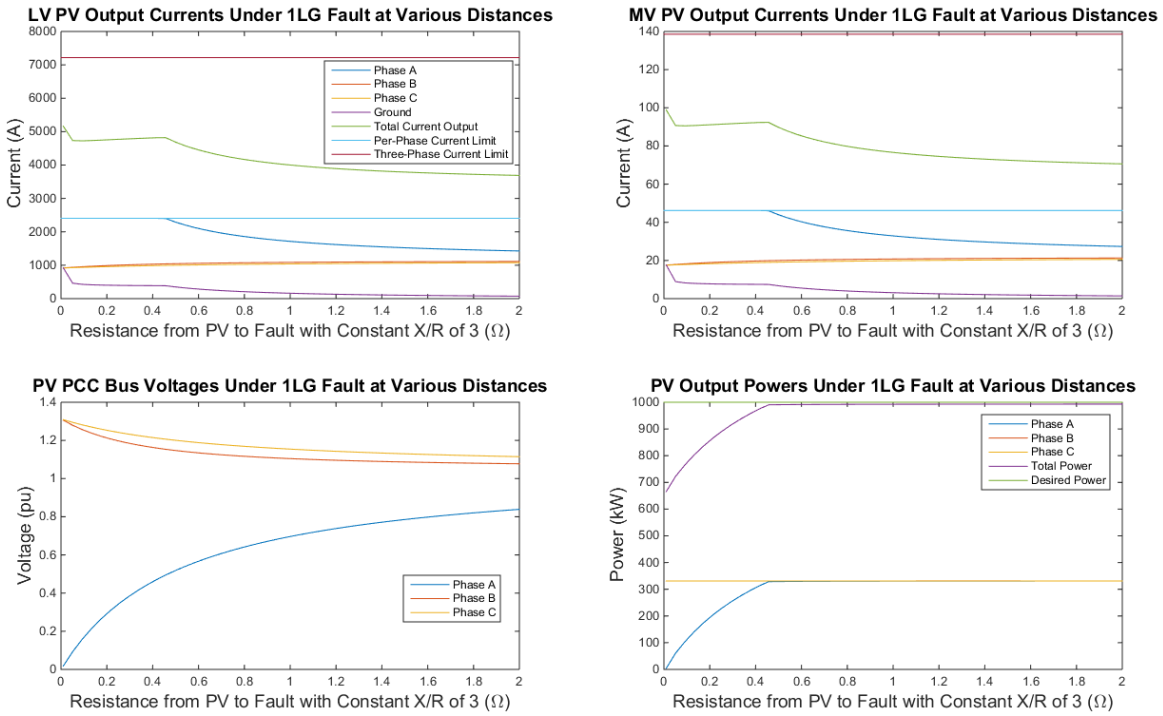

Figure A.3. PV output currents and powers and PCC voltage under various 1LG faults.

A.2 Current-Limited Generator Model Convergence Testing

The current-limited generator model exhibits convergence issues in the network solution under certain PV and fault conditions. OpenDSS recommends using the "direct" solution method when a fault is present on the network. This solution method represents all the network elements as admittances. However, this does not result in the desired

generator output seen in Section A.1. Therefore, the generator model in the standard "snapshot" solution mode must be tested to ensure solution convergence will not be an issue in the feeders under consideration. This research tests PV system sizes up to 10 MW on 12 kV feeders and up to 15 MW on 25 kV feeders. Several topology scenarios are tested on the 25 kV, four-bus network in Figure A.1 to determine if the size of the PV generator model can be increased up to the desired 15 MW and still retain solution convergence.

In the first scenario tested, the PV is placed some distance from the substation and a fault is placed very close to the PV system's terminals. The "distance" is varied by changing the impedance of line L1. The results are shown in Figure A.4 for the four different fault types. The surface colors indicate the last PV size to converge at the given impedances, and the colored lines indicate typical X/R ratios seen in distribution networks. Each subplot represents a fault type from Figure 3.5. Although the lower end of the color scale differs between the subplots, the important region is the bright yellow which indicates the maximum desired PV size to test of 15 MW. Any line impedances not in this region cannot be tested up to the desired PV size.

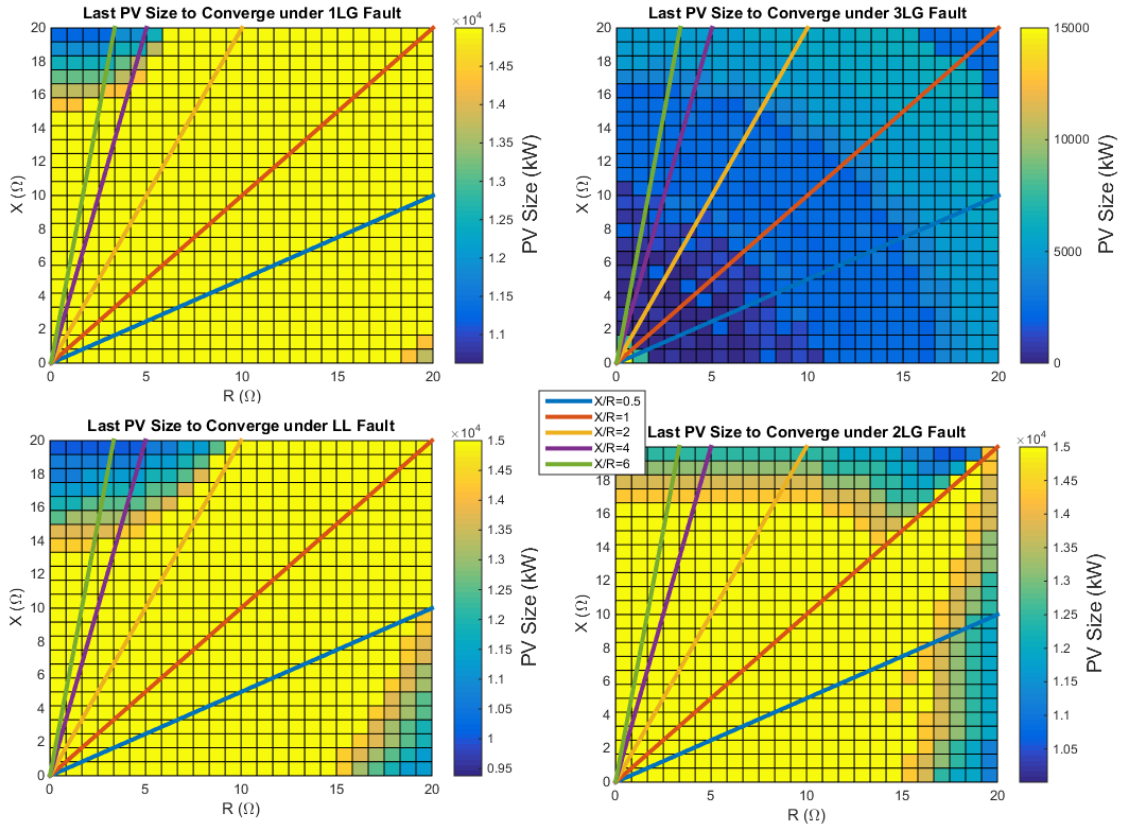

Figure A.4. Maximum PV size for convergence with different faults placed near the PV system at various distances from substation.

The most eminent feature in Figure A.4 is that three-phase faults placed near the PV any distance from the feeder cannot be tested. The other three fault types under this topology do converge at most impedances except for very large impedances with very high or very low X/R ratios. Most distribution feeder models to be studied in this research have X/R ratios between 1.0 and 4.0 on average so the majority of impedances of PV PCCs fall within the convergence region in Figure A.4. Although there are several other topology scenarios, even this first scenario indicates there may be many fault and PV placement locations that cannot be tested. The question now becomes, how many PV interconnection buses in actual distribution network models will have issues with converging using the PV modeled as a current-limited generator?

The smallest of the actual distribution networks that are tested in this research, named QL2, has 224 possible PV locations. It is a 12 kV network, so the maximum tested PV size

of 10 MW is placed at each possible PCC and then each of the four fault types are tested at all possible locations. It is a small circuit with low impedances and no extreme X/R ratios, so the model is expected to perform well in it. The percentages of these faults that allow the solution to converge at each PV placement are shown in Figure A.5. The PV buses are listed in order of nearest to furthest from the substation. The 1LG faults present no problems, however, the other three fault types generally begin to have more fault placements that fail to converge the further the PV is placed from the substation. As expected from the previous studies, the three-phase faults have the worst convergence rates. These are not encouraging results from the most robust of the feeder models.

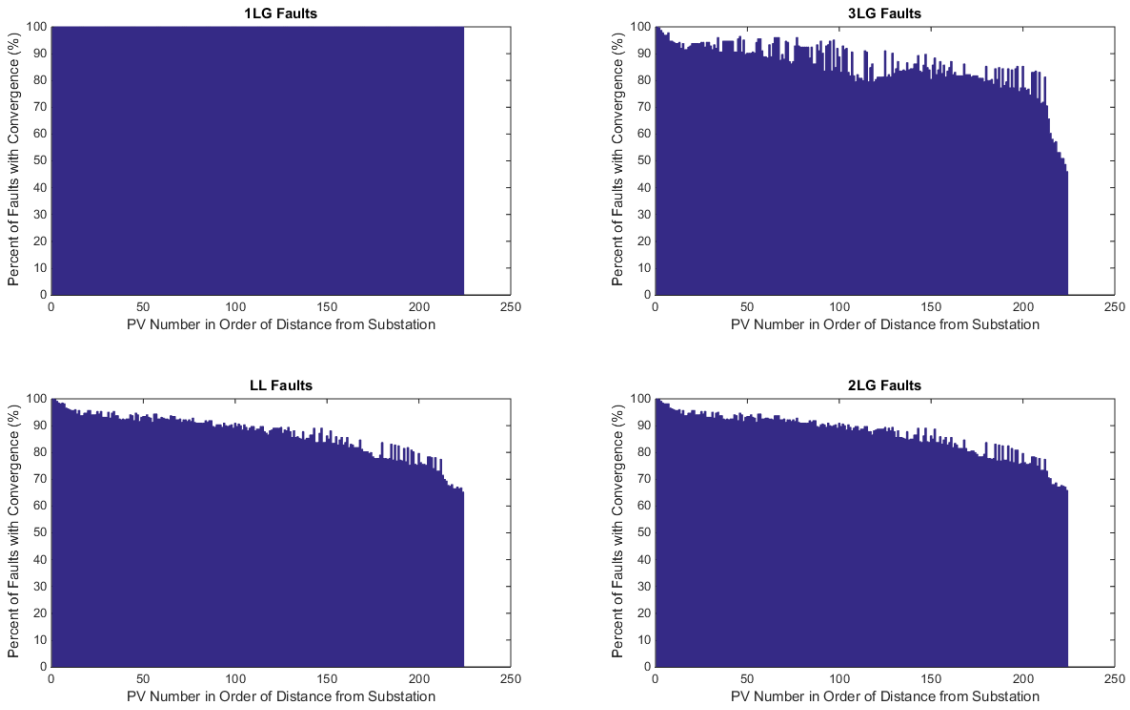

Figure A.5. Feeder QL2 percent of fault locations that result in convergence at largest PV size.

Looking at the feeder model to be tested with the worst impedances, named QW1, it becomes clear that another approach is necessary. This feeder is again 12 kV but it has very large line impedances with low X/R ratios. Figure A.6 shows the percent of faults that converge at each PV placement location for a small sampling of the buses (49 buses tested

out of 864 possible). Even without testing each possible PV placement location, it becomes clear that several PV placements fail to converge with just about any fault placed in the network.

These tests conclude that the OpenDSS current-limited generator model cannot be used in an exhaustive test of the impact of a PV system placed anywhere in a faulted network. The next section introduces a more stable model controlled outside of OpenDSS, developed for these fault studies.

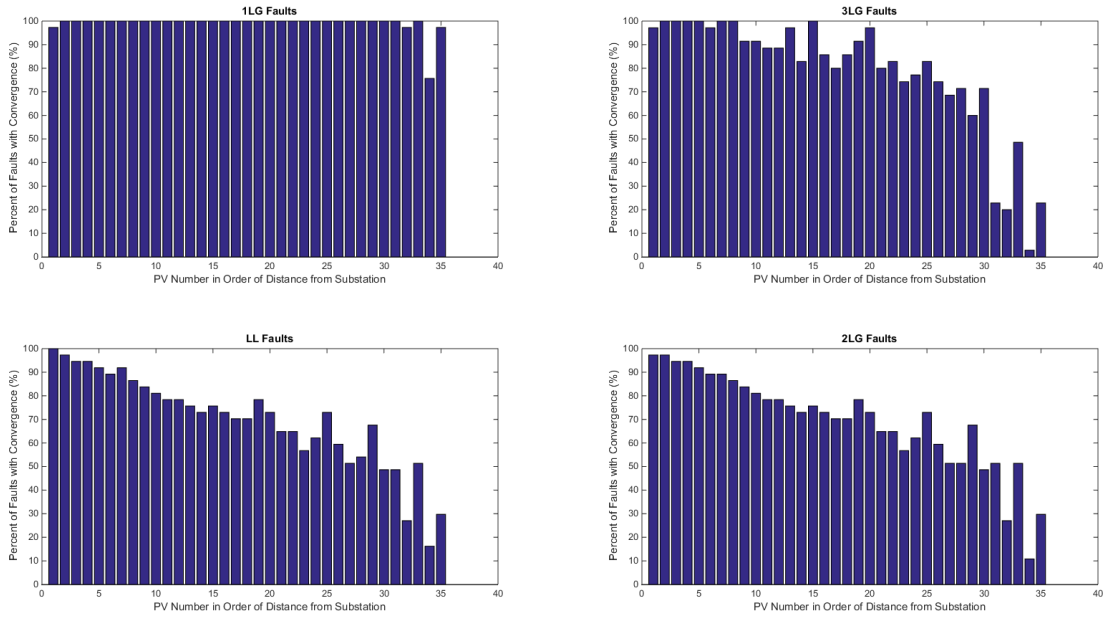

Figure A.6. Feeder QW1 percent of fault locations that result in convergence at largest PV size.

A.3 Voltage-Dependent Current Source Model

The last viable method of modeling the PV system for steady-state fault analysis is to use a voltage-dependent current source. This method uses three independent ISource components in OpenDSS to represent each unbalanced phase of the PV system. Since all loads, capacitor banks, and voltage regulators are disabled, with the PV as a current source the network equations can be represented as $V = YI$ and the faster "direct" solution method in OpenDSS may be used. The algorithm for setting the current of each ISource is summarized as follows:

1. With ISource disabled, enable fault.
2. Solve network, get PV bus voltages and angles.
3. Set ISource currents and angles according to (2.3). If PCC voltage is below 0.5pu, saturate current to 2.0 pu rated current.
4. Enable ISources and solve.
5. Stop if PCC voltage has not changed by more than a threshold. Otherwise, go back to Step 3 using PCC voltage halfway between the original and new voltage.

The current-source outputs under 3LG faults in the test network are shown in Figure A.7. These are comparable to the outputs shown in Figure A.2 and are nearly identical. Again, the cumulative and per-phase current outputs are compared to the 2.0 pu rated current limits for both low- and medium-voltages in the top two plots. The bottom left plot shows how PCC voltage decreases with lower fault distance. The bottom right plot shows the per phase and cumulative power output of the PV system against its rating. The outputs while under 1LG faults are shown in Figure A.8, 2LG faults are in Figure A.9, and LL faults are in Figure A.10. The results of Figure A.8 are comparable to those in Figure A.3 from the current-limited generator model. Using the current-source model, the unexpected increase in ground current is no longer present. The 2LG and LL faults are also similar to the generator models'. Although the currents are slightly different, the output power of the current-source model is closer to the expected value, indicating this model may actually be more representative of the desired output behavior.

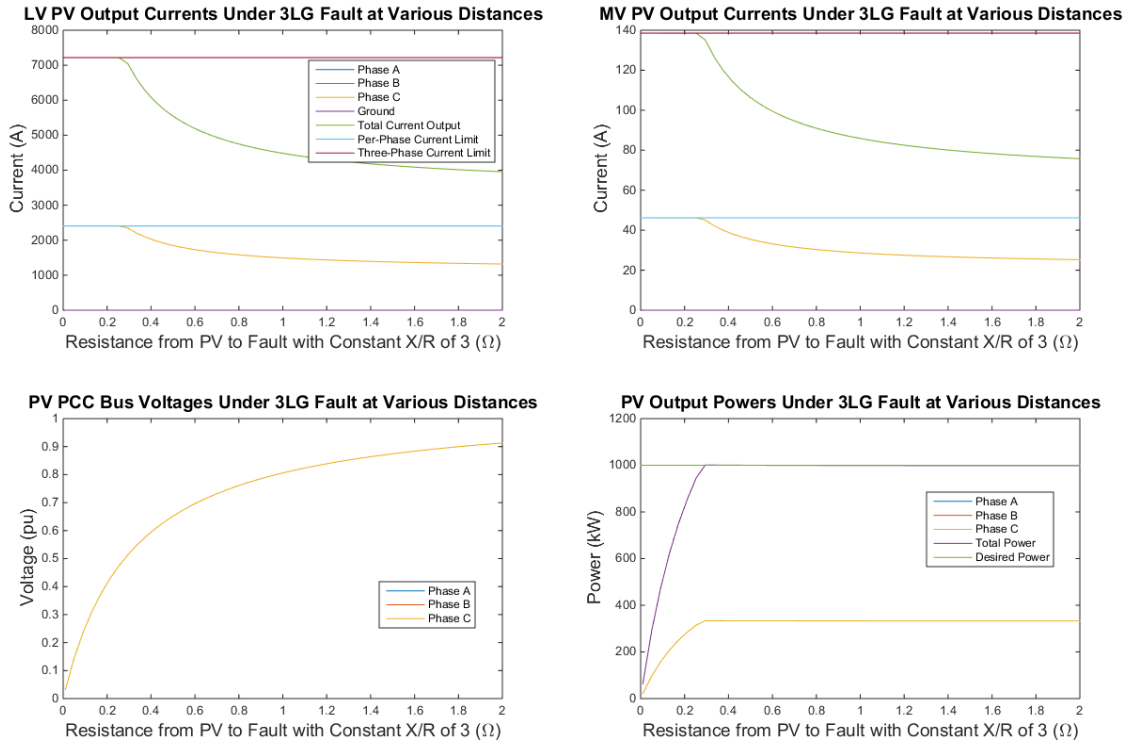

Figure A.7. ISource-PV output currents and powers and PCC voltage under various 3LG faults.

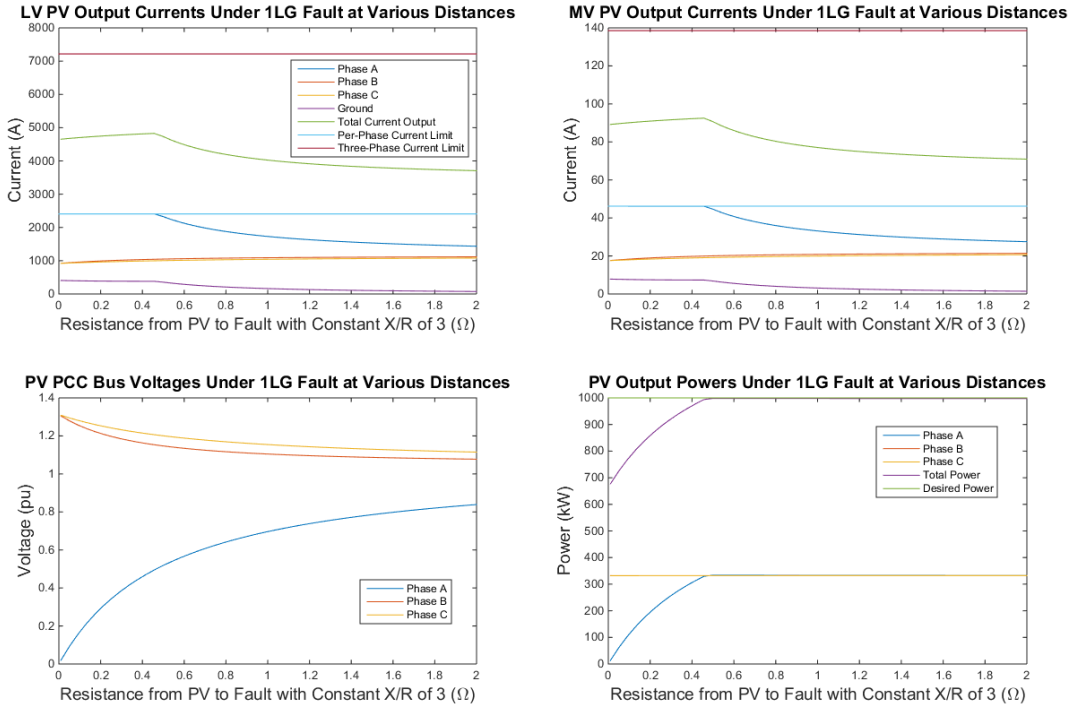

Figure A.8. ISource-PV output currents and powers and PCC voltage under various 1LG faults.

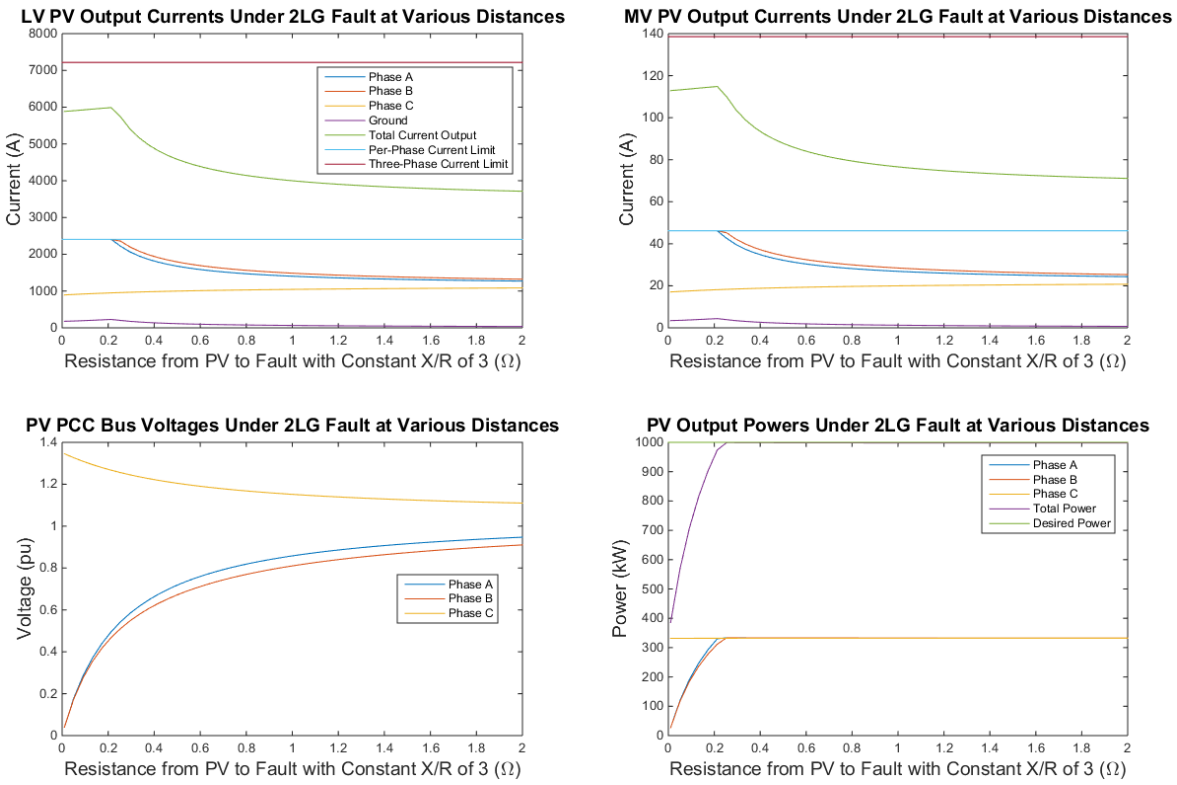

Figure A.9. ISource-PV output currents and powers and PCC voltage under various 2LG faults.

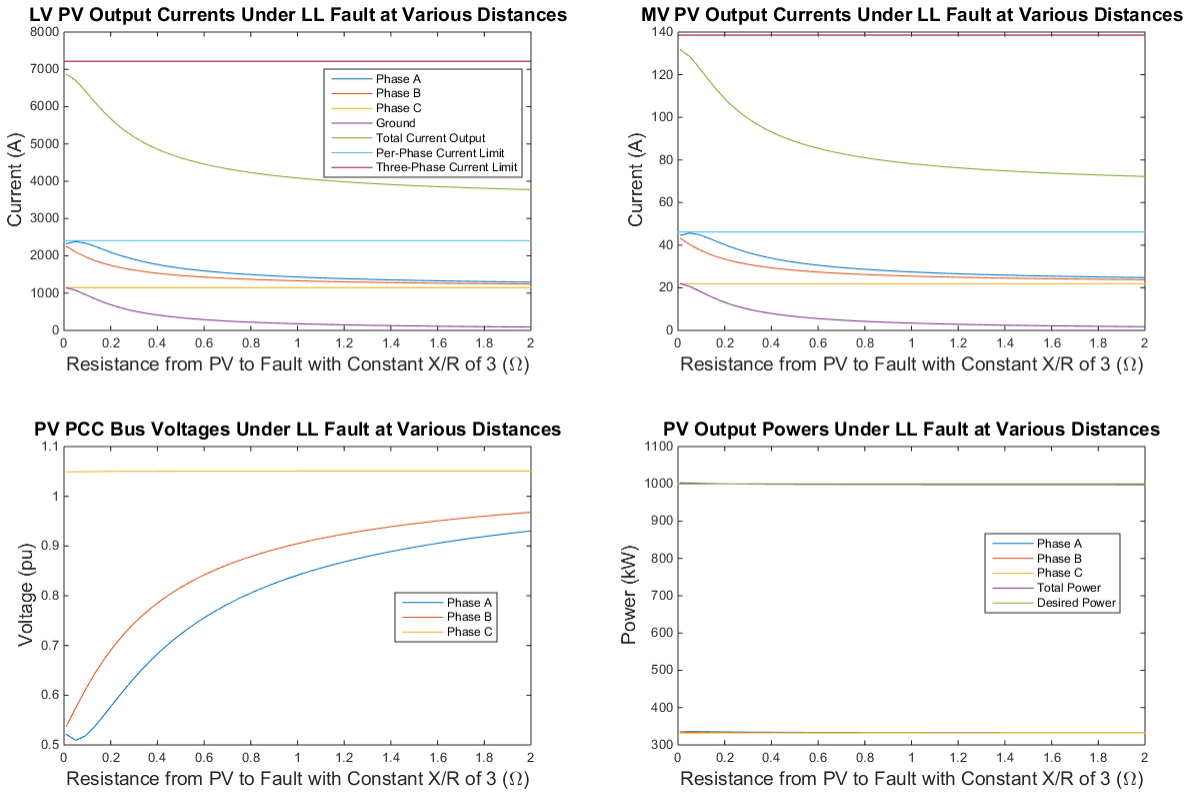

Figure A.10. ISource-PV output currents and powers and PCC voltage under various LL faults.

APPENDIX B PV SYSTEM INTERCONNECTION TRANSFORMER FOR FAULT CURRENT CONTRIBUTION STUDIES

The PV system requires a step-up transformer to interconnect with the medium-voltage distribution network, as previously depicted in Figure A.1. There are four transformer connection options considered: Y-Y, Y-Δ, Δ-Y, and Δ-Δ. There is a potential for circulating currents to develop in a transformer under fault conditions based on its winding connections. These currents will exist regardless of the size of the PV connected to the low-side of the transformer and will therefore tarnish the results of the study and must be avoided.

The results shown in the previous subsection are for a Y-Y transformer. This subsection validates the use of this connection type by performing the same study. Using a Y-Δ transformer, the 3LG balanced fault results are identical to the Y-Y case. However, looking at the results from using a Y-Δ transformer during the unbalanced 1LG and LL faults, shown in Figure B.1 and Figure B.2 respectively, shows a different story. During the 1LG fault, the Y-Δ transformer shows a massive increase in current at the medium-voltage side for the same size PV system. This large current is due to circulating currents in the transformer and would invalidate any analysis of fault current changes as it is mostly independent of the PV system size. Furthermore, even under fault conditions where there is no circulating current, as in the LL case, there is less fault current from the PV due to the voltages measured on the low-side or PV side of the transformer. Comparing Figure B.2 with Figure A.10, it can be seen that the Y-Δ transformer allows for less than 100 A to be injected at the MV level whereas the Y-Y transformer allows for roughly 130 A to be injected for the LL fault. This is the case for all transformers with a Δ-connection and although this is beneficial in practice, the Y-Y transformer is popular and can test for the worst-case scenario of a PV system's impact on the network since it injects more current.

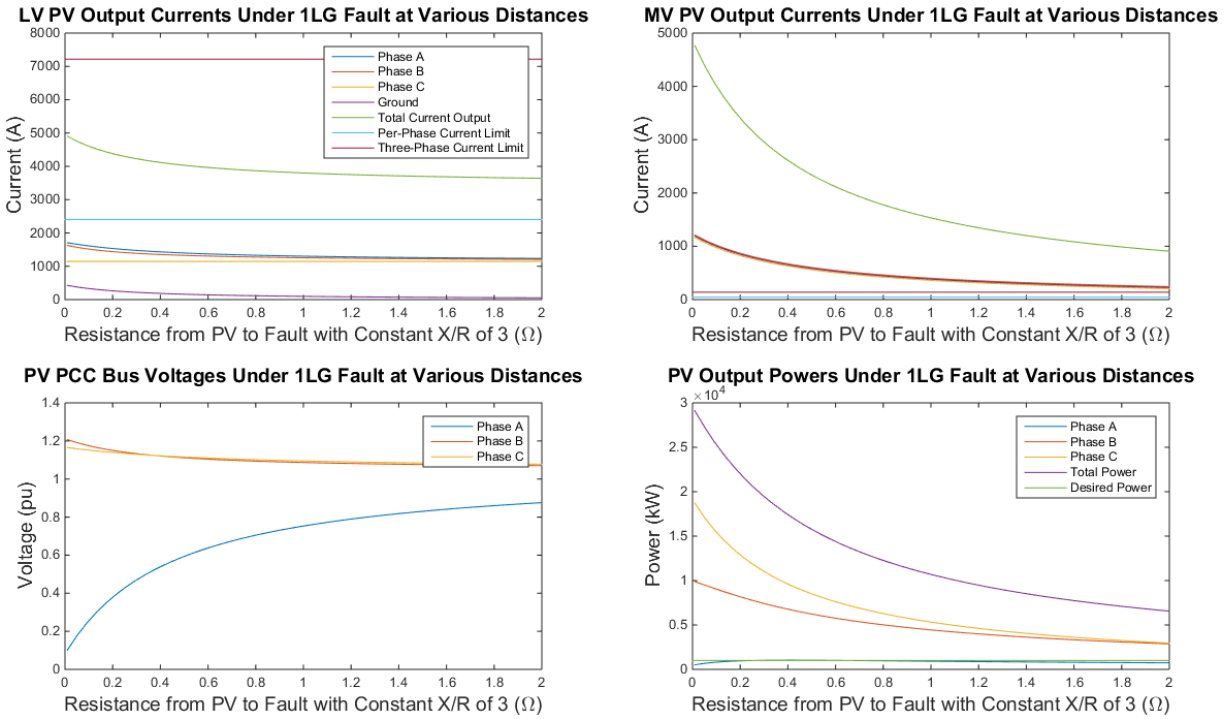

Figure B.1. Current-source PV output currents, power, and voltage using Y-Δ interconnection transformer under 1LG faults.

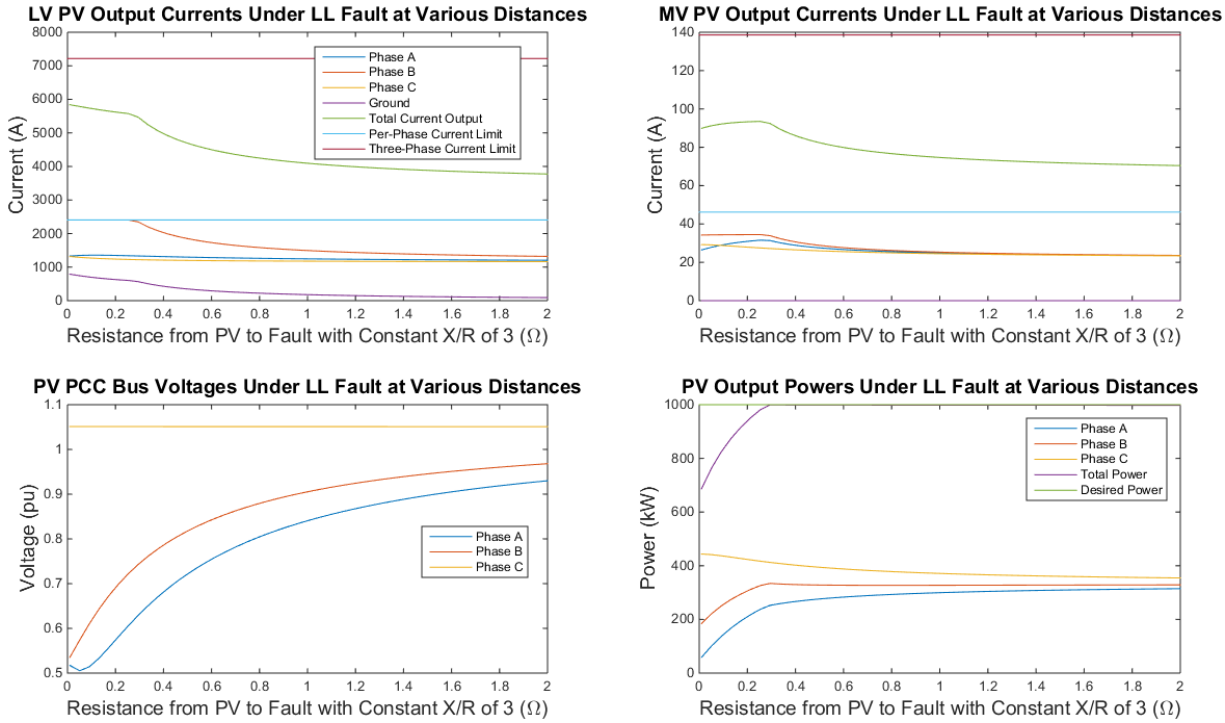

Figure B.2. Current-source PV output currents, power, and voltage using Y-Δ interconnection transformer under LL faults.

In the case of 3-wire feeders, a Δ-Y transformer is used but still with a Y-connected PV. The non-default OpenDSS transformer model parameters are listed in Table B.1.

Table B.1. Three-Phase, Two-Winding Interconnection Transformer Parameters

PARAMETER	HIGH SIDE	LOW SIDE
Rating (kVA)	$2P_{PV}$	$2P_{PV}$
Voltage (kV)	V_{PCC}	0.48
Connection	Wye	Wye
Winding resistance (%)	0.35	0.35
Winding reactance (%)	1.7	1.7
On-load loss (%)	0.7	0.7
No-load loss (%)	0.16	0.16

APPENDIX C APPROXIMATIONS MADE TO REDUCE THE COMPLEXITY OF INTERCONNECTION FAULT STUDIES

As described in Section 2.2, accounting for the impact of any possible PV placement under any possible fault condition increases the computation requirements of the analysis exponentially as the number of buses in the network increases. Due to this high dimensionality problem, efforts are made to reduce the computation time by narrowing the network buses considered. If N_1, N_2, and N_3 are all medium-voltage buses with a minimum of 1, 2, or 3 phases, then $N_1 \geq N_2 \geq N_3$ and the total number of power flow calculations that must be made to analyze each circuit is approximated by the following calculation:

$$T_{comp} \approx N_S N_3 (N_1 + 2N_2 + N_3) \quad \text{(C.1)}$$

In C.1, N_S is the number of PV system sizes tested. The next subsection discusses how the parameter N_S is constrained to further reduce computation time.

C.1 Interpolating the Change in Fault Current Due to PV System Size

Previous research has tested PV sizes at a granularity of $N_S = 100$. For this research to be achieved in a practical amount of time, this value needs to be reduced. For example, a hypothetical feeder has 500 three-phase buses only and achieves a power flow solution in 0.01s on average. This means the calculation of all the fault current impacts would take, based on C.1, $T_{comp} = (100)(500)(500 + 2 * 500 + 500)(0.01s) = 1{,}000{,}000s = 11.57 days$. By reducing the number of PV sizes tested to $N_S = 5$, the computation time is reduced significantly to 13.89 hours. However, this reduction is only valid if it can be assumed that the current output from the PV model changes in a smooth and continuous manner as its size is increased. Therefore, the change in fault current that flows through the protection devices (PDs) as a function of PV size is also smooth and continuous.

Smooth and continuous curves can be approximated by a function. Due to the nature of the network equations, a polynomial function is a good approximation in most cases.

Simply by testing five PV sizes and recording the fault current in the PDs at each size, a curve can be fit to the results in order to back-calculate the results for the remaining sizes. A third-order polynomial is chosen since it fits most of the nonlinearities with minimal error compared to first- and second-order fits. Although only four points are needed to define a third-order polynomial, a fifth point results in a better approximation and allows for the calculation of the fit's "goodness".

The coefficients that define the curve are calculated with the least-squares method described here. The approximate function of fault current change through a PD phase *m* due to fault *n* of type *f* and PV *p* approximated as a third-order polynomial is then:

$$\tilde{I}_{F,mnfp}(P_{PV,p}) = c_{mnfp,1}P_{PV,p}^3 + c_{mnfp,2}P_{PV,p}^2 + c_{mnfp,3}P_{PV,p} + c_{mnfp,4} \qquad \text{(C.2)}$$

The coefficients, $\boldsymbol{c_{mnfp}}$, are calculated as follows:

$$\begin{gathered} \boldsymbol{c_{mnfp}} = (\boldsymbol{A}^T\boldsymbol{A})^{-1}\boldsymbol{A}^T\hat{\boldsymbol{I}}_{\boldsymbol{F,mnfp}} \\ \boldsymbol{A} = [\hat{\boldsymbol{P}}_{PV}^3\ \hat{\boldsymbol{P}}_{PV}^2\ \hat{\boldsymbol{P}}_{PV}\ 1] \end{gathered} \qquad \text{(C.3)}$$

where $\hat{\boldsymbol{I}}_{\boldsymbol{F,mnfp}} \in \mathbb{R}^5$ are the measured fault currents at the five PV test sizes, $\hat{\boldsymbol{P}}_{PV}$. It is important that $\hat{\boldsymbol{P}}_{PV}$ spans the entirety of the PV sizes to be tested, since the third-order polynomial fit does not extrapolate well. Therefore, three test sizes are equally placed between the minimum and maximum PV sizes tested. To see how well the polynomial fits the points, its goodness is calculated from [73]

$$g_{nm} = 1 - \frac{\left\|\tilde{\boldsymbol{I}}_{\boldsymbol{F,mnfp}}(\hat{\boldsymbol{I}}_{\boldsymbol{F,mnfp}}) - \hat{\boldsymbol{I}}_{\boldsymbol{F,mnfp}}\right\|^2}{\left\|\hat{\boldsymbol{I}}_{\boldsymbol{F,mnfp}} - \overline{\hat{\boldsymbol{I}}_{\boldsymbol{F,mnfp}}}\right\|^2} \qquad \text{(C.4)}$$

where the bar operator represents the mean. This value will be equal to 1.0 if there is zero error between the curve and the test points. Smaller values of g_{nm} in (C.4) correspond to

worse fits of the polynomial to the PV sizes tested. The majority of fault current changes result in very good fits. A typical fit of measured fault current is shown in Figure C.1. The solid blue line in Figure C.1 represents the third-order fit to the red circles. These circles indicate the fault current measured through Phase C of the substation breaker due to a 1LG fault near the end of a feeder from Chapter 3 and the five sizes of PV placed at the first downstream bus of the breaker. The red dashed line shows the actual currents measured in this phase of the breaker at a granularity of $N_S = 100$ and the black dashed line shows the minimum pick-up current for this phase. Here the estimated change in fault current closely agrees with the actual change in a fraction of the computation time, as is typical.

However, the fit shown in Figure C.1 is not exact ($g \neq 1.0$), meaning the change in current is not perfectly represented by a third-order polynomial. The equations that dictate the physics of how current changes in the network can be represented as quadratic equations or the sum of sinusoids, so a polynomial or sum-of-sines regression should perfectly model this change in current. The change in positive-sequence current under balanced conditions can indeed be represented as a quadratic equation, which discussed in a later section, however, this is not the case for unbalanced faults.

The interaction between cross-impedances, network losses, and the reversal of direction of current flow through non-zero current all play a role in making this change in current much more complex. In fact, the latter situation can be seen in Figure C.1. The current reverses direction at the minimum of the curve, which is non-zero. This is due to the PV system supplying purely real power and at this point, it cancels out the real power being supplied to the fault on this phase, but not the reactive power so a non-zero, purely reactive current exists at this point. The worst scoring fault scenario according to (C.4) found in the circuits tested is shown in Figure C.2. To fit the actual currents in Figure C.2, much higher order polynomial or sum-of-sines models are required, requiring a greater number of PV sizes to be tested.

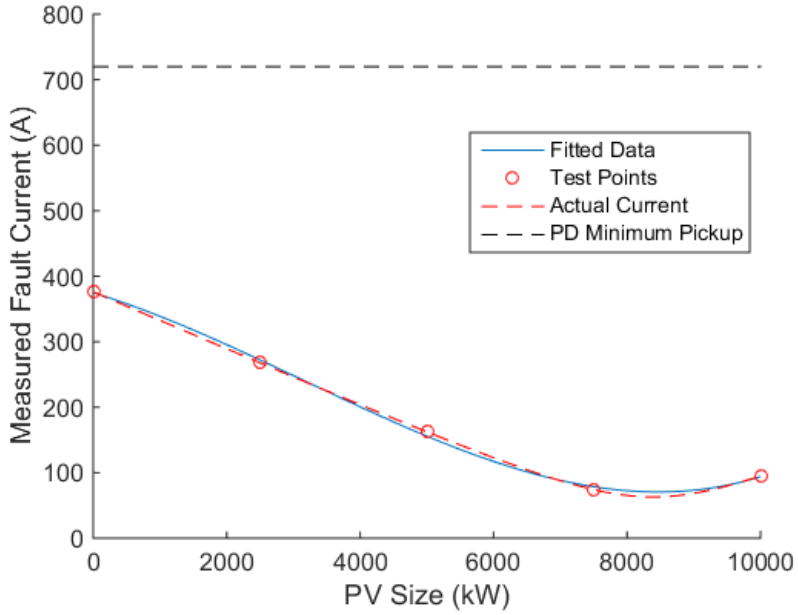

Figure C.1. Third-order polynomial least-squares fit of 1LG fault current through phase C of feeder breaker as a function of PV size resulting in a good fit.

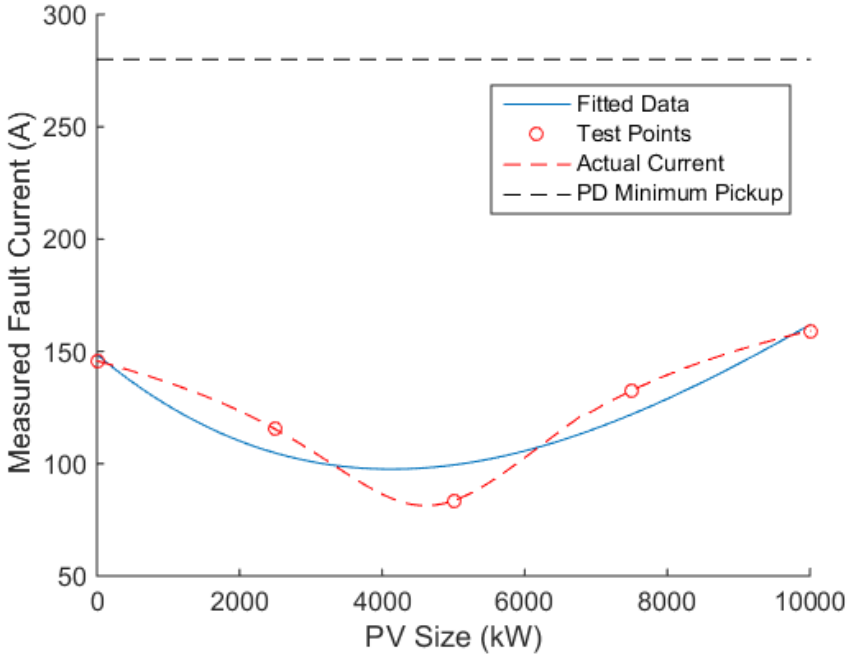

Figure C.2. Third-order fit of 2LG fault current as a function of PV size through phase B of a line recloser that results in a poor fit.

However, the vast majority of fault currents do not show poor fits. Furthermore, of the poor-fitted currents, most are below their PD's minimum trip, as shown in Figure C.2,

meaning there would be no change in protection tripping. For these reasons, a threshold of $g > 0.95$ has been established to weed out changes in current that do not result in good approximations. Any fits below this threshold are kept at their initial fault current with changing PV size by setting their fit coefficients to $\boldsymbol{c_{mnfp}} = [0\ 0\ 0\ c_{mnfp,4}]$. A summary of the quality of current estimations for the feeders presented in this paper is given in Table C.1. The bottom row gives the total number of fault cases tested in each feeder and the other rows represent how many curve fits are rejected for not meeting the minimum goodness of fit threshold. The number of fault current changes that do not meet the minimum fit requirements are insignificant and will not diminish the quality of the research if ignored. The protection analysis for feeder QB1 was not modeled at the time this analysis was conducted.

Table C.1. Summary of percent of fault current change estimations with adequate goodness of fit.

Feeder	QS1	QL1	QL2	QN1	QW1	QB1
Cases g>0.99 (%)	99.9903	99.9999	100	100	99.9495	100
Cases, g>0.95 (%)	99.9986	99.9999	100	100	99.9978	100
Rejected Cases (#)	37	4	0	0	6	0
Total Cases (#)	3.64×10^6	5.31×10^6	1.67×10^5	1.95×10^6	2.73×10^5	0.93×10^5

C.2 Setting the Change in Voltage Tolerance of the Voltage-Dependent Current Source PV-System Model

As discussed in Section 2.3.2, the voltage-dependent current source model of the PV under fault conditions requires an iterative solution to converge to its proper output level. This iterative process stops once the average voltage V_{PCC} at the PCC of the PV changes by less than some given tolerance between one iteration and the next, signaling convergence. The magnitude of this tolerance can have a significant impact on the computation time of the tests since it is directly related to the total number of power flow

solutions required per PV and fault placement. A larger voltage tolerance will reduce the computation time, but at the cost of solution accuracy. The largest problem occurs when the PV model is on the verge of switching to or from the saturated output mode. If the voltage tolerance is large, the switch can result in a discontinuity between PV sizes, which is seen in the dashed red line in Figure C.3. This discontinuity throws off the overall fit.

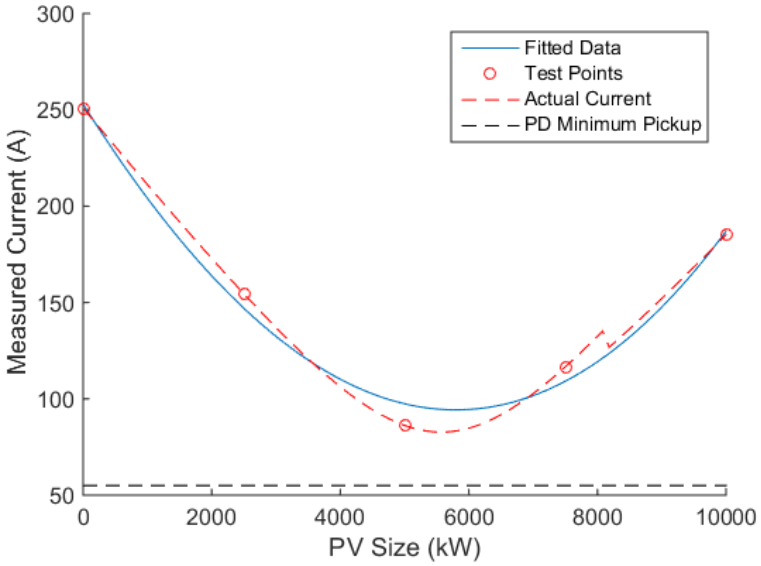

Figure C.3. Poor curve fitting of 1LG fault current measured by a line recloser due to using a PV model with a voltage tolerance setting of of 0.1pu.

The discontinuity in the actual current (red-dashed line) is the result of the PV system model becoming large enough to switch from saturated current mode to voltage-dependent mode once the PV system is large enough to raise V_{PCC} over 0.5pu. A voltage threshold of 0.1 pu is too large of a threshold for the exact size at which this switch occurs to not line up smoothly with the rest of the curve. This throws off all the data points and skews the entire curve fit. If the voltage tolerance is lowered to 0.01 pu the discontinuity disappears resulting in a better current change approximation, as shown in Figure C.4, which demonstrates the same fault current measurement as Figure C.3. Although using the lower voltage tolerance of 0.01 pu increases computation time, it is used in this research to ensure solution accuracy. But, if computation time reduction is absolutely necessary, it may be worth lowering this tolerance to still get an approximation of hosting capacity.

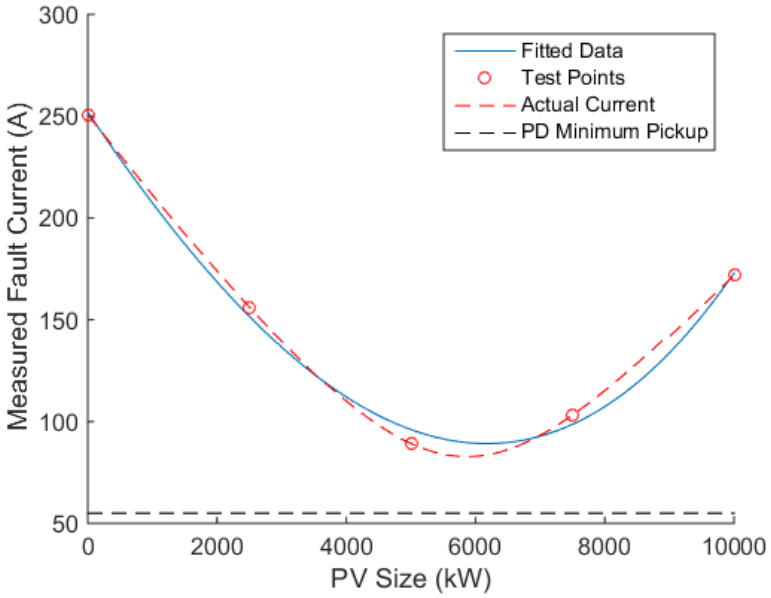

Figure C.4. Improved curve fit due to using a PV model with voltage tolerance of 0.01pu.

C.3 Using Reduced Network Models

The last, but perhaps the most time-saving, approximation is the use of reduced network models. These models provide an equivalent power-flow solution for a subset of buses of interest that are chosen to be kept from the original full network model. Details of the algorithm that produces the accurate reduced models can be found here . For this research, the reduction algorithm [72] keeps all buses with PDs and buses at the feeder ends. A summary of the scale to which the models were reduced in bus count is shown below in Table C.2. The "full model" columns refer to how many buses are originally in the feeder models as they are obtained from the utility and the "reduced model" columns show how many buses remain once the feeder model is reduced. Since the models are unbalanced, there are a greater number of buses with at least one phase, *N1*, than the number of three-phase buses, *N3*.

Table C.2. Summary of bus count reductions using reduced models for the five feeders considered.

Feeder	Full Model N1 Buses	Full Model N3 Buses	Reduced Model N1 Buses	Reduced Model N3 Buses
QS1	600	477	268	222
QL1	1237	550	424	206
QL2	321	226	131	87
QN1	1170	585	284	187
QB1	172	126	70	51
QW1	983	864	54	53

C.4 Summary of Computation Times for Tested Feeders

The scatter plot in Figure C.5 summarizes the computational time it takes to run the full protection analysis of each feeder. All of these times take advantage of each of the approximations laid out in Appendix C. The points are split by the amount of time it takes to estimate how PV changes the current of each fault and then the actual analysis of the impact which the estimated fault currents have on the PDs. The vertical scale is logarithmic, so the increasing nature with respect to number of buses suggests exponential growth in computation time. This is a key reason for the need to reduce the number of buses considered and use reduced order circuit models.

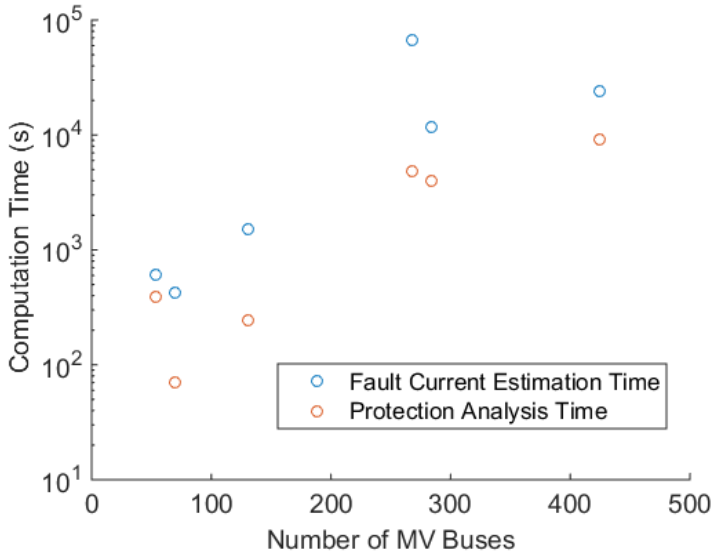

Figure C.5. Computation time for the estimation of fault current change due to PV and protection impact analysis for each feeder based on number of medium voltage buses.

APPENDIX D OTHER FEEDER MODELS TESTED FOR PV-INDUCED PROTECTION ISSUES

This appendix presents the detailed protection issue test results of three other feeder test models.

D.1 Feeder QL2

Feeder QL2 is a very stiff, 12 kV circuit with only one breaker and no reclosers. As such, its protection-limited hosting capacity is only limited by the point at which the reverse current from the PVs causes sympathetic tripping in the breaker when placed anywhere in the network, as shown in Figure D.1. Since all the PV locations pick up the breaker's reverse current on sympathetic tripping at the same size, due to the small size and stiff nature of this circuit, the hosting capacity is uniform at all buses in the network, as seen by the fact that all PV placement locations have the same hosting capacity in Figure D.2.

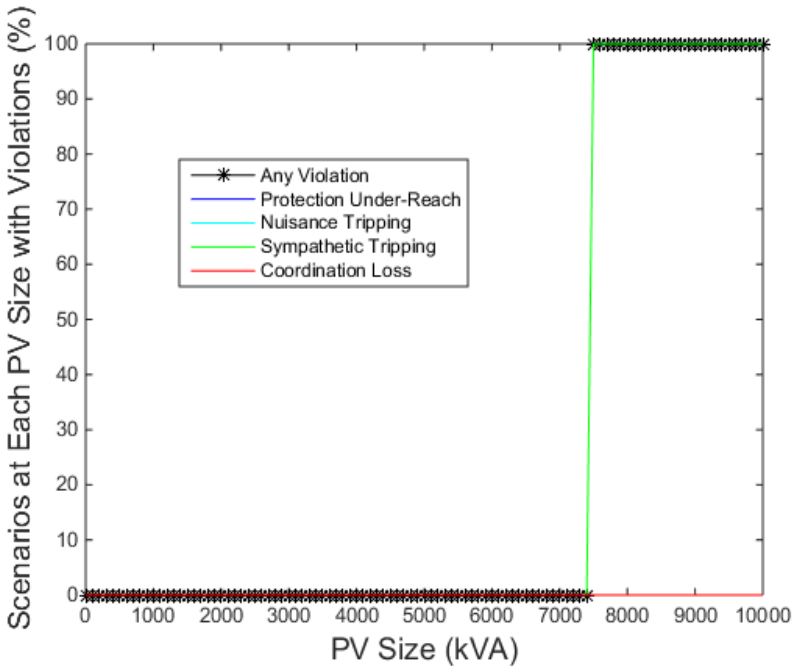

Figure D.1. Feeder QL2 PV installation location protection violation summary.

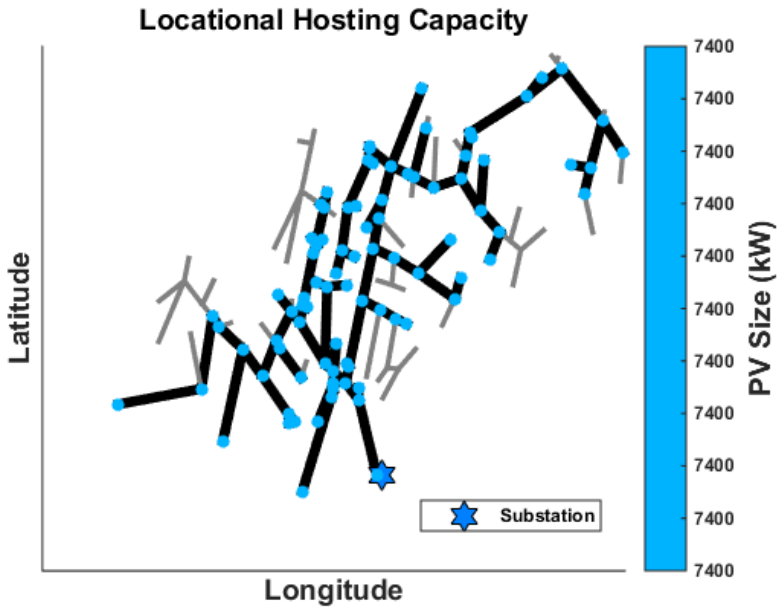

Figure D.2. Maximum PV size allowed at each viable PV placement bus in feeder QL2 due to any protection violation.

D.2 Feeder QN1

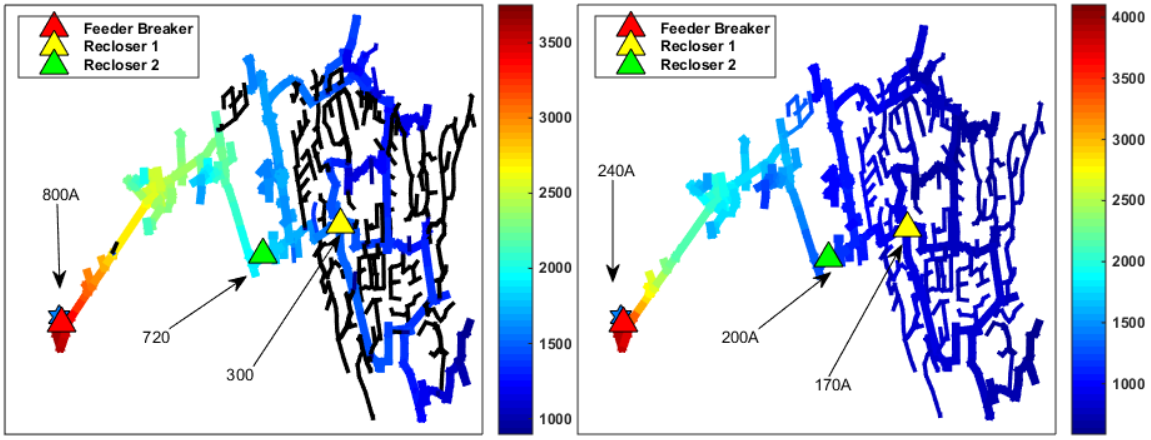

Figure D.3. Feeder QN1 with the breaker and recloser a) minimum phase pickup current, and b) minimum ground pickup current. The lines are colored by the a) phase current for a 3LG fault and b) zero-sequence current for a 1LG fault at the bus.

Feeder QN1 is a 20kV class feeder that has two line reclosers in addition to the substation breaker. It has a peak load of 16.71MW and its furthest bus is 10.3km from the substation. It has no coordination or under-reach issues, indicating its time-current curves (TCCs) are well buffered. It also has no nuisance tripping since its PDs are all in series. This leaves sympathetic tripping as the only issue, as shown in Figure D.4. This figure

shows that at 5.3 MW, a PV interconnection causes sympathetic tripping due to reverse power flow in about 15% of the feeder buses. The manner in which sympathetic tripping limits the allowable size of PV per location is shown in Figure D.5.

The recloser designated Recloser 2 is actually closer to the substation than the other reclosers in the feeder and has a phase pick-up current of 720 A. This is similar to the breaker's phase pick-up current of 800 A, hence the minimal distinction between the buses upstream and solely downstream of Recloser 2. Recloser 1 has a much lower pick-up current at 300 A, which is why its downstream buses are far more limited as to the amount of PV they can host without causing reverse current tripping.

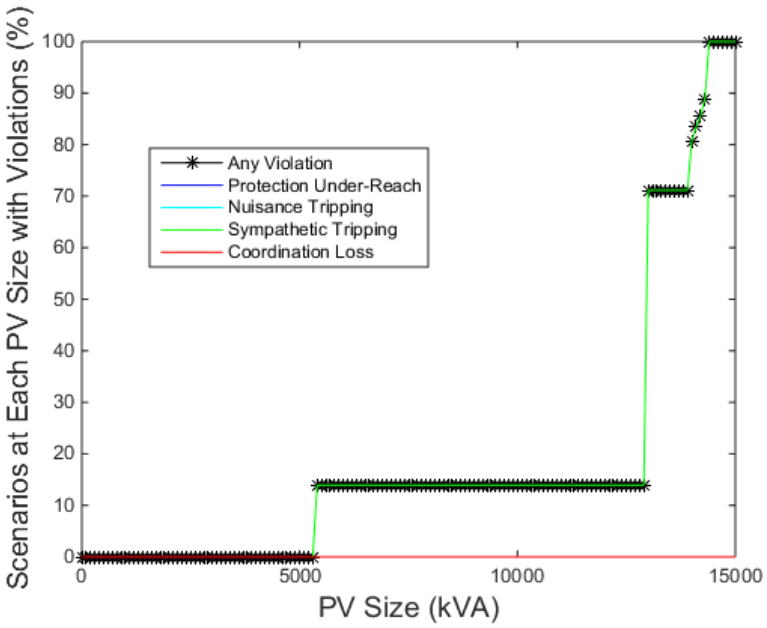

Figure D.4. Feeder QN1 PV installation location protection violation summary.

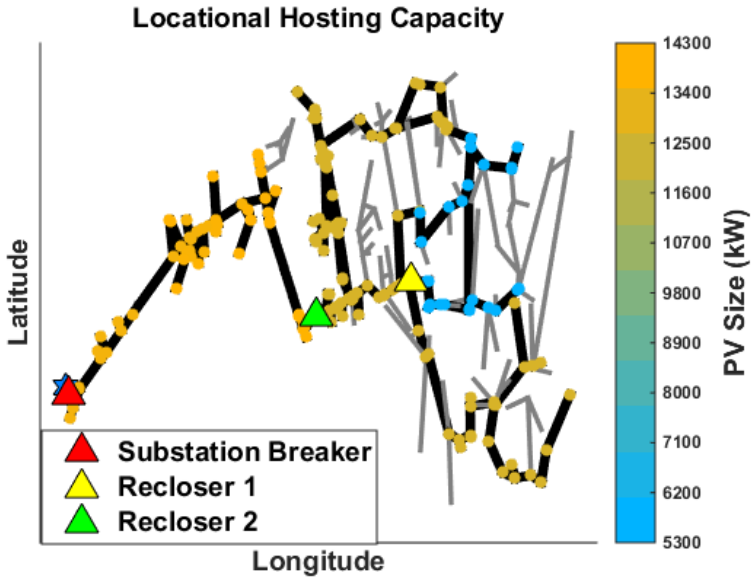

Figure D.5. Maximum PV size allowed at each viable PV placement bus in feeder QN1 due to any protection violation. The PD locations are also indicated.

D.3 Feeder QB1

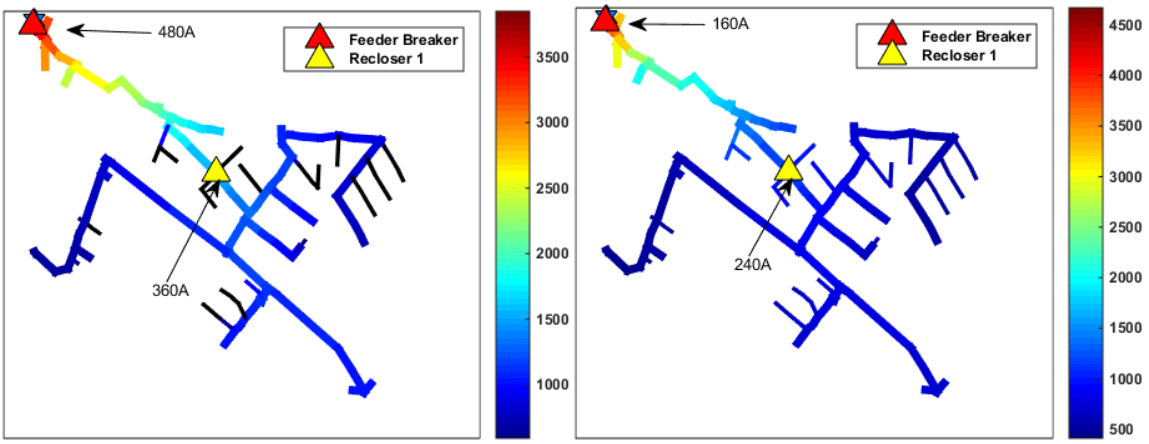

Figure D.6. Feeder QB1 with the breaker and recloser a) minimum phase pickup current, and b) minimum ground pickup current. The lines are colored by the a) phase current for a 3LG fault and b) zero-sequence current for a 1LG fault at the bus.

Feeder QB1 is a 4 kV feeder with one recloser in addition to the substation breaker. It has a peak load of 2.21 MW and the furthest bus is 2.8km from the substation. The location of the recloser in the feeder relative to the substation breaker is shown in Figure D.7, which also indicates the protection zones of the PDs by corresponding colors. Due to the much

lower voltage rating of this feeder, PV sizes are only tested up to 5 MW, and the size of PV that first causes an issue is 1.3 MW. As with the other feeders, the limiting issue is sympathetic tripping due to reverse current through the recloser, as shown in Figure D.8. In this figure, the red line indicates coordination does become a problem eventually, but not until after sympathetic tripping is already the PV size limiting factor. The coordination problems begin at PV installations of 1.8 MW. This is due to the fact that the TCCs of the ground current relays of the breaker and recloser intersect. As discussed in Section 5.1, this issue can be mitigated by redesigning the TCCs such that they do not intersect. There is no point in correcting it for this feeder since all PV locations are limited by sympathetic tripping. The split in locational hosting capacity levels of buses upstream versus downstream of the recloser is represented in Figure D.9 as a region of blue buses and a region of orange. The two hosting capacity zones correspond directly to the protection zones shown in Figure D.7. The difference in the average hosting capacities of these two regions is based primarily on the minimum pick-up levels of their upstream PD. However, as discussed before, a slightly larger PV can be placed towards the end of the feeder without picking up sympathetic tripping due to the PV being further from the upstream fault.

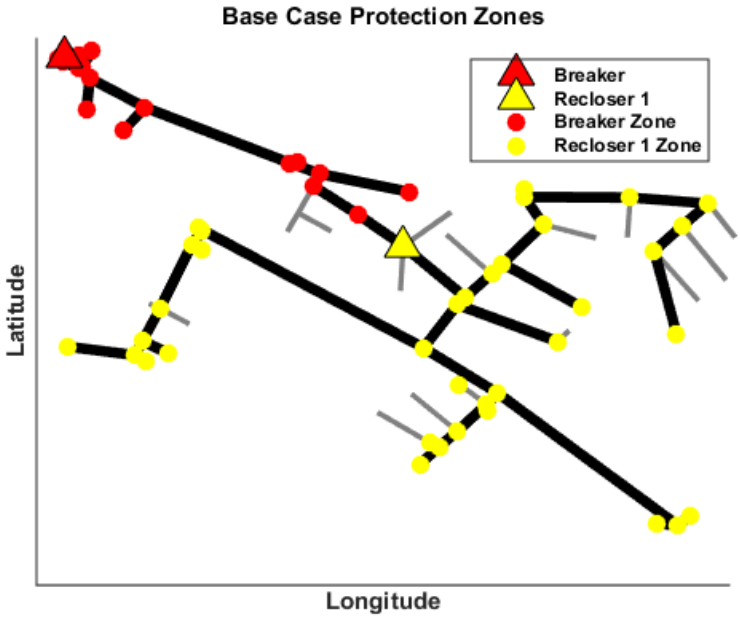

Figure D.7. Feeder QB1 baseline protection zones with no PV.

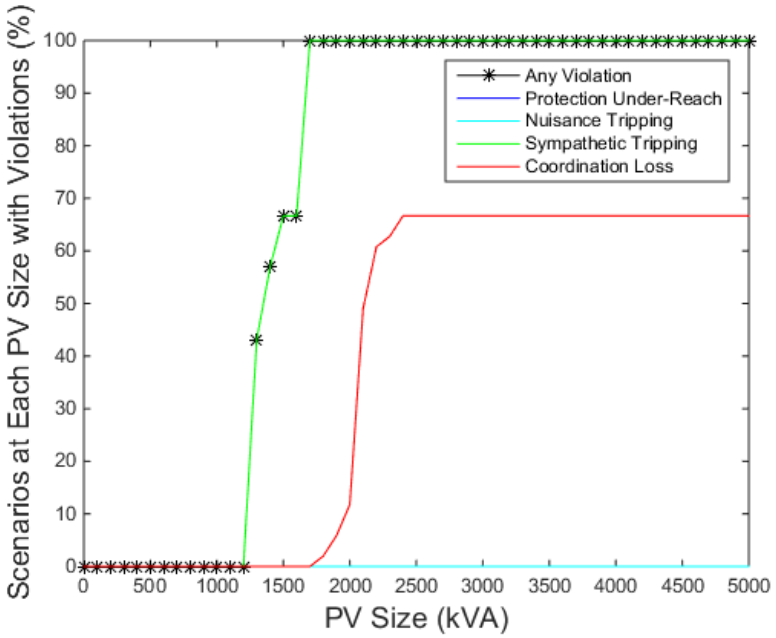

Figure D.8. Feeder QN1 PV installation location protection violation summary.

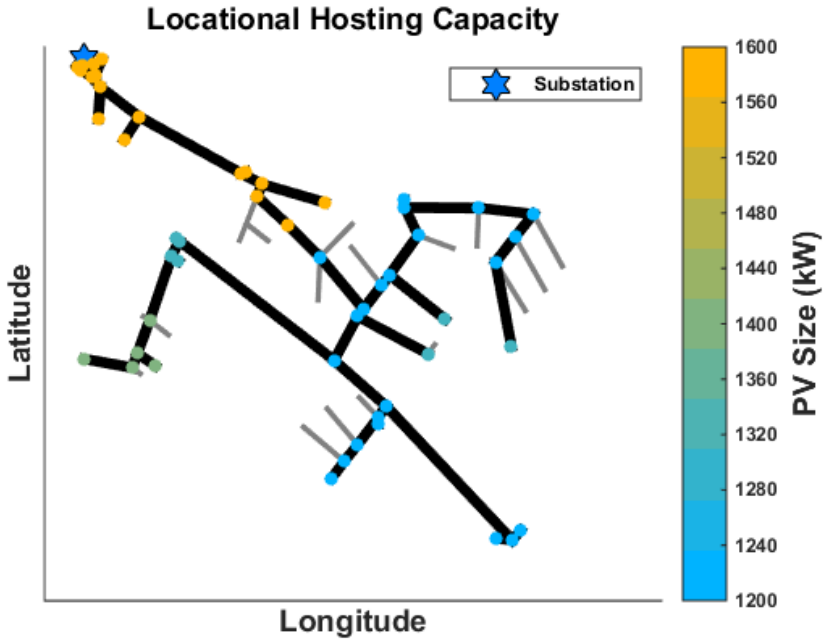

Figure D.9. Maximum PV size allowed at each viable PV placement bus in feeder QB1 due to any protection violation.

APPENDIX E GRAPH THEORY FOR DISTRIBUTION PROTECTION

A distribution network can be thought of as a series of nodes where loads, generation, or utility equipment can be connected. The topology of the network is defined by how the distribution lines connect the nodes. In a traditional radial distribution network, the network topology is a tree with one root starting at the transmission network. For example, the one-line diagram of a small radial distribution network is shown in Figure E.1. The network source is depicted as the hashed square to the far left. All nodes are "downstream" of the network source in a hierarchy or tree topology. Cycles, or nodes that form a loop, are not considered in this research.

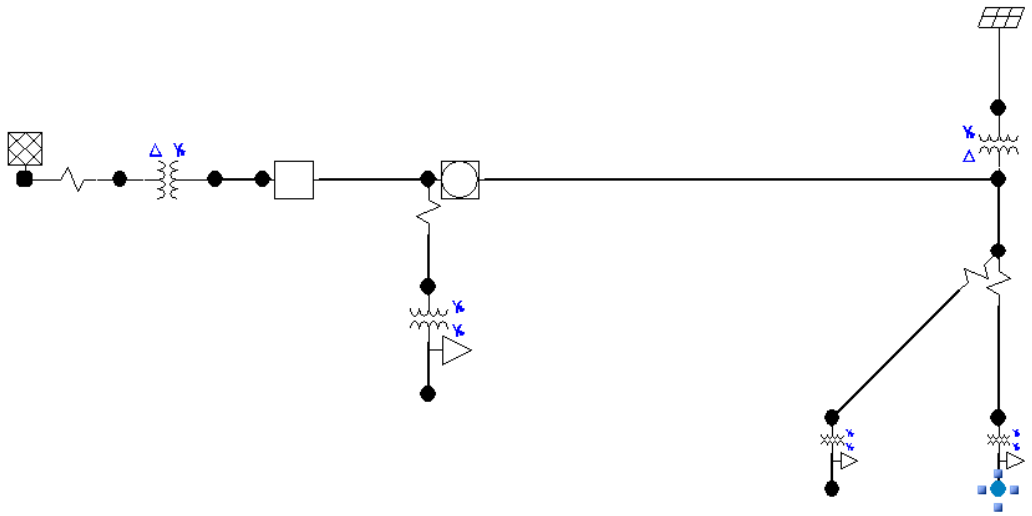

Figure E.1. Example radial distribution network.

Moreover, each piece of equipment, or item, in the network is connected in a tree topology as well. For example, in the example network in Figure E.1, there is a fuse downstream of the source, then a transformer, then a section of line, etc. Each item has exactly one item upstream of it, except the source, which has zero. These connection relationships can be visualized using the Matlab *treeplot* function, as shown in Figure E.2. This plot shows the order in which each item in the example network is connected to other items, starting at the top with the network source. This is the graphical representation of

the network item graph $\mathcal{G}_i$, where the nodes of the graph are the network items i. Using the knowledge that a single source exists in the network, the directed item graph $\mathcal{D}_i$ can be constructed by assigning a direction to each item connection. The set of edges E for the directed graph are only the ordered pairs of items (i_n, i_m) where i_n is upstream of i_m. This direction simply indicates that an item is downstream of another with respect to the network source, not the direction of current flow.

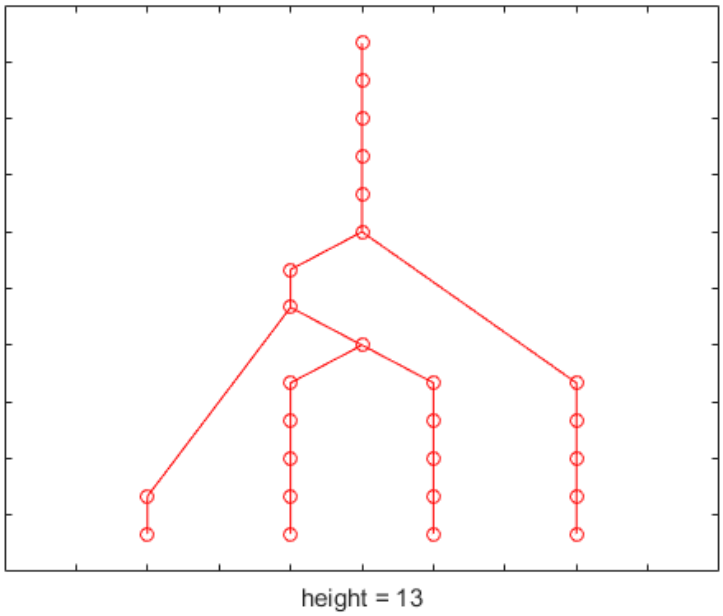

Figure E.2. Visualization of example network's item topology.

The connection relationship between items can also be represented in matrix form. The adjacency matrix [74] of the directed item graph, $A(\mathcal{D}_i)$, is defined as:

$$A(\mathcal{D}_i) = [a_{nm}], \qquad where\ a_{nm} = \begin{cases} 1, & if\ (i_n, i_m) \in E_i \\ 0, & otherwise \end{cases} \tag{E.1}$$

The adjacency matrix for a radial network is typically sparse. The adjacency matrix for the example network in Figure E.1 is visualized as a sparse matrix in Figure E.3(a) where a dot represents a matrix entry with a value. Each row in this matrix indicates which items are downstream of the item number corresponding to that row. The item numbers may be indexed arbitrarily. This matrix alone is not very useful for determining item relations beyond an item's immediate neighbor. However, it can be used to create a *path matrix*, $P(\mathcal{D}_i)$, with the following manipulation:

$$P(\mathcal{D}_i) = \left(I_N - A(\mathcal{D}_i)\right)^{-1} - I_N \tag{E.2}$$

The path matrix of the example network is visualized in Figure E.3(b). Each row in the path matrix, $\boldsymbol{p_{r,n}} \coloneqq \boldsymbol{row_n}(P(\mathcal{D}_i))$, has a 1 in the column of an item that is downstream of the item corresponding to that row. Also, each column in the path matrix, $\boldsymbol{p_{c,n}} \coloneqq \boldsymbol{col_n}(P(\mathcal{D}_i))$, has a 1 in the row of an item upstream of the item corresponding to that column. Therefore, an item's *rank* in the tree can be defined by how many items are upstream of it. The vector of integer ranks for all N items in the network is then the summation of the rows of the path matrix:

$$R(\mathcal{D}_i) = \sum_{n=1}^{N} P(\mathcal{D}_i)\,, \ni \mathbb{Z}^N \tag{E.3}$$

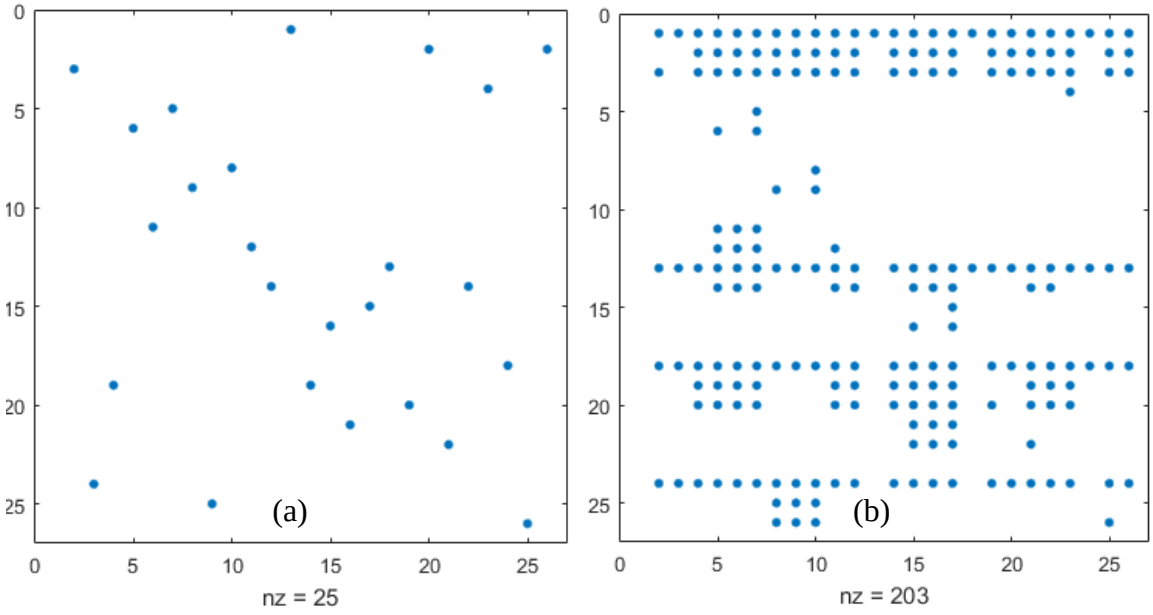

Figure E.3. (a) Adjacency matrix of example network. (b) Path matrix of example network.

With the path matrix and rank vector of the items in a network, relationships between items across the network can be quickly derived. These tools are useful in both setting network protection and validating that the correct device operated. For traditional overcurrent protection in radial networks, a protection device's zone is the section of network between it and the next protection device. If i_n is a protection device upstream of the set of protection devices $\boldsymbol{I}$, the protection zone of i_n is:

$$Z(i_n) = [\boldsymbol{p_{rn}} \setminus \boldsymbol{p_{rm}}] \forall i_m \in \boldsymbol{I} \tag{E.4}$$

In E.4, the operator '\' is the complement operator, meaning the zone of i_n is the set of items unique to the items downstream of i_n and not downstream of any i_m. If a protection device operates for a faulted item outside of that protection device's zone it is an invalid operation.

This organization is particularly useful for analyzing networks with multiple sources. If a network has *S* fault current contributing sources, then *S* directed item graphs, $\mathcal{D}_i$, may be created for that network using each source as a root. Network items exist in multiple graphs if the sources are connected through the network.

The connection topology of any subset of items can be determined from the path matrix as well. For example, it is of interest to know the connection hierarchy from a source of all protection devices $\boldsymbol{I}$ to validate coordinated tripping. Simply index the rows and columns of the path matrix that correspond to the subset of protection devices $\boldsymbol{I}$ to get the path matrix between those devices, $P_{\boldsymbol{I}}$. The rank of the subset of items is again found using E.3. When coordinating protection devices, protection curves are set to operate slower than the next downstream devices. These are the devices that are one rank higher than the device being set in the subset of protection items.

The tools laid out in this appendix have even more applications beyond the examples given. These tools are very useful in keeping track of the relationships between items in increasingly complex networks with multiple sources. Even for arbitrarily large networks, these methods scale well since the adjacency matrix is sparse and can be used to derive the other matrices and vectors as needed.

APPENDIX F EXAMPLE SIMULATIONS OF ADVANCED INVERTER CONTROLS

This appendix presents time-series examples of the advanced inverter controls tested in Chapter 4 to validate their proper steady-state control response for given parameters.

F.1 Ramp-Rate Control Example

The first control type is simply limiting the up-ramp of the PV system's real-power output to smooth out larger variability. The application of this control is shown below in Figure F.1. The top-left plot shows PV PCC voltage per-phase over a one-week period versus ANSI limits with ramp-rate limiting control active. The bottom-left plot shows the PV system output power. The right plot is a zoomed-in section of the left to make the control action clearer.

In the left plot of Figure F.1, the PV system is outputting less power than its base case on the cloudy days with large irradiance variability. However, the power output is smoother which makes the voltage less variable. The ramp-rate was set to limit the PV system to increase 0.4 P_{pu}/h, or 400 kW/hr (40% of its 1 MW rating). Zooming in on a period of high ramping in the right plot, it is shown that this control is indeed limiting the power output increases by the correct amount. Another example is provided in Figure F.2 at a ramp-rate limit of $0.1P_{pu}/h$, which shows the up-ramp of the PV limited to the correct amount of 100kW in a one-hour time period for the 1MW system. Here it is more clear that the down-ramp is not limited by this control, which physically makes sense. The fastest transients in the irradiance profile used will increase the output of the PV system by 0.5 pu in one minute, or 30 P_{pu}/h. Any ramp-rate settings above this value would have no effect.

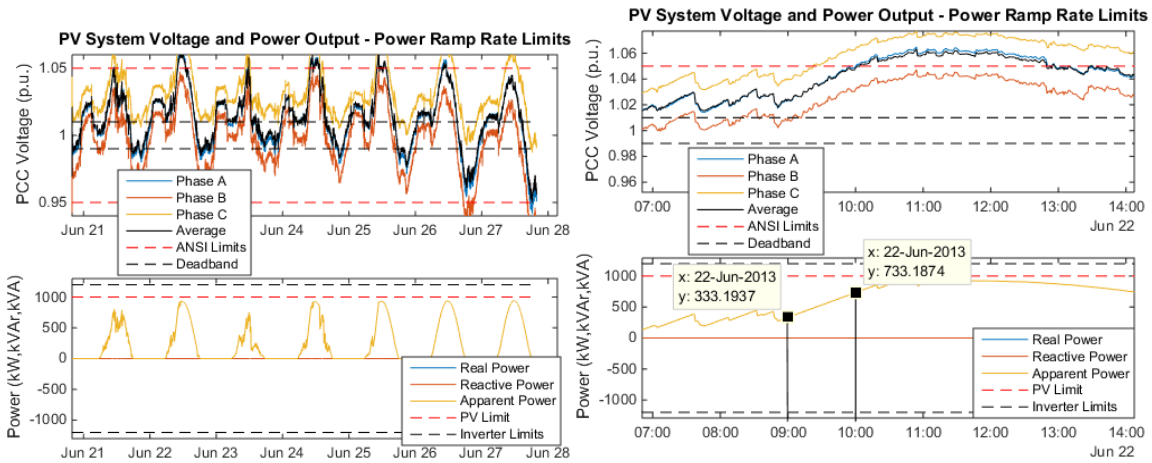

Figure F.1.(left) Power ramp-rate limiting applied to the PV inverter. (right) A zoomed-in segment of time showing ramp limiting.

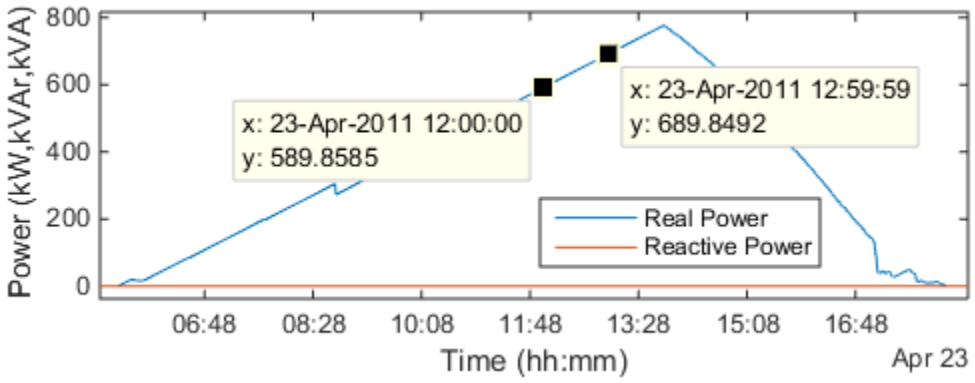

Figure F.2. Single day of PV power output with a ramp-rate limit set to $0.1P_{pu}/h$.

F.2 Volt/Var Control Example

The next two plots in Figure F.3 demonstrate the two options for performing Volt/Var control. In the left plot, the control is limited by the real power output of the PV system, while in the right plot the real power output is curtailed to prioritize the reactive power control.

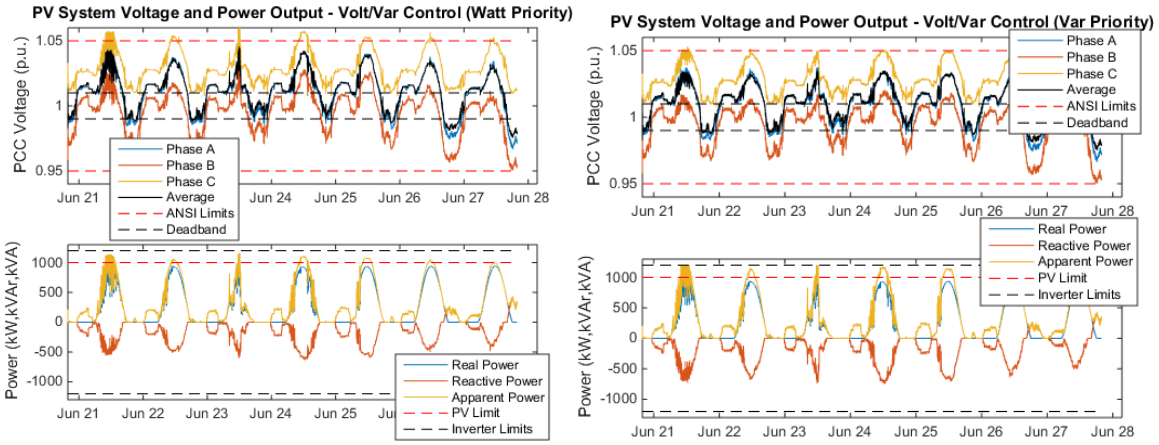

Figure F.3. 1MW, 1.2MVA PV system with (left) Watt-priority Volt/Var control and (right) Var-priority Volt/Var control.

Although the reactive power generated due to Watt-priority Volt/Var on the left is less than Var-prioirty on the right in Figure F.3, there is not a clear "prioritization" of reactive power in the Var-priority control evident by real power curtailment. To further demonstrate the functionality of the Var-priority control, since it is programmed in Matlab, a Volt/Var curve that attempts to regulate the voltage to 0.95 pu is applied. This case is shown in Figure F.4 below. The control now saturates at the inverter limits and completely curtails the real power output in the times where it cannot achieve the desired 0.95 pu voltage. This validates the desired behavior of the control.

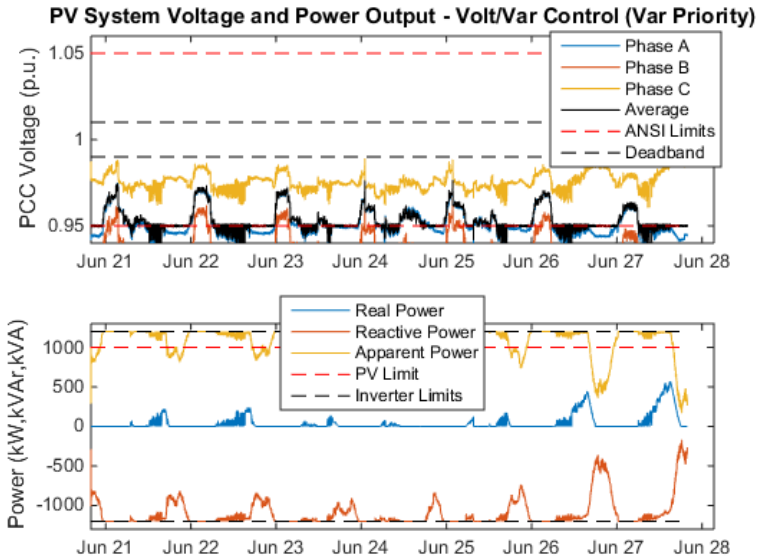

Figure F.4. Var-priority Volt/Var control attempting to regulate average voltage to 0.95p.u.

F.3 Power Factor Control Examples

The fixed and watt-triggered power factor controls are shown in Figure F.5. The fixed power factor control is set at 0.95 lagging and the watt-triggered power factor ranges from 0.98 lagging at zero PV output to 0.70 lagging at full PV output. The red curves of the bottom plots show the vars absorbed by the two control types. The watt-triggered power factor produces more vars than the fixed power factor since it changes as needed, but ultimately the control is still limited by the rating of the inverter, as shown by the yellow apparent power output in the right plot hitting the black dashed inverter rating limit.

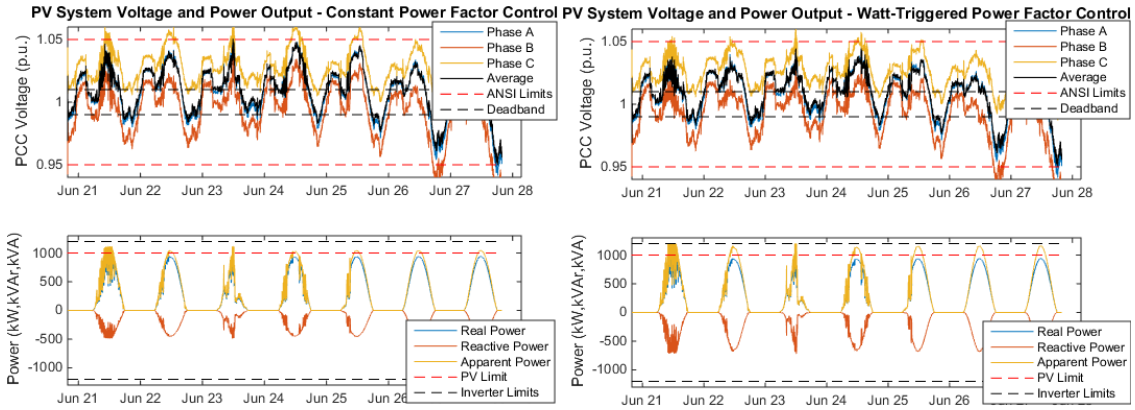

Figure F.5. (left) Fixed power factor control at 0.95 lagging. (right) Watt-triggered power-factor control from 0.98-0.7 lagging.

F.4 Volt/Watt Control Examples

The Volt/Watt control that curtails the real power output of the PV system based on the local measured voltage is demonstrated in Figure F.6. In this instance, the curtailing only begins past the 1.05p.u. voltage violation. Slightly less power is produced with this control type at times when the voltage deviates outside the ANSI limits, resulting in a slightly smaller over-voltage deviation between Figure F.6 and the right-hand plot of Figure 4.3. The fact that voltage violations still exist with the control shown here means that more aggressive curtailment is necessary with this control type to bring the voltages within the ANSI limits.

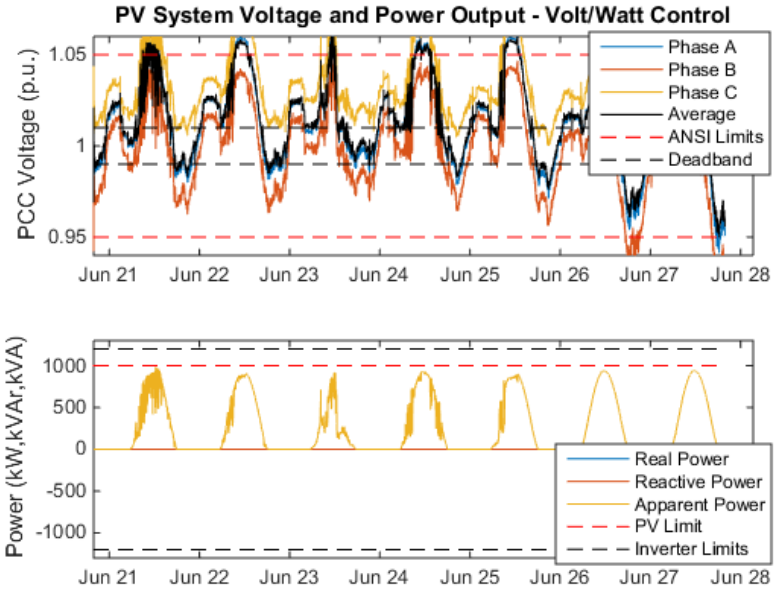

Figure F.6. Volt/Watt PV curtailing control.

REFERENCES

[1] D. Gauntlett and M. Lawrence, "Distributed Solar Energy Generation: Market Drivers and Barriers, Technology Trends, and Global Market Forecasts," Navigant Research, Report DSEG-15, 2013.

[2] J. A. P. Lopes, N. Hatziargyriou, J. Mutale, P. Djapic, and N. Jenkins, "Integrating distributed generation into electric power systems: A review of drivers, challenges, and opportunities," *Electric Power Systems Research,* vol. 77, pp. 1189-1203, 2007.

[3] C. Whitaker, J. Newmiller, M. Ropp, and B. Norris, "Distributed Photovoltaic Systems Design and Technology Requirements," Sandia National Laboratories, SAND2008-0946, 2008.

[4] R. A. Walling, R. Saint, R. C. Dugan, J. Burke, and L. A. Kojovic, "Summary of Distributed Resources Impact on Power Delivery Systems," *IEEE Transactions on Power Delivery,* vol. 23, pp. 1636-1644, 2008.

[5] F. Shahnia, R. Majumder, A. Ghosh, G. Ledwich, and F. Zare, "Voltage imbalance analysis in residential low voltage distribution networks," *Electric Power Systems Research,* vol. 81, pp. 1805-1814, 2011.

[6] C. Li, J. Savulak, and R. Reinmuller, "Unintentional Islanding of Distributed Generation - Operating Experiences from Naturally Occurred Events," *IEEE Transactions on Power Delivery,* vol. 29, pp. 269-274, 2014.

[7] A. S. Masoum, P. S. Moses, Mohammad, and A. Abu-Siada, "Impact of Rooftop PV Generation on Distribution Transformer and Voltage Profile of Residential and Commercial Networks," presented at the IEEE PES Innovative Smart Grid Technologies Conference, Washington, DC, Jan. 16-20, 2012.

[8] H. Ravindra, M. O. Faruque, P. McLaren, K. Schoder, M. Steurer, and R. Meeker, "Impact of PV on Distribution Protection System," presented at the North American Power Symposium, Champaign, IL, Sep. 9-12, 2012.

[9] IEEE, "IEEE Standard for Interconnecting Distributed Resources with Electric Power Systems," in *Amendment 1* vol. 1547a, ed. New York, NY: IEEE, 2014.

[10] G. Dötter, F. Ackermann, N. Bihler, R. Grab, S. Rogalla and R. Singer, "Stable operation of PV plants to achieve fault ride through capability - Evaluation in field and laboratory tests," *2014 IEEE 5th International Symposium on Power Electronics for Distributed Generation Systems (PEDG),* Galway, 2014, pp. 1-8.

[11] J. von Appen, T. Stetz, M. Braun and A. Schmiegel, "Local Voltage Control Strategies for PV Storage Systems in Distribution Grids," in *IEEE Transactions on Smart Grid*, vol. 5, no. 2, pp. 1002-1009, March 2014.

[12] B. Idlbi, A. Scheidler, T. Stetz and M. Braun, "Preemptive network reinforcement at LV level considering uncertainty in prediction of PV penetration scenarios," *2015 IEEE Eindhoven PowerTech Conference*, Eindhoven, 2015, pp. 1-6.

[13] R. Moghe, D. Tholomier, D. Divan, J. Schatz and D. Lewis, "Grid Edge Control: A new approach for volt-var optimization," *2016 IEEE/PES Transmission and Distribution Conference and Exposition (T&D)*, Dallas, TX, USA, 2016, pp. 1-5.

[14] B. Lundstrom, M. Shirazi, M. Coddington, and B. Kroposki, "An Advanced Platform for Development and Evaluation of Grid Interconnection Systems Using Hardware-in-the-Loop: Part III - Grid Interconnection System Evaluator," presented at the 2013 IEEE Green Technologies Conference, Denver, CO, April 4-5, 2013.

[15] *Revisions to Form, Procedures, and Criteria for Certification of Qualifying Facility Status for a Small Power Production or Cogeneration Facility,* FERC, Order No. 732, 2010.

[16] G. J. Shirek and B. A. Lassiter, "Photovoltaic Power Generation", in *IEEE Industry Applications Magazine*, vol. 19, no. 4, pp. 63-72, July-Aug. 2013.

[17] M. Rylander, J. Smith, D. Lewis, and S. Steffel, "Voltage impacts from distributed photovoltaics on two distribution feeders," presented at the IEEE Power and Energy Society Generation Meeting (PES), Vancourver, BC, July 21-25, 2013.

[18] A. Ballanti, F. Pilo, A. Navarro-Espinosa, and L. F. Ochoa, "Assessing the Benefits of PV Var Absorption on the Hosting Capacity of LV Feeders," presented at the 4th IEEE/PES Innovative Smart Grid Technologies Europe (SGT EUROPE), Copenhagen, Denmark, Oct. 6-9, 2013.

[19] A. Navarro, L. F. Ochoa, P. Mancarella, and D. Randles, "Impacts of photovoltaics on low voltage networks: A case study of North West of England," presented at the 22nd International Conference and Exhibition on Electricity Distribution (CIRED 2013), Stockholm, Sweden, June 10-13, 2013.

[20] R. K. Varma, J. Berge, I. Axente, V. Sharma, and K. Walsh, "Determination of Maximum PV Solar System Connectivity in a Utility Distribution Feeder," presented at the IEEE PES Transmission and Distribution Conference and Exposition (T&D), Orlando, FL, May 7-10, 2012.

[21] J. Keller, B. Kroposki, R. Bravo, and S. Robles, "Fault Current Contribution from Single-Phase PV Inverters," presented at the 37th IEEE Photovoltaic Specialists Conference (PVSC), Seattle, WA, June 19-24, 2011.

[22] R. Yan and T. K. Saha, "Investigation of Voltage Variations in Unbalanced Distribution Systems due to High Photovoltaic Penetrations," presented at the IEEE Power and Energy Society General Meeting, Detroit, MI, July 24-28, 2011.

[23] M. E. Baran, H. Hooshyar, S. Zhan, and A. Huang, "Accommodating High PV Penetration on Distribution Feeders," *Smart Grid, IEEE Transactions on*, vol. 3, pp. 1039-1046, 2012.

[24] H. Hooshyar and M. E. Baran, "Fault Analysis on Distribution Feeders with High Penetration of PV Systems," *IEEE Transactions on Power Systems*, vol. 28, pp. 2890-2896, August, 2013 2013.

[25] H. Hooshyar, M. E. Baran, and L. Vanfretti, "Coordination assessment of overcurrent relays in distribution feeders with high penetration of PV systems," presented at the IEEE PowerTech (POWERTECH), Grenoble, France, June 16-20, 2013.

[26] "Americal National Standard for Electric Power Systems and Equipment," in *Voltage Ratings* vol. ANSI C84.1-1995, ed. Rosslyn, Virginia: National Electrical Manufacturers Association, 1996.

[27] P. Kundur, *Power System Stability and Control*. New York: McGraw-Hill, 1994.

[28] W. H. Kersting, *Distribution System Modeling and Analysis*, 2nd Edition, Boca Raton, FL: CRC Press, 2007.

[29] J. J. Grainger and S. Civanlar, "Volt/Var Control on Distribution Systems with Lateral Branches Using Shunt Capacitors and Voltage Regulators, Part 1: The Overall Problem," *IEEE Transactions on Power Apparatus and Systems*, vol. PAS-104, pp. 3278-3283, November, 1985.

[30] M. E. Baran and F. F. Wu, "Optimal Capacitor Placement on Radial Distribution Systems," *IEEE Transactions on Power Delivery*, vol. 4, pp. 725-734, January, 1989.

[31] I. Ziari, G. Ledwich, and A. Ghosh, "Optimal voltage support mechanisms in distribution networks," *IET Generation, Transmission, and Distribution*, vol. 5, pp. 127-135, Sep. 2010.

[32] Y. Hen-Geul, D. F. Gayme, and S. H. Low, "Adaptive VAR Control for Distribution Circuits With Photovoltaic Generators," *IEEE Transactions on Power Systems*, vol. 27, pp. 1656-1663, 2012.

[33] C. Demoulias, "A new simple analytical method for calculating the optimum inverter size in grid-connected PV plants," *Electric Power Systems Research,* vol. 80, pp. 1197-1204, March, 2010.

[34] K. Turitsyn, P. Sulc, S. Backhaus, and M. Chertkov, "Options for Control of Reactive Power by Distributed Photovoltaic Generators," *Proceedings of the IEEE,* vol. 99, pp. 1063-1073, June 2011.

[35] H. Xin, Z. Qu, J. Seuss, and A. Maknouninejad, "A Self-Organizing Strategy for Power Flow Control of Photovoltaic Generators in a Distribution Network," *IEEE Transactions on Power Systems,* vol. 26, pp. 1462-1473, August, 2011.

[36] A. P. S. Meliopoulos, E. Polymeneas, Z. Tan, R. Huang, and D. Zhao, "Advanced Distribution Management System," *IEEE Transactions on Smart Grid,* vol. 4, pp. 2109-2117, December 2013.

[37] A. Bonfiglio, M. Brignone, F. Delfino, and R. Procopio, "Optimal Control and Operation of Grid-Connected Photovoltaic Production Units for Voltage Support in Medium-Voltage Networks," *IEEE Transactions on Sustainable Energy,* vol. 5, pp. 254-263, 2014.

[38] K. Turitsyn, P. Sulc, S. Backhaus, and M. Chertkov, "Distributed control of reactive power flow in a radial distribution circuit with high photovoltaic penetration," presented at the 2010 Power and Energy Society General Meeting, Minneapolis, MN, July 25-29, 2010.

[39] M. Farivar, C. R. Clarke, S. H. Low, and K. M. Chandy, "Inverter VAR Control for Distribution Systems with Renewables," presented at the IEEE Smart Grid Communications (SmartGridComm) Conference, Brussels, Belgium, Oct. 17-20 2011.

[40] R. A. Jabr, "Minimum loss operation of distribution networks with photovoltaic generation," *IET Renewable Power Generation,* vol. 8, pp. 33-44, 2014.

[41] E. Dall'Anese, S. V. Dhople, and G. B. Giannakis, "Optimal Dispatch of Photovoltaic Inverters in Residential Distribution Systems," *IEEE Transactions on Sustainable Energy,* vol. 5, pp. 487-497, 2014.

[42] M. Farivar, R. Neal, C. Clarke, and S. Low, "Optimal inverter VAR control in distribution systems with high PV penetration," presented at the IEEE Power and Energy Society General Meeting, San Diego, CA, July 22-26, 2012.

[43] X. Su and P. Wolfs, "Comprehensive Optimization of PV Inverter Reactive and Real Power Flows in Unbalanced Four Wire LV Distribution Network Operations," presented at the IEEE Power and Energy Society General Meeting, Vancouver, BC, July 21-25, 2013.

[44] J. Jung, A. Onen, R. Arghandeh, and R. P. Broadwater, "Coordinated control of automated devices and photovoltaic generators for voltage rise mitigation in power distribution circuites," *Renewable Energy,* vol. 66, pp. 532-540, 2014.

[45] Y. P. Agalgaonkar, B. C. Pal, and R. A. Jabr, "Distribution Voltage Control Considering the Impact of PV Generation on Tap Changers and Autonomous Regulators," *IEEE Transactions on Power Systems,* vol. 29, pp. 182-192, 2014.

[46] B. Seal, "Standard Language Protocols for Photovoltaics and Storage Grid Integration," EPRI, Report No. 1020906, May 14, 2010.

[47] M. J. Reno, R. J. Broderick, and S. Grijalva, "Smart inverter capabilities for mitigating over-voltage on distribution systems with high penetrations of PV," presented at the IEEE 39th Photovoltaic Specialists Conference (PVSC), Tampa Bay, FL, June 16-21, 2013.

[48] J. Smith, M. Rylander, and H. Li, "Determining Recommended Settings for Smart Inverters," in *Sandia/EPRI 2014 PV Systems Symposium,* Santa Clara, CA, May 5, 2014.

[49] I. Kim, R. G. Harley, R. Regassa, and Y. D. Valle, "The effect of the volt/var control of photovoltaic systems on the time-series steady-state analysis of a distribution network," in *Clemson University Power Systems Conference (PSC),* pp. 1-6, Clemson, SC, Mar. 10-13, 2015.

[50] I. Kim, R. G. Harley, and R. Regassa, "The investigation of the maximum effect of the Volt/Var control of distributed generation on voltage regulation," in *IEEE 42nd Photovoltaic Specialist Conference (PVSC),* pp. 1-6, New Orleans, LA, June 14-19, 2015.

[51] J. W. Smith, W. Sunderman, R. Dugan, and B. Seal, "Smart inverter volt/var control functions for high penetration of PV on distribution systems," presented at the IEEE/PES Power Systems Conference and Exposition (PSCE), Phoenix, AZ, Mar. 20-23, 2011.

[52] Z. Ziadi, A. Yona, T. Senjyu, M. Abdel-Akher, and T. Funabashi, "Real time voltage control of unbalanced distribution systems with photovoltaic generation," presented at the International Conference on Renewable Energy Research and Applications (ICRERA), Nagasaki, Japan, Nov. 11-14, 2012.

[53] K. Turitsyn, P. Sulc, S. Backhaus, and M. Chertkov, "Local Control of Reactive Power by Distributed Photovoltaic Generators," presented at the IEEE Smart Grid Communications (SmartGridComm) Conference, Gaithersburg, MD, Oct. 4-6, 2010.

[54] J. Smith and H. Li, "Potential Interaction Between Smart Inverters," in *Sandia/EPRI 2014 PV Symposium*, Santa Clara, CA, May 5, 2014.

[55] P. Jahangiri and D. C. Aliprantis, "Distributed Volt/VAr Control by PV Inverters," *Power Systems, IEEE Transactions on*, vol. 28, pp. 3429-3439, 2013.

[56] M. M. Zavlanos, M. B. Egerstedt, and G. J. Pappas, "Graph-theoretic connectivity control of mobile robot networks," *Proceedings of the IEEE*, vol. 99, pp. 1525-1540, 2011.

[57] Z. Qu, *Cooperative Control of Dynamical Systems: Applications to Autonomous Vehicles*. London: Springer Verlag, 2009.

[58] H. Xin, Z. Lu, Z. Qu, D. Gan, and D. Qi, "Cooperative control strategy for multiple photovoltaic generators in distribution networks," *IET Control Theory & Applications*, vol. 5, pp. 1617-1629, 2011.

[59] X. Huanhai, Z. Meidan, J. Seuss, W. Zhen, and G. Deqiang, "A Real-Time Power Allocation Algorithm and its Communication Optimization for Geographically Dispersed Energy Storage Systems," *IEEE Transactions on Power Systems*, vol. 28, pp. 4732-4741, 2013.

[60] Z. Ziang and C. Mo-Yuen, "Convergence Analysis of the Incremental Cost Consensus Algorithm Under Different Communication Network Topologies in a Smart Grid," *IEEE Transactions on Power Systems*, vol. 27, pp. 1761-1768, 2012.

[61] E. M. M. S. V. Gevorgian, "User Guide for PV Dynamic Model Simulation Written on PSCAD Platform," NREL, NREL/TP-5D00-62053, Nov. 2014.

[62] P. P. Dash and M. Kazerani, "Dynamic Modeling and Performance Analysis of a Grid-Connected Current-Source Inverter-Based Photovoltaic System," *IEEE Transactions on Sustainable Energy*, vol. 2, pp. 443-450, 2011.

[63] "IEEE Draft Guide to Conducting Distribution Impact Studies for Distributed Resource Interconnection," *IEEE P1547.7/D11, June 2013*, pp. 1-129, 2013.

[64] J. Keller and B. Kroposki, "Understanding Fault Characteristics of Inverter-Based Distributed Energy Resources," NREL, NREL/TP-550-46698, Jan. 2010.

[65] J. Smith, "Stochastic Analysis to Determine Feeder Hosting Capacity for Distributed Solar PV," EPRI, Report No. 1026640, Dec. 31, 2012.

[66] R. A. Walling, R. Saint, R. C. Dugan, J. Burke, and L. A. Kojovic, "Summary of Distributed Resources Impact on Power Delivery Systems," *IEEE Transactions on Power Delivery*, vol. 23, pp. 1636-1644, 2008.

[67] T. Gonen, *Electric Power Distribution System Engineering*: CRC Press, 2008.

[68] "IEEE Standard for Interconnecting Distributed Resources with Electric Power Systems - Amendment 1," *IEEE Std 1547a-2014 (Amendment to IEEE Std 1547-2003)*, pp. 1-16, 2014.

[69] S. Greenlee. (2014, California ISO breaks new solar production record. Available: http://www.caiso.com/Documents/CaliforniaISO_BreaksNewSolarProductionRecord.pdf

[70] Y. P. Agalgaonkar, B. C. Pal, and R. A. Jabr, "Distribution Voltage Control Considering the Impact of PV Generation on Tap Changers and Autonomous Regulators," *IEEE Transactions on Power Systems*, vol. 29, pp. 182-192, 2014.

[71] M. J. Reno and K. Coogan, "Grid Integration Distribution PV (GridPV)," Sandia National Laboratories, SAND2013-6733, Aug. 2013.

[72] M. J. Reno, K. Coogan, R. Broderick, and S. Grijalva, "Reduction of distribution feeders for simplified PV impact studies," in *IEEE 39th Photovoltaic Specialists Conference (PVSC)*, pp. 2337-2342, Tampa Bay, FL, June 16-21, 2013.

[73] MATLAB and Statistics Toolbox Release 2015b, The MathWorks, Inc., Natick, Massachusetts, United States.

[74] M. Mesbahi and M. Egerstedt, *Graph Theoretic Methods in Multiagent Networks*. New Jersey: Princeton University Press, 2010.

VITA

JOHN A. SEUSS

JOHN SEUSS was born in Boynton Beach, Florida. He attended public schools in Delray Beach, Florida and Farmington, Connecticut. He received a B.S. in Electrical Engineering from Georgia Institute of Technology, Atlanta, Georgia in 2006 and a M.S. in Electrical Engineering from the University of Central Florida, Orlando, Florida in 2010 before coming to Georgia Tech to pursue a doctorate in Electrical Engineering. When he is not working on his research, Mr. Seuss enjoys attending concerts and hiking.